Tracking coherences in a dissipative ocean: Analysing and controlling Br_2/Ar matrix

im
Fachbereich Physik
der
Freien Universität Berlin
eingereichte Dissertation
von

Heide Nadda Ibrahim

März 2008

Bibliografische Information der Deutschen Nationalbibliothek
Die Deutsche Nationalbibliothek verzeichnet diese Publikation in der Deutschen Nationalbibliografie; detaillierte bibliografische Daten sind im Internet über http://dnb.ddb.de abrufbar.
1. Aufl. - Göttingen : Cuvillier, 2008
Zugl.: Berlin, FU, Diss., 2008

978-3-86727-648-1

Diese Arbeit wurde in der Zeit von Oktober 2003 bis Februar 2008 unter der Aufsicht von Herrn Prof. Dr. N. Schwentner am Fachbereich Physik der Freien Universität Berlin durchgeführt.

Erstgutachter: Prof. Dr. N. Schwentner
Zweitgutachter: Prof. Dr. L. Wöste
Drittgutachter: Prof. Dr. M. Chergui
Disputationstermin: 04.07.2008

Picture on title: Two dimensional fluorescence - excitation spectrum, see Fig. 4.4.

Nonnenstieg 8, 37075 Göttingen
Telefon: 0551-54724-0
Telefax: 0551-54724-21
www.cuvillier.de

1. Auflage, 2008
Gedruckt auf säurefreiem Papier

978-3-86727-648-1

Kurzfassung

Am Modellsystem eines zweiatomigen Moleküls in einer Edelgasmatrix (Br_2/Ar) wird eine Methode vorgestellt, um verborgene kohärente Strukturen zu verstärken und somit aus einem überragenden, jedoch inkohärenten Untergrund heraus zu präparieren. Dies geschieht durch Überlagerung von phasenkontrollierten Pulssequenzen, die in direkter Weise aus spektroskopischer Information mit einem Pulsformer erzeugt werden. Dazu ist eine sehr präzise Kenntnis der energetischen Signatur des Zielzustands erforderlich. Diese wurde durch hochaufgelöste Anregungsspektroskopie von 630 bis 540 nm der X($v'' = 0$)→B(v') Übergänge, anhand der Emission von A', A und B(v')$= 0$, gewonnen. Schmale Nullphononen - Linien (NPL) wurden von $v' = 2$ bis $v' = 19$ isotopenaufgelöst detektiert. Sie werden von breiten Phononen - Seitenbanden (PSB) begleitet, welche die Phononen - Zustandsdichte der Matrix wiederspiegeln.

Mit höherer Anregungsenergie wurde eine Verbreiterung der NPL und ein Anstieg der PSB durch verstärkten Einfluss der Matrix beobachtet und quantifiziert. Anhand von Intensitätseinbrüchen der NPL, sowie von Linienverbreiterungen und spektralen Verschiebungen wurden zwei energetische Positionen zwischen $v' = 4-5$ und $v' = 7-9$ ermittelt, an denen repulsive Zustände den B Zustand kreuzen.

Der Populationsverlust aus B erfolgt schrittweise über repulsive Zustände in die tieferliegenden elektronischen Zustände A und A', welche auch durch direkte Absorption des matrixgebundenen, dominierenden A Zustands bevölkert werden. Der B Zustand zeigt eine Quanteneffizienz von nahe eins tief im Potential, welche durch matrixinduzierte Prädissoziation zu 10^{-3} bei $v' = 19$ reduziert ist.

Für die zeitaufgelösten Pump - Probe Experimente wurden ultrakurze und daher energetisch sehr breite Laserpulse verwendet. Die Dynamik des B Zustands wird bei Anregung mit 590 nm in einfachen Pump - Probe Experimenten von der A Dynamik vollkommen überlagert. Mit den Pulssequenzen jedoch wurden Wellenpakete im Abstand der B Schwingungsperiode erzeugt, welche, je nach relativer Phasenlage, konstruktiv oder destruktiv interferieren und somit spektral selektieren. Die dazu notwendigen phasenabgestimmten Pulszüge wurden durch Aufprägen der spektroskopischen Signatur des Moleküls auf die spektrale Zusammensetzung der ultrakurzen Pulse erzeugt. Eine phasengesteuerte Kontrolle verlangt eine andauernde elektronische Kohärenz. Diese wurde daher zunächst in Doppelpuls – Experimenten mit einem Michelson Interferometer zu minimal 1.5 ps bestimmt, welches der Länge der verwendeten Pulssequenzen entspricht. Für konstruktive Interferenz durch Anregung der NPL bildet sich die B Schwingungsprogression aus und die A Dynamik wird erfolgreich unterdrückt, da sie nur inkohärent zu einem unmodulierten Untergrund aufaddiert wird. Hierbei wurde eine überraschend lang anhaltende Kohärenz von mehr als 1 ps auch in den PSB durch ein Umkehrexperiment, welches auf destruktiver Interferenz basiert, bestimmt.

Da die Effizienz der Prädissoziation von der Stärke der Kopplung des Moleküls an die Matrix abhängt, wurde diese durch Anregung von Wellenpaketen, welche überwiegend aus NPL oder aus PSB bestehen, gezielt abgeschwächt bzw. verstärkt. So konnte die dynamische Entwicklung der Prädissoziation bestimmt werden. Die Messungen wurden polarisations – sensitiv durchgeführt und auf Temperaturabhängigkeit untersucht.

Meine Arbeit stellt daher eine Kombination aus spektral scharf definierter Anregung und zeitaufgelöster Abfrage vor, die nur durch kohärente Überlagerung ausgedehnter Pulszüge erfolgen kann. Unterstützend wurden Simulationen in erster Ordnung Störungstheorie zum zeitlichen Verhalten der interferierenden Wellenpakete am freien Molekül durchgeführt. Hierbei wurde eine schmalere energetischen Breite der Wellenpakete im Vergleich zur spektralen Breite des Anregungspulses festgestellt, deren Ursache hauptsächlich die Prädissoziation ist.

Abstract

With the model system of a diatomic molecule embedded in a rare gas matrix (Br_2/Ar), a method is introduced to enhance buried coherent structures and thus to prepare them out of an overwhelming, but incoherent background. Therefore, phase controlled pulse sequences are superimposed, which are generated with a pulse shaper in a direct way based on spectroscopic information. This requires a precise knowledge on the energetic signatures of the target state. This was accomplished via high resolution excitation spectroscopy covering 630 to 540 nm of the X($v'' = 0$)→B(v') transition, by detecting emission from A', A and B ($v' = 0$. Narrow zero phonon lines (ZPL) were observed with isotopic resolution from $v' = 2$ to $v' = 19$. They are accompanied by broad phonon sidebands (PSB), which reflect the matrix phonon density of states. With higher excitation energy, a broadening of ZPL and an increase in PSB due to an increase in matrix influence was observed and quantified. By means of intensity drops, line broadening and spectral shifts, two energetic positions between $v' = 4 - 5$ and $v' = 7 - 9$ were identified, where repulsive states cross the B-state. The loss in B population occurs step by step via repulsive states into the deeper lying electronic states A and A', which are also populated by the direct absorption of the matrix bound dominating A-state. The B-state shows a quantum efficiency close to unity deep in the potential which is reduced to 10^{-3} at $v' = 19$ due to matrix induced predissociation. The time resolved pump - probe experiments were carried out with ultrashort and thus energetically very broad laser pulses. The B-state dynamics is completely superimposed by A-state dynamics in single pump - probe experiments with 590 nm. However, with the pulse trains the wave packets were created delayed by the B vibrational roundtrip time, which interfere constructively or destructively and thus select spectrally, depending on the relative phase. The required phase adjusted pulse trains were generated by impressing the molecular spectroscopic signature on the spectral composition of the ultrashort pulse. A phase dependent control scheme requires persisting electronic coherence. This was first determined in experiments with double pulses with a Michelson interferometer to at least 1.5 ps, which corresponds to the length of the experimental pulse sequence. In the case of constructive interference due to ZPL excitation, the B vibrational progression builds up and A-state dynamics is suppressed, successfully, since it adds up incoherently to an unmodulated background. Because of this, a surprisingly long coherence of more than 1 ps - also in the PSB - was determined, due to an inverse experiment, based on destructive interference.

Since the efficiency of predissociation depends on the coupling strength of the molecule to the matrix, it was specifically attenuated or enhanced by excitation with wave packets which are predominantly composed of ZPL or PSB. Thereby, the dynamical development of predissociation could be determined. The experiments were carried out using polarisation sensitive schemes and varied temperatures.

My work thus introduces a combination of spectrally sharp defined excitation and time resolved interrogation, which can only be achieved by the coherent superposition of elongated pulse trains. Further on, simulations on the free molecule in first order perturbation theory were carried out, to investigate the temporal behaviour of the interfering wave packets. It was found, that the energetic width of the wave packet is narrowed in comparison to the spectral width of the excitation pulse, which origins mostly in predissociation.

Contents

List of Figures

List of Tables

Abbreviations

BBO	Beta barium borate, ß-BaB_2O_4
CCD	Charged coupled device
CPA	Chirped parametric amplifier
CT	Charge transfer
CW	Continuous wave
DFG	Difference frequency generation
FC	Franck - Condon
fcc	Face centred cubic
fs	femto second $(10^{-15}$s)
FWHM	Full width at half maximum
LiF	Laser induced fluorescence
LC SLM	Liquid crystal spatial light modulator
nm	nanometer $(10^{-9}$m)
NOPA	Noncollinear optical parametric amplifier
OMA	Optical multichannel analyzer
PLPP	Phase locked pulse pair
ps	pico second $(10^{-12}$s)
PSB	Phonon side band
SFG	Sum frequency generation
SHG	Second harmonic generation
THz	Tera Hertz $(10^{12}$s$^{-1})$
ZPL	Zero phonon line

Introduction

"That's funny," said Pooh, throwing sticks into a creek.
"I dropped it on the other side," said Pooh,
"and it came out on this side!
I wonder if it would do it again?"
It did [...]
Then he dropped two in at once,
but as they were both the same size,
he didn't know if it was the one
which he wanted to win,
or the other one.
So the next time he dropped one big one
and one little one.
A. A. Milne
Winnie - the - Pooh

From the very beginning, human beings tend to control their environment - sometimes with, sometimes without analysing the conditions on site, in advance. Environment can mean other creatures, it can be nature in general or - after several thousand years of development - a chemical reaction controlled by light, like in this work. The concept of control is not restricted to the traditional light – matter interaction by varying energy or power of light to yield for example photo-ionisation of molecules. In the past 15 years experiments have advanced to scales, where the quantum nature of systems become more and more apparent [1–4]. This requires sophisticated tools and they are found in femto second (fs, 10^{-15}s) lasers and pulse shapers. These pulses permit one to sample the movements of atoms on fs timescales [5], even combined with atomic spatial resolution [6] in X – ray diffraction. Pulse shapers allow for a computer controlled manipulation of the broad spectral distribution which is incorporated with ultrashort time events. By means of optical Fourier transformation, separated frequencies can be addressed in the Fourier plane. Herewith, nearly arbitrary temporal waveforms can be generated with respect to amplitude, phase and polarisation. Such a toolbox provides the capability to intervene in molecular dynamics and simplify the transient response of a system by enhancing one mode with respect to others due to wave packet interferences [7–13]. This selection is obtained by generating pulse trains which preferentially couple to one mode and this mode can be more and more amplified [14, 15], like in the picture of a child on a swing which is pushed with a period matching to the recurrence time.

A further development is the steering of chemical reactions due to varied compositions of molecular wave packets [16–18]. In the framework of this thesis, predissociation of a diatomic molecule embedded in a rare gas crystal is controlled.

How to find out which waveform is required to accomplish a distinct task? A common technique is the appliance of evolutionary algorithms in experiment [19] or on the theoretical side, optimal control theory (OCT). Both strategies record an observable and try to maximise its value by changing the field parameters, $i.e.$, in experiment a closed loop between computer, shaper and detector. Amazing results are obtained and recently reviewed in [20], however, two difficulties

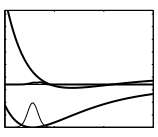

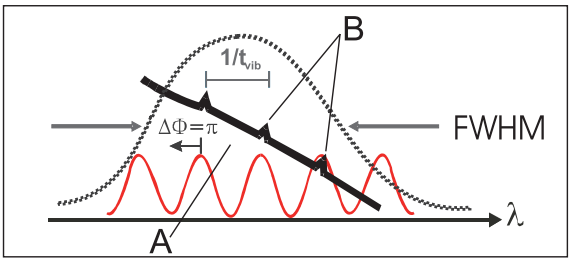

Figure 1: Spectral representation of the light absorption of a molecule when two pulses with a time separation of T_{vib} interfere. The first pulse excites a broad distribution indicated with the dashed envelope. Two pulses lead to a sinusoidal interference pattern (thin solid line). If their relative phase $\Delta\Phi = 0$, the spectral maxima match the vibrational progression on the absorption spectrum (thick solid line). For $\Delta\Phi = \pi$ it is shifted to the minima.

remain: First, one has to prevent the algorithm from getting trapped in a local extremum. And second, it is rather challenging to interpret the composition of the optimised waveform. In contrast, a straightforward strategy was chosen in this work: In tutorial experiments with a Michelson interferometer, time delay and relative phase between the two pulses were scanned and the molecular response due to the changing composition of wave packets was analysed [21]. To gain enhanced selectivity, sequences of several pulses are required, which can include spectral characteristics like the molecular anharmonicity and even shiftings of vibrational levels due to couplings with other electronic states. Access to their generation lies in the frequency domain. There, the vibrational progression which should be enhanced was directly written on the pulse shaper - pixel by pixel, based on a deep spectroscopic analysis [22]. This refrains from a description of complex analytic functions and works successfully, since the right timing and relative phases of the pulse sequence are adapted inevitably.

The halogen bromine, embedded in an argon crystal turned out to be an ideal model system for coherent control experiments. Absorption spectra are dominated by a structureless background labeled A - the dissipative ocean which is indicated in Fig. 1 as thick solid line. Latent coherent signatures marked as B, shown as small peaks on the background, were found in it. The spacing of B is inversely proportional to the vibrational roundtrip time T_{vib}. The aim is to amplify these peaks with pulse sequences designed in phase ($\Delta\Phi$) and amplitude. Each pulse individually excites non - selectively a broad envelope (dashed line). Sharp spectral features are the result of interference effects of several pulses which is indicated with the sinusoidal distribution (thin solid line). Playing with $\Delta\Phi$ allows for a shifting of selected frequencies with respect to the envelope and thus enhancing or attenuating the excitation of the faint coherent features.

The concept of wave packet interference and the required coherences are introduced in Ch. 1. Various knowledge on Br_2/Ar exists on a very high level and is collected in Ch. 2. However, the elaborate control experiments of this work which are introduced in Ch. 3, require even more detailed spectroscopic information concerning intensities, energetic positions or frequency resolution and the literature is contradictory. Thus, detailed frequency resolved experiments in Ch. 4 solving the inconsistencies, and a time resolved analysis in Ch. 5 were prefixed to the final control experiments in Ch. 6.

Two positions of curve crossings of repulsive states with the covalent state B were determined from a two dimensional spectrum of emission $vs.$ excitation wavelength, which covers nearly the whole bound area of the B-state. Sharp zero phonon lines (ZPL), representing the molecular vibrations, and broad phonon side bands (PSB) which were assigned to the crystal's phonon density of states are clearly pronounced. The side bands increase at higher matrix contributions and merge to a continuum. These signatures reveal information on matrix induced predissociation. This knowledge was applied in the control experiments to manipulate the efficiency of population transfer from the B-state to other electronic states. Investigating the bound part of the B potential is com-

plicated due to larger absorption probabilities of the A-state which is matrix bound in this energy region. The A-state interaction with the matrix causes the dominant unmodulated background in Fig. 1. This work succeeded in picking out the faint coherent signatures from the overwhelming background and in controlling matrix induced predissociation. It gives a deep insight into the complex interaction of guest and host and a straightforward method to track weak coherent dynamics in a dissipative ocean.

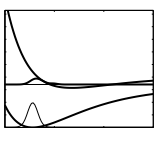

Chapter 1

Coherence and wave packet interferometry

Throughout this whole thesis the idea of Heisenberg's uncertainty principle restrictions will be present. It connects the resolution limits of time and frequency resolved spectroscopy. In the case of time resolved spectroscopy we deal with ultrashort laser pulses on the order of femto seconds (fs, $10^{-15}s$), which necessarily have an energetic width of several hundreds of wave numbers for visible light. Or to speak in molecular language, several vibronic eigenstates are covered by the pulse width. Applying the techniques of frequency resolved spectroscopy leads to the other extreme. The wavelength resolution is strongly enhanced, however, the pulses become long and time resolved information about molecular dynamics is lost.

We are well aware of these phenomena in the limiting cases of long and short pulse durations. In this work it will be tried to combine dynamical measurements with spectrally selected molecular excitation. Coherent control schemes will be applied, which rely on the flexible generation of sharp spectral features, $e.g.$, like a frequency comb whose wavelength and spacing can be adjusted. Therefore, it is of interest in which way the molecular system takes up the information of pulse durations. In Sec. 1.2 it is shown that the molecule does not "know" in the beginning of the control pulse how the electric field of the exciting light will evolve with time and whether it belongs to an ultrashort laser pulse or to a CW source [23, 24]. It does not even "know", whether it is excited in a bound or a repulsive potential. All this information has to develop in time due to interferences of the newly excited wave packet with the already propagating one. In the first moment of excitation the spectrum is comparable to a whitelight continuum.
Sharp spectral features are the result of constructive interferences at spectral maxima and destructive interferences at the minima. They can only be pronounced when the early part of the absorbed light and the late one act on the same conditions, $i.e.$, all coherences are preserved. But these coherences in a molecule will be affected by the presence of an environment. For molecules isolated in a rare gas crystal an electronic and vibrational transition will also lead to an electronic and vibrational coupling of the chromophore with the matrix, since molecule and cage atoms are close together, even in the equilibrium configuration of the ground state.

This chapter is arranged as follows: First, the concept of a wave packet, describing the motions of a molecule in a quantum mechanical way is introduced. Second, the term coherence is described classically and quantum mechanically being the basic requirement for the observation of sharp spectroscopic signatures. Then, the process of light absorption will be discussed in terms of wave packet interferometry. Electronic and vibrational coherences are essential for applying a coherent control of chemical reactions with light. In our case, this control acts on the coupling between the chromophore and the surrounding matrix, treated finally.

1.1 Wave packets

A short laser pulse exciting a molecule coherently couples several energy eigenstates $|\phi_n\rangle$ having their eigenvalues E_n [25, 26], due to its large spectral width. This superposition of eigenstates

leads to a wave packet $|\Psi(t)\rangle$:

$$|\Psi(t)\rangle = \sum_n c_n e^{-i\frac{E_n}{\hbar}t}|\phi_n\rangle, \tag{1.1}$$

with c_n being the excitation coefficients. In general, $|\phi_n\rangle$ can be electronic, vibrational or rotational eigenstates of the molecule, here only the vibrational ones will be treated. The absolute square of a such a vibrational wave packet is called the population of an electronic potential energy surface. A wave packet with the superposition of eigenstates always obeys Heisenberg's uncertainty principle restriction, which is in the time - energy representation:

$$\Delta E\, \Delta t \;\geq\; \hbar/2. \tag{1.2}$$

This requires for an ultrashort event a wide-stretched contribution of eigenstates. In the other extreme, with a long pulse duration it is possible to reduce the energetic width to a single eigenstate. In Sec. 1.2 these ideas will be taken up again.

1.1.1 Franck - Condon principle

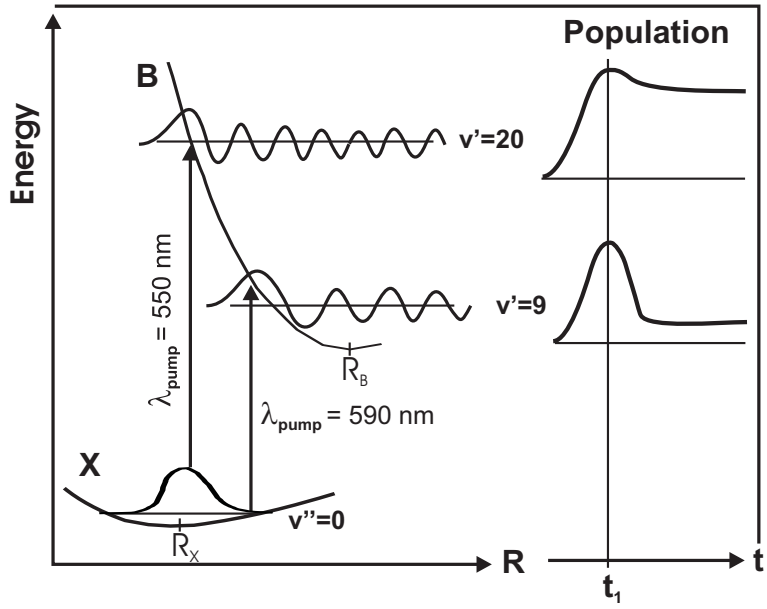

Figure 1.1: Franck - Condon principle with potential parameters of the Br_2 molecule. On the left hand side schematically the excitation of two different transitions X($v''=0$)→B($v'=9$) and X($v''=0$)→B($v'=20$) is displayed. R_X and R_B are the equilibrium internuclear distances. On the right hand side a plot of created population of the B-state $vs.$ time is given, where t_1 is the centre of excitation pulse.

The probability for transitions from a vibrational level v'' of the electronic ground state X to vibrational levels v' of an electronically excited state B depends on the overlap of wave functions of both states.

Figure 1.1 demonstrates the Franck - Condon (FC) principle with two different excitation energies shown on the left hand side. The specific numbers for wavelength and vibrational levels are chosen for the Br_2/Ar potentials. However, at this point they are not of major importance. In the case of bromine, the potential minima for ground and excited state are not at the same position and the equilibrium internuclear distance changes during the electronic excitation from R_X to R_B. On the ground state X the quantum mechanical wave function for $v''=0$ is plotted, the only occupied level in our case, having its maximum in the centre, at R_X, where the classical kinetic energy E_{kin}

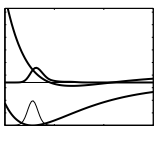

of the atoms is maximal. This is in contrast with the classical picture, where the largest probability of residence is expected to be at the turning points. For higher vibrational levels sketched on the electronically excited potential B, the expectation values better approximate this classical picture. The probability $P(\chi_{v''}, \chi_{v'})$ of a vibronic transition X($v'' = 0$)→B(v') is calculated in the Condon approximation with constant electronic transition moment by the FC overlap integral [27] with the nuclear vibrational functions of ground state X $\chi_{v''}(R)$ and excited electronic state B $\chi_{v'}(R)$:

$$P(\chi_{v''}, \chi_{v'}) = \int \chi_{v''}(R)\, \chi_{v'}(R)\, dR, \tag{1.3}$$

and integrating over the complete internuclear distance R. In the case of bromine, the transition to $v' = 20$ with $\lambda_{pump} = 550$ nm is close to the FC maximum. This can be immediately seen since the maxima of both wave functions are centred on top of each other. For the excitation at lower energy $\lambda_{pump} = 590$ nm, again the maximum in the $v' = 9$ wave function is met, however only in the far wing of the Gaussian wave function of the ground state and thus the value of the FC integral, called the FC factor, decreases dramatically. This effect will be part of the discussions in the experimental chapters, since the experiments utilize this energetic region. The gas phase FC factors of bromine are given in Fig. 4.20. The way in which the probability factors effect the population of an excited state versus time is demonstrated at the right hand side in Fig. 1.1 for a pulse that is short compared to the vibrational roundtrip time. Population is increasing as long as the intensity of the excitation pulse is increasing (until the envelope reaches a maximum) and this time is marked with t_1. For the transition close to the FC maximum $\lambda_{pump} = 550$ nm the excitation is called $resonant$ and nearly all population pumped into the B-state remains there when the pulse amplitude is decreasing. The more an excitation energy deviates from the resonant transition energy, the less population can stay in the excited state due to destructive interference effects at longer times. Instead of a further increase, population is dumped back to the ground state while the pulse is fading. For a $non-resonant$ transition like in the $\lambda_{pump} = 590$ nm case, only a small amount compared to the population reached for the pulse intensity maximum remains. Once the pulse is terminated, the amount of population is fixed. This effect shows up in the wave packet simulations of Sec. 6.3.3.

One idea to increase the population of the excited state accessed by the non – resonant transition would be to burn a hole in the ground state with a first pulse, in order to obtain a propagating wave packet which covers several $v'' > 0$. When the ground state wave packet reaches the outer turning point its expectation value there is raised and a second pulse coming at the right time would benefit from the increased FC factors for this transition [28]. However, an amount of 10-20% of the ground state population would have to be pumped to an upper state until this effect would be significant.

In the simulations discussed in Sec. 5.2.1, the overlap integral is inherently involved and FC factors can be derived.

The discussed control schemes require $coherence$, and this term will be introduced in the next section.

1.2 Coherence

The terminology of coherence, necessary for an understanding of the time resolved control experiments, but also of the frequency resolved spectra, is introduced from the classical point of view. The question to be addressed, is a loss of phase relations in between an ensemble of oscillators [29, 30], representing, $e.g.$, the vibrations of a number of molecules. For simplification the oscillators are treated as harmonic ones, in the beginning.

It is useful to represent this problem in classical phase space where the oscillations can be treated in momentum p $vs.$ space coordinate q in appropriate units. The oscillations follow iso-

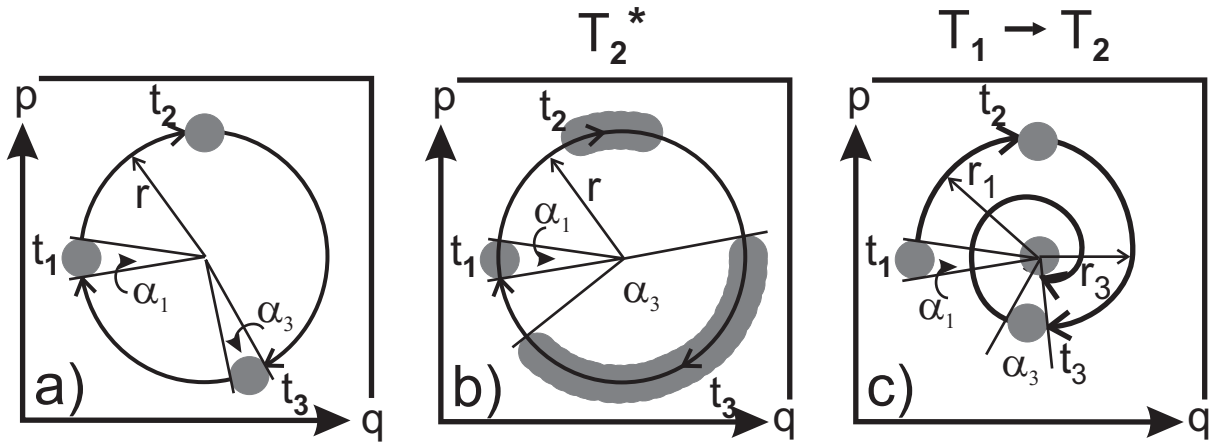

Figure 1.2: A sketch for dephasing is shown with the distribution of an ensemble of free harmonic oscillators at three different times $t_1 < t_2 < t_3$ in phase space with q (position) $vs.$ p (momentum). In the case of $full\ coherence$, $i.e.$, no dissipation or dephasing in a) the shape does not change, the constant energy shell is not left (r = const) and therefore the angle α related to the extension in classical phase space is constant in time. In b) $pure\ dephasing$ is depicted, with a distribution spreading over the course with time and inducing an increase in the angle thus $\alpha_1 < \alpha_3$. $Dissipation$ in c) leads also to an increase in α for the same extension in phase space due to a loss in energy. It spirals down to equilibrium energy in the minimum (r_1<r_3). This figure is adapted from Ref. [26]

energetic circles in these coordinates as long as no energy is lost. Those circles can be described with their radius r, where $r^2 = p^2 + q^2$ starting from the origin of phase space as can be seen in Fig. 1.2. Looking from this centre towards the phase - momentum distribution defines the angle α. Panel a) shows the situation of complete coherence, where no dephasing processes occur. As grey disks the momentum - space distribution of the ensemble of free harmonic oscillators at three different times ($t_1 < t_2 < t_3$) is shown. The ensemble propagates on the iso-energetic circle without changing its shape and thus the reference angle α is constant for all times. In plot b) $pure\ dephasing$, $e.g.$, due to elastic scattering of the molecules is depicted, the dephasing time T_2^* will be introduced soon. The overall energy of the ensemble of oscillators is conserved, therefore it still propagates on the same circle with time. However, different oscillators experience a slight change in phase and the disk of the whole ensemble smears out. For a large time (not shown), the ensemble would completely fill out the circle and $\alpha = 2\pi$; then it is called $fully\ incoherent$. In c) $dissipation$ due to inelastic scattering (concerning this thesis: vibrational energy relaxation) is illustrated where the shape of the distribution disk does not change since no pure dephasing occurs. Whereas, the whole ensemble looses energy and follows a spiral trace down to the centre of phase space. Measuring the angle from the centre, again, α is increasing until it reaches 2π at the end of the spiral, illustrating that dissipation (T_1) leads to dephasing (T_2) as well.

In a real molecular system embedded in a matrix cage one has to deal with different types of coherences and two shall be discussed, exemplified in Fig. 1.3. In a) the loss of electronic coherence is addressed. The cage can act as a static inhomogeneous or moving solvent and cause a relative shift of effective potentials B in energy ΔE and/or internuclear distance ΔR (solid and dotted lines), compared to the ground state X for individual molecules. This leads to electronic dephasing, since the phase will vary in individual transitions to B. The terms $dephasing$ and $decoherence$ are synonymously used and specified in the following.

For the experiments treated here, electronic and vibrational coherence will be necessary as long as the light pulse or pulse train acts on the molecule in order to couple the contributing electronic

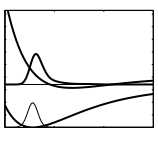

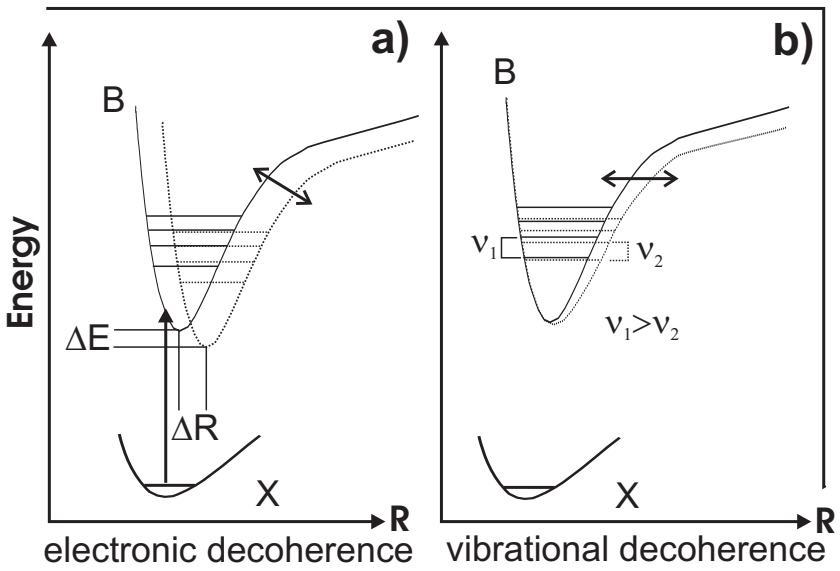

Figure 1.3: Model for electronic and vibrational decoherence. a) electronic coherence strongly depends on a fixed relation between ground state X and excited state B. Cage influence might lead to a shift of the upper potential and thereby the transition energy shifts by ΔE and leads to electronic dephasing. b) vibrational coherence is decoupled from electronic transitions but relies on the vibrational spacing ν. If the cage changes, $e.g.$, the outer wing of the higher lying potential of an ensemble, ν is affected and vibrational dephasing occurs.

states coherently. Only under this condition complete coherent control can be maintained. Depending on the density and symmetry of the environment, the electronic coherence is typically on the order of femto - to picoseconds for condensed systems [17, 21] and thus orders of magnitude shorter than for gas phase systems, as will be discussed in Sec. 2.2.7. In the scheme for electronic decoherence in Fig. 1.3a, the vibrational spacing of the oscillators is not affected, since the potential energy surface is not deformed. Therefore, vibrational coherence is preserved. Figure 1.3b shows a possible scenario for vibrational decoherence. Now, due to a change in the surrounding cage, the outer wing of the effective potential B (solid line) with vibrational spacing ν_1 may be flattened (dotted line) into another oscillator with smaller vibrational spacing ν_2. In that case, the ensemble of oscillators will no longer vibrate with one and the same period and this will cause decoherence and a line broadening of the spectroscopic signature corresponding to this vibration. Two kinds of line broadening have to be explained: Homogeneous broadening occurs for all members of an ensemble in the same way, in our case, due to a similar cage influence. Another effect is inhomogeneous broadening, $e.g.$, because of disorder or isotopic effects. Due to the different masses of isotopes, different members of the ensemble have slightly different oscillatory properties. Vibrational coherence, describing the undisturbed phase relations of two or more vibrational eigenstates can last even for solids in the pico second regime [2, 3, 21, 31–34].

Up to now the coherence effects were described from the classical point of view. Quantum mechanically, one introduces the density operator which will be described here briefly. For greater detail one is referred to the text books [25, 26]. The density operator ρ is in general defined as

$$\rho = \sum_k p_k |\Psi_k\rangle\langle\Psi_k| \tag{1.4}$$

where $|\Psi_k\rangle$ is a wave function or with Eq. 1.1 a wave packet and with the probability p_k the system will be found in the state $|\Psi_k\rangle$, where $\sum_k p_k = 1$. For of a pure state, the complete system is in

one state, otherwise it is called a mixed state.

In order to connect $\rho(x, x')$ as the density operator in the space representation to the wave packet in energy representation, a mathematical transformation, exemplified for a pure state, leads to:

$$\begin{aligned} \rho(x, x') &= \langle x|\Psi\rangle\langle\Psi|x'\rangle \\ &= \sum_{m,n} \psi_m(x)\rho_{mn}\psi_n^*(x), \end{aligned} \tag{1.5}$$

being the density matrix with elements $\rho_{mn} = c_m c_n^* e^{-\frac{i}{\hbar}(E_m - E_n)t}$. Diagonal elements

$$\rho_{nn} = \sum_k p_k \, |c_n^{(k)}|^2 \tag{1.6}$$

represent the $population$ of the energy eigenstate, since they do not include any time dependent behaviour. Only for all $|c_n^{(k)}|^2$ being zero it is possible to get a population equal to zero. All wave packet dynamic is kept in the off-diagonal elements

$$\rho_{mn} = \sum_k p_k \, c_m^{(k)} \, c_n^{(k)*} \, e^{-\frac{i}{\hbar}(E_m - E_n)t} \tag{1.7}$$

which are named $coherences$. These complex numbers are necessary to describe wave packet interferences. It is possible that the ρ_{mn} vanish, even if all $c_m^{(k)} \, c_n^{(k)*}$ are non-zero.
A matrix element $\rho_{mn} = 0$ means that interference effects smear out and the coherence between the states is lost.

Decoherence effects described earlier in the classical way can be transferred to density matrix calculations. However, the simulations described in Chs. 5 and 6 are based on a wave packet representation with complete coherence, instead of the density matrix. Thus, I refrain from the extension to decoherences, with referring to [35]. Only a brief connection shall be given: From the quantum mechanical point of view, the phase distributions in Fig. 1.2a and c) represent a minimum uncertainty wave packet. Pure dephasing in panel b) is associated in quantum mechanical calculations with the decay rate $1/T_2^*$ and dissipation in plot c) with $1/T_1$. Calculations for halogens in matrices, $e.g.$, the diatomics in molecules[1] (DIM) formalism, use in general a classical or semiclassical approach [36–38]. The latter combines a quantum wave packet with a dynamical potential obtained by classical interaction of the molecule with the environment. With reduced degrees of freedom also full quantum mechanical treatment was carried out [39–41].

Describing a real diatomic molecule, the harmonic approximation does not hold and an anharmonic potential, usually the Morse potential $V(R)$, related to the equilibrium nuclear distance R_e [27, 42] is required:

$$V(R) = D_e(1 - e^{-\alpha(R-R_e)})^2, \tag{1.8}$$

with

$$\alpha = \sqrt{\frac{\mu}{2D_e}}\omega_e, \tag{1.9}$$

where μ is the reduced mass, ω_e the harmonic eigen frequency and D_e the dissociation energy:

$$D_e = \frac{\hbar\omega_e}{4x_e}, \tag{1.10}$$

[1] The DIM formalism is based on the pair potentials between all atoms.

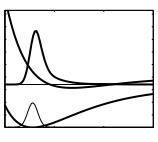

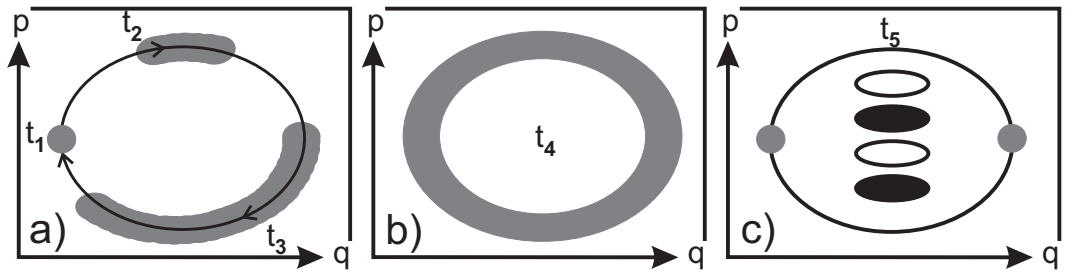

Figure 1.4: Dispersion and revival: In analogy to the dephasing picture in Fig. 1.2, this time a single anharmonic oscillator is plotted to demonstrate the effect of dispersion. In a) the spreading of the distribution with time (t_1<t_2<t_3) looks similar to Fig. 1.2b. At time t_4, after further propagation, it fills out the whole energy shell in b). However, this spreading is reversible as can be seen in c) for a 1/2 revival at t_5. The black and white ellipses indicate quantum mechanical interference effects.

The anharmonicity of a molecule is given by x_e.

In the case of complete coherence, a wave packet will never disperse in a harmonic potential since all energetic components of the wave packet travel with the same speed. This is different for an anharmonic potential: The vibrational spacing ν depends on energy E and is no longer equidistant like in the harmonic oscillator. It is described by

$$\nu(E) = \frac{\omega_e}{2\pi}\sqrt{1 - \frac{E}{D_e}}. \tag{1.11}$$

For the components of a wave packet having higher vibrational energy (blue), the vibrational spacing is smaller than for the low energy parts (red), resulting in a longer vibrational period $T_{vib,blue} > T_{vib,red}$ with

$$T_{vib} = 1/\nu \tag{1.12}$$

and ν being inserted in units of Hz. Blue components travel with a lower speed than red components. The wave packet spreads out and disperses as demonstrated in Fig. 1.4a and b). The phase space distribution of a wave packet is plotted with its meaning in analogy to the dephasing in Fig. 1.2. However, this time, only one anharmonic oscillator is necessary for the effect. Comparable to Fig. 1.2b the distribution also smears out in Fig. 1.4a and b). This wave packet spreading is not easily distinguishable from the effect of pure dephasing.
When exciting the molecules with a negatively "chirped" laser pulse (see Sec. 3.3.2) first the blue wave packet components will be excited, followed by the red ones. Thus, the effect of dispersion on the potential can be pre-compensated. The molecular wave packet starts broadened and is optimally localized at the focussing time T_{opt}. This will be discussed in detail in Sec. 3.4.1 and Eq. 3.22.

Also with an unchirped excitation, interference effects of the wave packet on an anharmonic potential can lead to focussing. The time T_{rev} until a socalled $revival$ occurs, depends on the anharmonicity [2, 26, 43]:

$$T_{rev} = \frac{2\pi}{\omega_e x_e}. \tag{1.13}$$

The anharmonicity x_e is the constant in the Morse potential corresponding to a similar phase slip of successive periods which accumulate to 2π after T_{rev}. Fractional revivals on the order of m occur due to wave packet interferences at times T_{rev}/m.

In Fig. 1.4c the 1/2 fractional revival is depicted, which appears at $T_{rev}/2$. The wave packet is not unified at one internuclear position on the potential, but at the inner and at the outer turning

point simultaneously. The quantum mechanical interference effects are indicated by the white and black ellipses in the plot. They are lost, when the interference pattern is projected to the q - axis. A variation of p and q due to different energies in pump - probe experiments, however allows for a sampling of the so-called quantum carpet [4].
A 1/2 revival pattern can also be achieved by exciting two wave packets of time delay $T_{vib}/2$ with phase locked pulses, as will be discussed in the Michelson experiments in Sec. 3.4.3. Simulations, which are not presented here, however showed that those two wave packets will never unify and no full revival can be maintained.

As a summary, concerning the terms $dephasing$, $decoherence$ and $dispersion$, I will strictly distinguish between irreversible and reversible processes. In this work, the terms dephasing and decoherence are used synonymously for an irreversible loss of phase information due to elastic or inelastic scattering. On the contrary, dispersion is a reversible spreading of phases of a wave packet in phase - space. It will result in a loss of clearly pronounced temporal features like wave packet dynamics. Nevertheless, this is only apparently a loss of phases. As was shown in our group [2], quantum effects like revivals or fractional revivals are a proof that the full phase relation will be observable again after some time T_{rev}, as long as there are no additional irreversible dephasing process.

Absorption and wave packet interferometry in the time dependent framework

This section compares molecular excitation with nanosecond (quasi CW) light with fs excitation by a pulse train. The ns excitation causes a kind of auto - correlation of a wave packet, which interferes with itself. A pulse train excitation on the other hand, can be considered as cross - correlation of several wave packets interfering on the potential, as will be shown in the following. Both types require coherent absorption of the light for a phase stable superposition.

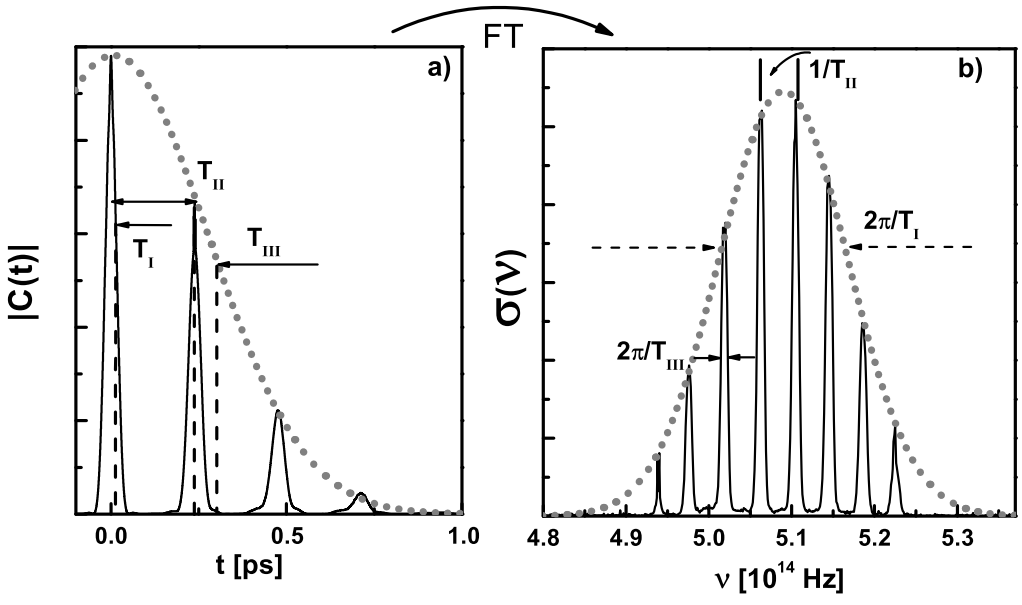

Figure 1.5: a) Time representation of a sequences of pulses with decay time T_{I}, spacing T_{II} and overall decay time T_{III} which are explained in the text. b) Fourier transformation of a) with spectral signatures of the displayed times.

Heller created the picture [23, 24, 26] connecting the dynamics of a vibrational wave packet propagating on an electronic potential with its frequency representation, the absorption spectrum $\sigma(\nu)$ via a Fourier transformation. Spacings in the time domain correspond to inverse spacings in the frequency domain, while the width of the overall envelope in one domain determines the inverse width of substructures in the other domain. He called this the auto - correlation of a wave packet.
This picture holds also for a sequence of ultrashort laser pulses being separated by the vibrational round trip time $C(t)$ and the corresponding signature in frequency domain[2] $\sigma(\nu)$:

$$\sigma(\nu) \;=\; \int_{-\infty}^{\infty} C(t)\, e^{-i\nu t}\, dt\,. \tag{1.14}$$

Figure 1.5a shows with $|C(t)|$ (in analogy to the nomenclature of Heller) parts of the pulse train (solid line) and its envelope (dotted line) and three exposed times $T_{\mathtt{I}}$, $T_{\mathtt{II}}$ and $T_{\mathtt{III}}$ marked by dashed lines. Coming back to Heller's picture, this would be the propagation of a wave packet, until it decays, $e.g.$, due to dissociation processes. With $T_{\mathtt{I}}$ the decay time of the shortest feature in time is described, which is the length of a laser pulse. In the spectral representation $\sigma(\nu)$ of plot b) this determines the overall envelope of contributing frequencies with the connection $2\pi/\mathrm{T}_{\mathtt{I}}$ shown by the two dashed arrows in panel b). Vice versa, the decay time of the time envelope $T_{\mathtt{III}}$ in a) determines the width of the narrowest structure in frequency marked by the two solid arrows to $2\pi/\mathrm{T}_{\mathtt{III}}$ in b). Finally, from the spacing in the time domain in a) displayed by $T_{\mathtt{II}}$ one can deduce the spacing in frequency to be $1/T_{\mathtt{II}}$ in b).

Principally, the very same connections can also be found in a modified Young's double slit experiment [44] which is extended to multiple slits examining interference effects of light. In that case, the number of slits determines the narrowest features in the interferogram, the width of the slits gives its envelope and the distance the period. The idea of a spacial double slit was transfered to the time domain, with two ultrashort laser pulses [45]. Their duration again assigns the envelope of the interferogram and their time delay specifies the steepness of interference structures. This will be the idea of control experiments described in Sec. 3.4 and performed in Ch. 6.

1.2.1 Auto - correlation on the molecule with ns excitation

Following Heller's idea, the excitation with CW light is treated as auto - correlation of a wave packet, which is helpful for the different excitation schemes applied in this thesis. Usually, one connects a light source being narrow in frequency domain with an event comparably long in time and this is of course right. Nevertheless, for the observation of sharp spectral features the duration in time is not the only necessary parameter. Also electronic coherence has to be preserved, since constructive interference of the wave packet requires stable phases. These conditions determines the spectral features of the evolving molecular eigenstates. Figure 1.6 displays this development at three different times; in the first column in plot a) the excitation on the potential for the first part of the exposure at $t = 0$ is shown as the grey shaded area. Even starting a CW – like light source with a final measurable spectral width on the order of 1 cm^{-1}, leads in the beginning to a continuous excitation in the complete left wing of the potential, similar to whitelight excitation. At time zero eigenstates are not yet existing, the wave packet does not "know", whether it is located on a repulsive or on a bound potential surface, therefore the positions of vibrational eigenstates are marked with dashed lines, only. The thick vertical arrow indicates that excitation still persists while the horizontal arrow to the right gives the direction of the wave packet's propagation. In b) the corresponding time scheme is given with a sharp edge indicated by the dashed line and in c) its

[2]Equation 1.14 shows the definition of a Fourier transform following the software Matlab.

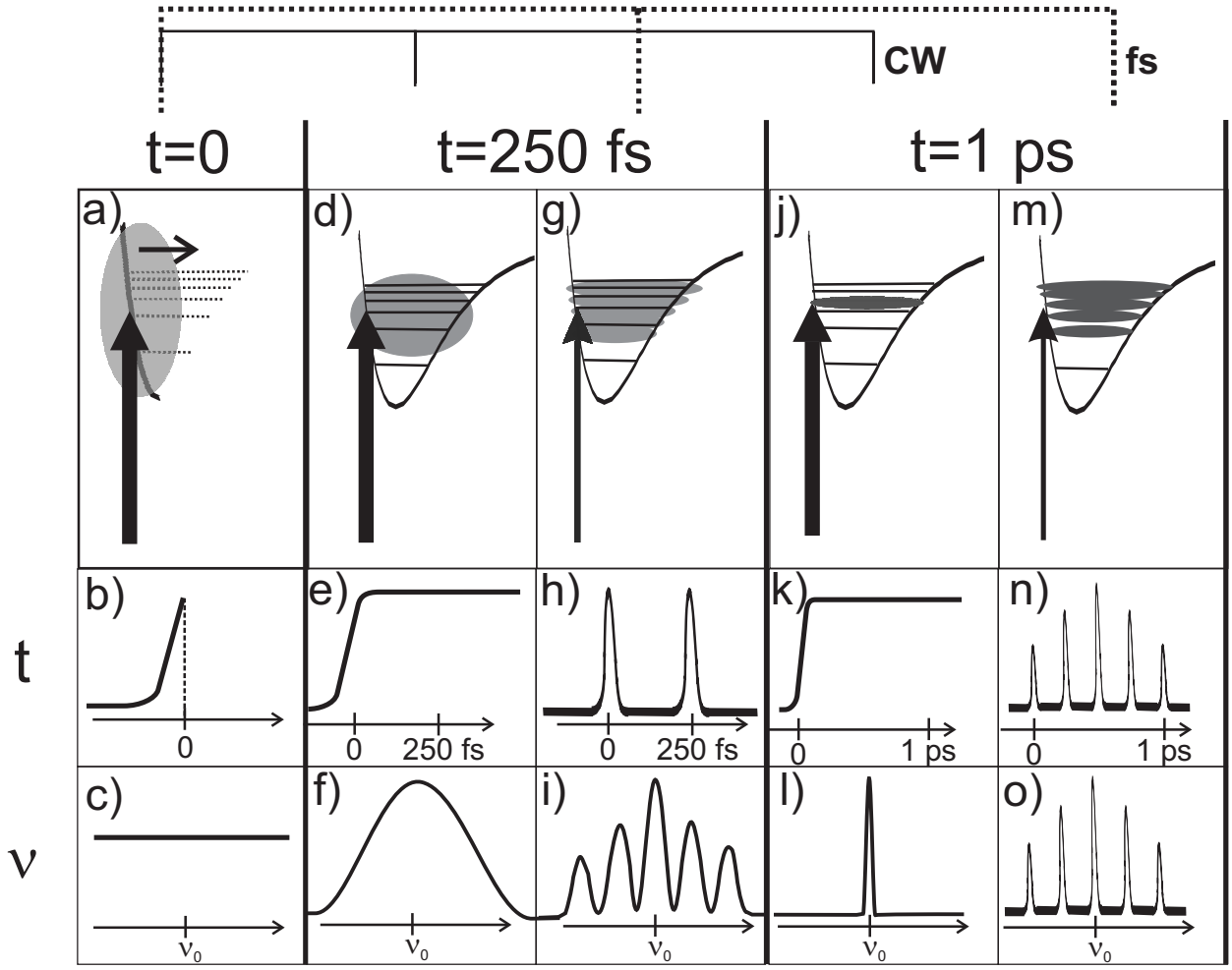

Figure 1.6: Wave packet scheme for auto - correlation with ns excitation and cross - correlation with a pulse train of ultrashort pulses at three different times ($t = 0$, 250 fs and 1 ps) in the first row. The second row displays schematically the time evolution of light with changing scale as given by the numbers and the third row the corresponding frequencies on a constant scale.

frequency representation, a continuum, obtained by Fourier transformation. Once, the wave packet has reached the outer turning point for the first time in d) it has experienced the potential shape, changed its direction at the outer turning point and returns to the inner limb of the potential after 250 fs. Still, the excitation light persists and new parts of the wave packet are furthermore created. Therefore, in- and outgoing components of the wave packet start to interfere. The longer the light wave continues in a coherent manner in e), the more the frequency distribution in f) narrows around the centre frequency ν_0, but still it is very broad. After $t = 1$ ps in the column starting with j) the first parts of the wave packet have travelled several times back and forth while still more population is excited from the ground state. This can continue, as long as electronic coherence between ground and excited state and vibrational coherence on the excited potential are preserved. The contributing energies on the potential shrink around the centre energy as indicated by the overlapping grey areas. It is also recognisable in the frequency spectrum of l), now with a sharp peak. For this evolution of sharp spectral features, light has to pump the excited state continuously and one spread-out wave packet interferes with itself and the newly created components, which requires electronic coherence. Inversely, from the linewidth and thereby the lifetime of a vibrational progression one

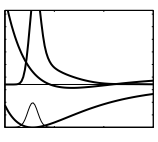

can draw conclusions about the minimal value of the electronic coherence, since it is usually the limiting factor of the linewidth.

Exciting with a phase stabilised sequence of ultrashort laser pulses can extend to similar long timescales, however, the principle effects are slightly different and also the result is quite different.

1.2.2 Cross - correlation on the molecule with fs pulse train excitation

At the very beginning $t = 0$ no difference between the two discussed types of excitation can be observed, but as soon as the first fs pulse of the sequence terminates, the remaining spectral width on the potential is determined and this is much broader than in the case of ns excitation described earlier. This development is also shown in Fig. 1.6, in the columns skipped before. In plot g) at $t = 250\,\text{fs}$ the first wave packet has completed one round trip and interferes with the second wave packet, which was just created. Its time representation shows the two laser pulses with a time difference of 250 fs in h) and the frequency pattern in i) has a broad envelope due to the short time duration of the pulses and a sinusoidal substructure due to the two-pulse interference. Again, after 1 ps in m) the interference structures are sharper and different from plot j) where the wave packet concentrates around one vibrational eigenstate. Now several of them are selected out due to constructive interference and the train of sharp events is visible in time (n) and frequency domain (o). Since the pulse train is over after 1 ps the picture does not change anymore for longer times.

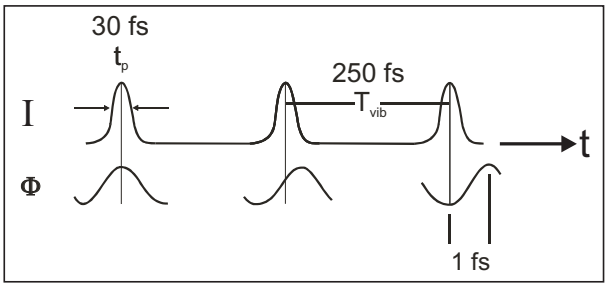

Figure 1.7: Scheme of a pulse train of ultrashort laser pulses (30 fs) where the relative phase Φ is controlled. This corresponds to a accuracy of 1 fs.

Summarising, excitation of a molecule with ns light pulses (and longer) allows for a preparation of one vibrational eigenstate, if the light is absorbed in a coherent way. Under the same conditions, the excitation with a phase controlled pulse train gives the opportunity to generate a frequency comb and thereby couple several vibrational eigenstates coherently. In the description up to now, the phase between the single pulses of the pulse train was kept constant to obtain constructive interference in this simple picture. Of course, this relative phase can also be varied and such phase differences will be used to steer the control experiments of Ch. 6. An example is given in Fig. 1.7, demonstrating the meaning of phase control on these timescales. As in the last figure, a pulse train is shown, consisting of 30 fs laser pulses with a time difference of 250 fs. For visible light, the electric field has a period of about 2 fs. A change in the relative phase between two laser pulses means controlling the electric field with a sub - fs time resolution.

This playing with the phases gives the possibility to change the composition of wave packets. It is used to manipulate the coupling of halogen and lattice to control predissociation effects and to coherently prepare out one electronic state with respect to another one, as will be shown in Chs. 3 and 6.

Chapter 2

System: Br_2/Ar

The experiments of this thesis were carried out on the halogen bromine embedded in an argon rare gas solid (RGS). It is an interesting system, since it unifies the simplicity of diatomic molecules with the complexity of the interaction with a surrounding bath.

This chapter firstly introduces the properties of halogens, in general and focusses on free bromine. Then the state of the art concerning halogens in RGS and especially Br_2/Ar will be discussed.

2.1 Gas phase properties

To put it in one sentence: Bromine is toxic, has a pungent smell, is highly corrosive, has a brown-orange colour... and it is an ideal halogen to study and control wave packet dynamics, as will be shown in this thesis.

2.1.1 Physical and chemical properties

Bromine is a liquid at room temperature, having a high vapour pressure of 220 mbar at 20°C. Its melting point is at -7.2°C and the boiling temperature is 58.8°C at 1 atm [46–48]. The molar mass at the same conditions is 159.81 g/mol.

Natural Br_2 has three isotopomers: 81/81, 79/81 and 79/79 in the ratio of 1:2:1 and that was the abundance used in these experiments. The different mass of the isotopes leads to a splitting of vibrational and rotational levels and the former will be observed and discussed in Ch. 4.

2.1.2 Electronic structure

All halogens are situated in the seventh main group of the periodic table and go for one further electron to complete their outer shell. This makes them highly reactive. The electronic configuration of the bromine atom is: [Ar] 3d10 4p5 4s2 with [Ar] standing for the structure of the core electrons. When Br_2 is electronically excited, first a redistribution of electrons in the molecular orbitals belonging to the sub-shell p takes place. Electronic molecular states are characterised as ${}^{2S+1}\Lambda_{\Omega\, parity}$, where $2S+1$ is called the spin multiplicity, Λ is the orbital angular momentum (0=Σ, 1=Π,...) and Ω is the combined angular momentum of spin and orbital angular momentum. The parity can be g (gerade) which means totally symmetric related to the inversion centre or u (ungerade) which is antisymmetric [27, 42].
The ground state X is a ${}^1\Sigma_{0g}$ state. Also, the low lying excited states will be investigated in this work and they are: A' ${}^3\Pi_{2u}$, A ${}^3\Pi_{1u}$, B ${}^3\Pi_{0u}$ and[1] the repulsive state C ${}^1\Pi_{1u}$.
The dissociation of the covalent states X, A', A and C leads to two ${}^2P_{3/2}$ atoms as shown in Fig. 2.1. The B-state dissociation energy is higher by 2660 cm^{-1} due to the spin-orbit coupling, since dissociation leads to one ${}^2P_{3/2}$ and one ${}^2P_{1/2}$ atom [49].

[1] For symmetry reasons, the B-state splits into a 0^+ and a 0^- state. The latter is called B' and was not observed experimentally.

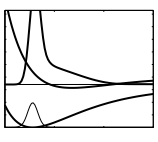

In the case of Cl_2 the spin orbit coupling is smaller than for Br_2, therefore, B-state emission of Cl_2 is quenched in matrices and the first repulsive states are located close to the gas phase dissociation limit. In I_2 the coupling is larger and thus a repulsive potential crosses already in the B potential minimum.
From the two charge transfer (CT) manifolds of Br_2, four states are included in Fig. 2.1 and their potential parameters are collected in Tab. 2.1.

2.1.3 Spectroscopic properties of free Br_2 molecules

First absorption measurements on bromine in the 1930s [50] were followed by a number of studies [51–53]. The absorption maximum at 420 nm was attributed to the C-state. The employed method of projection was also applied for Br_2 in an Ar matrix and is shown in Fig. 2.4a. Emission spectroscopy delivers a deeper insight on the B-state [54–56] and the A-state [57, 58]. Coxon provided FC factors for the B and for the A-state [57, 59]. The available spectroscopic data is collected in Tab. 2.1 and in Fig. 2.1. A review on the development of bromine potentials is given in Ref. [43].

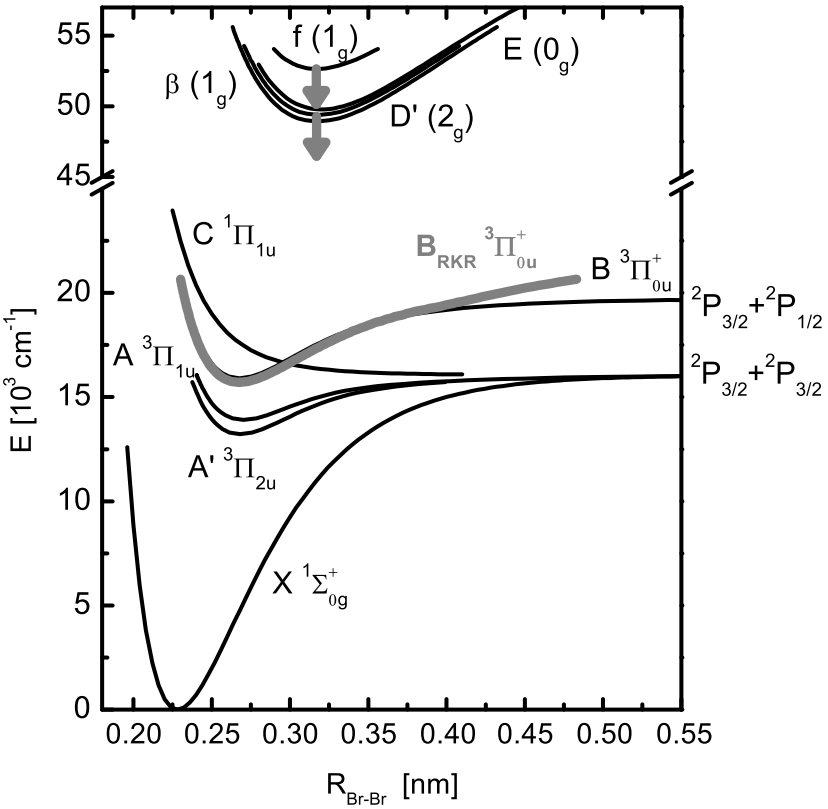

Figure 2.1: Gas phase potentials (black lines) of Br_2 and matrix potential of the B state, obtained with the RKR formalism (thick grey line). Redshifts of CT states are indicated with grey arrows [60].

Higher lying repulsive states from recent $ab-initio$ calculations by Yabushita [64, 65] will be introduced in the discussion of Ch. 4

2.1.4 Selection rules

Selection rules for electronic transitions in molecules for Hund's case c are assorted, following Ref. [42]:
Parity g↔u with each photon
Spin $\Delta S = 0$, which is however weakened for a heavy molecule like Br_2 and even more soften due to the matrix influence
Angular momentum $\Delta\Omega = 0, \pm 1$, at which $\Delta\Omega = 0$ is the stronger transition

Table 2.1: Spectroscopic data for the free Br_2 molecule up to the linear term in anharmonicity. States X, A', A, B, C are covalent, D', β, E and f are charge transfer (CT) states.

State	Isotope	T_e [cm^{-1}]	ω_e [cm^{-1}]	$\omega_e x_e$ [cm^{-1}]	r_e [nm]	Ref.
X	79,81	0	323.3069	1.0641	0.228107	[56]
A'	79,79	13223	165.172		0.25	[61]
A	79,81	13918	155.5	2.83	0.27	[57]
B	79,81	15902.47	166.5688	1.6159	0.26776	[56]
D'	79,81	48934	150.86		0.317	[61]
β		49398			0.319	[62]
E	79,79	49779.06	150.46		0.32	[63]
f	79,79	52641.554	153.8654	0.42863	0.318	[63]

Table 2.2: Polarisation dependence of electronic transitions X→A and X→B. Symbols "8" and ∞ stand for $cos^2\theta$ distributions, "0" and $\subset\supset$ for $sin^2\theta$, respectively. Relative efficiency values for one photonic (1p) and two photonic transitions (2p) from Ref. [43].

Transition	Molecular distribution	Pump	Probe	Efficiency 1p (2p)
$\Delta\Omega = 0$	8	$\updownarrow$	$\updownarrow$	3 (5)
$\Delta\Omega = 1$	$\subset\supset$	$\updownarrow$	$\updownarrow$	1 (1)
$\Delta\Omega = 0$	∞	$\leftrightarrow$	$\updownarrow$	1 (1)
$\Delta\Omega = 1$	0	$\leftrightarrow$	$\updownarrow$	2 (3)

X→A and X→B are $\Delta\Omega = 0$ and $\Delta\Omega = 1$ transitions, respectively and they lead to different angular distributions of excited molecules for linear polarised light: For $\Delta\Omega = 0$, the molecular axis and the electric dipole moment $\boldsymbol{\mu}$ are parallel to each other. A $cos^2\theta$ distribution of excited molecules is obtained for the angle θ between molecular axis and electric field vector, which look like a club. For the $\Delta\Omega = 1$ transition $\boldsymbol{\mu}$ is perpendicular to the molecular axis and the selection of molecules follows a $sin^2\theta$ distribution, in the shape of a bagel. These different distributions allow for photoselection in polarisation sensitive measurements and this method was introduced in Ref. [66, 67]. Concerning pump - probe experiments, not only the pump step selects molecules of distinct orientation, also the probe step does. The latter is assumed to be a $\Delta\Omega = 0$ transition since probing to CT states leads to a charge separation along the molecular axis which requires a parallel electric field. Table 2.2 compares different transitions for different relative polarisations between pump and probe pulse (the pump pulse was turned) and the excitation efficiencies for a one and two photonic probe step. The latter narrows the distribution to $cos^4\theta$. This separation of A and B-state contributions was applied for molecules in matrices in [34, 43] among others and also this work will refer to it.

2.2 Properties of halogens in the cage: State of the art

By doping rare gas solids (RGS, [68]) with halogens, one can isolate dopants and study their spectroscopic properties for blocked translational and rotational degrees of freedom.

Instead, interesting couplings of chromophore and matrix come into play. Various atoms and molecules were embedded in RGS [69]. Rare gas crystals are chemically inert and -in general- they do not react with the dopant[2]. Doped RGS are an ideal spectroscopic system for the purpose

[2]Exceptions are known for solid Xe, and even for solid Ar, novel rare gas molecules were found [70, 71]. Furthermore, for short wavelengths excitation with λ<150 nm excimers of chromophore and matrix can arise.

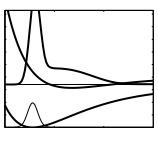

of this work, the control of wave packet interference and predissociation. It is not only experimentally accessible, but also theoretically treatable with new and sophisticated methods and enables calculations on a very high level.

2.2.1 Cage effect

At a temperature of -189.2°C and a pressure of 1 bar, Ar starts to crystallise in a face centred cubic (fcc) lattice due to Van-der-Waals forces. By choosing combinations of halogens and rare gases with comparable Van-der-Waals radii as given in Tab. 2.3, a configuration can be found, where the separation of two nearest neighbour atoms and the molecular size fit together. Then, the dopant replaces two nearest neighbour rare gas atoms and is trapped in a so-called double - substitutional site. This is the case for Br_2/Ar, as was shown with Raman spectroscopy [72]. The surrounding cage is only slightly deformed [40]. Rotational stiffness for the club-like geometry of the homo nuclear molecule Br_2 was proven in depolarisation studies in Refs. [34,43] and for I_2/Kr in [73]. Other systems like the hetero nuclear ClF, which has a more sperical shape embedded in a RGS take a single-substitutional site. A rotation of the molecule in the cage site is possible and calculations for high fields opened control scenarious [74–78]. However, the experimental study and control of chromophore rotation is a very challenging task and not treated here.

Table 2.3: Van-der-Waals radii for halogens (left) and rare gases (right) from Ref. [79].

Element	r [Å]	Element	r [Å]
Cl	1.8	Ne	1.6
Br	1.9	Ar	1.9
I	2.0	Kr	2.0

Schematically, an Ar fcc crystal with the dopant Br_2 is depicted in Fig. 2.2. The sketch shows exemplarily a Br_2 molecule along the <101> direction.
In reality, the molecules are statistically distributed among equivalent crystal directions. The Br_2 molecule is part of the plane closest to the viewer, which is indicated with light grey Ar atoms. Planes further away have dark grey and black spheres. Excitation generates vibrations along the molecular axis as indicated by the outgoing arrows. The expanding Br atoms hit specific Ar atoms as a direct collision partner. These head-on atoms are marked with H, and especially involved in vibrational energy relaxation, treated in Sec. 2.2.7. The outgoing bromine atoms open a vacant space in between them which is entered by the so-called belt atoms (B). They move inwards into the emerged clearance which is marked with the cross, following the arrows. Belt atoms are located in a deeper plane than the molecule, and also in front of the first plane, shown here. Another group of atoms is called coherent phonon atoms and marked with C. They are responsible for the creation of coherent phonons during the electronic excitation and will be introduced in Sec. 2.2.2. The first shell which surrounds the Br_2 molecule contains 18 atoms.

A dissociation of the chromophore, which occurs in the gasphase at energies above the dissociation limit is hindered by the cage atoms and this enforced recombination is called the cage effect. It was theoretically proposed by Franck and Rabinowitch in Ref. [80] and, $e.g.$, experimentally observed in RGS in the groups of Apkarian and Schwentner [3,31,32,81–84] They recorded I_2/RGS wave packet dynamics, at energies which lie above the gasphase dissociation limit. Interaction with cage atoms leads to an upwards bending of the molecular electronic potential. For the B-state of Br_2/Ar an effective potential was determined in Ref. [60] by applying the Rydberg– Klein – Rees (RKR) method. Therefore, an elaborated study on pump - probe signals with variation of

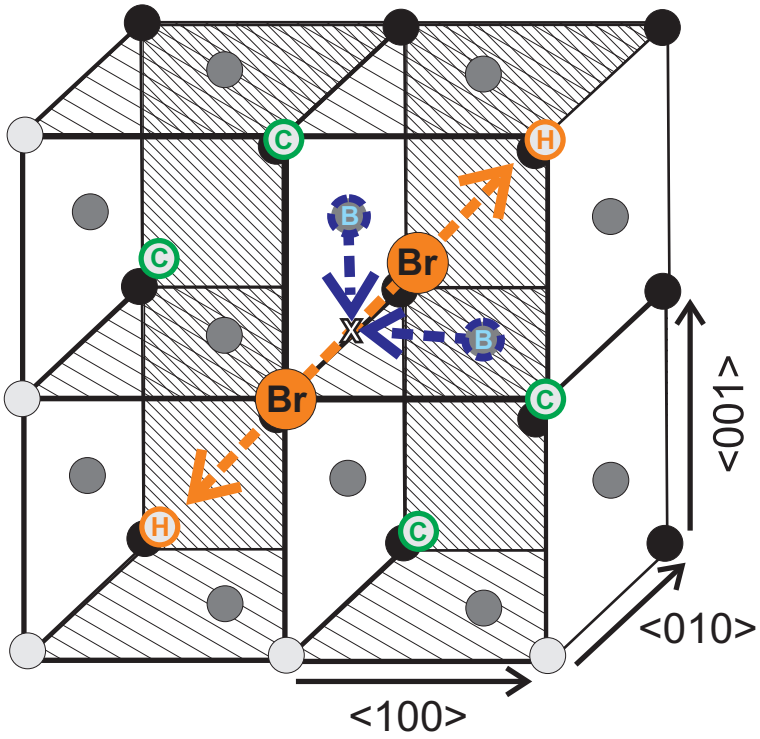

Figure 2.2: Br_2 molecule in a double substitutional site in an Ar fcc lattice (small balls). In the first plane (light grey atoms) the Br_2 molecule is embedded and shown as large spheres. Head – on atoms (H), belt atoms (B) and coherent phonon atoms (C) are explained in text. Those Ar atoms closest to the viewer are shown in light grey, those more far away are dark grey and black.

pump and probe wavelength was carried out. Outer turning points of the wave packets at energies far above the gasphase dissociation limit were determined by analysing the pump - probe spectra and this will be described in Sec. 3.3.3. This RKR potential is included in Fig. 2.1 as thick grey line.

Theoretical investigations were carried out in the groups of Gerber [85–89], Manz [38, 90–92] and Coker [93, 94]. Very recent studies, using the diatomics in molecules (DIM) formalism delivered matrix potentials for the lower 23 Hund's case c states [39, 40].

2.2.2 Electronic and vibrational coupling with the lattice

Exciting a molecule with visible light will nearly instantaneously change its electronic configuration and the Born - Oppenheimer approximation allows for a separate treatment of the much heavier nuclei which follow more slowly. These different timescales in the motion of electrons and nuclei lead to two different excitation schemes of phonons in the crystal: First, phonons created impulsively during the excitation of electronic transitions will be discussed. And second, phonons as the result of large molecular vibrational amplitudes are described.

In time resolved experiments in I_2/Kr and Br_2/Ar an omnipresent period of 650 fs and 500 fs, respectively was observed, which is independent of the excitation energy and the investigated electronic state [95, 96]. It corresponds to the frequency of the zone boundary phonon in the crystal which has a zero group velocity and stays at the centre of excitation, thus it was observed for several ps. This phonon mode can be detected via the dopant, since it lowers and raises the charge transfer states periodically, which are essential for recording a time resolved signal. The excitation mechanism was attributed to a displacive excitation of coherent phonons (DECP), due

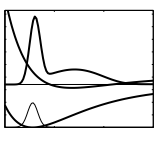

to an expansion of the electron cloud during excitation with a fs pulse. Mainly responsible for this mode are the coherent phonon atoms in Fig. 2.2.

Also the molecular vibration generates phonons in the crystal due to inelastic collisions of molecule and cage atoms. Higher modes have larger amplitudes and the interaction with the cage increases. They contribute to the phonon side bands (PSB) in the excitation spectra of Br_2/Ar (Fig. 2.4b) and Cl_2/Ar in Refs. [97, 98] and are simulated, $e.g.$, in Ref. [99]. How they evolve with v' will be studied in Ch. 4.

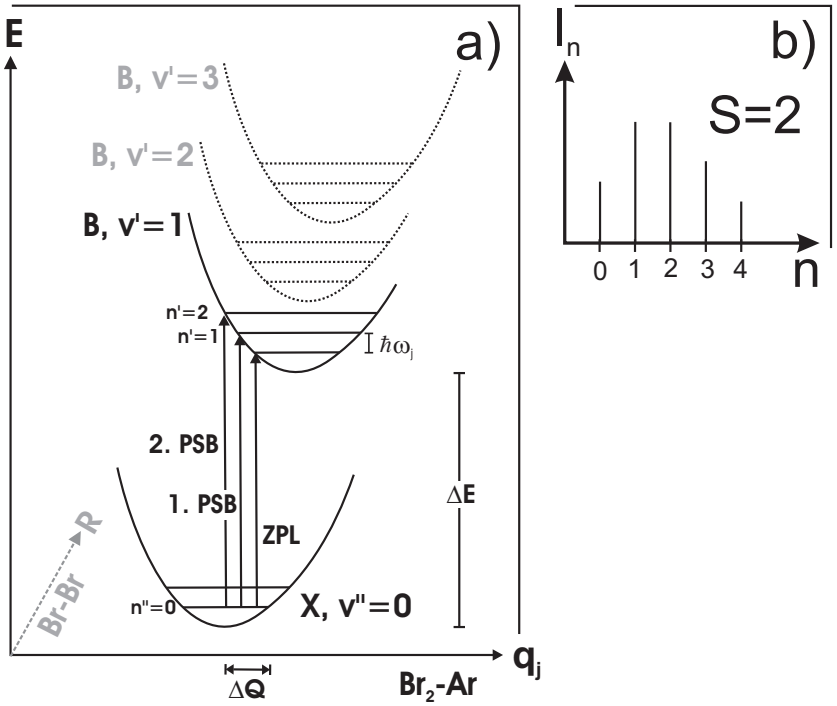

Figure 2.3: Configuration coordinate model: a) Depicted are harmonic oscillators, each representing one vibrational eigenstate of the electronic ground state X or of the excited state B, respectively. The configuration coordinate q_j represents one possible phonon mode of the crystal. The change in equilibrium position ΔQ is related to the Huang-Rhys coupling constant S, here $S = 2$. The intra molecular coordinate R is indicated by the dashed axis. b) Intensity distribution for $S = 2$ and $v' = 1$.

A vibronic excitation involves an excitation of chromophore vibrations and also of phonons in the cage. The energy necessary for those phonons has to be provided by the light pulse, resulting in a shift and broadening of the absorption line.

To describe such a transition, the configuration coordinate picture presented in Fig. 2.3a is chosen. It operates in the linear coupling regime [100–104]. Depicted are identical but shifted harmonic oscillators, each representing schematically the matrix - molecule potential for the electronic and vibrational ground state X $V_{X,0} = 1/2\,\mu\,\omega_j^2\,q_j^2$ and for each vibrational mode v' in the excited state B $V_{B,v'} = 1/2\,\mu\,\omega_j^2\,(q_j + \Delta Q)^2 + \Delta E$, respectively, $vs.$ energy E. Here, μ is the reduced mass, ω_j the phonon frequency, ΔE the energy difference of the potential minima and $\hbar\omega_j$ the spacing of the phonon eigenstates n. Modes of the ground state are characterised as n'' and those of the electronically excited state with n'. The configuration coordinate q_j represents one of many possible phonon modes of the crystal.

Following Ref. [101], the probability for a transition $T_{n'',n'}$ is determined by the Franck - Condon (FC) factors, depending on the displacement of the potential minima ΔQ. The probability is connected to the dimensionless Huang - Rhys coupling constant S [105] with: $S = \mu\omega_j\Delta Q^2/(2\hbar)$.

The intensity I_n for a transition from $n'' = 0$ to $n' = n$ follows

$$I_n \;=\; e^{-S}\, S^n \,/\, n!\;. \tag{2.1}$$

S represents the order n of phonons where the maximum of the FC factor is found, using the approximation that all coupled modes have the same phonon frequency. The intensity distribution I_n in Fig. 2.3b shows $S = 2$ and $v' = 1$. The coupling constant will be relevant for the evaluation of excitation spectra in Ch. 4. In a zero phonon transition no phonons are created, *i.e.*, $\Delta n = 0$ and this defines the zero phonon line (ZPL) in Fig. 2.3. Higher phonon modes build up the PSB. The first order of created phonons, displayed with 1.PSB in Fig. 2.3 results from transition $T_{0,1}$ and the second order of phonons (2.PSB) from the transition $T_{0,2}$. A broad PSB is now the composition of all contributing modes $\sum q_j$ of crystal phonons.

At low temperatures only X($v'' = 0, n'' = 0$) is occupied, therefore the only zero phonon transition is $T_{0,0}$. At higher temperatures also zero phonon transitions like $T_{1,1}$ or $T_{2,2}$ can occur, resulting in a displacement of the line maximum and a line broadening, since ground and excited state have in general different phonon energy spacings, yielding different transition energies.
The broad PSB absorption shows up on the high-energy side of the ZPL.

Often, ZPL are described in analogy to the Mössbauer effect[3] [100]. The existence of ZPL can be interpreted as a small probability that the phonon state of the crystal is unchanged during excitation. The first ZPL and their strong broadening with higher temperature was observed in F - centres of LiF in 1953 [106]. Observations for Br_2/Ar will be discussed in Fig. 2.4b and Ch. 4.

2.2.3 Absorption and excitation spectra of Br_2/Ar

First spectra on Br_2 in the argon matrix were taken in absorption by Andrews [108] and reproduced by Gühr [22,43] which is shown in Fig. 2.4a as thick black line. It was decomposed into three contributions which were calculated for transitions to A (dash-dotted), B (dotted) and C-state (dashed) using the projection method [109]. The ground state vibrational wave function was projected on the inner limb of the excited state potentials. The addition with optimised ratios of 1:0.48:0.067 for the absorbance maxima of C:B:A results in the solid line. This decomposition was found to be very close to that of the gas phase, from Ref. [65]. The reason is that the spectrum is determined by the inner limbs of the potentials which are least exposed to interactions with the matrix. The A'-state was not included in this decomposition since it mainly follows the A absorption but is weaker by a factor of around 100.

Unfortunately, the absorption spectrum does not give any structured spectral information on the bound parts of the B and A-states. It represents a challenge to my work, since the control experiments are - necessarily - situated in this energetic region marked with the two arrows. It is this range, where repulsive states are crossing the bound B potential. The fact, that no structure at all occurs in B-state absorption is caused by an extremely small FC overlap below 550 nm. Furthermore, the suspicion of an overwhelming A-state background in this area can arise. Indication for this can also be found in the excitation spectrum presented in b) which is adapted from [97]. The first B-state emission was recorded by Bondybey *et.al.* [97], together with a B-state excitation spectrum of B($v' = 0$) emission-intensity versus the excitation wavelength from a dye laser shown in Fig. 2.4b. It displays a vibrational progression of rather sharp ZPL (the FWHM of the line at 615 nm is, *e.g.*, 12 cm^{-1}). The PSB develop for higher v' and merge to a continuum around $v' = 12$. It was taken for ^{79}Br^{81}Br at a sample temperature of 4 K. This spectrum is qualitatively similar to the Cl_2/Ar case [98], including the increasing background with higher v'. Cl_2/Ar was

[3] A recoil-free recombination of γ-quanta with the nucleus shows up in extremely narrow lines, the Mössbauer lines. They are observed when the atom is embedded in a lattice which distributes the recoil momentum on a very large mass.

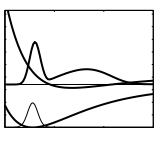

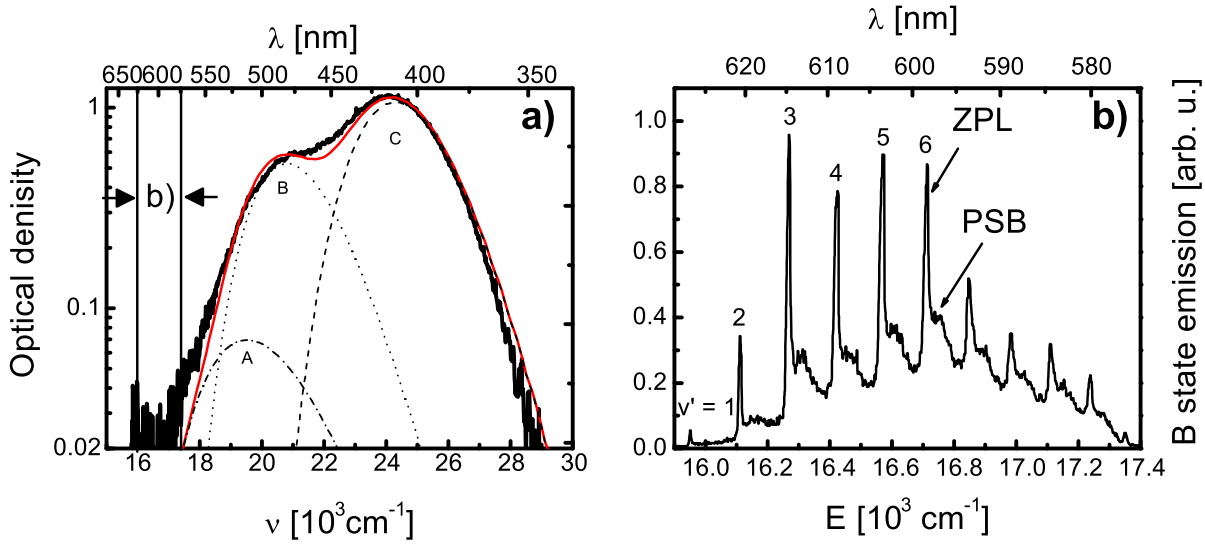

Figure 2.4: a) Measured optical density (thick solid line) and decomposition into A (dash dotted), B (dotted) and C-state (dashed line) components, using the projection method, where the thin solid line gives the summation (from Refs. [22, 43]). b) Excitation spectrum detected via B-state emission from Ref. [97] with resolved ZPL and PSB structures. Nomenclature of v' was adapted following Ref. [107]. The spectrum was not corrected for dye laser power. This spectrum was obtained in the low energetic region of the B-state wing and is indicated in a) with the two arrows.

modelled using mixed-order semiclassical dynamics calculations by Ovchinnikov *et.al.* [99]. They calculated the Huang-Rhys coupling constant S which was introduced in Fig. 2.3 as a measure of the dynamical guest–host or electron–phonon coupling out of the intensity ratio of PSB and ZPL and determined S $\leq$1 for $v' = 2$ to $v' = 9$ and $S = 2.5$ for $v' = 10$. The experiment shows nearly no coupling up to $v' = 8$ and for higher v' an exponential like increase to $S = 3.5$ for $v' = 13$. The background in Fig. 2.4b could occur due to A-state contributions in B or due to a superposition of PSB and its origin, as will be clarified in Sec. 4.2. Since the spectrum was not normalised to the excitation laser intensity, it does not resemble the real spectral trend at the energetic edges.

The assignment of vibrational levels v' used in Ref. [97] was corrected in a very extensive effort in Ref. [107] by the value of -2 and this re-assignment is also used in Fig. 2.4b. In my work a re-re-assignment will be presented, which solves all remaining discrepancies between these two literature versions. It will be discussed in detail in Sec. 4.1.

2.2.4 Emission spectroscopy of Br_2/Ar

Information about the covalent states was deduced in several studies [49, 97, 107, 110–113] on the fluorescence of bromine in argon. Experimental parameters and lifetimes for B, A and A'-state are collected in Tab. 2.4. Another state, called A* was only observed in the most detailed study with the best resolution by Langen *et al.* [107], but not further specified.

Only fluorescence from the lowest vibrational level of electronically excited states is observed, since internal vibrational relaxation is much faster than the fluorescence lifetimes of Tab. 2.4. All transitions from X to covalent bound states violate dipole selection rules. The only fully allowed one is that to the repulsive state C.

Transitions from B($v' = 0$) and A($v' = 0$) are only spin forbidden. The $\Delta\Omega = 0$ transition (X→B) is expected to be stronger than a $\Delta\Omega = 1$ transition (X→A) and this is displayed in the shorter lifetime of around 7 μs compared to 70 μs. The $\Delta\Omega = 2$ transition of X→A' violates

Table 2.4: Emission bands with lifetimes and spectral range for emission and excitation for Br_2/Ar. All transitions terminate in the electronic ground state $X^1\Sigma_{0g}$. The A* state in Ref. [107] is not closer specified.

State	Lifetime [μs]	Emission spectral range [μm]	Excitation wavelength [μm]	Temperature [K]	Ref.
$B^3\Pi_{0u}$	8.0 ± 0.5	0.7 – 1.1	0.38 – 0.55	12	[49]
	7.3	0.75 – 0.9	0.575-0.628	5	[97]
	6.57 ± 0.05	0.8 – 1.1	0.5	10	[107]
$A^3\Pi_{1u}$	67 ± 4	1–2	0.38 – 0.55	12	[49]
A*	61 ± 1	1 – 1.7	0.5	10	[107]
A	107 ± 7	1 – 1.7	0.5	10	[107]
$A'^3\Pi_{2u}$	$11\ 10^3$	1.1 – 1.35	0.50 – 0.54	15	[112]
A'	$(11 \pm 1)\ 10^3$	1 – 2	0.38 – 0.55	12	[49]
A'	$(44.2 \pm 3)\ 10^3$	1 – 1.7	0.5	10	[107]

additionally the $\Delta\Omega$ selection rule. However, for electric quadrupole moments and magnetic dipole and quadrupole moments $\Delta\Omega = 2$ is allowed, but the lifetime is strongly prolonged to $10 - 40$ ms.

With the parameters given in Ref. [107] a third order calculation in v'' was carried out for the vibrational progressions of B→X, A→X and A'→X in fluorescence from $v' = 0$. The results are shown in Fig. 2.5. The calculations were carried out for the three isotopomers and the insets on the left (A') and on the right (B) resolve three lines according to the isotopic splitting. In the range from 800-1000 nm the A-state lies either very close to the A'-state or to the B-state, and is additionally very weak due to the FC factors. This is the fluorescence region investigated in Ch. 4.

An overview of the Br_2/Ar characteristics was given in Refs. [49,111], including the rise times of B and A-state emissions (< 20 ns). It was found, that for concentrations up to 1:500 no intermolecular energy transfer takes place[4].

Concerning the matrix isolation spectroscopy, the potential parameters are rather close to the gasphase. Lifetimes of B($v' = 0$) are nearly unchanged from 10 μs for the free molecule to 8 μs for the isolated one [49]. In case of the A-state it is shortened by a factor of two, which was taken as signature for matrix perturbations. For all electronically excited states a redshift due to solvation effects in the polarisable cage was observed. For the covalent states the potential is shifted to lower energies by 200-250 cm^{-1}. Potential parameters for X and B-state are discussed in Sec. 4.2, an overview on covalent states can be found in Ref. [43].

For CT states the electric dipole moment $\boldsymbol{\mu}$ is much stronger and the lower manifold of CT states is shifted by 3300 cm^{-1} and of higher one by 2000 cm^{-1} [43,96], as indicated with the thick grey arrows in Fig. 2.1.

How the redshift by ΔE depends on $\boldsymbol{\mu}$ can be estimated with the Onsager model, which leads to $\Delta E \propto \boldsymbol{\mu}^2$ in Ref. [114].

Concerning aggregation of Br_2 molecules in the RGS, a reference peak depending on the dopant's concentration and attributed to clusters was found in Ref. [108] and thereby the monomer content in a 1:500 mixture was estimated to 95%.

[4]The intensity of the lowest emission line (81/81 isotopomer) was not enhanced compared to natural abundance.

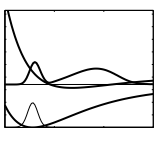

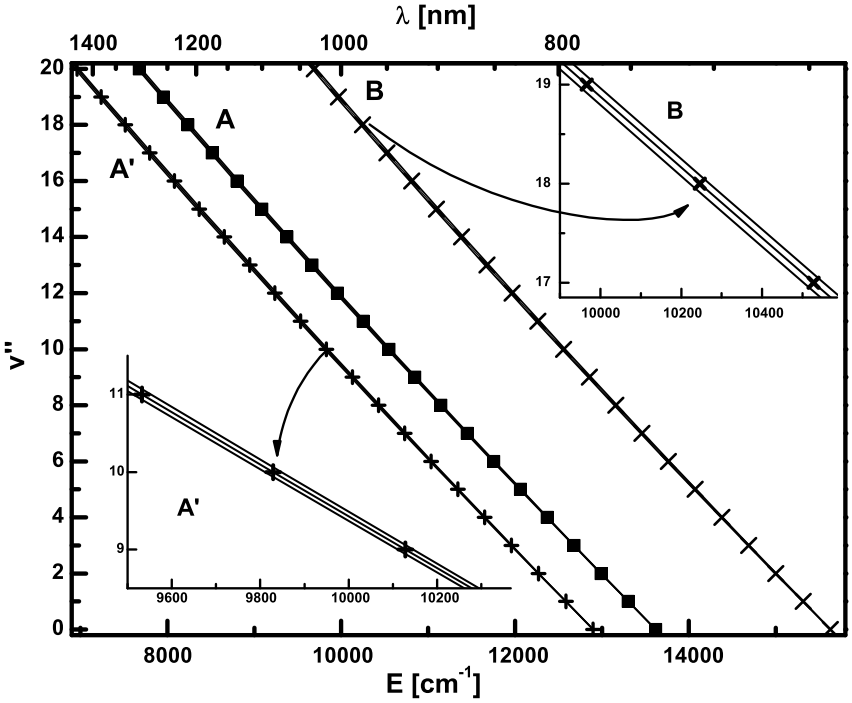

Figure 2.5: Calculated emission transitions using the third order approximation with Langen's parameters [107] for A→X (squares), A'→X (plus) and B→X (crosses) for the main isotopomer 79/81. In the two insets magnifications for A' transition (lower) and B (higher) are plotted. The 79/79 isotopomer gives the lower line and 81/81 the upper line of each set.

2.2.5 Predissociation

Apart from the radiating transitions, absorption and emission, also radiation less processes take place, especially in more complex systems like the one discussed in this work. The radiation less transitions discussed in this section will be predissociation and vibrational energy relaxation.

The predissociation of a molecule occurs due to the crossing of potential surfaces. It allows population to leave an electronic potential at a lower energy than the proper dissociation limit. A sketch of such a curve crossing is given in Fig. 2.6a. Two electronic states are depicted, a bound one B and a repulsive one called C. The wave packet located at the inner potential limb of B can remain on this covalent potential or it can change the potential surface to C at the crossing. The probability for predissociation depends on the coupling of the electronic states and is described in two different models. A semiclassical one, the Landau-Zener picture treats the non adiabatic crossing shown as solid line in Fig. 2.6a. The predissociation rate depends on the velocity with which the wave packet passes the crossing and thus on the kinetic energy above the crossing [115, 116]. A wave packet far above the crossing passes quickly and experiences a weak predissociation probability W_p, the more it approaches the crossing, the higher W_p gets:

$$W_p \;=\; 1 - exp\left[-2\pi V_x^2/(\hbar v_g(F_2 - F_1))\right] \tag{2.2}$$

with V_x being the coupling matrix element between the two potential surfaces, $(F_2 - F_1)$ the force difference due to different potential gradients and v_g the group velocity of the wave packet. The overall predissociation probability accumulates with every passage n of the crossing.

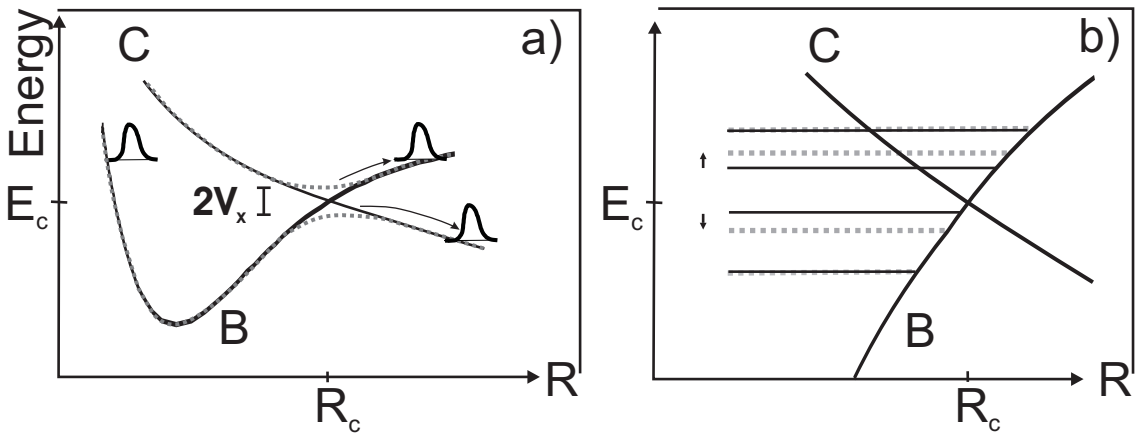

Figure 2.6: a) Non adiabatic (solid) and adiabatic (dotted) potential curves. The adiabatic curves split up by twice the coupling element V_X b) Shift of the vibrational eigenstates due to the coupling with a crossing curve. The strength of displacement (dotted lines), indicated by the arrows depends on the coupling strength and the spacing between undisturbed position (solid lines) and the crossing.

A problem in this semiclassical approach occurs, once the wave packet comes close to the crossing. This would cause predissociation with a probability of $W_p \rightarrow 1$, independent of the other characteristics. Quantum mechanical models like from the group of Nakamura [117, 118] include changes in the adiabatic potentials, which cause avoided crossings, as depicted with the dashed lines in Fig. 2.6a. The potentials split up by twice the coupling element V_x [119] and this model now provides more realistic rates at the crossing.

An intersection of two potential surfaces does not only affect their shape but leads also to a shift of eigenstates in the energetic region of the crossing. Figure 2.6b clarifies this with Ref. [119] as a zooming in the last figure. A cutout of the two crossing electronic potentials is shown together with undisturbed eigenstates of the lower bound potential plotted as solid lines. Due to the crossing the adjoining eigenstates are shifted away from each other, as indicated by the dashed lines and the arrows on the left hand side. This effect will be part of the discussion in Ch. 4 and it will get more complicated, if more than one crossing potential is involved.

In the gasphase a transition from C to B-state is symmetry forbidden and predissociation from B population to the C-state is very weak [54, 120–124]. However a coupling between those two states due to rotations is known and also in the investigations on Br_2/Ar the question on the strength of predissociation of B-state population via the repulsive C-state was often present: Bondybey proposed strong predissociation of the B-state by comparing lifetimes for high v' and for $v' = 0$, which differ by a factor of six. This was supported by the authors of Ref. [49]. They presented an A-state excitation spectrum with clear signature of A and C absorption and found B emission when exciting with wavelength > 470 nm, however the B emission was much to weak compared to the gasphase. From the gasphase a ratio of 1/5 for A/B absorption was established, however, a population ratio for A/B of 25/1 was found in the Ar matrix. According to the intensity distribution of emission among the valence states, the B-state quantum efficiency should be very small for excitation at short wavelengths high in the potential while the lifetime of the emitting v'=0 level of B is close to the expected radiative one, indicating a quantum efficiency for radiative decay near unity at the bottom of the potential. A decrease in this quantum efficiency by several orders of magnitude with increasing v' could explain the variation observed for the different excitation wavelengths. Since the absorption spectra of gasphase and matrix isolated bromine look rather similar, two mechanisms for radiation less population transfer from B→A were discussed: First

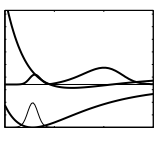

a climbing down of the vibrational ladder of B and A-state and a transfer in overlapping states. Second, predissociation via the $^1\Pi_1$ state. Predissociation rates are not yet available and will be ascertained in Sec. 4.2.

On the other hand, the authors of [112, 113] assumed the effect of matrix induced predissociation to be very weak, since the structured excitation spectrum in Fig. 2.4b covers the region of expected curve crossings, but no such signatures have been identified. A long range excitation spectrum by Bondybey covering the range from 440 – 550 nm showed a maximum at 488 nm [97] which was attributed to B-state absorption by a comparison to the gasphase. Absorption by the C-state would have its maximum around 420 nm and there the matrix spectrum of [97] is nearly zero. However, they do not report, whether this spectrum is corrected for laser power or not. The absence of B emission when exciting the C-state was taken by [112, 113] as a proof, that no population flow from C to B and vice versa takes place. Thus, they doubted the existence of a matrix induced predissociation.

However, assuming a matrix induced predissociation in contrast to [112, 113], what are the determining parameters? This was investigated, among others, for I_2 with respect to the parameters density and symmetry of the surrounding: A model by the group of Zewail [125] for collision induced predissociation of I_2 in a Kr gas claims a linear increase with density. Extending this model to higher densities, one would expect reduced lifetimes in liquids with higher densities and the shortest lifetimes due to very high predissociation rates in the solid phase obtaining the highest denistiy. However, the population lifetimes observed in the first experiments of Apkarian's group [126] for iodine in the matrix were $10 - 20$ times longer than those recorded in liquids [127, 128]. Thus the predissociation rates were opposite in trend with respect to the density by more than a factor of 10.

That has drawn the attention on the role of symmetry, and indeed, a symmetric surrounding leads to less coupling between electronic states. This was investigated theoretically in Refs. [127, 129, 130]. A highly symmetric surrounding of the crystal cage around the molecule would cancel antisymmetric coupling matrix elements and thereby hinder predissociation. On the other hand a non-symmetric environment like in liquids reduces this cancellation effect. This symmetry argument is an interesting aspect for control experiments, since phonons, created in the matrix might disturb the cage symmetry and this will be investigated in Ch. 6. It was also the topic of a theoretical study on Br_2 in an Ar solid in Ref. [39]. Large amplitude coordinates were introduced to reduce the number of treated modes in the multidimensional system. Two phonon modes at 60 and 63 cm^{-1} dominated the distortion of symmetry, since they cause a twisting and stretching/shrinking of the cage and thereby increase the coupling between the states C and B.

Calculations by Coker and coworkers demonstrated, that the presence of a matrix, surrounding the molecule in a distance of only atomic diameters, leads to strong perturbations in the molecular wave functions and interaction of electronic states [93, 94, 131, 132]. This can not be described sufficiently in an electric dipole approximation but requires higher orders in a multipole expansions.

2.2.6 Vibrational energy relaxation

A chromophore, excited at higher vibrational levels starts to vibrate along the molecular axis and collides with the matrix atoms. The momentum transfer creates the phonons described earlier. Figure 2.7 displays a potential scheme with a propagating wave packet in the direction of the dashed arrow, starting at the FC window with the ground state. It collides with the matrix at the outer potential branch. At this collision the molecule looses the vibrational energy ΔE and the wave packet's centre of gravity slides down into a deeper v' range [84, 133]. Nearly all loss in energy takes place in the first collision and the wave packet falls deep into the bound part where it oscillates with a constant period. In the gasphase the vibrational energy relaxation was

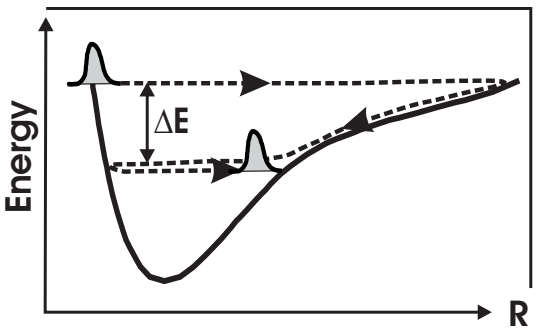

Figure 2.7: Vibrational energy relaxation of a wave packet excited high in the matrix bound potential which experiences collisions with the matrix and thereby looses energy ΔE.

found to depend on pressure and the number of collisions, $e.g.$, due to a higher mobility at higher temperatures [125]. It was treated theoretically in the group of Engel in Refs. [36, 134–138]. The process in the matrix is more complex, since the cage is not only present during the first vibrational expansion of the molecule. Pump - probe experiments in the Schwentner group [96] have stated, that also the recombination of chromophore atoms after the collision with cage atoms is retarded. It costs energy, since the vacant space of the outgoing bromine is entered by the belt atoms in Fig. 2.2. They have to be repelled and this leads to an asymmetric first round trip since the wave packet slowly slides down the outer potential arm before it reaches a stable position deep in the potential which was described in Sec. 2.2.6. This was also observed for I_2/Kr in experiments [83] and calculations in the Apkarian group [99]. Collision with the cage happens in an impulsive way, and vibrational coherence is not destroyed, but transfered to lower lying states with the wave packet undergoing vibrational energy relaxation [133]. It was also investigated in the group of Apkarian with time resolved coherent anti - Stokes Raman scattering (CARS) or six-wave mixing measurements, $e.g.$, in [33].

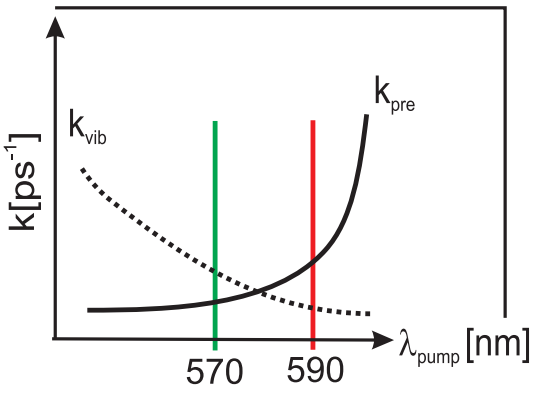

Figure 2.8: Sketch of vibrational energy relaxation rate k_{vib} (dotted line) and predissociation rate k_{pre} (solid line) $vs.$ λ.

The cage influence does not allow for a separate treatment of predissociation and vibrational energy relaxation as shown for I_2/Kr in Ref. [84]. For a free molecule, the population remaining on the initial potential follows $(1 - W_p)^n$ if only predissociation after n passages is taken into account. However, including vibrational energy relaxation in the matrix leads to another behaviour: A wave packet excited high up in the B potential is far away from the crossing repulsive state and, using the Landau - Zener scheme, it has a small predissociation probability. Nevertheless, high up in the potential the competing process of energy relaxation rate is very large for Br_2/Ar, therefore population can be efficiently transfered towards the crossings located deep in the potential and thereby the predissociation efficiency W_p per passage is strongly enhanced. For the overall predissociation probability all passages have to be summed up until the wave packet falls below the crossing. This probability $\sum W_p$ increases for excitation higher up in the B potential.

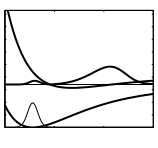

This competition is sketched in Fig. 2.8 with a schematically rate for vibrational energy relaxation k_{vib} plotted as dotted line and the predissociation rate as solid line. While k_{vib} is decreasing with longer wavelength, the independent predissociation rate is increasing. Fluorescence observations from the bottom of the potential are determined by the combined effects, which will be relevant in Sec. 4.2.

Energy relaxation is very effective at large vibrational amplitudes with more than 2000 cm^{-1}/period or 3500 cm^{-1}/ps highly above the gas phase dissociation limit, as was shown for Br_2/Ar in Ref. [21, 34, 60]. Dissipation of molecular energy creates phonons in the matrix and the zone boundary phonon has the highest energy with 67 cm^{-1} corresponding to a period of 2 THz. Thus, exciting the B-state at high vibrational levels in the potential, generates around 30 phonons in the first collision. The lowest B-state energy, where an energy relaxation rate for Br_2/Ar was determined, corresponds to $\lambda = 570$ nm with $k_{vib} = (250 \pm 500)\,cm^{-1}$/ps. Deeper in the potential it is further reduced, since the vibrating chromophore is in less contact with the matrix atoms.

As discussed in Sec. 1.2 and Refs. [139, 140] this dissipation also leads to dephasing, treated next.

2.2.7 Coherence times

Vibrational coherence exceeds 3 ps [2] deeper in the B potential of Br_2/Ar. A focussing experiment with negatively chirped[5] pulses was applied, which allows for a separation of dispersion and decoherence effects (see Secs. 1.1 and 3.4.3). In another experiment, the excitation pulse was chirped positively which allows to go forward in the history of a wave packet in an anharmonic potential. Since indications of the 1/6th fractional revival were observed, four vibrational levels could be determined to be coupled coherently. A dephasing time of >1.2 ps for these four levels was identified. The appearance of the fractional gave information on the electronic decoherence time, because the chirp prolonged the pulse to a duration of 300 fs. A revival relies on phase stability and thus, electronic coherence must have been preserved during the excitation process. This is in accord with the trend of ZPL linewidth in Fig. 2.4, however, the centre wavelength of the revival experiment with 570 nm was not covered by the excitation spectrum.

For Cl_2/Ar electronic coherence times of even 660 fs were determined in experiments with phase locked pulse pairs (PLPP) in Ref. [17]. This method was also applied in this work and is presented in Ch. 6.1.

These electronic coherence observations yield surprisingly long times, since in CARS experiments on I_2/Kr and Ar no wave packet dynamics on the excited state B was observed and this was taken as evidence, that electronic coherence lasts for less than one vibrational roundtrip time ($\approx$ 300 fs) [31–33, 141].

The expectations for electronic dephasing in multidimensional systems would be on the order of hundred fs, however, exceptions like α-perylene, a crystal which preserves electronic coherence for 10th of ps, are known [7]. Coherence requires a stability of phases. The Ar atoms are spatially fixed and lead thus to a symmetric surrounding of all molecules. A change in positions ($e.g.$, due to matrix phonons) can cause electronic decoherence when it changes the molecular transition energy differently for diverse molecules. Also semiclassical simulations of environmental effects pointed out, that a solid environment of a diatomic molecule can preserve electronic coherence [142]. Extrapolations from ballistic gasphase models [143] do not take any symmetries into account and thus are not applicable for a matrix host [43].

[5] The term chirp will be introduced in Sec. 3.3.2.

Chapter 3

Experimental technique

This chapter describes the experimental setup including the fundamentals concerning light sources and control instruments. It will start with experimental basics concerning sample preparation and signal detection. The following sections are arranged in the same way than the experimental chapters: First, the "traditional" frequency resolved spectroscopy will be described, afterwards the time resolved experiments. It will end with a detailed description of the tools used for the control experiments: Michelson interferometer and computer controlled pulse shaper.

3.1 Experimental basics

3.1.1 Sample preparation

To prepare the samples, Ar gas with a purity of 99.9999 % (Linde) was mixed with the highly corrosive Br_2 molecules (99.99$^+$%, Sigma Aldrich) having isotopomeres in the natural abundance[1], in a glassvessel. The concentration of halogen and rare gas Ar was regulated via the ratio of particular gas pressures with an end dilution of 1:500 [43]. The gas mixture was sprayed onto a CaF_2 or MgF_2 window which was kept at a temperature of 20 K and the gas flow was controlled by a needle valve. In this way the doped polycrystalline matrix grows continuously, reaching a thickness of around 700 μm within three hours[2]. A temperature range down to 14 K was reached with a closed cycle refrigerator which allows to keep a sample over several days under stable conditions. To access temperatures as cold as 6 K a liquid He flow cryostat was used; this was the temperature used for all frequency resolved experiments and it is also necessary for the control experiments. The sample chamber was kept at ultrahigh vacuum conditions with a pre-pump and a downstream turbo-pump, reaching 10^{-8}mbar at room temperature. At condensation temperature the He – cryostat acts like a cryo-pump, reducing the pressure to 10^{-9}mbar. During the sample deposition a pressure of 5x10^{-5}mbar (flow cycle) or 1x10^{-5}mbar (closed cycle) was adjusted, depending on the used cryostat.

3.1.2 Fluorescence detection

All experiments described in this thesis used the laser induced fluorescence (LiF) of the Br_2 molecules, detected in transmission direction as the observable. Either fluorescence from the electronically excited covalent states B, A and A' (see Sec. 2.1) in the near infrared (NIR) or from the charge transfer (CT) manifolds in the UV at 300 nm and 322 nm were recorded (see the CT fluorescence spectrum in Fig. 3.1). Therefore a 100 mm fused silica lens, positioned behind the sample chamber collected the emitted fluorescence into the entrance slit of a monochromator (bottom part in Fig. 3.3). Stray light of the fundamental excitation light was blocked using adequate filters for transmitting the NIR (Schott RG725, 2 mm) and the UV radiation (Schott UG11, 2 mm

[1] The three isotopomeres 79/79, 79/81 and 81/81 naturally exist in the ratio of 1:2:1

[2] The rate of growth was determined interferometrically to 340 μm/100 min.

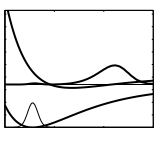

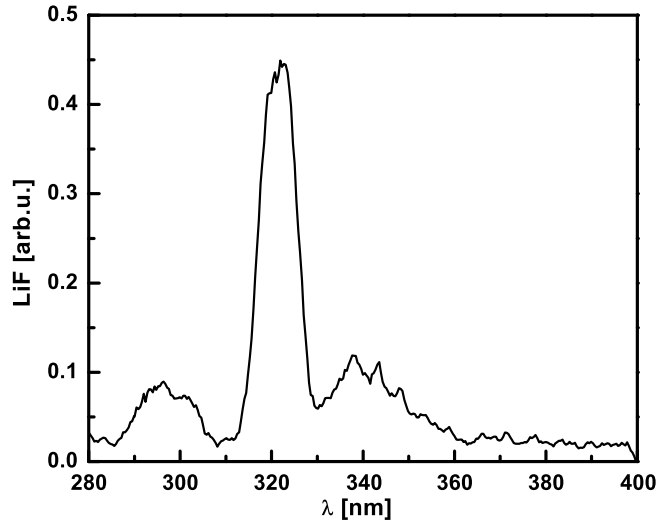

Figure 3.1: Laser induced fluorescence (LiF) from charge transfer states to covalent states. The excitation wavelength of the ultrashort laser pulse was 590 nm. In the time resolved experiments the bands at 300 nm and 322 nm were used.

or an interference filter for 322 nm, respectively).

In the case of NIR detection a B&W 25 cm monochromator with a 600 l/mm grating and a 10 μm entrance slit was used. Instead of the exit slit a liquid N_2 cooled sensor of a charged coupled device (CCD) camera (OMA 4000, EG&G) was positioned enabling a very low noise level. Its chip with 256 X 1024 pixel allowed to cover simultaneously a spectral range of 125 nm in NIR, delivering a resolution of 0.1 nm/ pixel. The detector sensitivity shows a strong wavelength dependence in the NIR until it cuts off at 1100 nm or 9500 cm^{-1}. The spectra are not corrected for the CCD sensitivity, hence a typical curve from the camera manual [144] is presented in Fig. 3.2. Exposure times of the CCD camera were typically 2 seconds, averaged to include about 160 laser pulses.

Broadband UV fluorescence was detected by a photo multiplier tube (PMT) behind the exit slit of a 25 cm monochromator (ORIEL CORNERSTONE). The pre-amplified analogue signal was gated by a boxcar integrator. For noise reduction 4000 samples were averaged. Usually, the timescale was scanned in 10 fs steps. For longterm studies it was increased to 30 fs. For polarisation dependent frequency resolved experiments, the second exit of this monochromator was equipped with the CCD camera mentioned earlier, which allows for an easy exchange between single and multichannel detection. It was observed that the grating efficiency strongly depends on the polarisation direction of the linear polarised incoming light. The polarisation of LiF was always detected parallel ($\parallel$), since the ratio of $\parallel : \perp$ (with the plane of table as reference) was 3:1 measured for 590 nm. For pump - probe experiments the polarisation of the pump pulse was usually varied and the polarisation dependence will be explicitly analysed in Sec. 5.1.1. In order to reduce dispersion of the ultrashort pulses an absorption polarisation foil was used (Codixx, colorPol VIS700 BC3).

3.2 Frequency resolved spectroscopy

The light source for measuring frequency resolved spectra was a XeCl excimer pumped dye laser (Lambda Physik FL 2002) at 20 Hz, delivering a linewidth of 0.5 cm^{-1} (dashed grey line in Fig. 3.3). A frequency range of 15625 to 19230 cm^{-1} was covered with the dyes Coumarine, Rhodamine 6G and Rhodamine B. This spectral range corresponds to the bound part of the Br_2 B state in gas phase. The excitation wavelength was scanned slowly and assigned to the emis-

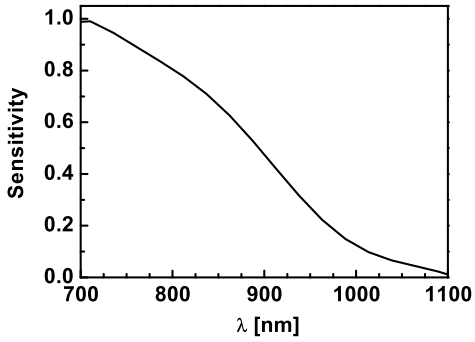

Figure 3.2: CCD sensitivity curve in the relevant wavelength range from Ref. [144], normalised to unity at the maximum.

sion spectra taken with the CCD camera. The dye laser intensity was monitored with a diode to normalize the spectra to dye power.

High resolution in excitation and emission spectra was employed to resolve isotopic splittings and the natural linewidth. For all observed vibrational levels in X and B the isotope splittings were recorded and calibration errors were minimized by calibrating the dye laser with a 2 m monochromator and the cornerstone monochromator with a Xe calibration lamp. The recorded emission spectrum contains A, A' and B-state fluorescence contributions in the NIR, separated by the isotopic effect. Scanning the excitation wavelength results in a two dimensional grey scale plot of the stored fluorescence spectra versus excitation wavelength, which contains the isotopic splittings in B and X states with high resolution on the same footing. It will be presented in Sec. 4.1.2.

3.3 Time resolved spectroscopy

This section deals with different aspects concerning time resolved spectroscopy. It starts with an overview on the experimental setup which was built up in a flexible way to change easily between different control schemes and gives the most relevant data of the devices. Next, a brief description on fs laser pulses is given, including their generation with a fibre oscillator and amplification in a Ti:Sa chirped pulse amplifier (CPA), the conversion tunable pulses in the VIS using a noncollinear optical parametric amplifier (NOPA) and the techniques required for detection of those ultrashort events. Finally, the pump - probe method as a flexible tool on analysing wave packet dynamics is introduced.

3.3.1 Experimental overview

Figure 3.3 displays the experimental setup. For time resolved experiments the fs pulses of two independently tunable NOPA sources (460-650 nm, 25 fs pulses, 5-6 μJ), pumped by the fundamental beam of a Ti:Sa laser (CPA 2001, 775 nm central wavelength and 8 nm band width delivering 170 fs pulses of around 750 μJ which are polarised parallel to the table, see Sec. 3.3.2) were compressed in FS prism compressors (PC) and then adjusted in a way that they overlap in time and space on the sample, after passing a distance of approximately 10 m in the laboratory[3]. The pump pulse out of NOPA II could be expanded to double pulses with the Michelson interferometer (MI) or pulse sequences with the pulse shaper (PS, see Sec. 3.4) inserted in the setup, as marked by the two labelled boxes. One prism compressor is surrounded by a dashed line in Fig. 3.3, because it is obsolete when using the pulse shaper, since pulse compression is included in the shaper setup as will be described later. Optionally, the light passes a $\lambda/2$ plate to turn the linear polarisation from parallel to perpendicular. The probe beam from NOPA I is time delayed by a

[3]Control experiments were performed with one NOPA only, which was divided in a 50/50 beam splitter, proving, that half the laser power was sufficient for this experiment.

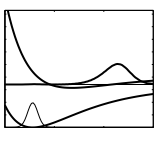

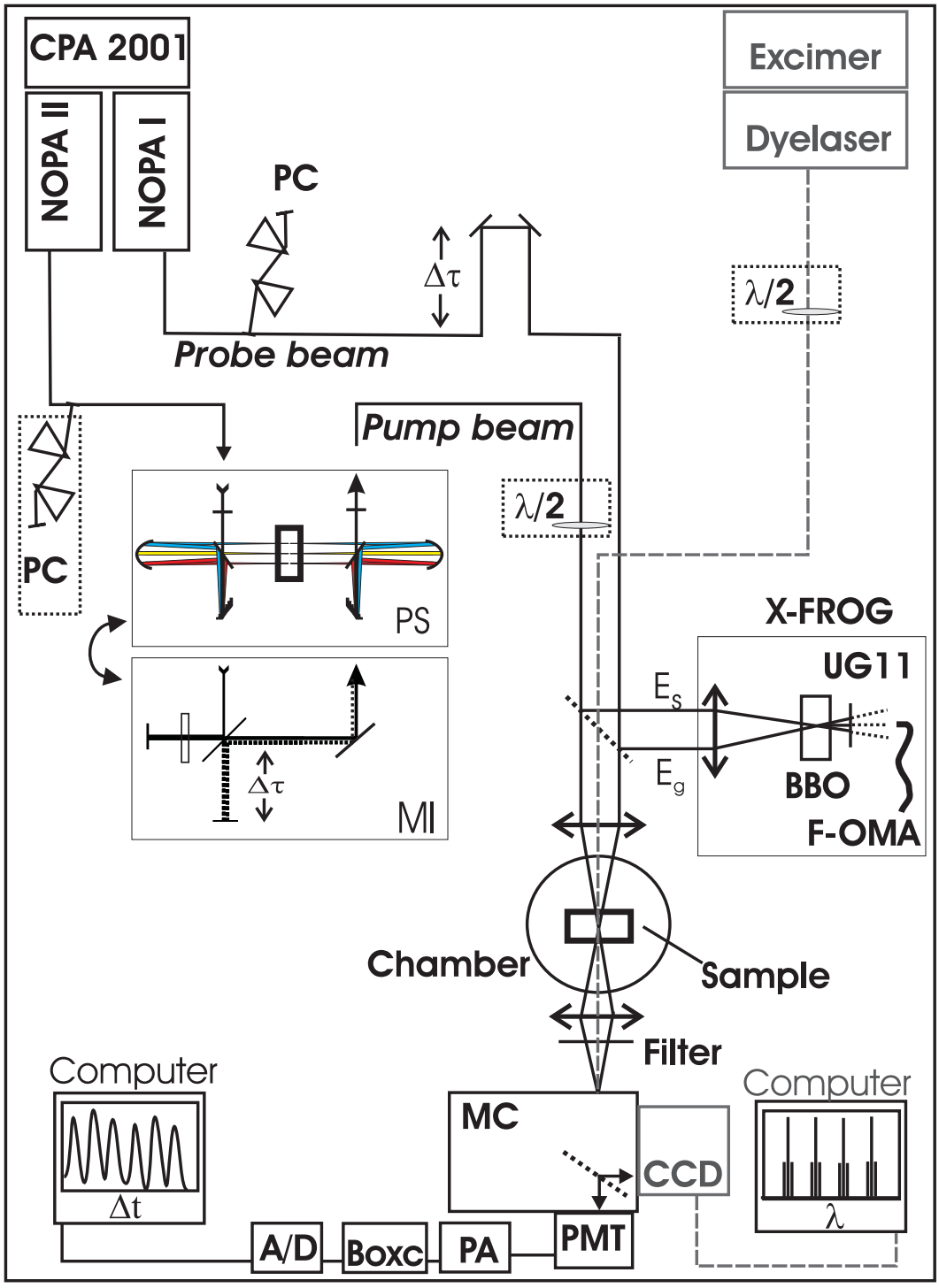

Figure 3.3: Experimental setup including the optical paths for frequency resolved (grey dashed line) and for time resolved (black) experiments. Abbreviations are: *PC*: Prism compressor, *PS*: Pulse shaper, *MI*: Michelson interferometer, *F-OMA*: Fibre spectrometer, *MC*: Monochromator, *PMT*: Photo multiplier tube and *PA*: Preamplifier. With the two computers displaying λ and Δt the paths belonging to frequency or time resolved experiments are labeled. For a detailed description see text.

computer controlled stepping unit, allowing a time resolution of 3 fs. Both beams were focussed with a 100 mm fused silica lens onto the sample, located in the ultrahigh vacuum chamber. On the sample the remaining pulse energy was between 0.1 and 1.0 μJ at a focus diameter of about 50 μm. Detection of LiF took place as described in Sec. 3.1.2. To determine the time overlap between pump and probe beam and to measure the time profile with the technique of frequency resolved optical gating (FROG), as described in Sec. 3.3.2, the optical path inside the chamber was repeated outside and accessed via a flipping mirror.

3.3.2 Ultrashort laser pulses

The pulse durations employed in the experiments described here are ultrashort in a moderate way. Pulse widths between 25 and 40 fs are optimal for our purpose, because longer pulses would reduce the time resolution in the vibrational dynamics while shorter pulses lead to an unwanted strong dispersion in the anharmonic molecular potential. Ultrashort laser pulses are the result of nonlinear light matter interaction processes. Their generation in a fs Ti:Sa laser, the NOPA, and the pulse detection using the technique of FROG will be discussed.

Pulse generation and the influence of chirp

Gaussian pulses will be treated since they describe experimental reality best and are conveniently handled by Fourier transformations. A linearly polarised electromagnetic wave, $E(t, \mathbf{r})$ leads at a specific position to an electric field

$$E(t) = Re(E_0 \underbrace{\mathrm{e}^{-\frac{\mathrm{t}^2}{2\tau^2}}}_{Gauss.\ env.} \mathrm{e}^{-\mathrm{i}\Phi(\mathrm{t})}) \,, \tag{3.1}$$

where $Gauss.\ env.$ is the envelope with duration τ. The duration is chosen in such a way, that $\Delta\tau$ corresponds to FWHM duration of the intensity of a pulse, with $\Delta\tau = 2\sqrt{\ln 2}\tau$. In the following, "Re" for the real part will be no longer explicitly written but implicitly meant. Developing the phase $\Phi(t)$ in a Taylor expansion with t leads to:

$$\Phi(t) = \phi_0 + \omega_0 t + \frac{\gamma}{2} t^2 + ... \tag{3.2}$$

with a constant phase ϕ_0 and ω_0 as the carrier angular frequency. Higher order terms beyond γ are indicated but will not be discussed here. Deriving the phase with time gives the angular frequency $\omega(t)$:

$$\omega(t) = \frac{\partial \Phi}{\partial t} = \omega_0 + \gamma t + ... \,, \tag{3.3}$$

γ is the parameter of the quadratic temporal phase and causes a linear chirp, $i.e.$, it changes the composition of angular frequencies with time [82, 145]. Applying chirped pulses will be important in the following in order to manipulate the dispersion of vibrational wave packets introduced by molecular anharmonicity.

In general a chirp describes a frequency variation with time in analogy to acoustics[4]. Intuitively, a travelling electromagnetic wave is handled in the time domain. However, to reveal information on the contained frequencies of a short Gaussian pulse, a spectral decomposition using Fourier transformation (FT) with the following relations from text books [146–148] is needed:

$$\begin{array}{rcl} E(t) & = & E_0\, e^{-\frac{(t-t_0)^2}{2\tau^2}}\, e^{-i\omega_0(t-t_0) - i\frac{\gamma}{2}(t-t_0)^2} \\ FT \downarrow & & \uparrow FT^{-1} \\ \varepsilon(\omega) & = & \varepsilon_0\, e^{-\frac{(\omega-\omega_0)^2}{2\eta^2}}\, e^{+i\frac{\beta}{2}(\omega-\omega_0)^2} \end{array} \tag{3.4}$$

[4] Another type of chirp, the spatial chirp, a frequency variation across the spacial beam profile, will be discussed in Sec. 3.4.2

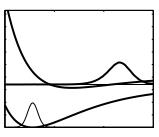

with t_0 and ω_0 as the temporal and spectral pulse centres, η the spectral width and β the chirp parameter in frequency domain.
The Fourier transformation between $E(t)$ and $\epsilon(\omega)$, $i.e.$, between the temporal and spectral representation of the pulse (Eq. 3.4) leads to the connection between time and spectral chirps and durations:

$$\gamma = \beta\frac{\eta^2}{\tau^2} \tag{3.5}$$

$$\tau = \frac{1}{\eta}\sqrt{1+\beta^2\eta^4}. \tag{3.6}$$

where the spectral width of the electric field η is, analogous to τ, tied with the FWHM spectral width in intensity by $\Delta\eta = 2\sqrt{\ln 2}\eta$. The Fourier limit of an unchirped Gaussian pulse can than be found with relations $\Delta\eta\Delta\tau = 4\ln 2$ and $\Delta\eta = 2\pi\,\Delta\nu$, to be

$$\Delta\nu\,\Delta\tau = \frac{4\ln 2}{2\pi} \approx 0.441. \tag{3.7}$$

For non – Gaussian pulse shapes, the Fourier limit has different numerical values [147].
A calculation illustrating how a linear chirp affects an electric field in time or in frequency domain is given in Appendix A.

Chirp generation and material dispersion: A positive chirp will be introduced when light is passing a normal dispersive medium[5], following the dispersion relation $k(\omega) = n(\omega)\omega/c$, with c being the velocity of light. It leads to a stronger retardation of blue components with higher frequencies compared to red parts with lower frequencies. The influence of dispersion on the wave vector $k(\omega)$ when light is passing material of length x is discussed conventionally in angular frequency domain:

$$\varepsilon(\omega, x) = e^{-\frac{(\omega-\omega_0)^2}{2\eta^2}} e^{-ik(\omega)x}. \tag{3.8}$$

Expanding $k(\omega)$ in a Taylor series to second order gives

$$k(\omega) = k(\omega_0) + k'(\omega-\omega_0) + \frac{1}{2}k''(\omega-\omega_0)^2 + ... \tag{3.9}$$

with $k'(\omega) = (\frac{dk}{d\omega})_{\omega_0}$ and $k''(\omega) = (\frac{d^2k}{d\omega^2})_{\omega_0}$[6]. This is inserted it in Eq. 3.8 and leads to the frequency chirp parameter $\beta(\omega)$, comparable to the phase description of Eq.3.2 with the temporal chirp parameter γ:

$$\beta(\omega) = \frac{d^2\Phi(\omega)}{d\omega^2} = k''(\omega)x. \tag{3.10}$$

Here, $k''(\omega)$ is a material constant which is called group velocity dispersion (GVD) and can be found for several optical materials, $e.g.$, in the software of Ref. [149]. The retardation of blue components leads to a prolongation of the pulse caused by β, which is correlated to its spectral width η:

$$\tau = \sqrt{\tau_0^2 + \beta^2\eta^2}. \tag{3.11}$$

Here τ_0 gives the transform limited length of an unchirped Gaussian pulse.

[5] refractive index $n(\lambda) > 1$

[6] The term $\omega_0/k = v_{phase}$ is called phase velocity and gives the velocity of a plane of constant phases. The pulse envelope travelles with the group velocity $v_{group} = 1/k' = d\omega/dk$.

Negative chirps (blue components are advanced with respect to red ones) are in general produced using special optical devices like prism [150] or grating [151] compressors. An advanced type of a grating compressor is presented in Sec. 3.4.2.

CHIRP UNITS

Since the linear chirp parameters β and γ are connected to the relative phase in frequency and time domain, respectively, their units must provide dimensionless arguments when multiplied by the squared frequency or time. This is fulfilled with [β]=fs^2 and [γ]=fs^{-2}. However, another "experimental" unit for the spectral chirp is very useful to visualise how many fs have passed when the center of gravity is shifted by one cm^{-1}:

$$\beta'(\nu)[fs\ cm] \mathrel{\widehat{=}} \frac{\beta(\nu)[cm^2]}{c} \mathrel{\widehat{=}} c\,\beta(\nu)[fs^2], \tag{3.12}$$

where c is the velocity of light. The angular frequency domain of ω was changed to the frequency domain of ν with

$$\beta(\nu) = 4\pi^2\beta(\omega)\,. \tag{3.13}$$

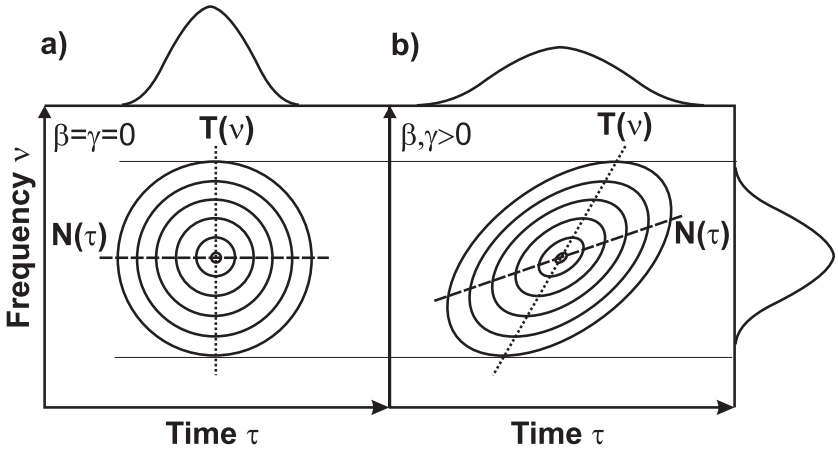

Figure 3.4: Wigner representation with equal intensity lines of an unchirped (a) and a positively chirped pulse (b). $T(\nu)$ is the FOSM, representing the time dependent center of gravity of the involved frequencies. Its slope is proportional to the chirp parameter β. Reciprocally, the FODM, included as $N(\tau)$, contains the chirp parameter of time, γ in its slope.

Wigner representation: The Wigner function $W(\omega, t)$ as a phase space description allows to unify the effects discussed above and in Appendix A on broadening of pulses due to chirp:

$$W(\omega,t) \;=\; \int_{-\infty}^{\infty} d\tau\; E(t+\frac{\tau}{2})\; E^*(t-\frac{\tau}{2})\; e^{i\omega\tau}. \tag{3.14}$$

For the description and simulation of wave packet evolution the Wigner representation is very helpful [2]. Here, it will be used to illustrate the description of frequency and time linear chirp parameters. The so-called first order frequency marginal (FOSM) $T(\nu)$ represents the centre of gravity in time against frequency ν. Contrary, the first order delay marginal (FODM) $N(\tau)$ visualises the time dependence of the frequency centre of gravity:

$$N(\tau) = \frac{\int \nu I_{FROG}(\nu,\tau)d\nu}{\int I_{FROG}(\nu,\tau)d\nu}. \tag{3.15}$$

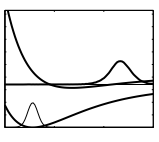

Figure 3.4a shows the Wigner representation of an unchirped light pulse ($\beta = \gamma = 0$) in an iso-energetic plot. On top the projection on the time axis is shown and on the right hand side the projection on the frequency axis. The horizontal dashed line is the FODM $N(\tau)$ which is constant for all times. The same holds for the FOSM $T(\nu)$ indicated with the vertical dotted line, all frequency components are present at the same time. Plot b) displays the Wigner function for a positively linearly chirped pulse ($\beta, \gamma > 0$). The circle of a) has changed to an ellipse and the two marginals get tilted, both straight lines having a positive slope. This leads to a broadening of the time envelope, again projected to the top, and the overall frequency slope is unchanged. In the case of $N(\tau)$ the chirp parameter β can be determined to be [43]:

$$N(\tau) = \frac{\beta\tau\eta^2}{2\pi\Delta\tau_{\mathrm{cc}}^2} \,. \tag{3.16}$$

A linear chirp can only act, as long as the Gaussian envelope in time or frequency permits it. The chirp parameter γ will cause the creation of new frequencies, however only, if it acts for a time being long enough and in a nonlinear process higher than $\chi^{(1)}$ (Eq. 3.17). In the experiments described here, γ only causes a redistribution of frequencies with time and a pulse prolongation, like the frequency parameter β.

Nonlinear light matter interaction: Nonlinear optics become relevant at high intensities when the linear approximation for the dependence of the polarisation $\mathbf{P}(t)$ on the electric field $\mathbf{E}$ no longer holds. This is a prerequisite for generation of ultrashort laser pulses in general, and especially for tunable pulses like in NOPA. It is also applied in pulse characterisation processes as will be discussed in the following subsection. This nonlinear polarisation $\mathbf{P}(t)$ can be expressed in a Taylor expansion in power of the electric field $\mathbf{E_n}(t)$:

$$\mathbf{P}(t) = \epsilon_0 \left\{ (\chi^{(1)} + \chi^{(2)}\mathbf{E_2}(t) + [\chi^{(3)}\mathbf{E_3}(t)]\mathbf{E_2}(t) + ... \right\} \mathbf{E_1}(t), \tag{3.17}$$

where ϵ_0 is the dielectric constant and (n) gives the order in field powers of the material dependent susceptibility χ. The fields $\mathbf{E_n}(t)$ can originate from one or several pulses. Orders higher than one lead to a generation of new frequencies as will be shown for the quadratic term:

$$\begin{aligned} \mathbf{E_1}(t)\mathbf{E_2}(t) &= E_{01}\, E_{02}\, (e^{i\omega_1 t} + e^{-i\omega_1 t})\, (e^{i\omega_2 t} + e^{-i\omega_2 t}) \\ &\quad \text{and with } \omega_1 = \omega_2 = \omega \\ \mathbf{E}^2(t) &= E_0^2\, (e^{2\omega t} + e^{-2\omega t} + 2), \end{aligned} \tag{3.18}$$

the latter for identical electric fields $\mathbf{E}(t)$ yields second harmonic generation (SHG), whereas different frequencies ω_1 and ω_2 result in sum (SFG) or difference frequency generation (DFG), respectively.

Second order processes occur in non - inversion symmetric media[7] only. Further conditions must be fulfilled to preserve energy and momentum of initial (ω) and created (2ω in case of SHG) frequencies. The phase matching condition describes the momentum conservation of photons, which allows a coherent propagation and amplification during the whole passage of the medium. Birefringent crystals like BBO (beta barium borate, ß-BaB_2O_4 [30]) provide ordinary and extraordinary refractive indices n_o and n_e for different polarisations. Thus, they allow both frequencies to travel under the phase matching angle through the crystal, which is described in detail in the standard literature [146–148].

[7] Air consists of inversion symmetric molecules like O_2 and N_2, therefore no SHG takes place.

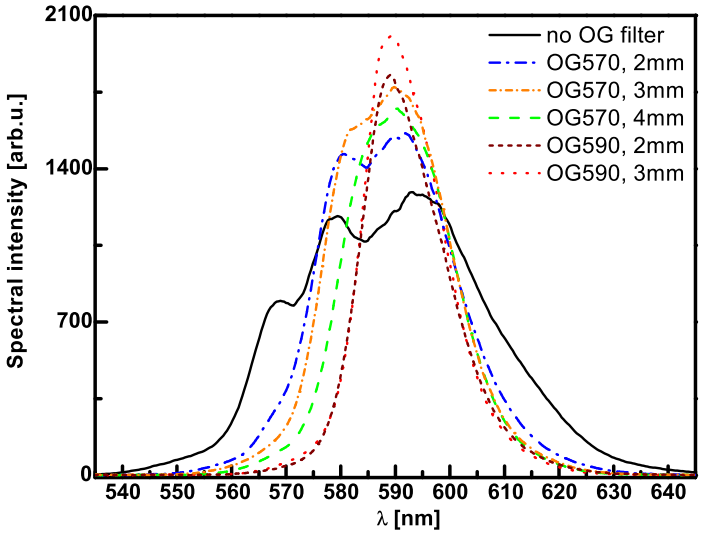

Figure 3.5: Variation of NOPA bandwidth using Schott orange glasses OG570 and OG590 in different thickness additionally to a BG38, 2mm filter.

CPA laser system: Core of the setup for time resolved experiments is the commercial fs laser CPA 2001, Clark MXR which is described briefly: Pumping an Er-doped quartz fibre oscillator with a diode at 980 nm generates sine-waves with distinct frequencies which are superimposed in a phase controlled way when passive mode-locking is achieved. This endless train of nearly Gaussian laser pulses with a repetition rate of several MHz at a wavelength of 1.55 μm is compressed in a Ge prism compressor to around 130 fs and afterwards frequency doubled to 775 nm, a frequency, suitable for efficient amplification in the Ti:Sa crystal. Prior to amplification the oscillator pulses are stretched to ps to avoid high energy damages (chirped pulse amplification, CPA). In the regenerative amplifier, energy was deposited in the Ti:Sa crystal by pumping with the second harmonic (532 nm) of a Q-switched Nd-YAG laser at a repetition rate of 1 kHz. After 8-10 roundtrips a Pockels cell selects the amplified pulse out and it is re-compressed again to 170 fs pulses at 775 nm with a power of 800 mW at 1 kHz.

NOPA system: This fundamental beam is used as pump light for four homebuilt NOPA [43, 152–154]. In each, a small portion is split off to generate a whitelight continuum with positive chirp in a sapphire plate following a $\chi^{(3)}$ process. Remaining fundamental light is filtered out with Schott glass BG38, 2 mm. The remaining fundamental light leads to SHG in a BBO crystal. This pump light of 387.5 nm overlaps with the whitelight continuum in a second BBO crystal in a non – collinear way. It parametrically amplifies the whitelight if the phase matching condition is fulfilled. Thereby the pump photon splits up into a visible (signal) and a NIR (idler) photon. Parametric amplification processes are reviewed in [155]. By varying the time delay between the pump and the chirped whitelight pulse, DFG provides a selective amplification of the thereby chosen frequency range. We use the resulting signal beam in the visible, which can be tuned in colour by changing the phase matching angle and the time delay. Using the signal delivers laser pulses with sub 30 fs FWHM length, tunable from 460 nm to 640 nm with a spectral width of more than 60 nm at 590 nm. A reduced NOPA bandwidth was desired for experiments with the pulse shaper. Therefore the whitelight spectrum was narrowed with a Schott OG570, 3mm filter, giving the best spectral and intensity performance of the amplified NOPA light as shown in Fig. 3.5

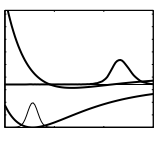

Characterisation of ultrashort pulses

The spectral profile of the laser pulses was measured with a fibre coupled optical multichannel analyser (OMA, Ocean Optics SD2000) consisting of three sections, each providing a CCD line with 2048 pixel and a 10 μm entrance slit: First the VIS I section having a grating of 600 l/mm for the range from 350-850 nm, second the VIS II section (1800 l/mm, 470-640 nm) and third the UV section specified for 200-400 nm with a 1200 l/mm grating.

For displaying the pulse duration during alignment a commercial SHG auto - correlator (AC, APE Pulse Check) was used. To facilitate the time characterisation of ultrashort pulses or even of a sequence of pulses, the technique of frequency-resolved optical gating (FROG) in a cross correlation setup was applied [156] and will be described below. This so-called X-FROG is one member of the huge family of pets for pulse characterisation, which includes SPIDER, SHG – FROG, TG – FROG or PG – FROG[8]. In the SHG – FROG, $e.g.$, two pulses which overlap in time and space in a nonlinear crystal, generate a separated frequency doubled third pulse.
First, these FROG methods were applied as auto - correlations, described in Refs. [158–160]. They all have advantages and disadvantages. One problem is the competition between strong signal (thick nonlinear crystal) and large capable bandwidth (thin crystal). Another question is the intuitivity of FROG traces, which is at hand in third order FROG and also in the second order X-FROG, which was chosen in this work. It gives an intuitive picture of the time - frequency distribution. The absolute number of pulses in the sample field is directly represented, since gating is performed by only one short pulse[9]. Also a chirp can be directly seen: A linear chirp will for example cause a tilted shape where the inclination gives the information on magnitude and sign of the chirp as was introduced in the FODM and FOSM definitions of the Wigner representation (Eq. 3.15).

The setup for a cross - correlation FROG of Ref. [156] is displayed in the inset in Fig. 3.3. Here, two pulses, signal $E_s(t)$ and gate pulse $E_g(t)$, were frequency doubled in a BBO crystal by superimposing their foci in time and space. In the case of phase matching a third beam with the sum frequency occurs in between them, in the direction of momentum compensation. Blocking the fundamental VIS pulses with a 2 mm glass filter (Schott UG11) allows to detect the isolated SFG FROG signal with the UV section of the fibre OMA. By scanning the gate pulse a time dependent profile is obtained. This signal has to be deconvolved to obtain the real pulse FWHM duration since the cross-correlation duration $\Delta\tau_{cc}$ behaves like:

$$\Delta\tau_{\mathrm{cc}}^2 = \Delta\tau_s^2 + \Delta\tau_g^2, \tag{3.19}$$

with $\Delta\tau_s$ and $\Delta\tau_g$ as single pulse durations. For auto - correlation with identical pulses a division by $\sqrt{2}$ yields the real pulse FWHM in intensity. Time and frequency resolution are determined by duration and spectral bandwidth of the gate pulse, which plays an important role for the investigation of narrow spectral features being sampled with an ultrashort and thereby spectrally broad pulse as will be shown in Sec. 6.2.

The intensity I_{FROG} of the X-FROG follows:

$$I_{\mathrm{FROG}}(\tau,\omega) \propto \left| \int_{-\infty}^{+\infty} E_s(t) E_g(t-\tau) e^{i\omega t} dt \right|^2, \tag{3.20}$$

$E_s(t)$ can be reconstructed utilising a phase retrieval algorithm [161, 162], if E_g is known. This works beautifully for clean calculated pulses but involves difficulties for experimental values of

[8] SPIDER (spectral phase interferometry for direct electric field reconstruction) is an interferometric approach [157]. TG – FROG (transient grating) and PG (polarisation gating) are based on $\chi^{(3)}$ processes.

[9] Contrary, the auto - correlation trace of multiple pulses includes more pulses than were present due to the convolution.

complex pulse structures, including noise. Therefore, in this work supplementary information was derived from Fourier transforming measured frequency resolved spectra, as will be discussed in Sec. 6.3.1.

3.3.3 Single pump - probe experiment

All time resolved experiments contained in this thesis are based on the pump - probe method which allows for an interrogation of ultrashort molecular dynamics by means of detecting signals which last several orders of magnitudes longer ($e.g.$, laser induced fluorescence LiF, as done here). Early experiments in the gas phase were carried out by the group of Zewail [5, 163] on, $e.g.$, ICN. It was transferred to many other systems, including molecules in rare gas matrices like I_2/Kr or Br_2/Ar [60, 83, 95, 126, 164]. Concerning interactions of the chromophore with the matrix happening at excitation energies high up in the excited state's potential, the advantage of pump - probe spectroscopy is, that it displays vibrational coherence long after electronic coherence has decayed. The latter is required only during the action of the pump pulse [60]. This is a major difference between pump - probe and CARS[10] spectroscopy because CARS needs electronic and vibrational coherence during the complete investigated time evolution. Section 3.4 gives another experiment dealing with electronic coherence, based on the coherent excitation with phase controlled double pulses and pulse sequences.

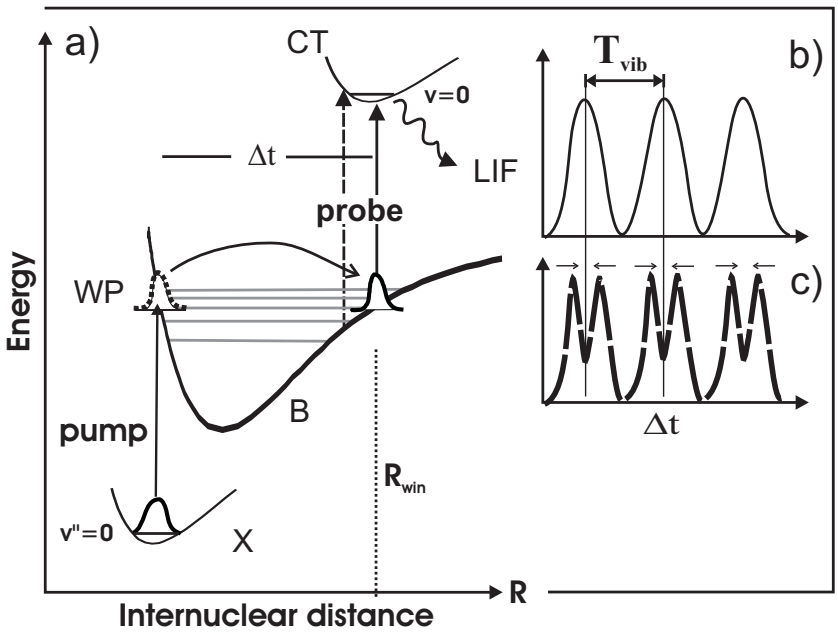

Figure 3.6: In this pump - probe scheme of a) the first laser pulse (pump) transfers population from the ground state X ($v'' = 0$) to the electronically excited state B. The wave packet on B propagates and parts of it are sampled by the second pulse (solid arrow "probe") which is time delayed by Δt. Population is transfered to a charge transfer (CT) state at R_{win} at the outer turning point. The population relaxes to the potential minimum before it fluoresces. Such a time dependent signal $vs.$ pump - probe delay Δt is given in b), where the peak maxima occur at multiples of T_{vib}. The dashed probe arrow in a) with higher quantum energy samples the wave packet at another probe window and leads to the pump - probe signal of c). For a detailed explanation see text.

[10] CARS: Coherent anti-Stokes Raman scattering. A nonlinear four-wave mixing process where three beams obeying energy and momentum conservation, create a spatially separated transient coherent Raman signal [147].

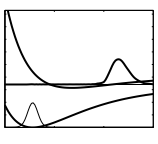

Figure 3.6 displays the pump - probe method by means of the Br_2 molecule: The first laser pulse (pump) connects the ground state X with the electronically excited state B (and other covalent states A and A', as will be discussed in Sec. 5.1). At experimental temperatures below 20 K, almost all population is situated in $v'' = 0$ [43]. Only a small fraction of it is transferred to B where several vibrational eigenstates are coupled coherently due to the large bandwidth of the pump pulse. Their coherent superposition creates a wave packet (see Sec. 1.1) in the Franck - Condon (FC) region. This wave packet propagates along the internuclear distance R on the potential and parts of it are sampled at R_{win} at the outer turning point by the second pulse in the probe step. This probe pulse (solid arrow) is delayed in time by Δt using a delay stage controlled by a stepping motor. The probe step couples the B-state with a higher lying charge transfer (CT) state and transfers population which has entered the probe window. The central energy (corresponding to λ_{probe}) and the energetic width of the probe pulse determine the position R_{win} and width of the probe window, since it defines the location of the FC window, where an excitation to CT states is most probable. Momentum and energy conservation require that

$$hc/\lambda_{probe} = \Delta V(R_{win})\,, \tag{3.21}$$

where $\Delta V(R_{win})$ is the difference potential between the B-state and the CT state. It was calculated and adapted in Ref. [43] for Br_2/Ar. This coincides for higher v' with the quantum mechanical picture of the largest FC overlap of vibrational wave functions on the two electronic states.

Due to fast vibrational relaxation processes the population reaches the minimum of the CT state before it decays as LiF from $v = 0$ to lower electronic states, $cf.$ Sec. 2.2. The wave packet oscillates on the B potential between the inner and the outer turning points and passes the probe window periodically. This oscillation can be sampled by varying the time delay Δt between pump and probe pulse. Only population being in the probe window can be transferred to the CT state. Such a time dependent signal is given in Fig. 3.6b). The first peak is observed at T_{vib}/2. The following peak maxima occur at multiples of T_{vib} which is the vibrational roundtrip time, if R_{win} is located at the outer turning point.
Otherwise, the wave packet is probed twice per roundtrip and this is indicated by the dashed probe arrow in a), which corresponds to a higher probe energy. In the corresponding pump - probe signal of c) a wave packet splitting is visible with minima at T_{vib}. The horizontal arrows mark the outwards ($\rightarrow$) and inwards ($\leftarrow$) motion of the wave packet oscillation. By varying the probe energy at a constant pump energy one can determine the position of the turning point of the wave packet. In Ref. [60] a variation of pump and probe energies was used, to determine the outer wing of the effective B potential for Br_2/Ar with this method.

The same effect of wave packet splitting would occur with the probe energy corresponding to the solid probe arrow and a wave packet excited higher up in the potential. This was the situation for pump - probe experiments with $\lambda_{pump} = 560\,\text{nm}$ in Ch. 5.

A propagating vibrational wave packet on the electronically excited potential energy surface of a molecule embedded in a rare gas crystal will strongly be influenced by radiationless processes leading to energy dissipation and – in the case of Br_2/Ar – matrix induced predissociation as mentioned in Secs. 1.2 and 2.2.5.

Predissociation is depicted in Fig. 3.7 via the repulsive state C, which is plotted deputily[11]. Due to collisions with the environment, the wave packet will loose vibrational energy, as shown by the dashed serpentine line in Fig. 3.7 and though it leaves the probe window. This causes a reduction of the pump - probe signal, indicated by the dashed line in the inset on the right hand

[11] In Ch. 4 it will be shown, that three positions with crossing repulsive states can be determined. However, for simplification in the schemes discussed here, only the C-state is named.

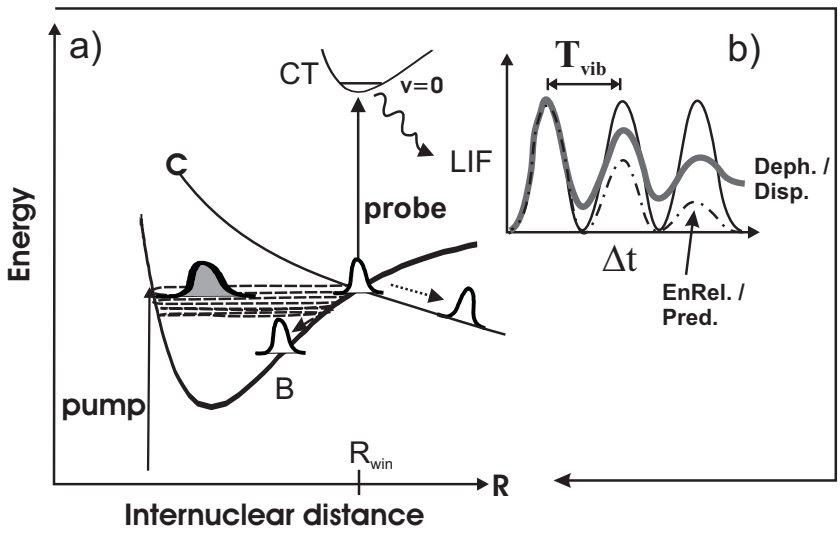

Figure 3.7: Extension of the pump - probe scheme including pure dephasing, dispersion, dissipation and predissociation via the crossing repulsive electronic state C. The wave packet at R_{win} in a) has now several possibilities how to proceed. First, it undergoes none of the mentioned effects and behaves like discussed before, this corresponds to the time resolved signal in b) shown as black solid line. Second, pure dephasing can occur due to vibrational dephasing or third, because of dispersion, the wave packet can be broadened as depicted with the broad grey wave packet on the left hand side. Those two effects induce a contrast reduction as is shown by the thick grey line of the pump - probe trace in b). A fourth effect would be predissociation of the wave packet via the repulsive state as indicated by the dotted straight arrow in a). Furthermore, the probe window might loose population due to vibrational energy relaxation shown by the bent dashed arrow. Both are resulting in a decreasing signal with time in b) plotted as the dash dotted line.

side. In order to determine an effective potential it is therefore not only required to vary the pump but also the probe energy as was done in [60] to sample the outer branch of the potential. It is difficult to separate the signal decrease due to vibrational energy relaxation from a similar effect caused by predissociation. The latter "nibbles" on the B-state population and transfers it into other electronic states (here, the C-state) which again causes an overall decrease of the B signal. In addition, population excited above the actual probe window position can relax into it, resulting an increasing pump - probe signal as will be the case in the A-state spectra presented in Chs. 5 and 6.

Radiationless processes are not the only ones, affecting a pump - probe signal. Furthermore, dephasing and dispersion, as discussed in Sec. 1.2 lead to a loss of contrast in the oscillation and an increase of the unmodulated background of the pump - probe signal. This effect is demonstrated in the inset sketch in Fig. 3.7 as the solid grey line. Dispersion as a reversible phase slip process (phases only seem to be lost) causes a broadening of the wave packet (broad grey filled wave packet on the left hand side) which smears out the pump - probe modulation. An irreversible loss of phases meant by the term dephasing leads to a similar reduction of modulation depth.
A separation of these two effects is possible with pulses of variable negative chirp [2]. While the dispersive part of the wave packet focusses at T_{opt} (Eq. 3.22) with restored contrast, the dephased fraction of the wave packet leads to a constantly increasing background.
Apart from energetic positions of pump and probe pulses also the relative polarisation influences the strength of a signal, according to the selection rules of the electronic dipole transition as discussed in Secs. 2.1.4 and 5.1.1.

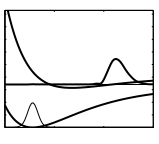

3.4 Control instruments for the generation of pulse sequences

This section will introduce the techniques for shaping laser pulses and thereby coherently controlling molecular vibrational wave packets. It starts with the interferometric control by phase locked pulse pairs (PLPP) using a Michelson interferometer. More advanced, pulse trains are generated applying a pulse shaper. Finally, in analogy to the earlier pump - probe experiments, the extension to multiple pump pulses will be described.

3.4.1 Michelson interferometer

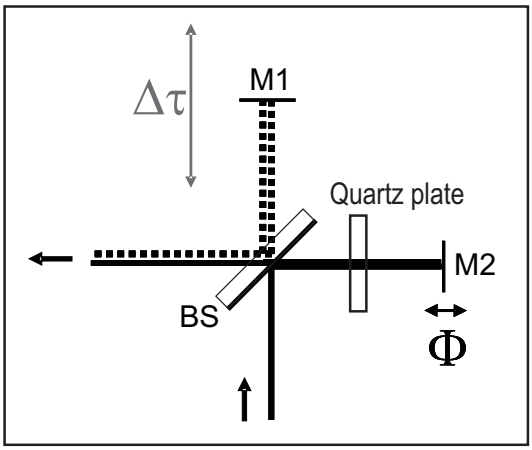

Figure 3.8: Sketch of a Michelson interferometer, where one mirror M1 is controlled by a μ m stepping motor to vary the time delay $\Delta\tau$ between the two out-coming pulses. The other mirror M2 is tuned in the nm range by a piezo drive to adjust their relative phase Φ. Beam splitter BS and the quartz plate add a relative chirp due to GVD, as described in the text.

The experiments with PLPP (Sec. 6.1) were performed using an unbalanced Michelson type interferometer which was set up with a 50/50 beam splitter BS (BK7, 5mm thick at 45°) dividing the incoming light into two beams, see Fig. 3.8. Each arm of the interferometer is terminated by a mirror, and the reflected beams overlap after passing the beam splitter in the outgoing direction. Interference can occur when the pulses overlap in space and time and coherence is preserved. The experiments require independent control of time delay $\Delta\tau$ and the relative phase Φ between the two pulses leaving the interferometer. The length of the first arm is adjustable by mirror M1 positioned on a micrometer stepper motor (PI, M505) to vary the time delay $\Delta\tau$. Fine tuning of the path difference, $i.e.$, varying the relative phase Φ, is done in the second arm with a piezo transducer (PI, E663), controlling M2. By changing the piezo voltage the relative phase of the electric fields was varied in steps of $2\pi/14$.

With the term "unbalanced" a wavelength dependent difference in effective interferometer arm length is described. It serves to pre-compensate the dispersion which a wave packet in an anharmonic potential undergoes during one roundtrip. A chirp difference of 0.29 fs cm between the two pulses at 590 nm was induced by introducing a 6 mm thick compensation plate, which counteracts to the beam splitter. The pre-chirped excitation leads to a focussing of the first wave packet at the FC region after one roundtrip. Thus the overlap with the second wave packet is increased which enhances interference effects. In the Wigner representation the propagation of the wave packet in time and frequency domain is illustrated in Fig. 3.14. The optimal focussing time T_{opt} of a wave packet in a Morse potential was determined in [43, 82] to be :

$$T_{opt} = -\frac{\beta'\nu^2}{4\pi\omega_e x_e}, \tag{3.22}$$

where ν is the vibrational spacing around the centre energy of a wave packet[12], β' is the chirp parameter in units of fs cm (cf. Eq. 3.13) and $\omega_e x_e$ the anharmonicity. By adjusting the compensation

[12] A 590 nm pulse is centred around $v' = 9$ on the B-state with $\nu = 135\ cm^{-1}$ between $v' = 9$ and $v' = 10$.

plate made of fused silica at an angle of approx. 22° a GVD of 745 fs^2 was induced which acts opposite to the 990 fs^2 which are introduced by the BK7 beam splitter and pre-compensated by the prism compressor. The overall $\beta' = -255\,\mathrm{fs}^2$ results in a focussing of the first wave packet at 240 fs.

The spectral fringe patterns for all time steps $\Delta\tau$ and all relative phases Φ were recorded using the fibre spectrometer behind the Michelson interferometer. Detecting an interference pattern of two pulses being well separated in time is enabled by the pulse elongation which takes place in the spectrometer since different wavelengths follow different paths. To resolve the modulated spectra obtained by the pulse shaper very well, the VIS II section of the fibre OMA was used. During the Michelson interferometer experiments this one was not yet available, therefore measured narrow spectral features only had weak contrast. In contrast to the experiments of Scherer [165, 166] and also earlier experiments done in the Schwentner group [17] the relative phase in the experiments described here was not locked. It was sinusoidal varied, but with an arbitrary starting point due to vibrations of the stepping motor. Therefore, for each $\Delta\tau$ and every one of the applied 16 phases, covering more than 2π the corresponding spectral fringes were recorded. The value of Φ was reconstructed from the measured spectral interferograms, as will be shown in Sec. 6.3.1. To avoid microphonics, mechanical pumps where switched off during the experiment which allowed for an interferometrical contrast of 0.9 which was determined using the common modulation relation [167]

$$M = (I_{max} - I_{min})/(I_{max} + I_{min}). \tag{3.23}$$

3.4.2 Pulse shaper

Computer controlled pulse shaping devices allow the generation of nearly arbitrary waveforms (for a review see Ref. [168]). In general a masking of the spatially dispersed optical frequency spectrum in the Fourier plane is performed in a 4-f-setup consisting of two optical Fourier transformations. Several techniques for spectral masks were used: The first fixed amplitude or binary phase masks [169] were followed by holographic realisations [170]. To gain flexibility in phase manipulation movable and deformable mirrors were employd. The number of flexible control parameters was extended by the amplitude with acusto optical modulators (Dazzler [171], AOM [172, 173]) and liquid crystal spatial light modulators (LC SLM, [168, 174–178]); the latter allow for independent amplitude, phase and even polarisation shaping [179–181].

Optical Fourier transformation and the LC SLM as the modulator used in this work, will be described in detail in this section.

Optical Fourier transformation

From electrical engineering, the concept of manipulating waveforms is well known and described as linear filtering in Fig. 3.9. In the time domain, the ingoing function $E_{in}(t)$ is transformed by a convolution with the impulse response function $H(t)$ to the outgoing function $E_{out}(t)$:

$$E_{out}(t) = E_{in}(t) * H(t) = \int_{-\infty}^{\infty} dt'\, E_{in}(t) H(t - t'), \tag{3.24}$$

where $H(t)$ characterises the system response to a delta function. This corresponds to a multiplication in frequency domain of $\varepsilon_{in}(\omega)$ with the frequency response function $h(\omega)$

$$\varepsilon_{out}(\omega) = \varepsilon_{in}(\omega) \cdot h(\omega). \tag{3.25}$$

Fourier transformation realises the connection of time and frequency domain. Therefore $E_{in}(t) \leftrightarrow \varepsilon_{in}(\omega)$, $E_{out}(t) \leftrightarrow \varepsilon_{out}(\omega)$ and $H(t) \leftrightarrow h(\omega)$, are Fourier transformation pairs which are given explicitly for the outgoing functions.

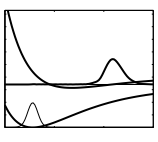

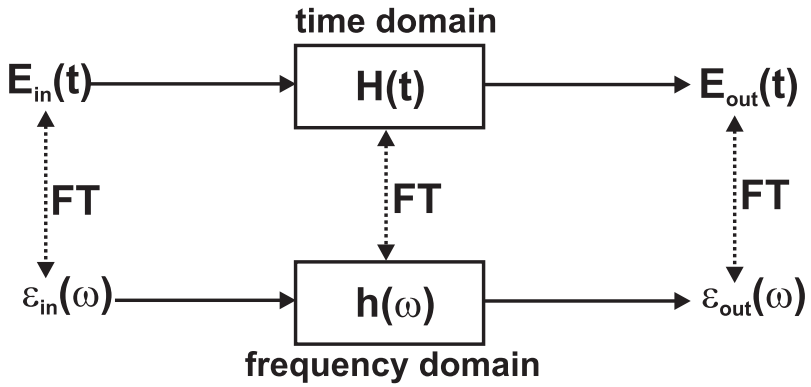

Figure 3.9: Scheme for linear filtering where the initial function $E_{in}(t)$ in time domain is transformed by the impulse response function $H(t)$ to the outgoing function $E_{out}(t)$, and similarly with the frequency response function $h(\omega)$ in frequency domain. Dashed arrows indicate the Fourier transformation pairs.

$$\begin{aligned} \varepsilon_{out}(\omega) &= \int_{-\infty}^{\infty} dt\, E_{out}(t) e^{-i\omega t} \\ E_{out}(t) &= \frac{1}{2\pi} \int_{-\infty}^{\infty} d\omega\, \varepsilon_{out}(\omega) e^{i\omega t} \end{aligned} \tag{3.26}$$

This consideration is transfered to optical Fourier transformation which is accomplished in a 4–f–setup, see Fig. 3.10a. Many realisations are possible, the one described here was chosen to reduce chromatic and geometric aberrations in experiments with visible broadband pulses. The change from time to frequency domain takes place by dispersing the frequencies of the incoming light, after they passed the aperture A and the polariser P, angularly with grating G1 (2000 l/mm) aligned near Littrow configuration[13]. To keep the height at the grating constant the incoming beam passes folding mirror FM1 laterally and hits the cylindrical mirror CM1 (f = 130 mm). CM1 is located in the distance of one focal length, centred, to image the frequencies, dispersed in one plane, to infinity. The second cylindrical mirror CM2 is adjusted to a 1:1 telescope with CM1, with the Fourier plane FP in between them. Concerning the height CM1 is optically inactive, so the level is changed to pass FM1 above. This results however in a tilted Fourier plane, as depicted in the elevation profile in Fig. 3.10b. Beam diameter and frequencies follow antipodal optical paths. The diameter is constant within the telescope while the separated frequencies are focussed in the Fourier plane, allowing a distinct manipulation of the spectrum. In the Fourier plane, one no longer deals with a fs pulse but with "CW" frequency distributions due to their spacial separation. To transform back to the time domain a second grating G2 is placed in the fourth focal length merging all frequencies again over the spacial beam profile in the back transformation. The incoming and outgoing polarisation direction is horizontal. Cylindrical optics are used instead of spherical onces, to avoid high intensity damages on the LC pixel.

Up to now the setup was described as a zero dispersion compressor. Without any manipulation in the Fourier plane, the incoming and outgoing beam should be identical. This was however not

[13]Littrow configuration means that the first diffraction order goes back into the direction of incident light. The grating holder was home made, since commercial ones do not allow for rotation around the grating surface.

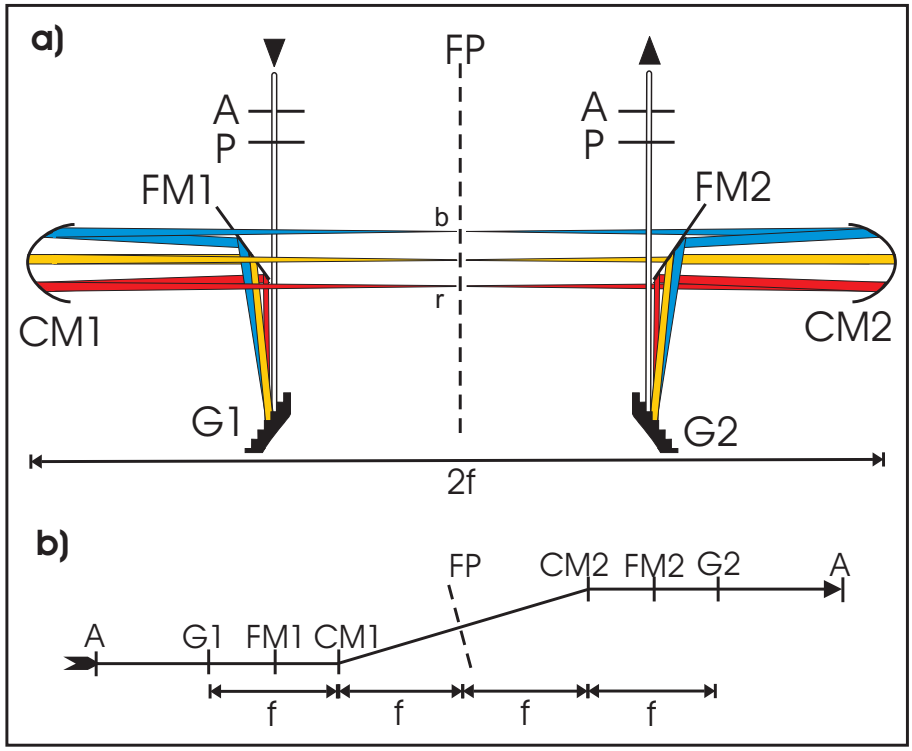

Figure 3.10: a) This 4–f–setup allows for an optical Fourier transformation of light to switch between time and frequency domain. The incoming broadband light is dispersed by grating G1 positioned in the focal plane f of the cylindrical mirror CM1 where "b" indicates blue and "r" red components. In the following focal distance - the Fourier plane FP - the frequencies are focussed and can be manipulated by a pulse former in amplitude and phase. The back transformation is performed with the symmetrically aligned second part. (Other abbreviations: A aperture, P polariser / analyser, FM folding mirror) b) Elevation profile.

the setup used in the experiments described here. To pre-compensate dispersion of other elements like lenses and filters and to avoid an additional prism compressor, grating G2 was adjusted at a longer distance $f + x$ to cause a negative chirp [151, 182–184]. The price one has to pay for this is a spatial chirp[14], depending on the size of the induced temporal chirp, since frequencies are no longer perfectly mixed along the beam profile. This effect was however negligible. A description of the alignment process is given in Refs. [168, 184].

Pulse modulator

To shape the NOPA pulses in Fig. 3.5, a LC SLM (CRI, SLM-256 GPIB) with two electronically addressable arrays, each having 128 pixel, was used [158]. The liquid crystals are nematic, consisting of a thin layer of long, thin and rodlike molecules. They are birefringent, having the optically active axis (extraordinary) along the molecular axis and the ordinary direction perpendicular to it. Without an electric field the LC are aligned[15] in the x-y plane under 45° (Fig.3.11). Applying a voltage V through a transparent film of indium tin oxide (ITO) causes a tilt by the angle θ along the z axis which yields a change in the refractive index $n_e(\theta)$ of light components polarised along the extraordinary axis. Polarisation along the ordinary index of refraction n_o is not affected. The response time of the LC is on the order of ms. A change in $n_e(V)$ causes a phase retardation $\Delta\phi$ of the influenced frequency component and thereby - like in an electronically variable wave plate

[14]This spatial chirp could be avoided by passing the whole grating compressor a second time, like done, $e.g.$, in a CPA, to recombine the frequencies again, see Sec. 3.3.2.

[15]The glass plates around the LC are brushed to force orientation of LC.

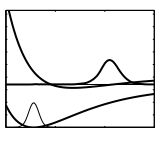

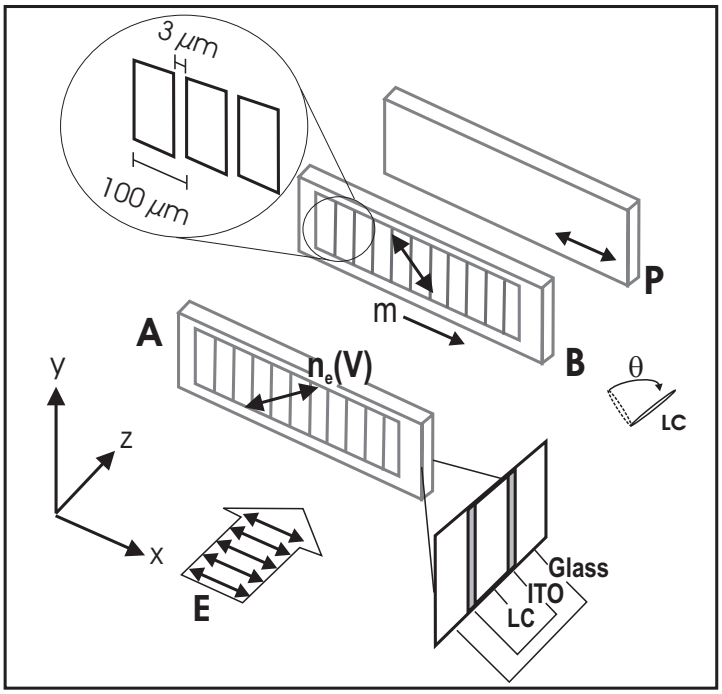

Figure 3.11: Scheme of a SLM consisting of two arrays, see also Refs. [168, 185]. A spectrally dispersed light field E incident along z and polarised along x direction enters the two arrays A and B, each array consisting of 128 pixel of 97 μm width and separated by a 3 μm gap as indicated in the inset - circle on the left. A voltage V is applied via an ITO film to tilt the LC molecules by the angle θ as depicted on the right of array B and thereby change the extra-ordinary index of refraction $n_e(V)$. The outer shell of this sandwich is a glass wall, as shown on the right hand side of array A. The tilted arrows on arrays A and B display the orientation of LC extraordinary axis at -45° / +45°, respectively. To perform amplitude shaping the light has to pass an analyser P which filters out the horizontal components of the partially turned polarisation and thereby reduces intensity. For details see text.

- a change of polarisation state of light:

$$\Delta\phi\,(V) = 2\pi n(V) d/\lambda_0\,, \tag{3.27}$$

with $n(V) = n_e(\theta, \lambda) - n_o(\lambda)$ being the voltage dependent index of refraction, λ_0 the centre wavelength and d the active thickness of around 10 μm per array. In this SLM the voltage range of 10 V can be varied with 12 bit leading to 4096 voltage steps.

SLM containing one array allow for pure phase or amplitude shaping only, since each turn of polarisation to change the amplitude also affects its phase. Amplitude shaping requires an analyser at the exit of the setup to block those frequency components with turned polarisation.

For independent phase and amplitude modulation a combination of two arrays with LC oriented with their extraordinary axis at -45° and +45° is required. The molecular orientation between arrays A and B differs by 90°, therefore the rotation of resulting polarisation and thereby amplitude modulation depends only on the difference of both phase retardances ($\Delta\phi_A$ - $\Delta\phi_B$)/2. Phase modulation is determined by their average value ($\Delta\phi_A$ + $\Delta\phi_B$)/2, for a detailed description see Ref. [184]. For each pixel m the mask function R_m is then

$$R_m = \{\widehat{x}\,cos\,((\Delta\phi_A - \Delta\phi_B)/2) + i\widehat{y}\,sin\,((\Delta\phi_A - \Delta\phi_B)/2)\} \cdot exp\,((\Delta\phi_A + \Delta\phi_B)/2). \tag{3.28}$$

The outgoing field is

$$E_{out,m} = E_{in,m}\, R_m. \tag{3.29}$$

After passing the analyser which is transmitting light polarised along the x direction, this field is reduced to

$$E_{out,m} = E_{in,m} \cdot \underbrace{cos\left((\Delta\phi_A - \Delta\phi_B)/2\right)}_{amplitude\ modulation} \cdot \underbrace{exp\left((\Delta\phi_A + \Delta\phi_B)/2\right)}_{phase\ modulation}. \tag{3.30}$$

To program the desired modulation the phase retardation as a function of applied voltage $\Delta\phi\,(V)$ has to be known. Hence, a phase - voltage calibration for each array is necessary and the procedure can be found described in detail in Ref. [184]. The result is wavelengths dependent and the elaborated way, which has to be chosen when one handles, $e.g.$, octave spanning continua, would require a single pixel calibration. For a bandwidth of 35 nm, as in our experiments, it turned out to be sufficient, to introduce a linear phase correction with λ and only measure the transmittance of a complete array

$$\Delta\phi\,(V) = \Delta\phi'\,(V)\,\lambda_0/\,\lambda. \tag{3.31}$$

One has to keep in mind the discreteness of the pixel. They are separated by gaps (see Fig. 3.11) and furthermore, the entrance window to the shaper is rectangular. Thus the continuously distributed frequencies are cut sharply causing replica pulses in time domain. Reference [186] gives an analysis of these pixelation effects. Characterising the outgoing light with auto - correlation and X-FROG methods (see Sec. 3.3.2) however showed no evidence of them in our experiments.

Concerning the extinction coefficient between maximally transmitted and maximally blocked light through the shaper, it was possible to reach a ratio of 200:1 when the setup is calibrated with polariser and analyser perpendicular to each other. To yield a transmittance higher by a factor of two, the setup was used with the two polarisers parallel to each other and to the table, with the phase–voltage calibration performed under these conditions. This reduces the extinction coefficient to 160:1, which was sufficient, nevertheless.

Generation of pulse sequences

Optimal control experiments, to coherently manipulate a molecular system, are applied by many groups [19,177,178,187,188]. Hereby, a closed loop between detection of a signal and addressing the pulse former is set up. Optimising the yield of one or more observables is performed with an evolutionary algorithm which combines systematic and arbitrary variations of parameters written on the shaper.

This is very helpful when starting with an unknown and maybe very complex system or to prove results obtained with other spectroscopic methods. The aim of this work was however, to exploit the spectroscopic information obtained in chapter 4 in an optimal way and to test to which extent the molecular dynamics in a dissipative environment can be coherently controlled. Those known spectroscopic signatures are therefore written on the pulse shaper and thereby control of the chromophore and its matrix surrounding is performed.

In a first step double pulses like in the Michelson experiments (Sec. 3.4.3 and 6.1) were generated and the experiment was expanded by an additional probe pulse. The comparison provides a good test for both methods. Phase controlled double pulses are achieved in a combination of phase and amplitude shaping, where the parameters of unchirped double pulses, corresponding to a sinusoidal spectral pattern were optimized using the LabView - environment for pulse shaping of Lab2 [189]. These parameters were then adapted for the spectral anharmonicity through comparison of the resulting frequency interferogram with the measured excitation spectrum. Programming the phase on the pulse former was carried out with the function $F_p(m)$:

$$F_p(m) \;=\; A_p\, rect(\frac{(\beta_p m - 1)2\pi m}{\Delta t_p} + \phi_p), \tag{3.32}$$

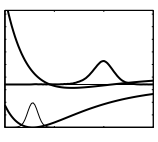

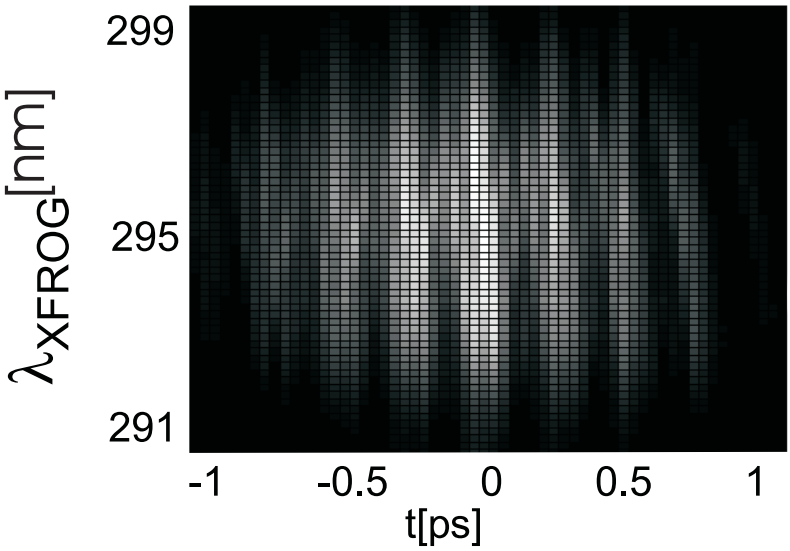

Figure 3.12: Pulse train in X-FROG trace. Spectral features are smeared out since the gate pulse is very short in time and thereby broad in frequency (see Sec. 3.3.2).

where $rect$ is a rectangular function, and for the amplitude

$$F_a(m) \;=\; A_a\, sin^2(\frac{(\beta_a m - 1)2\pi m}{\Delta t_a} + \phi_a) \tag{3.33}$$

with m the actual pixel, ϕ the phase, β a chirp parameter, correcting the anharmonicity and Δt a period. Typical parameters for 590 nm pulses are given in Tab. 3.1.

Table 3.1: Parameters for phase and amplitude shaping to achieve double pulses. Those numbers are only guiding values for 590 nm excitation and have to be adapted at each measurement. Two phase values are given, for optimal excitation of ZPL and PSB, adapted while monitoring the spectral fringe pattern and the double pulse pattern in the auto - correlator.

Parameter	Phase	Amplitude
A	3.14	1
β	0.00175	0.00175
Δt	23.50	23.50
ϕ for ZPL	3.95	3.95
ϕ for PSB	3.00	3.00

The ultimate experiments were carried out with a sequence of 7 ultrashort pulses of different chirp, again to overcome dispersion effects of the molecule and to maintain a maximal overlap of the vibrational wave packets. This sequence of phase controlled pulses is obtained by amplitude only shaping, setting the transmitted frequencies to the spectral vibrational progression. An X-FROG trace of such a pulse train is given in Fig. 3.12.

Shaping the spectral amplitude also creates a modulation of the light phases in the time domain, despite the fact that the phases in the frequency domain were kept constant. An analysis will be given in Sec. 6.3.1

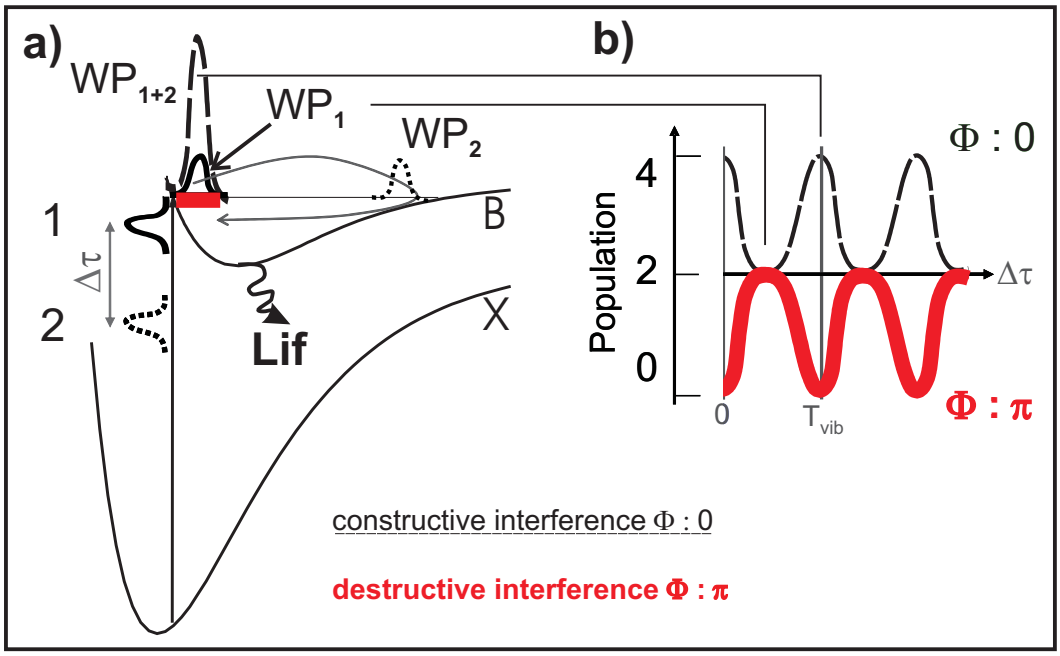

Figure 3.13: a) Scheme for wave packet preparation of WP_1 (solid, depicted after one full roundtrip) and WP_2 (dashed, shown at 1/2 roundtrip) on the B-state by phase controlled laser pulses 1 (solid) and 2 (dashed) separated by the time delay $\Delta\tau$. Laser induced fluorescence (LiF) from this covalent state and the lower lying A'-state (not shown) is observed. The wave packets are born at the inner turning point and propagate on the potential. Interference requires an overlap and electronic coherence. For a time separation of $1/2\,T_{vib}$ where one wave packet is located at the inner and one at the outer turning point no interference effects would be observed. For $\Delta\tau = n\,T_{vib}$ the wave packets overlap at the inner turning point where destructive (thick line) or constructive (dash-dotted WP_{1+2}) interference can occur, depending on their relative phase Φ. b) Phase Φ and time delay $\Delta\tau$ dependence of the fluorescence intensity. Two coherently created wave packets lead to constructive (upper trace) or destructive (lower trace) interference on the potential. Extrema occur at multiples of the vibrational roundtrip time T_{vib}. This scheme does not include any losses. In the real experiments of a chromophore in the bath, a strong decay at longer time delays will be observed.

3.4.3 Double pump experiment

Experiments with femto second phase-locked pulse pairs (PLPP) provide a direct and flexible way to investigate electronic coherence. A PLPP can be generated by splitting a femto second pulse with a Michelson interferometer where the end mirror of one arm is controlled by a micrometer step motor to change the time delay $\Delta\tau$, between the PLPP while the other arm has a piezo controlled mirror to adjust their relative phase ϕ (see Sec. 3.4.1).

The first application of PLPP experiments to a molecular system was carried out by Scherer *et al.* in 1990 [190] to study decoherence of rovibronic transitions of gaseous I_2 molecules [128,165]. Later, other isolated systems [191–197] as well as molecules in the condensed phase [198–219] were studied. The PLPP method was applied to coherently control matter-wave interferences and determine decoherence times in large molecules [220], small molecules [4, 12, 16, 221] and atoms [45]. Other techniques benefit from "coherence observation by interference noise" (COIN [206, 212, 216, 222]) where the phase between the Michelson pulses is randomized and only quantum intereference fluctuations, being stronger or weaker due to constructive or destructive interferences, are detected. Nevertheless, the overall decoherence time can be deduced from the amplitude decay of the noise envelope. However, this approach can only be used to analyse a system and is not

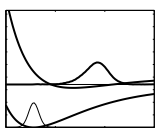

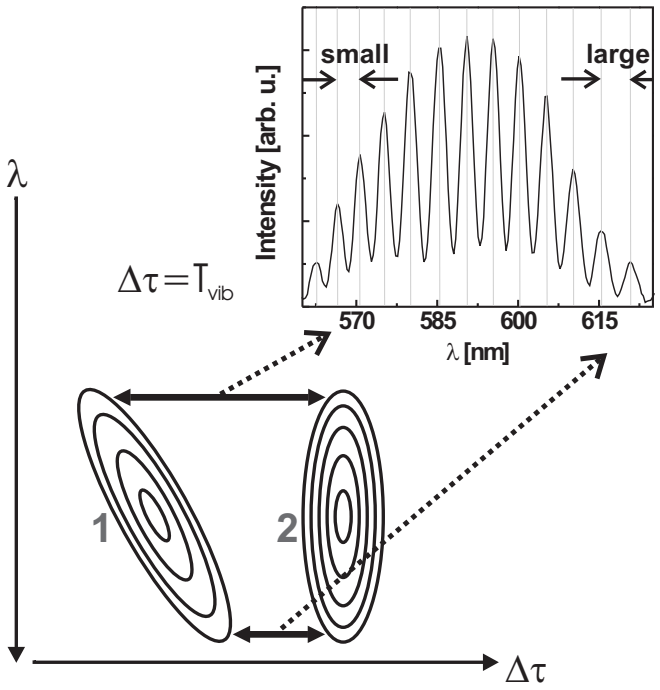

Figure 3.14: Time and spectral representation for a negatively chirped laser pulse 1 and an unchirped pulse 2, which interfere after a time delay $\Delta\tau = T_{vib}$. A large separation in time $\Delta\tau$ at shorter wavelength λ lead to narrow spectral fringes in the interference pattern shown on top and vice versa, compensating the anharmonicity of the molecule.

applicable to control interference effects.

In molecular wave packet interferometry, the coherence in the electric field of the first pulse is imprinted to a molecular wave packet on the excited electronic state. A second phase-locked pulse creates another wave packet on the excited electronic state after a time delay $\Delta\tau$ (Fig. 3.13a). The two wave packets interfere on the excited state. If the first wave packet is located in the FC range with the ground state at the time of the second excitation, the interference leads to a change of the overall excited state population. One can record this in a variation of the fluorescence intensity as sketched in Fig. 3.13b. Since the wave packet created by the first pulse leaves the Frank - Condon region and oscillates in R on the upper potential surface, the second pulse can interfere with it and thereby modulate the population only, when the wave packet returns to the Frank - Condon region. Furthermore, if the electronic or vibrational coherence of the ground and excited state is lost within the delay time $\Delta\tau$, the interference phenomena are averaged out[16]. A similar effect will be observed for a wave packet that does not return to the FC region because of vibrational energy relaxation.

Through the interference, population is transferred to the excited state in a constructive ($\phi = 0$) or destructive ($\phi = \pi$) way, depending on the relative phase ϕ between the PLPP[17]. The interference effects can be observed as vibrational recurrences in an interferogram if molecules preserve coherence. The decrease in modulation contrast of the recurrence provides the electronic decoherence time, in the case that vibrational coherence lives much longer (which is often the case). In analogy to Young's double slit experiment [44] the energetic correspondence of an interference pattern caused by two pulses having a time delay $\Delta\tau$ shall be treated next [45]. The fringe spacing $\Delta\nu$ is given as

$$\Delta\nu = 1/\Delta\tau. \tag{3.34}$$

[16]Usually, the electronic decoherence is much faster than the vibrational one, see Sec. 2.2.7

[17]Phase Φ is related to the shift between lock frequency ω_{lock} as carrier frequency and the maximum of the envelope. In case of the double pulse experiments discussed here, no real phase locking was performed, although the phase was determined afterwards out of the collected spectral fringes. This will be explained in detail in the discussion of pulse train experiments in Sec. 6.3.

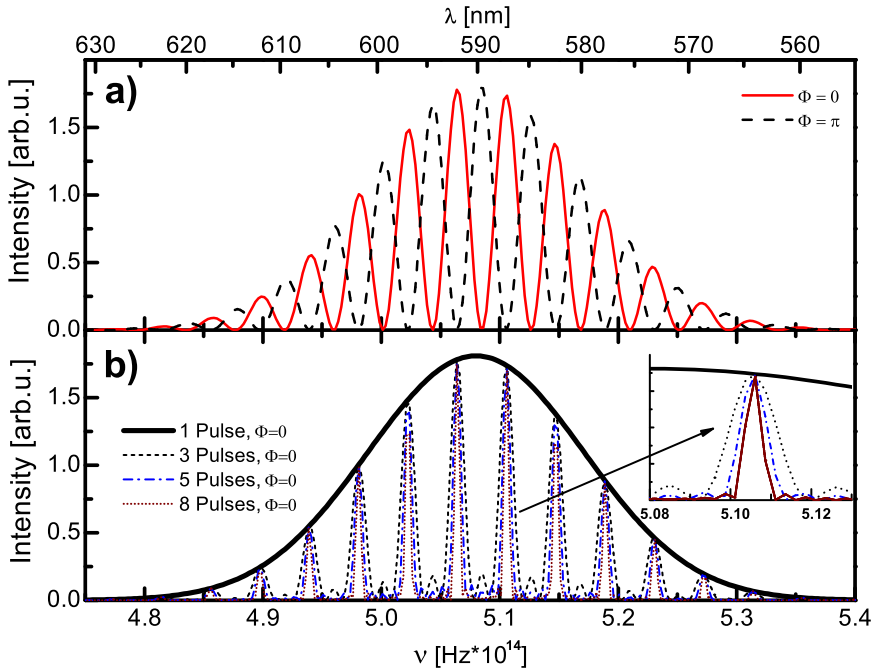

Figure 3.15: a) Simulated spectral fringes for two pulses with a phase shift of π in between them. b) Demonstration of the spectral sharpening when up to eight pulses are applied, enlarged for one peak in the inset.

Figure 3.14 displays this correspondence for $\Delta\tau = T_{vib}$. At this time delay of one vibrational roundtrip, the spacings match to the spectral vibrational signature. In the lower part a Wigner representation of two time delayed laser pulses is shown, pulse 1 with a negative chirp, pulse 2 is unchirped. This leads different frequency spacings shown in the upper part of the figure. The shorter time delay at lower frequencies causes a larger spacing and vice versa. This pre-chirping of the first pulse is required, since the molecular potential is anharmonic. Spectral spacings are not equidistant and this behaviour must be included in the two pulses. The time domain effect of this anharmonicity is dispersion of the wave packet which has to be compensated by chirping of one pulse to achieve a focussing of the wave packet, see Sec. 3.4.1 and Ref. [2].

A shift of the relative phase in time between the PLPP does not change the relative spacing. However, the absolute position of the fringes moves and this is simulated in Fig. 3.15 for a relative phase difference of π between the solid and the dashed spectrum with sinusoidal modulation due to the interference of two pulses. It shows the Fourier transformation of two unchirped pulses, time delayed by one roundtrip time; the solid line has the phase $\phi = 0$, fitting to a ZPL excitation and the dashed line with $\phi = \pi$ belongs to the PSB.

In Sec. 6.2 of this work it is shown, that the phase can be used to excite predominantly ZPL or PSB, carrying on experiments on Cl_2/Ar [17, 18].

3.4.4 Multiple pump - probe experiment

Fundamental concepts in coherent control were introduced, *e.g.*, based on interfering pathways, to steer the modulation of a final state, by Brumer and Shapiro [223]. Followed by the experiments in the group of Elliot [224]. A method to control distinct products of chemical reactions was proposed by Kosloff, Tannor and Rice [225]. Hereby, a wave packet propagating on a complex potential surface is dumped at appropriate timing by another laser pulse to the desired reaction pathway. This concept was applied in experiments, e.g., in the group of Gerber [226]. These principal studies

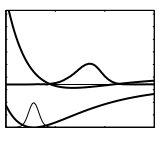

were extended to complex laser fields in the optimal control theory, where exemplarily the group of Herschel is named [227].
Some example experiments of weak field control are given: First applications with tailored pulses in the group of Wilson [228] permitted the manipulation of fluorescence ratios and the absolute signal increase of dyes in the liquid phase, applying an evolutionary algorithm. Vibrational ladder climbing was another task, which succeeded, $e.g.$, in the group of Heilweil [229] on liquid $W(CO)_6$. Closest to the experiments presented here, are the pulse train investigations of Weiner and Nelson [7]. They applied a pulse train whose spacing matched the vibrational spacing of α-perylene. In recent experiments in the group of Motzkus, Raman modes of β-carotene were enhanced. This allows for selecting of single modes and stronger coherences. Reviews on quantum control are found, $e.g.$, in Refs. [20, 168].

The basic concept of the double pulse experiments of Sec. 3.4.3 is naturally preserved in a multiple pulse experiment, where a phase stable sequence of pulses acts in the pump step and an additional probe pulse samples the time dependent wave packet propagation as indicated in Fig. 3.16. However, in comparison to the two pumping pulses, spectral definition and coherence requirements are enforced. A longer lasting electronic coherence time is necessary to let all those sub-pulses of a pulse train interfere. If this is fulfilled, much sharper frequency structures are imposed on the molecule and with each pulse the excitation is more selective, as can be seen in Fig. 3.15b. As labelled in the legend the superposition of 1, 3, 5 and 8 pulses is simulated. With each additional pulse the spectral peaks get sharper. In the experimental realisation for each peak three pixel were set to maximal transmittance. This spectral feature was shifted over the frequency range to optimally excite ZPL, PSB and an area in between them, as will be discussed in Sec. 6.2.3.

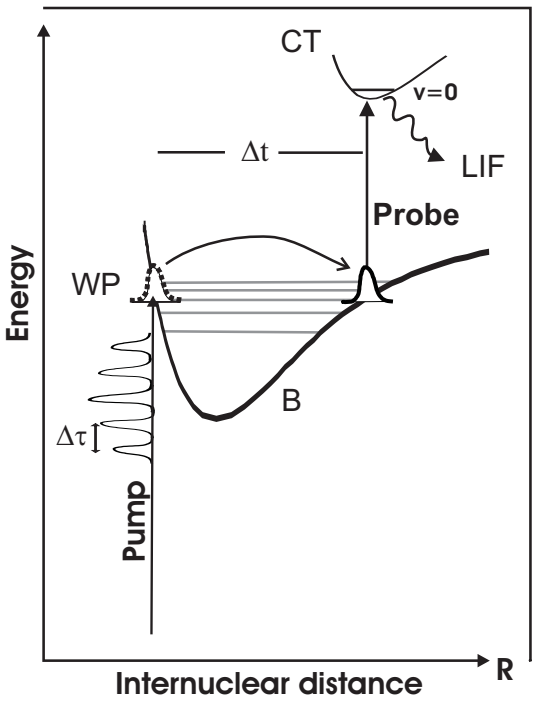

Figure 3.16: Scheme of multiple pump - probe experiment. A pulse sequence with delay $\Delta\tau$ excites wave packets which interfere depending on their distinct phase properties. These wave packets are probed with a second laser pulse to the higher lying CT states.

Chapter 4

Analysis 1: Frequency resolved spectroscopy

This work improves earlier frequency resolved studies of Br_2/Ar, to derive a quantitative insight on curve crossings of the B-state with repulsive states. They are displayed, $e.g.$, in the intensities of zero phonon lines (ZPL) and on the coupling of chromophore and matrix which is mirrored in the phonon sidebands (PSB). The purpose of this chapter is to resolve open questions concerning spec-

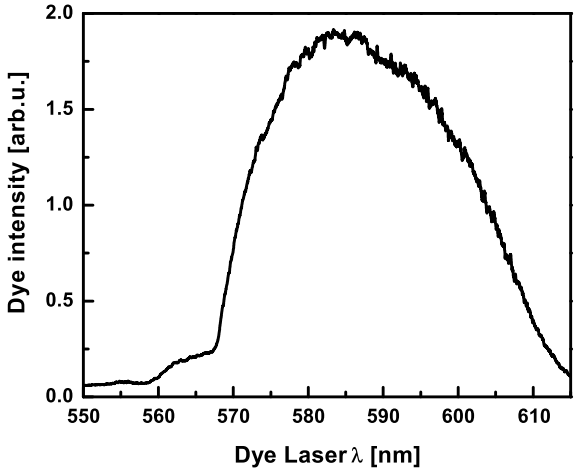

Figure 4.1: Dye laser power curve for Rhodamine 6G.

troscopic characteristics by an improved set of emission and excitation spectra. In the following we motivate shortly the measures taken to clarify the specific points. Neither $v' = 0$ in the B-state nor $v'' = 0$ in the X-state could be observed with certainty in excitation or fluorescence spectra in Sec. 4.1.1, respectively, due to very small Franck - Condon (FC) factors. A unique assignment of the v' and v'' numbering had to be based on the isotopic splitting of vibrational transitions. The interpretation of our fluorescence spectra will be consistent with that in [107]. Our isotopic data in excitation differ from those in [97] and compared to [107] we will increase v' in B by one unit. This correction now leads to consistent T_e values in absorption and emission. The experiments were carried out with several dyes to cover the full range from the bottom of the B-state nearly up to the FC maximum and the intensities in the fluorescence spectra are corrected for dye laser intensity profiles. Indeed pronounced drops in ZPL intensities in Sec. 4.1.2 show up with rising v' which indicate the onset of loss processes, $i.e.$, curve crossings with repulsive states opening predissociation channels. In addition a further rather monotonic decay of quantum efficiency with energy above the curve crossings will be presented. It displays the competition of population relaxation with predissociation and the increased overall residence time of population above the crossings with larger excitation energy according to modells suggested in Sec. 2.2.6. For these considerations a more sophisticated treatment of the intensity distribution between ZPL and PSB will be necessary because spectral weight is shifted to the sidebands with increasing v'. The two

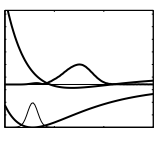

dimensional plots of fluorescence $vs.$ excitation contain also the excitation spectra of the A and A' fluorescence and the A-state continuum will be determined. Furthermore, the cross talk between the nested A, A' and B-states is displayed in these two dimensional spectra. It will be shown that indeed only about 10^{-3} of the population fed into the B-state near the FC maximum, remains in the B-state and fluoresces after relaxing to $v' = 0$. Predissociation funnels out more than 99% into the other valence states and this flow for example into the A'-state generates B-state vibrational structure in the A' excitation spectrum. The flow is however unidirectional and no feeding of the B-state from A or A' is observed. Directionality will be attributed to the different types of energy loss in the B-state potential-well, compared with that in the matrix bound repulsive states and A-state dissociation continuum. Finally the spectral composition of the PSB and its relation to the matrix phonon density of states (PDOS) will be treated, together with the temperature dependence of the ZPL shape and intensity.

Additionally to this spectrally narrow excitation, in Sec. 4.1.5 ultrashort pulse experiments with excitation of the repulsive state C and the covalent B-state are included.

4.1 Results

Our dye laser excitation spectra provide the spectroscopic bases for the control experiments and have been published recently in Ref. [22]. First, emission spectra are introduced, later on the excitation spectra, reconstructed out of this emission at different excitation wavelengths will be presented. The spectra have been taken at different dyes, as described in Sec. 3.2. For illustration a typical intensity curve of the standard dye Rhodamine 6G is plotted Fig. 4.1.

4.1.1 Emission spectra from covalent excited states B, A and A'

Figure 4.2a shows an example of an emission spectrum displaying strong B→X transitions. Indeed, a progression of six sharp, strong lines belongs to emission from $v' = 0$ in the B-state to several ground state vibrational levels v''. The absolute numbering of v'' is still open at this point. However, to avoid confusion the final assignment from analysis of the isotopic splittings is used which is presented later on. In fact, always a triplet of lines is observed which represents the emission from the three isotopomers 79/79, 79/81 and 81/81. The central line is enhanced by the chosen excitation wavelength of 593.13 nm which is just on top of an absorption peak of the 79/81 isotopomer as will be evident in Fig. 4.4. On the red side in Fig. 4.2a two members of a new progression show up which belong to emission from A'($v' = 0$). The spectrum in Fig. 4.2b displays the longer wavelength range. It can be seen that the A'($v' = 0$) → X(v'') progression becomes more pronounced since the emitting A'-state lies lower in energy than the B-state. Decreasing intensity at higher wavelengths is caused by the reduced CCD sensitivity. Finally a further emitting state comes into play with the A($v' = 0$) → X($v'' = 12$) line. The A'$^3\Pi_{2u}$ state, which was not mentioned yet, is spectroscopically well-known and included in Fig. 2.1. This transition breaks the spin and the Ω selection rule for Hund's case c and is therefore too weak to be seen in absorption (Fig. 2.4). It is however the lowest excited electronic state and nonradiative transitions funnel population with high efficiency into this bottle neck. The long A' lifetime of 44 ms compared to 107 μs and 6.57 μs of the A and B-state according to Ref. [107] reflects this hierarchy of oscillator strengths.

How the strength of B emission varies with excitation wavelength is depicted in Fig. 4.3. The thin black line shows a zooming in in Fig. 4.2b where the strongest isotopomer 79/81 is excited with the wavelength 579.6 nm. A variation of λ_{exc} to 579.28 nm gives the thick grey line with the enhanced 79/79 isotopomer on the right hand side. Now the middle peak of 79/81 is reduced to its normal heights, which is still a factor of two stronger than the 81/81 line on the left hand side, due to the natural isotopomer abundance of 1:2:1.

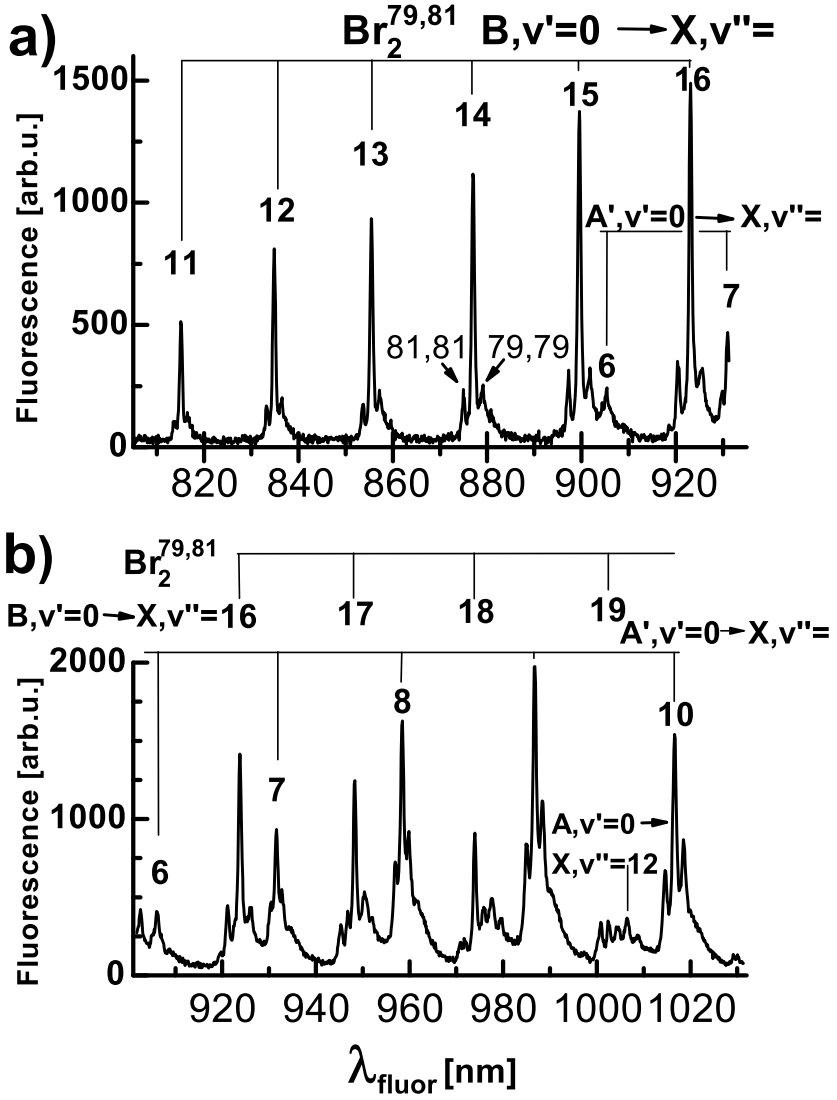

Figure 4.2: Emission spectrum obtained with excitation wavelengths of 593.13 nm (B, $v' = 8$, panel a) and 579.58 nm (B, $v' = 11$, panel b). Panel a) is dominated by B-state emission from $v' = 0$ to the ground state X (here from $v'' = 11$ to $v'' = 19$). Panel b) shows contributions of B($v' = 0$), A'($v' = 0$) and A($v' = 0$) emission. Each triplet of sharp peaks corresponds to the three isotopomers of Br_2 (81/81 ; 79/81; 79/79). The centre one (79/81) is strongly enhanced since its ZPL - energy was selected.

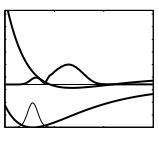

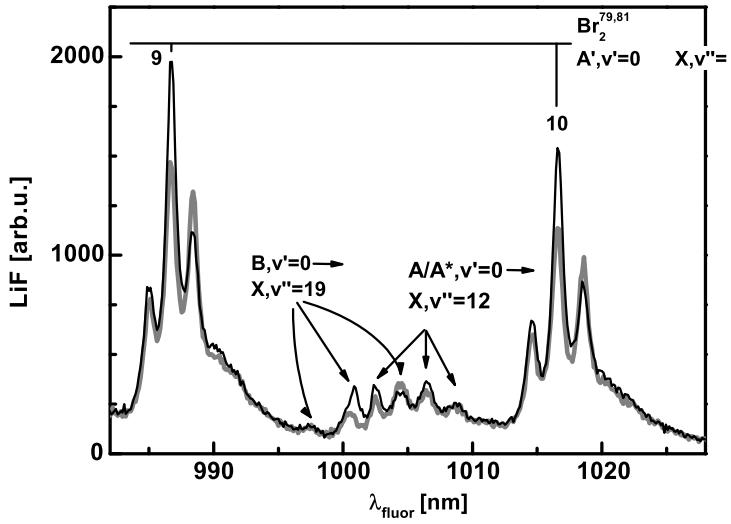

Figure 4.3: Zoom into the last figure with the excitation wavelength of 579.58 nm, exciting the 79/81 isotopomer (thin black line) together with an emission spectrum taken at $\lambda_{exc} = 579.28\,\text{nm}$ which is absorbed by the 79/79 isotopomer (thick grey line). This time the centre isotopomer is attenuated and the right one is enhanced. Around 1005 nm the overlapping emission lines of B and A transitions are indicated by three arrows, each for the three isotopomers.

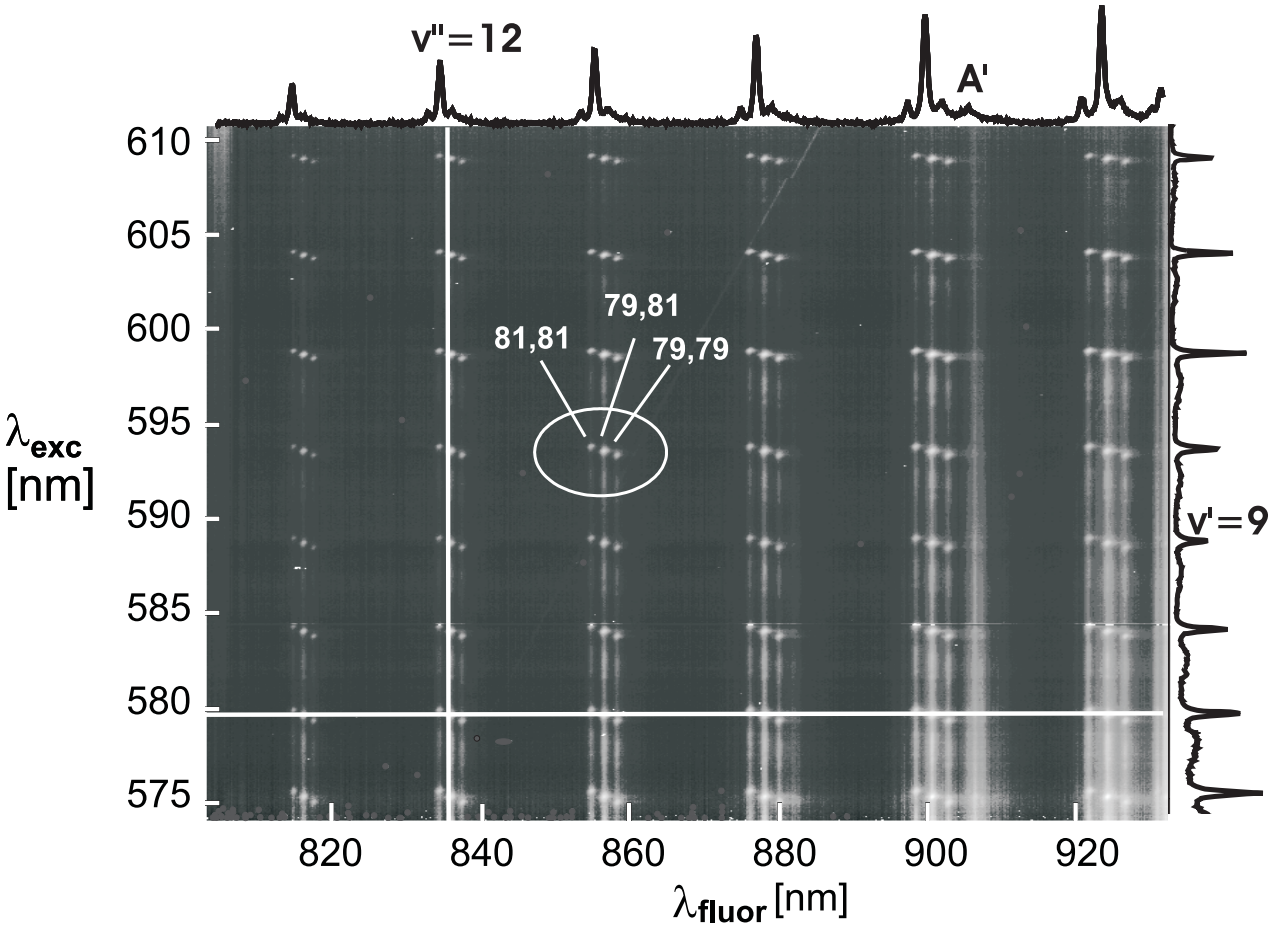

Figure 4.4: Combining emission spectra (λ_{fluor}) obtained by scanning the excitation energy (λ_{exc}) leads to this two - dimensional grey scale plot. The spots show the zero phonon lines (ZPL). A trio of spots along the λ_{fluor} direction represents the isotopic splitting of the ground state; the shift along λ_{exc} corresponds to the B-state isotopic splitting. The large spectral extension of the phonon sidebands (PSB) yields vertical "lines". A fluorescence spectrum (top, like the one in Fig. 4.2a) corresponds to a cut along the horizontal line and an excitation spectrum (right hand side) to the vertical white cut.

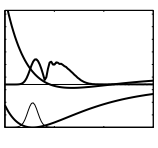

4.1.2 Excitation of covalent states

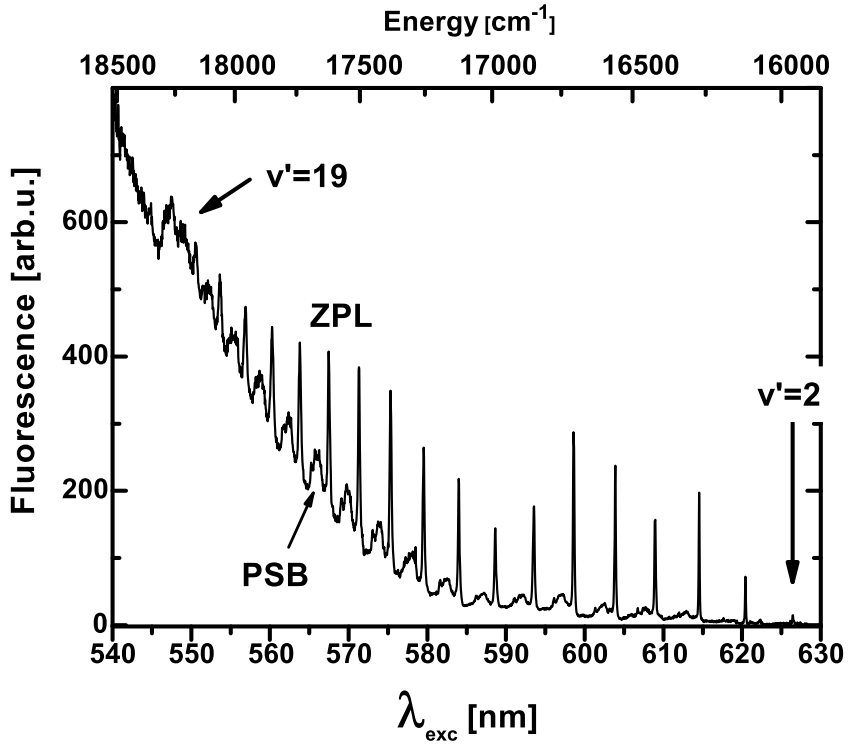

Figure 4.5: B-state excitation spectrum measured at 6 K. It consists of sharp ZPL and broad PSB, which are summing up to the increasing background with higher energies. A vibrational progression is visible from $v' = 2$ to $v' = 19$, which is far below the gas phase dissociation limit at about 510 nm.

Energetics

Now the excitation wavelength was scanned and the successive emission spectra were stored, as reproduced in the two dimensional grey scale plot in Fig. 4.4. The horizontal axis represents once more the range of emission wavelengths. A horizontal cut, for example along the white line at an excitation wavelength of 580 nm, shows the B and A'-state emissions like in Fig. 4.2a, however with a variation in the relative intensities. Indeed in the vertical direction, $i.e.$, with changing excitation wavelength, the emission bands form bright lines with a substructure consisting of superimposed even brighter spots. A cut along the central isotopomer 79/81 of a B emission indicated by the vertical white line shows that these dots represent sharp excitation bands (right hand side in Fig. 4.4) which correspond to ZPL in the X($v'' = 0$) $\rightarrow$ B(v') vibrational progression. The dots are slightly shifted along excitation wavelength for the emission lines of different isotopomers due to the isotopic splitting in the B (v') progression. The sharp lines are followed by broad bands which represent the PSB. It is immediately evident in Fig. 4.4 that the relative strengths of the sidebands increase towards shorter excitation wavelength. Finally, the A' excitation in Fig. 4.4 is predominantly a strong continuous line. However, closer inspection indicates already a slight enhancement at excitation wavelength positions parallel to the bright dots in the B excitation. Obviously, strong B excitation increases also A' emission intensity and this represents cross-talk from B to A'.

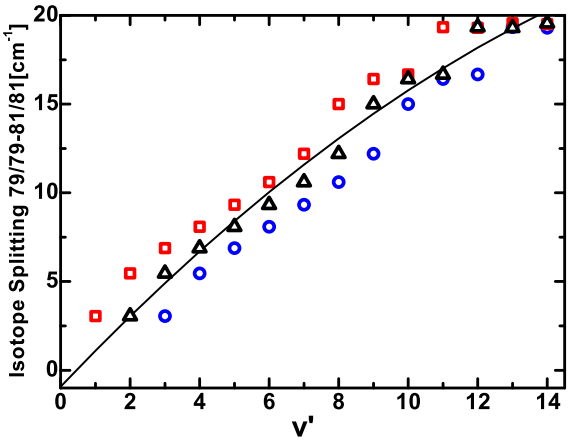

Figure 4.6: Assignment of B-state vibrational levels v' using the calculated isotopic splitting $\Delta\nu$ (Equ. 4.1.2, solid line) as a reference. The measured data points are positioned according to Bondybey's ([97], open circles at $v'+1$), Langen's ([107], open squares at $v'-1$) and our numbering (open triangles).

To clarify the assignment of vibrational numbering, the energies of the B $\rightarrow$ X emission bands are collected for the three isotopomers from all of our data and compared with the four previous sets of data [49, 72, 97, 107] and the excitation spectrum of Ref. [97] was shown in Fig. 2.4b. Our results fully agree with respect to transition energies and isotopic splitting with the most recent and most detailed investigation of Langen *et al.* [107]. Therefore, our assignment is in full accord also with their analysis. It could not be improved, so we consider their results for the X-state concerning ω_e, $\omega_e x_e$ and also the T_e in emission for X-B in Tab. 4.3 as confirmed by these new data. This result however strengthens the discrepancy in v' assignments. B-state excitation spectra were presented only in Ref. [97] where for the v'' in X a value higher by one unit was taken. Since the ω_e in X is about twice as large as in B, the reinterpretation of the spectrum from [97] in [107] suggested a jump in B(v') assignment by two units to lower values. The source of the problem rests with the B-state excitation spectra. An example for the 79/81 isotopomer is presented in Fig. 4.5 with an averaged accumulation of the intensities of emission bands to reduce noise. The energy differences ΔG between subsequent v' levels were extrapolated in a Birge - Sponer plot to $v'=0$ in order to derive w_e and $w_e x_e$. Transition energy ν_{00} and from it T_e where derived by an anharmonic approximation of the energy levels. With the original v' choice of [97] one ends up at a T_e which is too high by one ω_e of B, while with the suggested one in [107] it is too low by the same value compared to T_e from emission data. This is a strong indication that the correct numbering lies just in between. Indeed the T_e values of (15708.5 $\pm$ 0.5) cm^{-1} for the three isotopomers in absorption and the new B numbering which is used throughout this paper lies just in the uncertainty range of the emission T_e for the different isotopomers (Tab. 4.3). The final confirmation delivers the isotopic splitting versus v'. With the standard expression for the isotopic splitting of electronic transitions in absorption [42]

$$\begin{aligned}\Delta\nu &= (1-\rho)\omega'_e(v'+1/2) - (1-\rho^2)\omega_e x'_e(v'+1/2)^2 \\ &\quad -(1-\rho)\omega''_e(v''+1/2) + (1-\rho^2)\omega_e x''_e(v''+1/2)^2.\end{aligned} \tag{4.1}$$

Taking the mass ratio ρ=0.9876 for 79/79 and 81/81 isotopomer combinations and spectroscopic constants of the B-state from this work and for the X-state from [107] (see Tab. 4.3) the predicted $\Delta\nu(v')$ dependence shown by the solid line in Fig. 4.6 is obtained. The experimentally determined splittings of this work follow the expected trend with the new assignment (open trian-

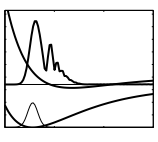

gles) very well while the previous assignments according to Ref. [107] (open squares) or [97] (open circles) lie systematically either above or below the required behaviour. Thus, the new isotopomer data are only consistent with the new assignment.

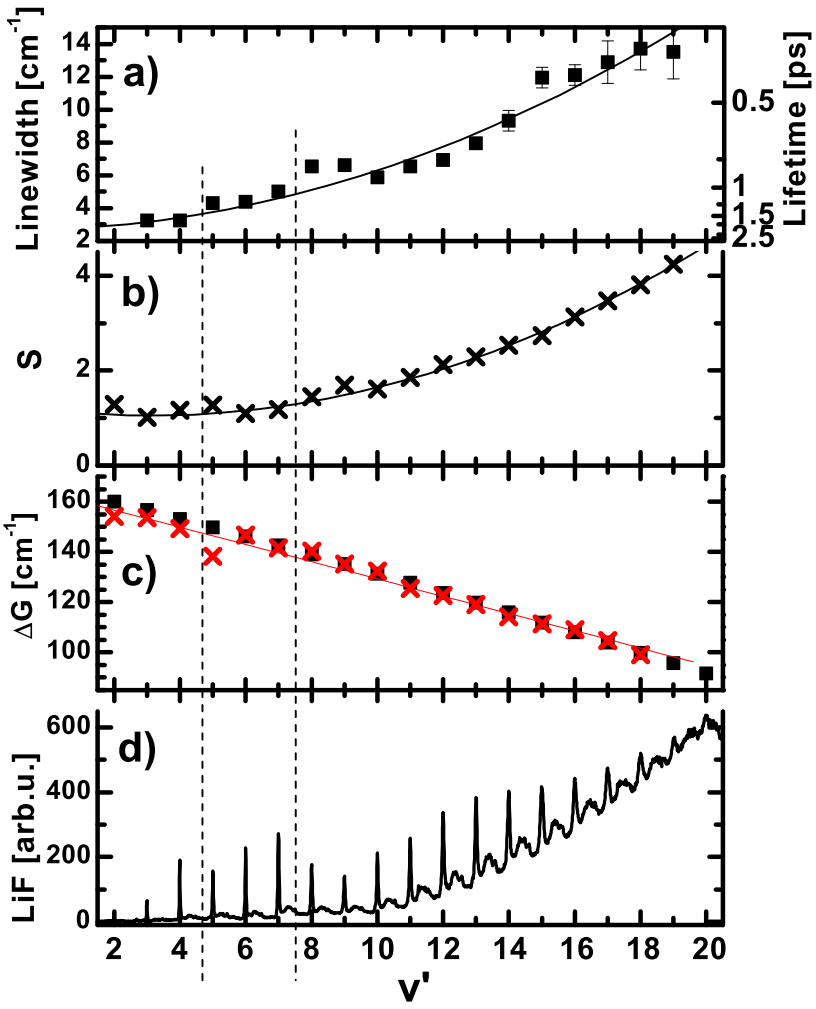

Figure 4.7: a) Linewidth (FWHM) and lifetime of ZPL. b) Coupling constant S calculated following Equ. 2.1. c) Birge - Sponer plot with the energy distance $\Delta G(v')$ between two vibrational levels v' and $v'+1$ with matrix data (crosses) and gas phase (squares, calculated using data from [59]). d) B-state excitation spectrum. Crossings with two repulsive states are marked by vertical dashed lines. Solid lines are quadratic fits, see text.

Next, the ZPL and their sidebands are considered in more detail. At low temperature (here 6 K) the probability for thermal excitation of the lattice and chromophore vibration is small. In this case a transition from X($v'' = 0$) in the vibrational and ($n'' = 0$) phonon ground state of the surrounding lattice, to a vibrational level v' of the Br_2 B-state can occur without changing the phonon state n in the environment. This is called a zero phonon transition. The Br_2 molecule is embedded in a double substitutional site of the Ar lattice and it was shown that rotations are blocked (Ref. [43] for Br_2 and [73] for I_2). Therefore, one deals with an exclusive excitation of the

vibrational modes of the Br_2 molecule. Accordingly, a sharp line with the linewidth determined by the lifetime (given by decoherence and depopulation) and by inhomogeneous broadening is expected. The experimentally determined full width at half maximum (FWHM) values at 6 K for the resolved v' levels are collected in Fig. 4.7a. Values in cm^{-1} (left hand scale) are converted to a time constant in picoseconds (right hand scale) based on a Lorentzian line-shape. As described in Ch. 3 the samples are prepared very carefully in order to reduce inhomogeneous broadening and achieved smaller line widths as for example in Ref. [97]. The smallest lines with a FWHM of 3 cm^{-1}, corresponding to a lifetime of 2 ps, appear at low v'. A residual inhomogeneous contribution cannot be excluded, the excitation resolution (0.5 cm^{-1}) however, does not affect the linewidth. Such a long decoherence time is consistent with time resolved investigations [2]. If inhomogeneous contributions are still present, the underlying lifetimes would be even longer. A significant lifetime effect is the systematic decrease as a function of v' by about a factor of five (Fig. 4.7a). This reflects the increasing interaction strength with the lattice at larger vibrational elongations and also predissociation as will be shown later on.

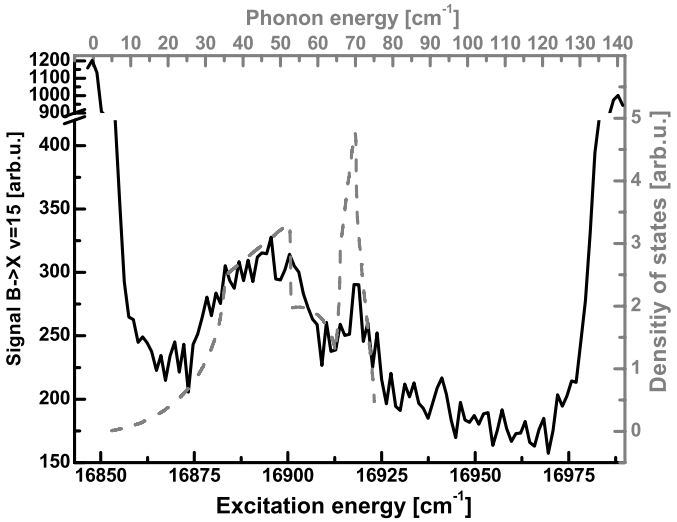

Figure 4.8: Cut-out of the B state excitation spectrum (solid line), showing a PSB ($v' = 8$) in the centre and two ZPL at the edges ($v' = 8$ left and $v' = 9$ right). The phonon density of states at 10 K is included as dashed line. It was obtained by neutron scattering by Fujii *et al.* in 1974 [230], and scaled from ^{36}Ar to ^{40}Ar.

Besides these ZPL also transitions are excited in which a single phonon in the vicinity is created together with the electronic and vibrational excitation of the chromophore. The additional energy required for the phonon leads to the formation of a PSB on the blue wing of the zero phonon transition. A wide spectrum of phonon modes can come into play [139], including local [32] and lattice phonons [95, 96]. The PSB of the $v' = 8$ vibrational transitions is enlarged in Fig. 4.8. On the left hand side the $v' = 8$ ZPL appears which is cut in intensity for comparison. It serves as a reference energy scale for the phonon spectrum given on top in Fig. 4.8. The next ZPL $v' = 9$ shows up on the right hand side. To give a feeling for the energy distribution of the modes, the phonon density of states of the pure Ar crystal (dashed line), by Fujii [230] is also included. It was scaled by $\sqrt{36/40}$ to account for the mass difference of the used isotopes[1]. There is a remarkable

[1] In natural abundance of Ar, which is used in our experiments the isotopomer ^{40}Ar dominates with 99.6%.

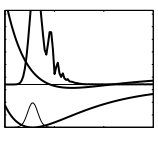

similarity in the overall extension up to about 75 cm^{-1} and even in qualitative features like the maximum at 70 cm^{-1}, the two minima around 60 cm^{-1} and 20 cm^{-1} as well as the broad hump between 30 and 50 cm^{-1}. The very same features show up in all resolved single PSB from $v' = 4$ up to $v' = 17$.

The sideband rests on a background which increases systematically with v' (Fig. 4.5 and 4.7d). It arises since next to single phonon creation processes also two-phonon creation processes can occur. Any two phonons in the available distribution can be combined. Therefore, the two-phonon spectrum lies below the one-phonon spectrum and extends up to twice the maximum one-phonon energy. Their superposition washes out structures in the phonon density of states. This explains why the two-phonon part builds up to a background with no prominent features. There is a clear trend visible in Figs. 4.5 and 4.7d that the two-phonon contribution rises in a similar way with v' as the single phonon one. The probability of three and multi phonon processes should also become important. Since all of them lie on the blue side of the v' levels they add up to a continuous background which starts to dominate the spectrum beyond $v' = 12$, until around $v' = 19$ structures are no longer resolvable. Obviously, the treatment of such a multitude of degrees of freedom is quite demanding [99, 139] nevertheless it is being tackled now on a quantum mechanical footing [39]. To parameterize the data a rather crude model, the linear coupling model [101,104,231], is applied widely and successfully. It works with configuration coordinates in the following sense: If the excited lattice would remain in the ground state configuration, $i.e.$, the transition generates no driving force and thus no displacement, then only a zero phonon transition would occur. If additional lattice changes are induced, then they are summarized in a single configuration coordinate and treated as one displaced harmonic oscillator. The FC factors can be calculated analytically and cast in the Huang-Rhys coupling constant S [105], already introduced in Eq. 2.1. It gives the phonon number with the largest FC factor and is well suited to describe the relative intensity distribution I_n among n phonon states by

$$I_n = e^{-S} S^n / n! \; .$$

A larger shift in the configuration coordinate causes a larger S, a wider distribution of multiphonon transitions and a reduction of the ZPL intensity. The ratio $\sum_{n=0}^{\infty} I_n / I_0$ of the area of all phonon bands $\sum_{n=0}^{\infty} I_n$ normalized to that of the ZPL I_0 for a specific v' corresponds to e^S. This expression was used to derive $S(v')$ from

$$S(v') = ln \left(\sum_{n=0}^{\infty} I_n(v') / I_0(v') \right) , \tag{4.2}$$

where $I_0(v')$ follows from the ZPL area in Fig. 4.5. For $\sum_{n=0}^{\infty} I_n(v')$ the whole area between two successive v' ZPL was taken. In this way one systematically underestimates the steepness of the rise of $S\ (v')$ with increasing energy, since the contributions of larger n bands are included in the next higher v'. On the other hand, the procedure is consistent and takes into account the intensities of all sidebands. Thus at this point a rather speculative decomposition into unresolved sidebands is avoided and it is not necessary to rest on the intensity of specific ones. The hidden assumption in the linear coupling model of separating the time scales of fast intra molecular motion (v') and slow lattice vibrations (n) is only weakly fulfilled in our case. The $n = 2$ contributions of v' are for example already resonant with the ZPL of $v' + 1$ and the anharmonicity in v' brings both time scales even closer together. Thus for large v' the high energy wing even of the $n = 1$ band starts to merge with the ZPL of $v' + 1$ and irregularities in the sequence of I_n intensities would not be surprising. Figure 4.7b demonstrates the systematic increase of S with v' from a value around 1 in the range of $v' = 2 - 8$ to a value of 4 at $v' = 19$. One should keep in mind that for $S = 4$ only 2% of the intensity remains in the ZPL and 98% accumulate in the prominent background.

Population flow and predissociation

Until now the energetics and lattice coupling in the B-state was treated. The crossing with the C-state was ignored, which is expected deep in the potential-well according to Fig. 2.1, and also crossings with many other repulsive states, situated at higher v' [39, 40]. If the C and B-state do not interact as essentially in the gas phase [122], then spectral distortions are not expected and also the predissociation probability is negligible. A matrix induced predissociation as it happens for I_2/Kr [126] however, requires a significant coupling matrix element between these states, leading to an avoided crossing and can manifest itself in specific spectral signatures. All relevant parameters are collected in Fig. 4.7. Figure 4.7d repeats the intensity plot of the excitation spectrum (Fig. 4.5), now versus v'. According to the decomposition in Fig. 2.4, this is the far red wing of the B-state where the FC factors and thus the intensity should rise steeply and monotonically. This increase is visible in Fig. 4.7 for $v' = 2$, 3 and 4. However, at $v' = 5$, the intensity drops instead of the expected increase by a factor of two or three. This is a strong signature of population loss in the B-state due to predissociation, because the B excitation spectrum represents the population which has relaxed down to $v' = 0$. This observation is consistent with a crossing situated between $v' = 4$ and 5. In this case $v' = 4$ lies below the crossing being little affected by predissociation while v'=5 just above the crossing should show the highest predissociation rate. Indeed, above $v' = 5$ the intensity increases again, however slowly. The lattice coupling S rises smoothly (Fig. 4.7b). It may cause a steadily decreasing lifetime due to interaction with the lattice as illustrated by the solid line in Fig. 4.7a which serves as a guide for the eye. Indeed, just from $v' = 4$ to 5 a jump in the lifetime from about 1.7 to 1.3 ps coincides with the drop in intensity in Fig. 4.7d. The lifetime approaches the solid line at larger v' until, from $v' = 7$ to 8 once more a jump occurs from 1.2 to 0.8 ps. Going back to the intensity curves in Fig. 4.7d, a drop from $v' = 7$ to 8 is observed and a rise only from $v' = 9$ on. Hence a second crossing can be located between $v' = 7$ and 9 in which the coupling seems to be even stronger. The avoided crossing should in principle push the two adjacent vibrational levels apart and the level which is closer to the crossing will be affected more strongly. In the Birge - Sponer plot in Fig. 4.7c the gas phase vibrational spacings ΔG are shown as filled squares which behave completely smooth with v' since there are no relevant couplings. In the matrix (crosses) a drop in the interesting region at $v' = 5$ is seen. The ΔG of $v' = 5$ corresponds to the energy of $v' = 6$ minus that of $v' = 5$ and the drop corresponds to a $v' = 5$ level lying too high. Thus the first crossing should be very close to $v' = 5$ which is pushed up by the interaction. The deviations from the smooth behaviour are weak around the second crossing ($v' = 7$ to $v' = 9$ in Fig. 4.7c). Most likely the crossing lies rather centered between $v' = 7$ and 8. More subtle effects can be contained in small changes of the isotopic splittings. In Fig. 4.6 they show a weak oscillation at $v' = 5$ and $v' = 8$ around the solid line. However, the effect is very weak and difficult to assign. Returning to Fig. 4.7a, a further jump in lifetime is observed from $v' = 14$ to 15 which is quite likely due to a third crossing. It is not obvious in ZPL intensities since these are already affected strongly by other crossings and the lattice coupling. All three crossings show a strong jump and a leveling off in lifetime and intensity changes within the few following v' levels. This is a general feature of rates above curve crossings. The rates decrease with the increase of velocity above the crossing, as expressed by the Landau - Zener formula [115] (Eq. 2.2). Crossings are collected in Tab. 4.4.

The intensity of the A'($v' = 0$) $\rightarrow$ X(v''=7) band (932 nm in Fig. 4.2b) versus excitation energy is displayed in Fig. 4.9. The overwhelming impression is that of a continuum and only in the central part between 595 and 550 nm a rather weak vibrational structure is resolved. The inset shows a comparison of the A' excitation spectrum with the B spectrum in Fig. 4.5 which demonstrates that the structure corresponds to the B-state vibrational progression.

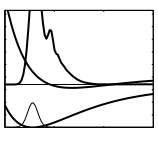

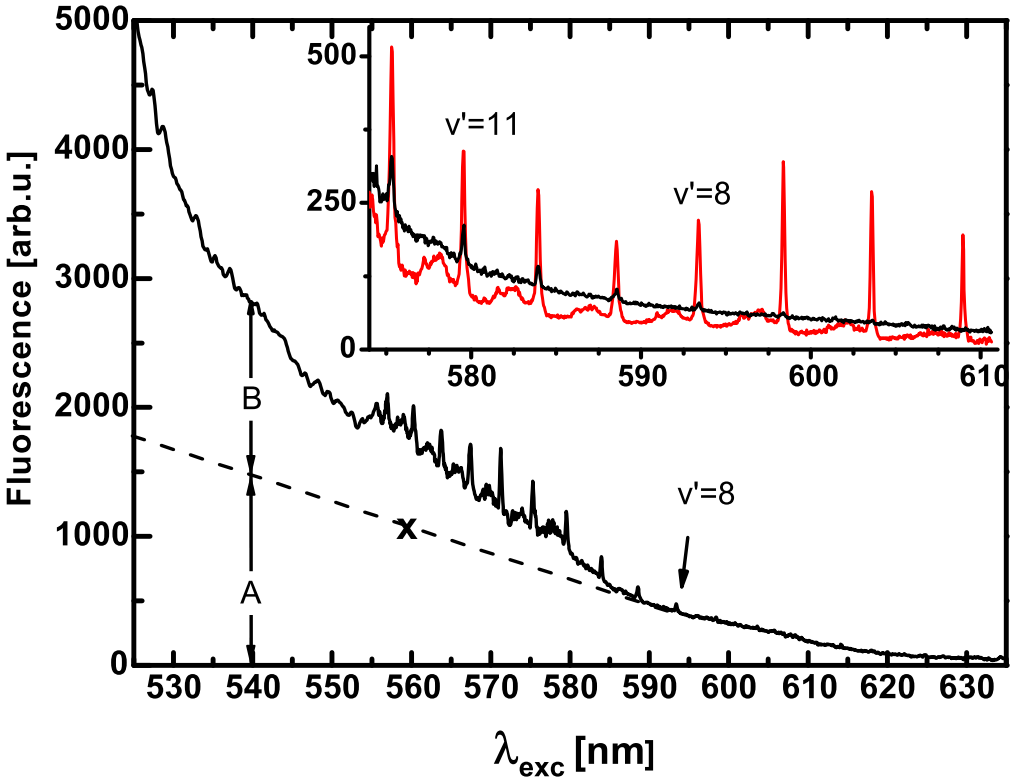

Figure 4.9: Intensity of the $^{79,81}Br_2$ A'($v' = 0$)→ X($v' = 9$) emission band $vs.$ excitation wavelength (solid black line). The structured part results from B excitation and predissociation to A', according to the B excitation spectrum (line) in the inset. The non-structured part on the low energy side results exclusively from A-state excitation. The one on the high energy side follows from A and B, as indicated with the tentative dashed division line (see text). Absolute intensities for the two A' excitation spectra differ due to different emission bands.

4.1.3 Temperature dependence

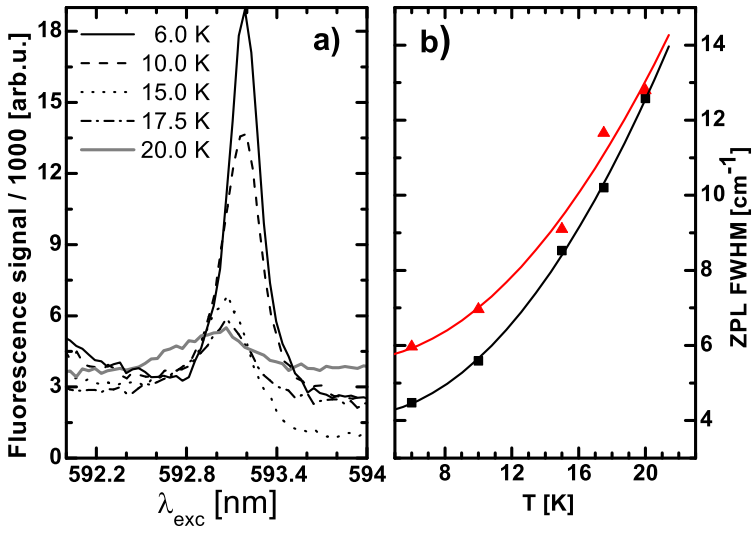

Figure 4.10: Temperature dependence of ZPL in the B state. a) Increase of $v' = 8$ linewidth with increasing temperature. For higher temperatures the line maximum shifts to the blue. b) Linewidth broadening for two chosen lines ($v' = 7$, squares and $v' = 8$, triangles) with quadratic fits.

Finally, at elevated temperatures one expects transitions starting from thermally activated phonons in the ground state. If the number of phonons is not changed in a transition then it contributes once more to the ZPL. The ZPL will broaden however and even shift if the phonon energies differ in the ground and excited state. The temperature dependence of the ZPL of $v' = 8$ is depicted in Fig. 4.10a and shows all these features. At high temperatures T also transitions with phonon emission from the excited phonon state become relevant and therefore the intensity of the ZPL decreases which can be handled with the phonon occupation number versus T [101, 104]. The processes are not linear in T as evidenced in Fig. 4.10b for the linewidth. The lines connecting the points represent a fit quadratic in T. Treatments for different phonon modes become quite involved [232] and no deeper analysis will be given here.

4.1.4 Polarisation dependence

A polarisation dependent study of the excitation process is shown in Fig. 4.11 following the principle of photoselection introduced in Sec. 2.1.4 and Refs. [66], [67]. At a temperature of 14 K the ZPL are broadened as discussed earlier, *e.g.*, see Fig. 4.10. For this investigation the dye laser polarisation was rotated relative to an analyser in front of the Cornerstone monochromator. In this wavelength region the grating of the monochromator shows a polarisation dependent efficiency of 3:1 for ∥ to ⊥ polarised light, related to the plane of the table. The data shown in Fig. 4.11 are corrected for this effect. Plot a) shows the B excitation spectrum for the transition B($v' = 0$)→X($v'' = 14$) with parallel excitation (solid line) and perpendicular one (dashed). The intensities of the modulated ZPL (no background at the low energy edge) due to the change in polarisation vary from ratios of 1:1.5 to 1:2.9 for ⊥:∥. The ratio depends on the excitation wavelength according to Tab. 4.1. The continuous background has a constant ratio of 1:2. For the A'($v' = 0$)→X($v'' = 8$) emission in b) the ratio is inverted and the perpendicular excitation gains a signal being higher by a factor of 1.3 at the low energy side, increasing to 1.5 at 575 nm. Additionally, the perpendicular excitation is very smooth, representing predominantly an absorption to

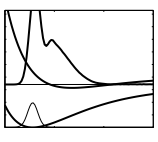

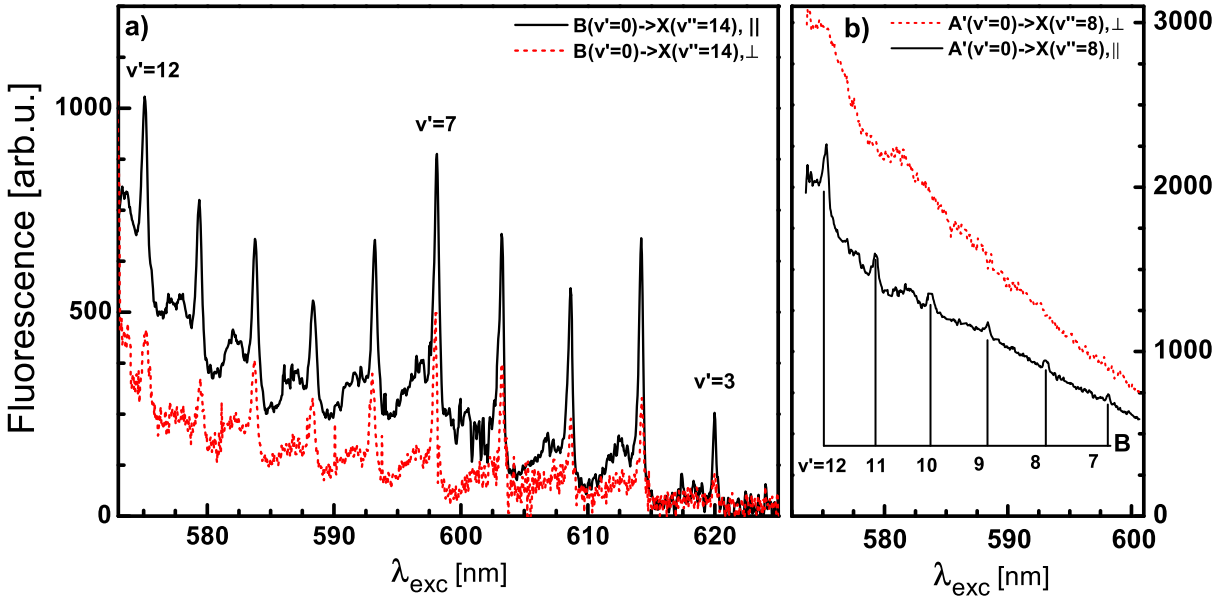

Figure 4.11: a) Polarisation dependence of B excitation spectrum taken at 14 K with parallel excitation (solid line) and perpendicular one (dashed), related to an analyser behind the sample. The ratio of ZPL ∥/⊥ ranges from 1:1.5 to 1:2.9, see Tab. 4.1. b) Polarisation dependence of A' excitation spectrum obtained at 14 K. Bad data points due to camera breakdown had been removed, curves were averaged over three points.

A, above the gas phase dissociation limit (see Sec.4.2). On the other hand, the parallel configuration enhances the B-state contribution and a weak predissociated B population shows up with its vibrational progression labeled in Fig. 4.11b.

The X→B transition is a $\Delta\Omega = 0$ transition, therefore a parallel signal being stronger by a factor of three nicely agrees with the predictions from selection rules of Sec. 2.1.4. In the case of X→A' the situation is more complicated due to $\Delta\Omega = 2$, which allows for quadrupol transitions. The A' excitation spectrum is stronger by a factor of 1.4 for the perpendicular excitation than for the parallel one. This turning in preferred excitation compared to the B-state is consistent with the fact that 10 times more signal is absorbed by the A-state rather than by the A'-state. The A-state represents a $\Delta\Omega = 1$ transition which enhances the perpendicular configuration by a factor of two, compared to parallel. Analysing the ratio of ZPL heights in case of parallel and perpendicular excitation, as done in Tab. 4.1, gives values between 2.9 and 1.6 with the minimum around $v' = 7$ to $v' = 9$ where the second crossing (Sec. 4.2) is localised. The reason is not yet clear.

Table 4.1: Ratio of ∥ and ⊥ ZPL on B excitation spectrum in Fig. 4.11. For evaluation the modulated part on the low energy side of each peak was taken.

v'	3	4	5	6	7	8	9	10	11	12
∥	2.9	2.6	2.6	1.9	1.5	1.7	1.6	1.7	2.6	2.5
⊥	1	1	1	1	1	1	1	1	1	1

4.1.5 Bleaching experiments

Experiments in this section are concerned with the stability of caged Br_2 molecules with respect to dissociation. Therefore, excitation at two wavelengths above the gas phase dissociation limit of the B-state was employed. By varying the dopant concentration and excitation intensity, effects due to aggregation and power dependence were investigated.

The sample was pumped with ultrashort laser pulses, either with the second harmonic of the CPA at 387.5 nm or with NOPA pulses at 490 nm. Relating this with the absorption spectrum in Fig. 2.4 shows that with 387.5 nm the C-state (and also higher lying repulsive states), delivering large kinetic energies, are excited. With 490 nm the B-state is excited close to its maximum, above the gas phase dissociation limit.

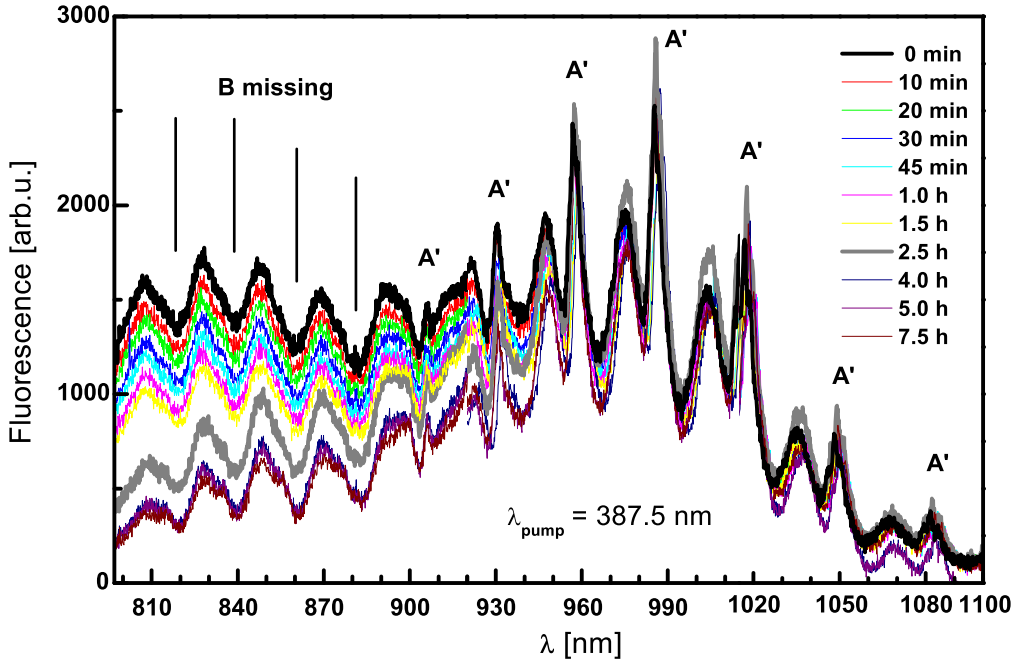

Figure 4.12: Bleaching of covalent states with circular polarised SHG excitation at 387.5 nm. Curves from top to bottom: 0 minutes of bleaching up to 7.5 h. Around 800-900 nm the sharp B lines from Fig. 4.2 are absent. The strong decay at higher wavelengths is caused by the weak CCD sensitivity in this region. Br_2/Ar concentration was 1:1000 and the pumping energy was 2.0 μJ.

Figure 4.12 shows the LiF in the wavelength region of covalent states A', A and B from 800 to 920 nm when pumping a sample with a Br_2/Ar concentration of 1:1000 with the second harmonic light of the CPA. Going to higher fluorescence wavelengths, the A' progression grows, as is the case in Br_2/Ar spectra like in Fig. 4.2, where also a detailed nomenclature of the electronic transitions can be found. The C-state is excited preferentially with 387.5 nm. This repulsive state has a common dissociation limit with the A and the A'-states, shown in Fig. 2.1, which lies below that of B. Thus, the B-state can be passed and relaxed C population accumulates in A and A'. The sharp lines from B are missing in Fig. 4.12, however, a progression of broad bands is visible. It shows up also in Fig. 4.13, in the wings of the sharp B lines. The broad bands are tentatively assigned to Br_2

aggregates[2] due to their concentration dependence. The sharp lines are assigned to Br_2 monomers, accordingly. The set of curves was taken after different bleaching times, starting with the thick black curve at $t = 0$. In the cluster region the signal decreases strongly with longer bleaching time, up to the lowest one with 7.5 h of radiation. For the A' part the situation is different. The signal at $t = 0$ is high, however it increases and the maximum is reached at bleaching time of 2.5 h, shown as the thick grey line. For longer times, the signal decays also here. This increase in the first two hours can come from bleached, $i.e.$, broken up dimers, which contribute then as monomers to the A' fluorescence. A more detailed interpretation would require a more extensive set of data.

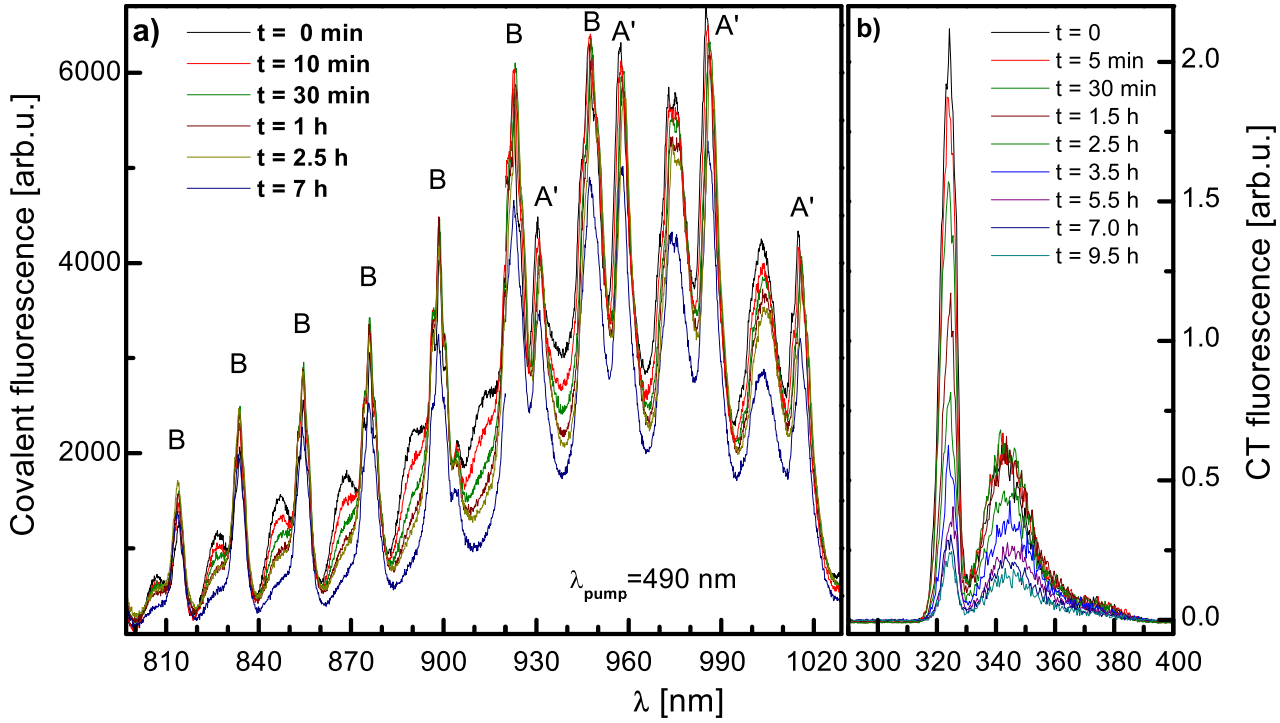

Figure 4.13: a) Bleaching of covalent states with circular polarised 488.5 nm excitation. Curves from top to bottom: 0 minutes of bleaching up to 7.0 h. Br_2/Ar concentration was 1:500 and the pumping energy was 0.9 μJ. b) At a concentration of 1:1000, two fluorescence bands at 322 and 345 nm with different bleaching behaviour were observed. The band at 300 nm is missing for this excitation with 490 nm, as will be discussed in Sec. 5.2.

In Fig. 4.13, excitation with a 50 fs pulse at 490 nm (the B-state maximum) just above the gas phase dissociation limit is performed. For this direct excitation of the B-state indeed, a signal with sharp lines attributed to B is observed, despite the higher concentration of 1:500, compared to Fig. 4.12. The aggregates remain in Fig. 4.13 and are visible as wings of the sharp lines. These wings decrease with time, as expected. The increase in peak intensities from left to right follows the one observed in Fig. 4.2 due to increasing FC factors. Observed sharp B and A peaks bleach only slightly during the 7 hours of recording, while the humps attributed to aggregates decay again strongly. Figure 4.13b shows two fluorescence bands from CT states with maxima at 322 nm and at 345 nm. The stronger band at 322 nm bleaches from the beginning on, whereas the broader band at 345 nm stays constant for 1.5 h before it is also decreased. Possibly, the "cluster contributions" of panel a) decay into monomers and contribute to the fluorescence band at 345 nm, analogue to the

[2]The terms aggregates and clusters are used synonymously.

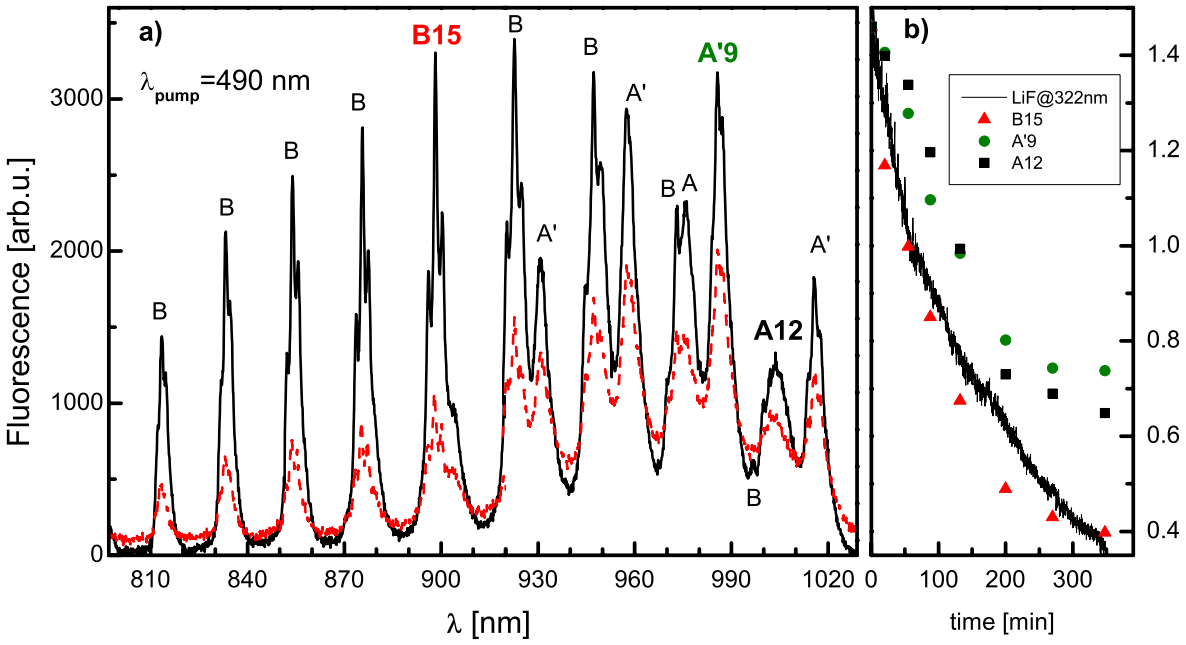

Figure 4.14: Bleaching of covalent states with circular polarised 490 nm excitation. Without bleaching (solid line) and after 5.5 h (dashed line). Br_2/Ar concentration was 1:1000 and the pumping energy was 1.0 μJ. Plot a) has the emission spectrum from covalent states A', A and B. Three of them are marked with their transition, where the abbreviation B15 stands for B($v' = 0$)→X($v'' = 15$) and A'9 and A12 analogously. The intensity values of those three lines at several bleaching times are plotted in panel b). Simultaneously the LiF from CT states at 322 nm was recorded, included as a solid line.

increasing A' emission in Fig 4.12. Another band at 300 nm used in the time resolved experiments of Chs. 5 and 6 with lower excitation energies does not show up in this signal.

In Fig. 4.14 the bleaching behaviour of covalent and CT states is directly compared, again for 490 nm circular polarised excitation of 1.0 μJ and a reduced Br_2 concentration of 1:1000. In panel a) the fluorescence from covalent states is shown. At this low concentration no cluster bands are observed. The high solid line is taken at $t = 0$ and the lower dashed line after a bleaching of 5.5 hours. One B, A' and A transition is specially marked, *e.g.*, B15 for B($v' = 0$)→X($v'' = 15$). Their intensity behaviour with exposure time is plotted in panel b) with B15 as triangles, A'9 as circles and A12 as squares. The broad background for A'9 and A12 is included. The decay over 300 min is compared with the simultaneously recorded[3] CT fluorescence at 322 nm shown as solid line. While B-state fluorescence and CT fluorescence at 322 nm nicely agree, the ones from A' and A-state deviate. At short exposure times they show a slower decay. At larger times they seem to reach a plateau. The plateau might be related to the broad background around $\lambda_{fluor} = 950\,\text{nm}$ in plot a). Roughly, with a pulse energy of 1.0 μJ a signal decay by a factor of two in 30 min is observed. Intensity dependent experiments for the 322 nm emission displayed in Fig. 4.15 were carried out with $\lambda_{pump} = 490\,\text{nm}$ at a Br_2/Ar concentration of 1:500 and with linear polarised light. With a linear variable grey filter the pumping energy was reduced stepwise from 0.88 μJ to

[3] A wavelengths separating beam splitter was set up behind the sample chamber and so the fluorescence in NIR from covalent states and the one in UV from CT states could be recorded at the same time using two monochromators.

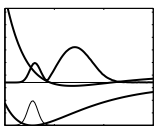

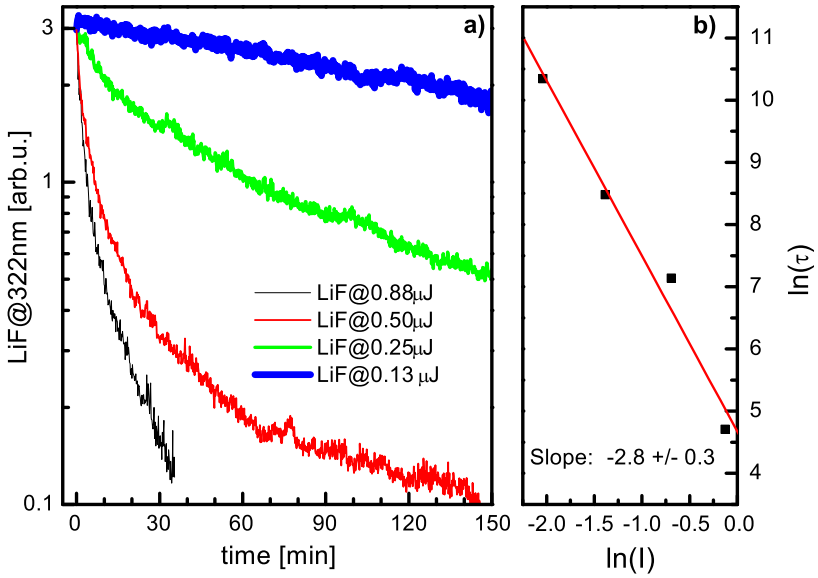

Figure 4.15: Bleaching energy dependence of 322 nm emission. a) Bleaching curves at energies: 0.88 μJ (thin line with steepest decay), 0.50 μJ, 0.25 μJ and 0.13 μJ (thickest line with slowest decay) with $\lambda_{pump} = 490$ nm and a Br_2/Ar concentration was 1:500. b) shows the logarithm of exponential decay times τ of a) $vs.$ the logarithm of intensities, indicating a three photonic absorption.

0.13 μJ.

The signal decrease at this concentration of 1:500 is faster by a factor of 30 in the first 30 min, compared to the signal decay in Fig. 4.14b with reduced concentration for the same $\lambda_{pump} = 490$ nm and pulse energy. The faster decay in Fig. 4.15 has to result from the increased aggregation. In panel a), the excitation energy was varied from 0.88 μJ shown as thin line with strongest decay down to 0.13 μJ as the thickest line. These exponential decays were fitted with the decay times $\tau_{0.88} = (1.9 \pm 0.1)$ min, $\tau_{0.50} = (21 \pm 2)$ min, $\tau_{0.25} = (81 \pm 8)$ min and $\tau_{0.13} = (520 \pm 50)$ min. A double logarithmic plot of τ $vs.$ pulse intensity is given in panel b). Its slope corresponds to 2.8 ± 0.3, indicating a three photonic absorption for this CT fluorescence at 322 nm.

In conclusion, three different energetic regions for two concentrations of halogen in the rare gas solid were covered within the experiments in this chapter. Their characteristics concerning aggregation are summarised in Tab. 4.2. In the bound potential well of the B-state no evidence for the excitation of aggregates was found. Excitation with higher energies close to the B-state maximum or even more pronounced in the C-state maximum demonstrate, that a small amount of clusters exist[4]. However, they do not contribute at excitation wavelength between 640 and 550 nm, being the region for the following control experiments. In general, an increase in intensity helps in the excitation of aggregates and an increasing concentration promotes their formation.

A hole burning experiment is presented in Fig. 4.16a with $\lambda_{fluor} = 322$ nm. A bleaching in one orientation of initially isotropically distributed Br_2 molecules in the sample with linear polarised light at 490 nm is studied. This setup for detecting polarisation dependent LiF sketched in b) was more efficient by a factor of two for the perpendicular than for the parallel case and spectra are

[4]In further experiments [43] it was estimated, that the monomer content for a concentration of 1:500 is 95%.

Table 4.2: Aggregation behaviour of bromine for different excitation energies.

Energetic region	concentration	aggregates	bleaching
bound B-state 640 - 550 nm	1:500	no, only real B signature	no
B absorption max. 490 nm	1:500 1:1000	yes, + real B signature no, only real B signature	aggregates fast, B moderate B moderate
C-state 387.5 nm	1:1000	yes, no real B signature	aggregates very fast

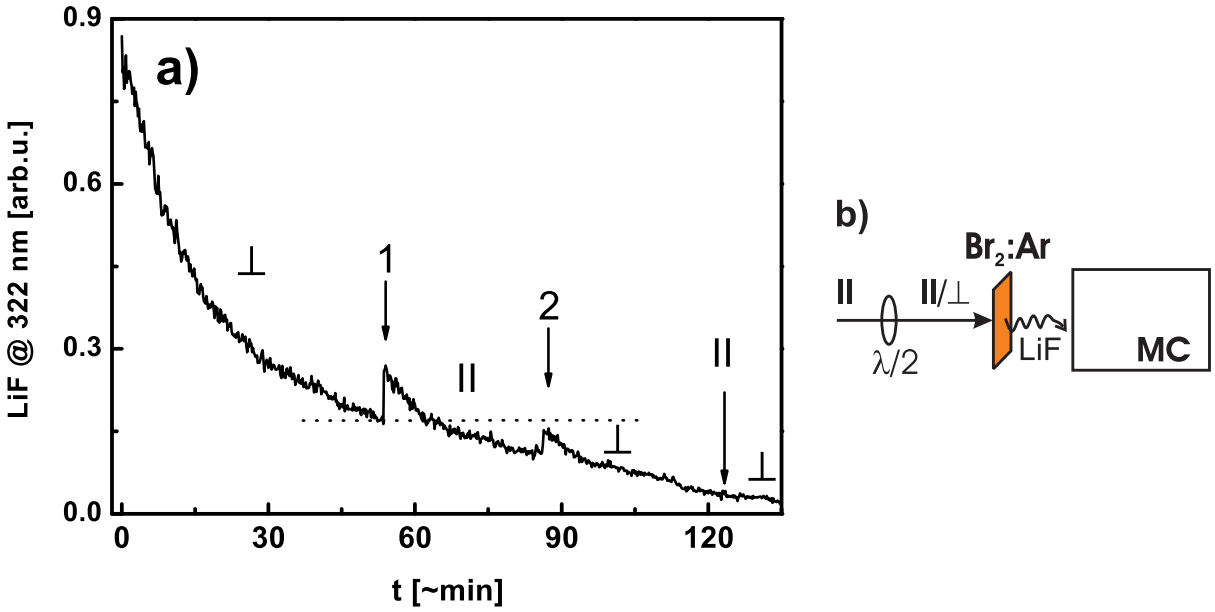

Figure 4.16: Polarisation hole burning with 490 nm pump wave length and a Br_2/Ar concentration of 1:1000. Bleaching of Br_2 molecules favouredly in one direction when exciting with linear polarised light perpendicular to the plane of reference. At t=54 min the polarisation direction is turned to parallel (arrow 1) and at 86 min it is changed again to perpendicular (arrow 2). The last two switchings sink in the reduced bleaching effects at longer times. Data are corrected for the polarisation dependence of the setup.

corrected for this effect. This scaling factor is a combination of grating efficiency for different polarisations (which was also discussed in the polarisation dependent excitation spectra earlier) and the excitation processes in the molecule, since a combined absorption of electronic states preferring parallel ($e.g.$, the B-state with $\Delta\Omega = 0$) and perpendicular ($e.g.$, the C-state with $\Delta\Omega = 1$) transitions takes place. Initially, the polarisation was perpendicular to the optical table. The signal in a) decreases with time, as expected. After some irradiation time (here, 55 min, marked with arrow 1) the polarisation direction of the pump light is turned to parallel. The signal jumps up, however not to the original value at $t = 0$ but to roughly 1/3 of it. At 86 min the polarisation is rotated back to perpendicular (arrow 2) and the signal jumps up once more. Again, it stays below the last value with the same polarisation at 54 min, as indicated with the dashed line. A comparison with the bleaching slopes in Figs 4.14b) and 4.15 shows, that only monomers contribute to the signal, as expected from Tab. 4.2. The excitation of molecules and thereby bleaching occurs not exclusively in one orientation but in a cos^2 distribution as discussed in Ch. 2. Due to the cage, the molecules are kept in their orientation. Which scenarios for the bleaching of Br_2 monomers can be

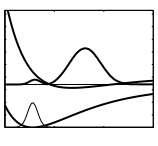

imagined?

1. They can dissociate into atoms and never recombine
2. They can dissociate into atoms and recombine in a distribution of orientations

Contributions due to the second point are not evident in Fig. 4.16a, since no gaining signal in one orientation, after bleaching with the perpendicular polarisation direction, shows up. Thus, to a large extend, the molecules are permanently dissociated and do not recombine.

In a similar experiment for I_2/Ar in the Apkarian group [31] a recombination of molecules could be determined from the bleaching signal, due to a stronger signal increase when re – changing the polarisation.

4.2 Discussion

Now we turn back to the spectroscopic properties of monomer Br_2/Ar.

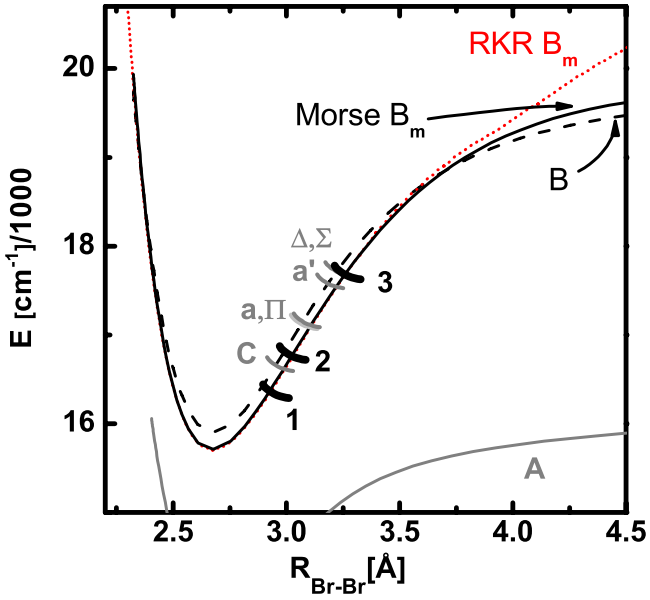

Figure 4.17: B-state matrix potential Morse B_m (black solid line from Tab. 4.3) and curve crossings 1, 2, 3 (thick black) compared with the matrix potential (RKR B_m, dotted line) from Ref. [60], gas phase potential (dashed [42]) and gas phase crossings (thin grey [64]). All crossings from Tab. 4.4. The A gas phase potential is included in grey.

Energetics

The absorption spectrum in Fig. 2.4 is rather similar to that in Ref. [108]. The shoulder and a more extended wing on the red side of the literature spectrum originate presumably from clusters of Br_2 due to the larger concentration employed. The position of the maximum and of the B-state shoulder in the simulation with the gas phase spectroscopic constants coincide with the matrix spectrum within the accuracy, indicating that the repulsive part of the potential is very little influenced by the matrix, as stated already previously [107]. The somewhat larger extension of the blue and red wings in the gas phase can be attributed to $v'' = 1$ and 2 contributions in the X state which widen the ground state wave function. The similarity between gas phase and matrix justifies the use of the gas phase FC factors in absorption which is relevant for the discussion of intensities and population flow by predissociation. At first sight it is puzzling why the progression of ZPL in the B-state excitation spectrum displayed in Fig. 4.5 does not show up in absorption (Fig. 2.4). However, for Fig. 4.5 the underlying A-state continuum was suppressed by selecting the B fluorescence bands. Closer to a real absorption spectrum is the complete A' excitation spectrum in Fig. 4.9. The resolved structures are restricted to the range of 550 to 630 nm. Those weak features are

buried in the noise in Fig. 2.4 since they are situated in the very far red wing of the B-state FC range. Therefore it would be necessary to increase the optical density by a factor of ten either by a larger concentration which would lead to aggregation or by a larger thickness which would cause an increased scattering background and again low contrast. I tried these experiments, verified the problems and have thus to rest with the excitation spectra.

Table 4.3: Spectroscopic constants $\nu_{0,0}$, T_e, ω_e, $\omega_e x_e$ in [cm^{-1}] of Br_2/Ar. Comparison of values obtained by Bondybey, Langen and our group. Cursive numbers are calculated using the given parameters.

state	isotope	method	ν_{00}	T_e	ω_e	$\omega_e x_e$	reference
X state	79,79	emission		0	318.65	0.82	[107]
	79,81	emission			320	1.11	[107]
	81,81	emission		0	317.0	1.04	[97]
		emission		0	314.91	0.858	[107]
B-state	79,79	emission	*15625.6*	15701.2	167.14	1.588	[107]
		absorption		15415.0	169.5	1.59	[97]
		absorption		15722			[107]
		absorption	15634	*15709*	168.6	1.74	this work
		Birge Sponer			168	1.72	this work
	79,81	absorption	15636	*15709*	167.3	1.70	this work
		Birge Sponer			167	1.72	this work
	81,81	emission	*15632.2*	15705.9			[107]
		absorption	15636	*15708*	166.2	1.68	this work
		Birge Sponer			166	1.68	this work

The B-state T_e value (Tab. 4.3) reflects the superposition of repulsive and attractive parts of chromophore and matrix pair potentials. It shows again a weak matrix influence only, with a red shift of 193 cm^{-1} which can be attributed to a slightly attractive superposition [96]. The T_e value should not depend on the isotopomer which is fulfilled by our excitation data within 1 cm^{-1}. For the emission data of Ref. [107] the variation with 4 cm^{-1} is somewhat larger, probably due to the more extended extrapolation. With this in mind, both T_e values are in very good agreement. Concerning the vibrational assignment of the ground state the T_e values confirm the increase of v'' by one digit with respect to Ref. [97]. This is in agreement with Ref. [107] that most likely a scrambling of isotope transitions occurred in [97]. The mentioned preliminary excitation spectrum in Ref. [107] also seems to be problematic since according to our results their numbering of v' should result in a significantly larger T_e compared to the given value of 15722 cm^{-1} [107]. It has to be noted that also the v' numbering of the B excitation spectrum in Ref. [21] has to be increased by one digit according to our new results. In Fig. 4.17 the gas phase B potential and the B-state Morse potential from this work ω_e and $\omega_e x_e$ (Tab. 4.3) are displayed. The latter does not include the far outer wing at high energies, which is strongly influenced by the matrix. The repulsive and deeply bound parts are very similar as discussed before and one could assume that the matrix contribution is weak in general. This assertion would be wrong and the PSB are a signature for a coupling to the matrix even near the potential minimum. The value of $S = 1$ from the lowest observed $v' = 2$ up to about $v' = 7$ (Fig. 4.7b) means that ZPL and first PSB have equal strength. This is just not obvious from the spectrum in Fig. 4.5 since the ZPL is very sharp (Fig. 4.7a) and the sideband intensity is spread out over 80 cm^{-1} (Fig. 4.8). To strengthen this aspect, a B potential in Fig. 4.17

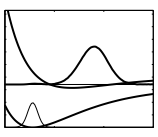

shifted to the blue by an average phonon energy of about 50 cm^{-1} (thus even closer to the gas phase) would be equally justified. This $S = 1$ value appears to be a constant minimal value deep in the potential-well and therefore a property of the X-B electronic transition itself. A coherent and prompt generation of phonons is observed in Ref. [96] and attributed to the "displacive excitation of coherent phonon" mechanism. An expansion of the electronic wave function in the B-state with respect to the X state induces a lattice expansion around the chromophore. The spectroscopic counter part of this change in configuration coordinate is the PSB with $S = 1$. For larger v', $i.e.$, $v' \geq 8$ a monotonic increase of S (Fig. 4.7b) is observed which is a vibronic contribution to the lattice coupling. The equilibrium internuclear distance increases with anharmonicity and the size of the molecule increases with v'. Thus a shift of the configuration coordinate with the lattice, analogous to the electronic X-B term can be expected, now however increasing with v'.

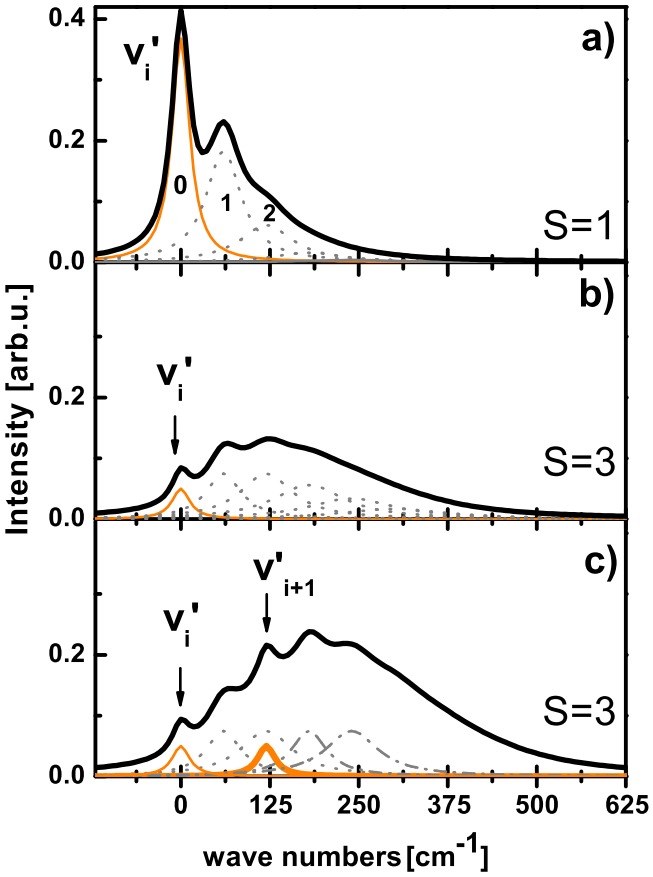

Figure 4.18: Simulation to demonstrate the contribution of higher order phonon modes to the background of the excitation spectrum. a) The case of weak coupling ($S = 1$): The thin solid line is the ZPL, the dotted grey lines are the one and two phonon contributions and the thick solid line is the additive envelope. b) Stronger coupling with $S = 3$, the ZPL is only slightly visible on the background. c) Again $S = 3$ but now the contributions of two subsequent vibrational transitions were included. The solid thin ZPL and the dotted phonon lines belong to v'_i, the thick ZPL and the dash-dotted ones to v'_{i+1}.

A simulation for the increasing phonon background with increasing S is presented in Fig. 4.18, following a simplified scheme: The Huang – Rhys picture was introduced for a distinct configuration coordinate in Fig. 2.3. Instead of a single phonon mode, now Lorentzian shaped lines are modelled, to approach the experimental excitation spectrum. ZPL (indicated with 0), first (1) and second phonon contributions (2) are designed initially with equal intensity and separated by 63 cm^{-1}. It is assumed, the the 1. PSB is twice as broad, the 2. PSB three times broader than the ZPL, to take into account, that all bands originate in zero. For $S = 1$ in a) the band intensities are scaled following Eq. 2.1. The thick solid line represents the contributions of a single vibrational level v'_i. In b) the coupling is increased to $S = 3$, thus the maximum contribution is shifted to the 3. band and hence, phonon contributions up to the sixths order are considered. Indeed, only a weak modulation from the zeroth and first contributions remain in the thick solid line.

This effect intensifies in c), when additionally a second vibrational level v'_{i+1} is taken into account. Thus, even those two contributions in the simplified model illustrate, how the background evolves.

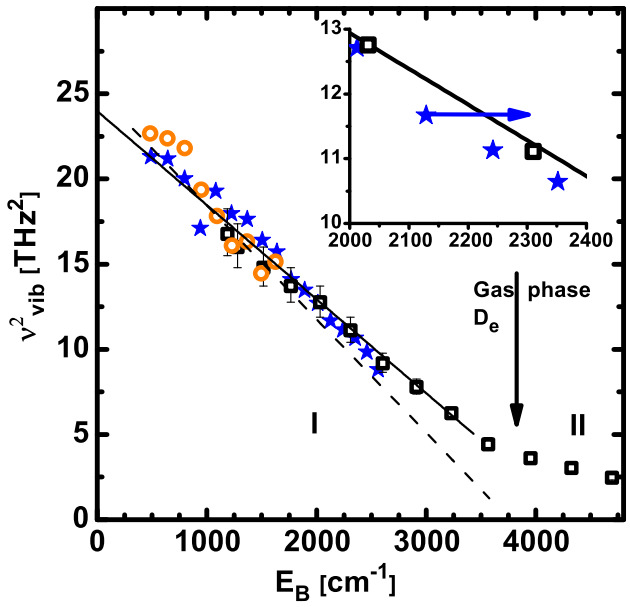

Figure 4.19: Square of vibrational frequency ν_{vib} *vs.* energy E_B above the B potential minimum for our excitation spectrum (stars) and the one obtained by Bondybey [97] (open circles). Time resolved data (open squares) and their Morse fit (solid line) are from Ref. [60]). The dashed line shows a calculation for the free molecule. The gas phase dissociation limit (D_e, vertical arrow), separates the chemical bound part I from the matrix bound regime II. The horizontal arrow in the inset denotes the energetic shift from ZPL (stars) by four phonon energies, *i.e.*, towards pump probe data (solid line).

A more dynamical picture would consider the increase in vibrational amplitude on the outer potential limb and a stronger repulsive interaction with the matrix cage atoms. The increase of S with v' is certainly stronger than linear and for the limited range of v' values a quadratic fit works quite well. This seems to be consistent with the dynamical repulsive picture. The general increase in ZPL width and corresponding decrease in lifetime with v' is also progressive and can again be approximated by a quadratic dependence (Fig. 4.7a) when the breaks by the onsets of predissociation are ignored. Coupling of a chromophore vibration to the lattice is a longstanding and difficult subject [139, 233]. In the electronic ground state coupling is in general weaker which facilitates studies on a larger v' range. An example is a very detailed recent CARS study for I_2/Ar and Kr [32]. In this case the coupling is too weak to deliver PSB. For the lifetime a linear dependence with v' is observed in case of the tight Ar matrix and even powers of v' show up in the looser site of Kr. Thus our Br_2/Ar results are closer to the I_2/Kr case. Beyond v' >19 the vibrational structure is lost (Fig. 4.5). Fortunately, in this high energy regime with very strong coupling, vibrational frequencies have been determined from the roundtrip times in pump - probe spectra [60]. A survey on the results of vibrational frequencies ν_{vib} from the ZPL in Ref. [97] (open circles), our new results (stars), the pump - probe data (filled squares and the solid line) and the gas phase (dashed line) is presented in Fig. 4.19, all with the corrected v' numbering. The ν^2_{vib} values are plotted versus energy E_B above the B potential minimum. Gas phase dissociation energy is indicated by the vertical arrow. Early zero phonon data (circles) just covered the lower quarter of the potential-well and did not really overlap with the pump - probe results (squares). The much longer vibrational progression in our case covers now the lower half of the potential-well and provides extended overlap with pump - probe data. So the consistency of the results in this regime of strong interaction with the matrix can be considered to be very satisfying. Furthermore, one has to keep in mind that at large v' with $S = 4$ most of the oscillator strength lies in the PSB and the ZPL keep only 2% of it. Pump - probe data reflect of course the center of gravity of a transition.

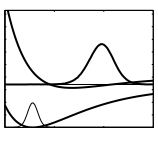

For $S = 4$ the intensity maximum lies at the fourth PSB or about 200 cm^{-1} blue from the ZPL. The corresponding shift in E_B is indicated by a horizontal arrow in the inset in Fig. 4.19. Including this effect the two sets of data obviously agree within the error bars. Finally, the matrix bound potential very close to the dissociation limit differes drastically from the gas phase one. It remains bound by the cage wall (range II in Fig. 4.19 the lattice however responds flexible to the fragment impact which causes even in the first round-trip a loss of most of the kinetic energy, leading to a return already in the chemically bound part I of the potential, according to the discussion in Ref. [60]. A similar behaviour is expected in the dissociative part of the A-state (Fig. 4.17) which will be important for the flow of population after predissociation, treated next.

Population flow and predissociation

Table 4.4: Crossing positions of repulsive states with the B-state potential. The second column gives the energy above the B potential minimum for our matrix values, where the accuracy is determined by half the vibrational spacing ΔG. The third value is set in brackets since it is a tentative one, observed only in the linewidth in Fig. 4.7a and the FC factor comparison in Fig. 4.20. The forth column contains gas phase $ab-initio$ calculations by Yabushita.

Crossing	matrix [cm^{-1}]	v' matrix	state	gas phase [cm^{-1}]	v' gas phase
1. crossing	680	4-5	$C\,^1\Pi_{1u}$	763	4-5
2. crossing	1080	7-9	$^3\Pi_g(2g)$	1208	7-8
			$a(1g)$	1227	7-8
3. crossing	(1970)	(14-15)	$a'(0_g^+)$	1680	11-12
			$^3\Delta_u(3_u)$	1812	12-13
			$1^3\Sigma_u^+(0_u^-)$	1812	12-13

To estimate predissociation probabilities the jump in lifetime from about 1.7 to 1.3 ps or in linewidth from 3 to 4 cm^{-1} in Fig. 4.7a is used. Their difference of 1 cm^{-1} corresponds to a lifetime contribution due to predissociation of around 5 ps. This coincides with a predissociation probability of roughly 5% per roundtrip (about 250 fs) according to the B-state ω_e. The lifetime remains short and approaches, however, the solid line until, from $v' = 7$ to 8 once more a jump from 1.2 to 0.8 ps or 4 to 6 cm^{-1} occurs. Considering the linewidth difference yields a predissociation contribution to the lifetime of around 2.5 ps. Thus approximately 10% per roundtrip exit at this second crossing.

Next, the intensities in Fig. 4.7d are considered more quantitatively. The squares in Fig. 4.20 reproduce the gas phase FC factors [55] which correspond also to the decomposition in Fig. 2.4. They rise from $v' = 2$ to $v' = 19$ by 5 orders of magnitude. The intensity of the ZPL (dots) increases by a factor of 50, only. This low efficiency demonstrates that the overwhelming part of intensity is funneled out of B by predissociation. This point of view is a bit too simplified because there is also a shift of intensity with v' from the ZPL towards the multitude of PSB which accumulate in the background. For an order-of-magnitude estimate one can use the relative weight of all phonons relative to the ZPL given by e^S as mentioned before (Eq. 2.1). Multiplying the ZPL intensity (dots) with e^S roughly represents the overall intensity of a v' excitation (crosses) in Fig. 4.20. They give now a very clear picture on the intensity flow out of B via the two crossings above $v' = 4$ and 7. The increase from FC factors levels off at a crossing and the loss of intensity increases smoothly and continuously above it. A careful inspection reveals a third plateau coinciding with the third crossing around $v' = 14$. To describe these plateaus, the information on FC factors (Fig. 4.20) is combined with that on vibrational relaxation, curve crossings, lifetimes and intensities. We draw a qualitative picture on the population flow. From the FC factors it would be

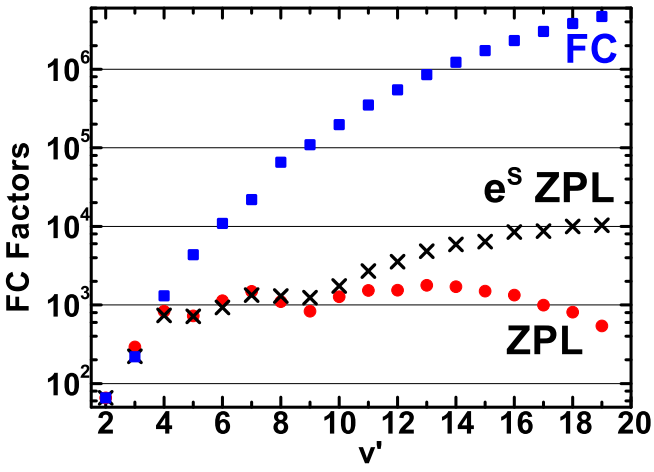

Figure 4.20: FC factors from the gas phase [56] (squares) in comparison with the measured area of the ZPL (dots), normalized to $v' = 2$. The logarithmic scaling emphasises the strong discrepancy, *e.g.*, a factor of 1000 for $v' = 11$. The intensity in the PSB is included in the black crosses by multiplying the ZPL one with e^S, see Eq. 2.1.

expected that the intensity of the B-state excitation spectrum monotonically increases by five orders of magnitude going from $v' = 2$ to $v' = 20$. This behaviour is observed only up to $v' = 4$. Just above the first crossing at $v' = 5$, predissociation to the C-state has the highest rate and competes with vibrational relaxation in B. Predissociation is about five times more effective than relaxation and both processes occur on a time scale of 5 to 20 ps. Going to higher v' increases the vibrational relaxation rate [60] and decreases the predissociation rate due to the passage of the crossing with larger kinetic energy [115]. However, since vibrational relaxation occurs within the B-state, all population surviving predissociation higher up in the potential flows towards the crossing and thereby the predissociation probabilities above the crossing accumulate. An increase in FC factors is compensated by this overall increase in predissociation probability. At the second crossing an additional predissociation channel opens with an even larger predissociation rate-constant and a similar competition of vibrational relaxation and curve crossing occurs. The overall residence time above the crossing increases with v' and thus the overall predissociation probability increases accordingly, as was modelled for I_2/Kr [84]. For approaching the FC maximum of the B-state, Fig. 4.20 predicts that the quantum efficiency for reaching $v' = 0$ drops to 10^{-3} and more than 99% of the population is depleted by predissociation.

All considered repulsive surfaces meet with the asymptotically degenerated A, A' and X-states at large internuclear distance as shown for the C-state in Fig. 2.1, allowing for population transfer. The relative transition strength from X to A' is too weak to contribute to absorption (Fig. 2.4), nevertheless the A'($v' = 0$) $\rightarrow$ X(v'') progression carries most of the intensity for excitation at high energies (Fig. 4.2b and [107]). Thus the A'-state serves as the most efficient reservoir above X for collecting the population flow out of A, B and C.

Figure 4.9 shows the A' excitation spectrum consisting of the structured part in the centre and featureless continua at higher and lower energies. In the long wavelength range beyond 600 nm the B-state has a very low oscillator strength compared to A (Fig. 2.1) and would furthermore contribute solely sharp ZPL. Therefore, the continuum at long wavelengths originates exclusively from a continuous absorption of the A-state which feeds the A'-state. The branching ratio from A to A' can depend on the excitation energy. The smooth decay of the continuum towards longer wavelengths in Fig. 4.9 resembles that in the corresponding red wing of the A-state absorption (Fig. 2.1). No severe variation in the branching ratio is obvious. On the short wavelength side

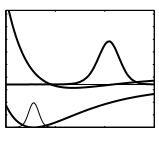

beyond 550 nm once more only a continuum is observed. The A-state contribution of course would remain flat and the B-state excitation has also already merged to a continuum due to the coupling with the lattice (Fig. 4.5), therefore, the superposition should be unstructured as observed. To estimate the relative contributions information from the structured part is used. The insert in Fig. 4.9 shows identical energetics of the vibrational structures in A' and B excitation while the intensity variations with v' are antipodal. The strongest ZPL in B excitation are $v' = 4$ to 7 which do not show up at all in the A'-state excitation spectrum. A drop in intensity occurs for $v' = 8$ in B while this corresponds to the first hardly discernible contribution to A' excitation. From $v' = 8$ on the intensities of the B structures in A' excitation increase steadily as expected for example from the B-state FC factors in Fig. 4.20. The intensities depend on three factors: The absorption strength, the predissociation probability and the branching ratio among A, A' and X after predissociation. The predissociation probability acts with opposite signs to the B and A' intensities since it diminishes B and strengthens the chances for feeding A'. For example for $v' = 6$ the predissociation probability reaches already 90% according to Fig. 4.20. The absorption cross - section of B($v' = 6$) is however so much smaller than that of the A-state (Fig. 2.1) that it is still lost in the continuous A background. For $v' = 8$ the predissociation probability increases to about 95% which means a dramatic loss for B, however, only a mild increase of only 5% for A' (assuming a fixed branching ratio). Here, the B-state absorption cross-section improves by a factor of 8 and this explains why $v' = 8$ becomes visible in A'. The further increase in predissociation probability with v' keeps the B intensity low, while the intensity in A' excitation is hardly affected by a change from 95% to 99%. This saturation carries over an increase in B absorption to a population rise in A'. Therefore, the intensities in the A' excitation spectrum reflect the B-state FC factors much better than those in the B spectrum. Following the B-state structure on A' to beyond $v' = 11$ a division in ZPL and PSB is observed which is very similar to that in Fig. 4.5. Transferring the intensity ratio of ZPL and phonon continuum in Fig. 4.5 for example for $v' = 16$ (around 560 nm) to the A' excitation spectrum yields the marking cross in Fig. 4.9. It indicates that roughly 1/3 of the A' intensity originates from B and 2/3 from A excitation. We can now attempt to draw a coarse dividing line (dashed) from the exclusive A continuum contribution at long wavelengths through this point. The extension to, for example 540 nm predicts a rough 1:1 contribution from both channels to A'. In this range the absorption cross-section of the X-A and X-B transitions just cross and become equal (Fig. 2.4). Thus on a coarse scale ($i.e.$, within a factor of two) it seems that the branching ratio from predissociated B to A' and from A to A' is rather independent on excitation energy and even quite similar. Finally, the question about a flow from A and A' towards B is concerned. The best spectral range to search for such a contribution is the region between 610 and 630 nm in Fig. 4.5. There A absorption is much stronger than that of B and the B spectrum consists nearly exclusively of sharp ZPL. A transfer from A and A' to B would lead to a continuous background which would dominate the spectrum if these processes have significant efficiency. Carefully searching brought no evidence for such a contribution. In this sense the population flow from B to A and A' is unidirectional with no counterpart in the other direction.

Concluding, three crossings with repulsive states (Tab. 4.4) were identified from the intensities, lifetimes and Birge - Sponer plot in Figs. 4.7 and 4.20. Their energetic positions in the B potential-well are shown in Fig. 4.17 together with the gas phase crossings. The matrix shift in the calculated energy positions of curve crossings is rather small and less than a vibrational quantum [39]. According to this prediction the energetic ordering (and even the near degeneracies which occur) in the gas phase can be expected to show up in the matrix, too. From spectroscopic evidence the two vibrational levels between which the crossing is situated can be derived , determining the accuracy at the order of half a vibrational spacing $\Delta G/2$ or about 70 cm^{-1}. Therefore, it is sufficient to compare only with gas phase data, as was done in Fig. 4.17 and Tab. 4.4. $C^1\Pi_{1u}$ is the lowest

repulsive state which is well separated from the next ones. The very good agreement of the lowest energy crossing in the matrix with that of the gas phase C-state leaves no doubt on its assignment (Tab. 4.4). The $^3\Pi_g(2g)$ and $a(1g)$ crossings in the gas phase are nearly degenerate and coincide with the second crossing in the matrix very well. From the experiment it is not possible to single out which one dominates in the matrix induced coupling and this discrimination has to be left with theory [39, 40]. Perhaps even both contribute and the intensity drops on v'=8 and v'=9 originate from two crossings; here it is treated as only one. The third crossing around v'=14 in the matrix is less well documented in our data and has to be taken with some caution. It is consistent either with a crossing by the $a'(0_g^+)$, the $^3\Delta_u$ or the $^1\Sigma_u^+$-state. The comparison confirms the prediction of rather small matrix shifts at least in a qualitative way. Shifts of one vibrational quantum enhance the importance of a reference energy. Table 4.4 uses the B-state minimum as reference energy and Fig. 4.17 the electronic ground state X. The B-state potential is red shifted near the minimum and blue shifted in the region of the dissociation limit. The crossings extend from deep in B (C) to half the dissociation limit (a', Δ, Σ), along the inflexion from red to blue, which is reflected in the trends of matching states for different references.

Lifetimes with respect to predissociation of 5 and 2.5 ps just above the crossing have been estimated from the jumps in linewidth of the ZPL (Fig. 4.7a). But lifetimes taken from linewidth data can be contaminated by inhomogeneous contributions and deliver only lower limits.

Experiments with phase-locked pulses [21] delivered an electronic decoherence time of 1.5 ps for wave packets generated with 590 nm central excitation energy which is consistent with the deduced lifetimes of $v' = 7$ in Fig. 4.7a. The control of vibrational wave packets with chirped pulses provided an electronic decoherence time exceeding at least 300 fs in the region around 570 nm [2] which is consistent with the ZPL width around $v' = 13$. Vibrational population relaxation becomes very fast at even higher v' close to the dissociation limit [60] and continues the trend of lifetime shortening, apparent also in the linewidth.

Finally the population flow on the repulsive surfaces is shortly addressed. Different to the gas phase picture of the A-state in Fig. 4.17, all states are bent up at large internuclear distances due to the repulsive interaction with the cage, analogous to the cage bound extension of the B-state above its dissociation limit (see RKR potential). Thus population from the repulsive states is transferred to the bound states in the degenerate and cage bound region [43, 234]. The lattice potential is flexible so the cage takes up the kinetic energy above the dissociation energy analogous to the B-state. Thus again the A and A' populations drop in energy below the dissociation energy in the first return from the outer turning point and are now situated below the B-state potential minimum. A return on the repulsive surfaces is prohibited by the lack of kinetic energy which would be necessary to climb up in energy. This explains why a branching into A and A'-state population induced by predissociation is observed, but no feeding back to B.

From this study, the region of the second curve crossing was identified as the most promising for realizing coherent control of predissociation as done in Ch. 6. The electronic decoherence times exceed those for predissociation and vibrational relaxation. A fraction on the order of 10% per passage should switch from B to the repulsive states which is large enough that changes can be recognized, yet small enough that the effect can be followed for several round trips. Two problems can however be recognized. This region lies on the far red wing of the B-state and a low absorption cross sections will reduce the signals. Even worse, the B-state vibrational wave packets have to be discerned from a strong background due to the larger A-state absorption in this region as indicated by Fig. 4.9.

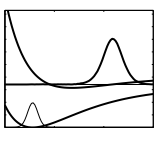

Chapter 5

Analysis 2: Time resolved spectroscopy

In this short chapter the measured vibrational wave packet dynamics, excited at the electronic states B and A will be inspected at two selected pump wavelengths. A variation in relative polarisation between the two ultrashort laser pulses allows for an insight in the complex excitation path up to the CT states, from where LiF is observed. The most likely pump and probe sequences will be discussed considering also information how the signal depends on intensity. Furthermore, the discussion includes the simulation of vibrational wave packet dynamics on the B-state of the free bromine molecule.

5.1 Pump - probe spectroscopy results

As described in the technical introduction of Sec. 3.3.3 the single pump - probe experiment consists of two steps. The first pulse excites population from the ground state into the excited states A and B, the second pulse transfers parts of this population to higher lying CT states from where LiF is observed. Two fluorescence bands were used, as introduced in Fig. 3.1, the band at 322 nm from the lower lying CT states manifold and the band at 300 nm from the higher lying one. These states are plotted with their gas phase values in the potential energy scheme in Fig. 2.1. It is known, that the 300 nm band allows for selecting B-state dynamics and the 322 nm band contains a superposition of B and A-state. A very detailed investigation of Br_2/Ar was carried out by M. Gühr [43, 60] with a broad variation of pump and probe energies, covering nearly the hole bound area of the B-state. The results are known to be non-linear, thus new spectra were required as a check in consistency. My work will concentrate on two pump wavelengths: 560 and 590 nm. With $\lambda_{pump} = 560\,\text{nm}$ the bound part of the B-state is excited around $v' = 16$, with reasonable efficiency due to the Franck - Condon (FC) factors plotted in Fig. 4.20. The second type of excitation around 590 nm ($v' = 8-9$) is very interesting, since the second crossing with repulsive states (see Sec. 4.2) is energetically located here and this is the energy region chosen for the control experiments discussed in the next chapter.

5.1.1 Polarisation dependence

In the following, two different relative polarisations between pump and probe pulses were realised: The parallel ($\parallel$) and the perpendicular ($\perp$) configuration.

Pump parallel to probe beam

For the experiment with parallel relative polarisation between pump and probe beam, four spectra are displayed in Fig. 5.1. The left column (a,b) presents results for $\lambda_{pump} = 560\,\text{nm}$ and the right one (c,d) for 590 nm. In the upper panel the signal at 322 nm and in the lower, that at 300 nm fluorescence wavelength are shown. In all cases, the probe wavelength was 590 nm and this defines distinct positions for the probe window in R, depending on the involved electronic states. This position is indicated by $R_{win,B}$ in Fig. 5.2 for the B-state (solid line) . Pump excitation

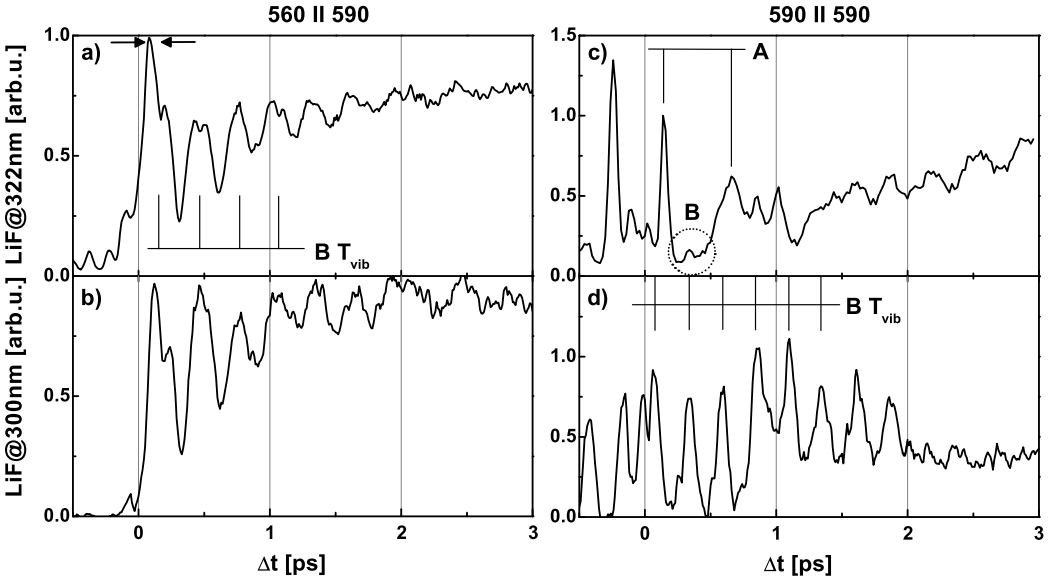

Figure 5.1: Observation of the pump - probe signal at two different fluorescence wavelengths of 300 and 322 nm with $\lambda_{pump} = 560$ nm and $\lambda_{probe} = 590$ nm in a) and b) and by pumping and probing with 590 nm in c) and d). The upper panels consist of the signal from the lower lying CT manifold at 322 nm and the lower panel with the fluorescence from the higher laying CT manifold at 300 nm. The spectra on the right hand side show a superposition of B and A dynamic with stronger (c) or weaker (d) A admixture.

with $\lambda_{pump} = 560$ nm is depicted with a thick grey arrow, creating a wave packet on the B-state (grey filled), which oscillates with a period of 300 fs and and the outer turning point is at R_{turn}. Since the probe window $R_{win,B}$ lies at a shorter internuclear distance than R_{turn}, the wave packet is caught up twice per roundtrip time as sketched in Fig. 3.6. This leads to a splitting of the signal peak in the spectrum in Fig. 5.1a) at small delay times. Outward ($\rightarrow$) and inward ($\leftarrow$) motion are indicated. However, the centre of each split peak corresponds to the vibrational roundtrip time B T_{vib} of 300 fs at this energetic region. All spectra are normalised to the first peak at positive time delays and afterwards averaged over three data points. The background increases monotonically with longer time delay Δt between pump and probe pulse and the wave packet modulation fades out at 3 ps. For LiF taken at 300 nm in b) the behaviour looks very much the same as in a), but the original signal is reduced by a factor of 10 due to a weaker cross section to this higher lying CT state. No clear A-state signature is observed. These two signals were obtained using to different NOPA, each with a direct energy output of roughly[1] 6 μJ.

The experiments shown in Fig. 5.1c and d) with $\lambda_{pump} = \lambda_{probe} = 590$ nm were performed with only one NOPA whose output was divided by a beam splitter. At this wavelengths combination $R_{win,B}$ and the turning point of the wave packet coincide, thus no peak splitting occurs. Nevertheless, the spectrum in c) looks very complicated, due to a superposition of strong A and weak B dynamics. The two strongest A peaks are marked with the sticks, opening a valley in between them. The weakly superimposed B-state dynamic can be identified by the small peak marked with the dotted circle at $\Delta t = 340$ fs, where the A-state wave packet is far away from the probe window. To observe a more pronounced B dynamics one has to record LiF from 300 nm in plot d). A clear period of 260 fs is observed for the first ps, as pointed out. Afterwards an increasing background

[1]The reference point for measuring the energy is before or in the prism compressor. Energy is lost at every optical component and when the pulse enters the sample, it is reduced down to roughly $0.3 - 0.1\mu$J. Only for the bleaching experiments in Sec. 4.1.5 power was optimised to reach $1 - 4\mu$J at the sample.

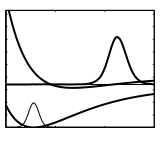

comes up, like in b). An explanation for this energetic region is displayed in Fig. 5.2. The pump pulse of 590 nm simultaneously prepares vibrational wave packets on the A and B-state, shown with the dotted and solid black arrows, respectively. The observed vibrational roundtrip time T_{vib} of around 260 fs for the B wave packet (solid) is indicated by the solid horizontal two-sided arrow. A two-photonic probe step depicted as solid arrow transfers population from B to the higher CT manifolds shown as black dashed potential on the top and fluoresces at a wavelength of 300 nm. An interpretation suggests, that part of its population relaxes to the lower lying CT manifold, from where it then emits with 322 nm to the covalent states (dashed downward arrow in Fig. 5.2). Light absorbed by the A-state (dotted potential) highly above the gas phase dissociation limit generates the dotted wave packet. It propagates on the potential until it reaches the matrix bound outer turning point (dotted arrow). Thereby, it makes a single pass of the A-state probe window, very rapidly. In the matrix collision the wave packet looses a lot of energy, slides down the outer wing of the A potential and continues its vibrational motion after 600-700 ps. Now, it is located in the bound part of the A potential, marked by the dotted horizontal two-sided arrow and propagates with a vibrational round trip time of 300 fs. In the two-photonic probe step, population is transfered to the lower lying CT manifold, included as grey dashed line, from where fluorescence at 322 nm is emitted. A small amount of A population also reaches a higher lying CT state to fluoresce at 300 nm (not shown). The observed emissions in the UV correspond to transitions from the CT states to the covalent states.

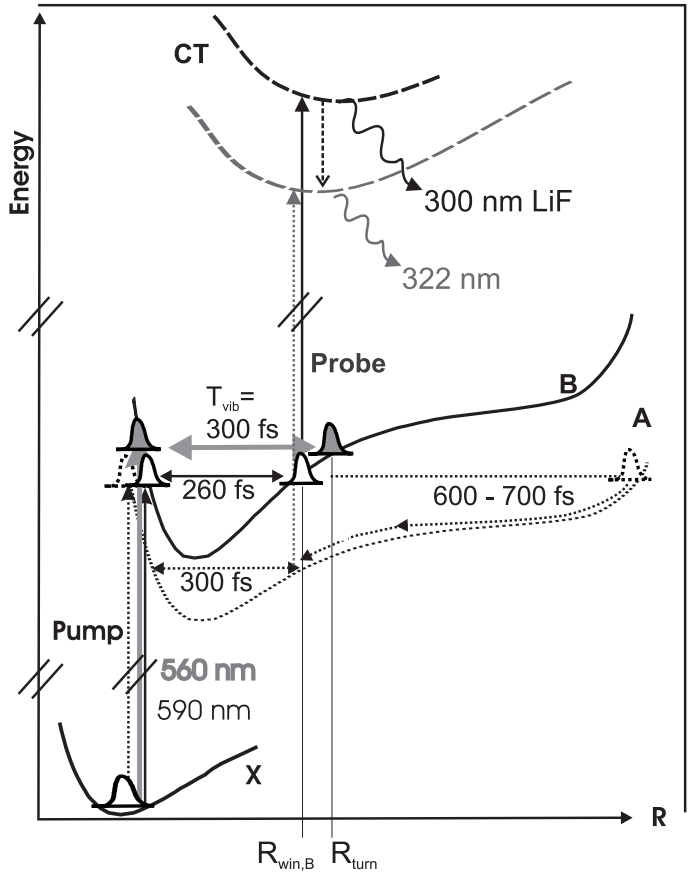

Figure 5.2: Sketch of pump - probe experiment. Pump excitation to covalent potentials A (dotted) and B (solid) are drawn for different energetic positions (grey thick arrow: X→B for 560 nm, thin solid arrow: X→B for 590 nm and X→a for 590 nm as dotted arrow) and create wave packets which are indicated with their round trip times. Probing takes place mainly from B to higher lying CT states (solid arrow) and from A (dotted arrow) to the lower ones (dashed potentials), from where fluorescence at 300 nm and 322 nm is observed. Exemplarily, for the 560 nm excitation, the outer turning point (R_{turn}) of the wave packet and the probe window position $R_{win,B}$ are indicated.

Pump perpendicular to probe beam

For the spectra in Fig. 5.1 the polarisation of pump and probe pulse was kept parallel to the plane of the optical table. For the following experiments the polarisation of the pump beam was changed by

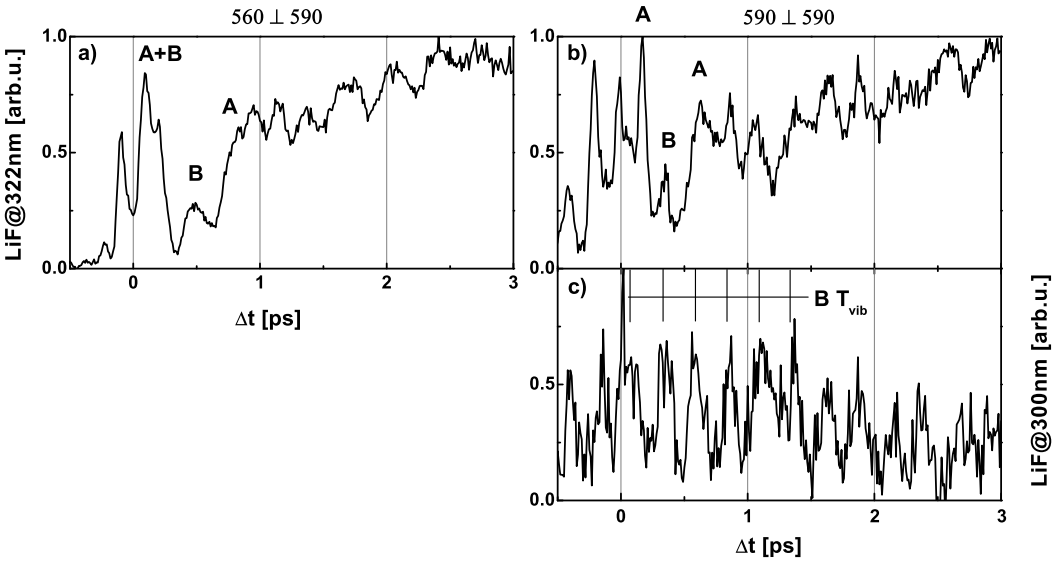

Figure 5.3: Pump - probe spectra for 590 nm probe wavelength, perpendicularly polarised to $\lambda_{pump} = 560$ nm for plots a) and b) and 590 nm for c) and d). Again, the upper panels contain LiF taken at 322 nm and the lower at 300 nm.

90°, since a difference in the polarisation behaviour for X→B and X→A due to the different $\Delta\Omega$ in the two transitions is expected. Different intensities for A and B contributions were observed in the polarisation investigations of the frequency resolved experiments in Ch. 4 and in Ref. [43]. Another parameter is known to depend on the polarisation: The monochromator sensitivity increases by a factor of three from parallel to perpendicular. Since LiF is emitted parallel to the polarisation of the probe beam [43, 235], its polarisation direction was not changed. Only the one of the pump pulse was varied.

Normalised spectra with perpendicular relative polarisation are given in Fig. 5.3, again for 560 and 590 nm as pump wavelength and 590 nm as the probe. At 322 nm fluorescence in a) the shape of the spectrum has completely changed, compared to Fig. 5.1a. Now it is also dominated by A-state dynamics which can be recognized by the "valley" at 500 fs between the maxima marked as A. In this "valley" the weak B signature is again identified, however it looks broader than in Fig. 5.1c since the wave packet has passed the probe window twice.

For an excitation wavelength of 590 nm in Fig. 5.3b the signal has not significantly changed compared to Fig. 5.1c. One can speculate that no A contribution in the background shows up, however, the signal to noise ratio is not satisfying. The change in polarisation leads to slightly enhanced B contributions. This was an unexpected result and will be discussed in Sec. 5.2.2.

To complete the polarisation dependent study, pump only experiments were carried out to observe fluorescence from CT states in Fig. 5.4a and from covalent states in panel b). For plot a) the sample was excited in a three photonic transition with one ultrashort pulse at $\lambda_{pump} = 565$ nm. The LiF wavelength at the monochromator was scanned and the fluorescence was detected with the photomultiplier. For the parallel setup (thin black line), both – pump and probe beam – were polarised parallel to the table, which is also the direction where the monochromator is more sensitive by a factor of 2 at 320 nm. For the perpendicular detection (thick grey line), at this experiment the probe beam's polarisation was rotated by 90° leading to the less efficient detection[2], and therefore

[2]The dye laser itself emits elliptical polarised light, when no polariser is introduced in the resonator. This was the case for all the 6 K experiments. For the polarisation dependent studies a polariser was introduced and excitation was

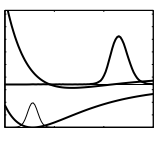

this spectrum was corrected by a factor of two. With this correction, the LiF emitted in perpendicular setup is nearly twice as strong as the parallel one. In the spectra with fluorescence from covalent states in Fig. 5.4b, obtained with ns - excitation using a dye laser at 583 nm, the B-state fluorescence is slightly stronger in the parallel configuration (thin black line) and the A' fluorescence is stronger by 1/3 in the perpendicular one (thick grey line).

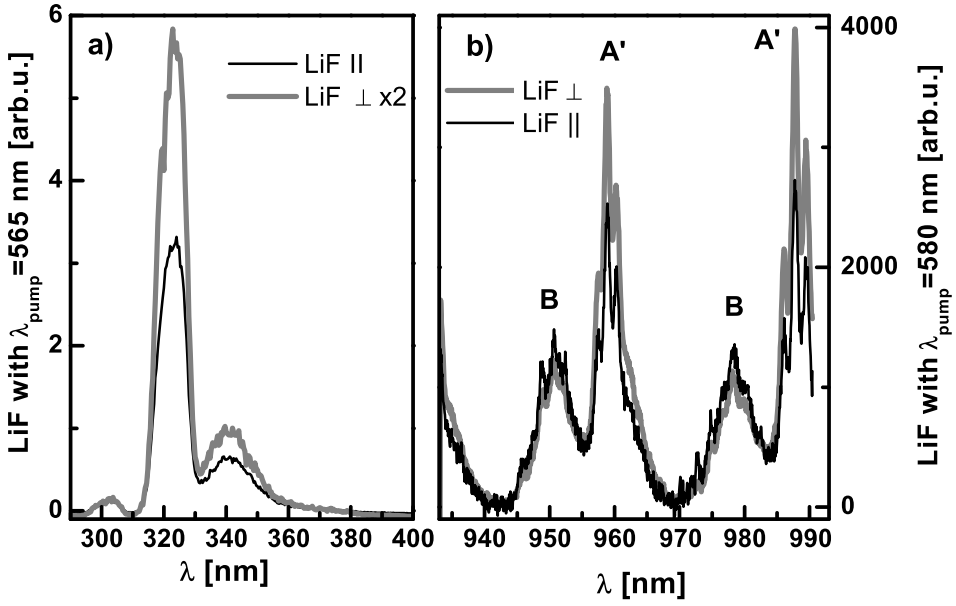

Figure 5.4: a) Polarisation dependence of CT fluorescence obtained with a three photonic excitation of $\lambda_{pump} = 565$ nm of 30 fs pulses with fixed polarisation of the pump pulse and relative parallel or perpendicular polarisation of the probe pulse. In b) the fluorescence from covalent states was detected. This time for excitation a dye laser at 583 nm was used. An analyser in front of the monochromator was kept at the direction of maximal sensitivity parallel to the table and the dye laser polarisation was tuned. Since those experiments were done with the closed cycle cryostat, the temperature was 14 K.

5.1.2 Intensity dependence

The excitation scheme from ground state X to the CT states in Fig. 5.2 requires at least three photons. To confirm this in experiment, the intensity dependence of the pump - probe signal is plotted in Fig. 5.5. Three curves are presented, since it was observed in pump - probe experiments that pump and probe NOPA are not exchangeable. It turned out that for probing with NOPA1 at 590 nm no vibrational wave packet of the B-state was observed. On the other hand, for NOPA1 as pump and NOPA2 as probe pulse, the B dynamics is present. The three traces correspond to three different NOPA configurations: NOPA1 only (squares), NOPA2 only (circles) and both NOPA with the same intensity (triangles). The wavelength was kept constant at 590 nm and fluorescence was detected at 322 nm. The trace of NOPA1 alone shows in the double logarithmic plot a slope of 2.5±0.1 in a linear fit, which can be attributed to a two to three photonic process. In the case of NOPA2 the slope is much steeper with 3.7±0.1, indicating, that a four photonic process takes

carried out with linear polarised light parallel or perpendicular to the table.

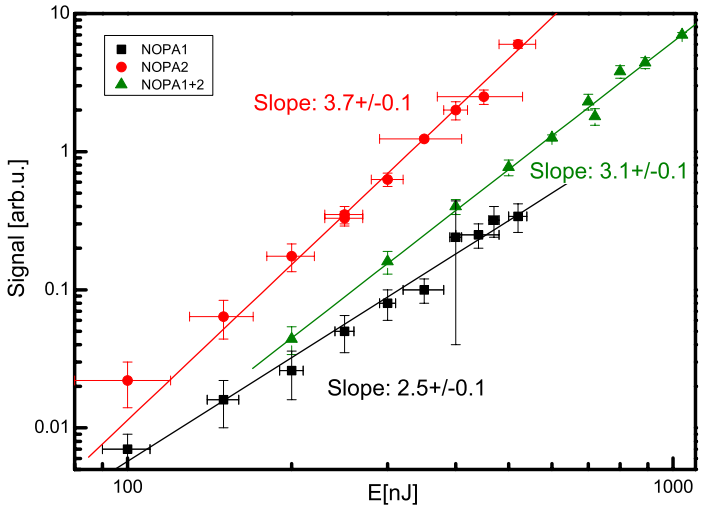

Figure 5.5: Pump - probe signal intensity dependence at $\Delta t = 0$, for two different NOPA, both set to 590 nm and having the same energy of 5μ J and a pulse length of 35 fs. Fluorescence was recorded at 322 nm.

place, here. For the combination of both NOPA with a time delay of $\Delta t = 0$ the steepness averages to 3.1 ± 0.1. For the control experiments of the next chapter NOPA2 was split into two beams. The requisite of minimally three photons being involved to create population of CT states is fulfilled. It seems however, that the photonic order in all $\lambda_{pump} = 590\,\text{nm}$ experiments is higher than expected and extended excitation schemes are discussed in Sec. 5.2.2.

5.2 Discussion of pump - probe spectroscopy

Comparing the periods for B wave packet dynamics in Fig. 5.1b and d) with the vibrational spacings ΔG of the B excitation spectrum in Fig. 4.5 show an agreement: For 560 nm $\Delta G = 109$ cm^{-1} which corresponds to $3.27 \cdot 10^{12}$Hz or a roundtrip time of 306 fs. This matches the observed period of 300 fs in Fig. 5.1b. In case of $\lambda_{pump} = 590$ nm the spacing $\Delta G = 138$ cm^{-1} or $4.14 \cdot 10^{12}$Hz leads to a period of 242 fs. The period of 260 fs detected in Fig. 5.1d is slightly longer.

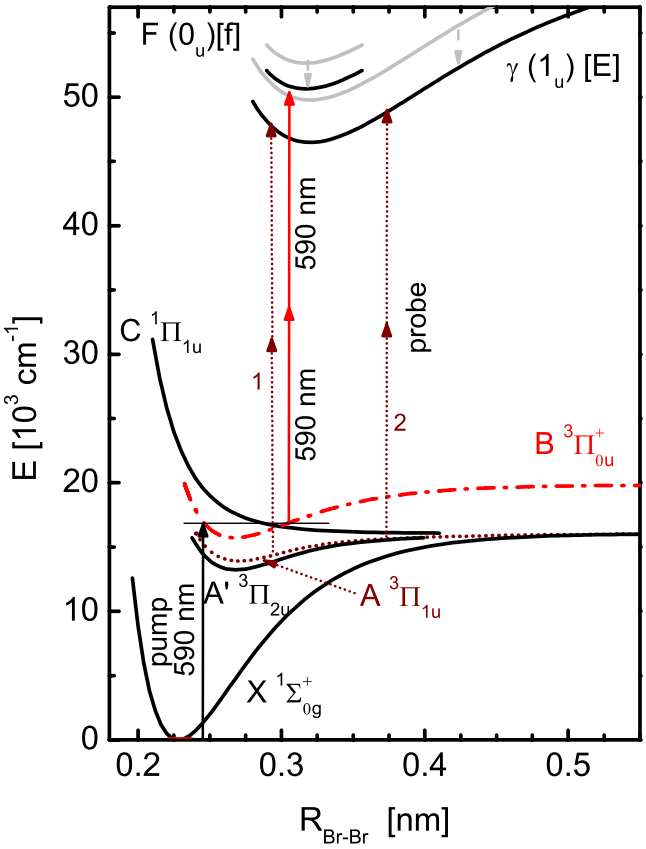

Figure 5.6: Potential scheme for pump 2 - photonic - probe excitation. The B-state (dash dotted) as a constructed Morse potential with matrix parameters (this work) is valid for energies below 18000 cm^{-1}. Other covalent states are shown as gasphase potentials. The gasphase CT states (grey) are redshift (black) as indicated by the dashed grey arrows, following the assumptions of Ref. [43]. Pump excitation from X→B with 16950 cm^{-1} (590 nm) is indicated by the labeled vertical arrow and the centre height on the B potential is marked with the horizontal line. Two - photonic - probe transitions are possible from the B-state to states of the higher CT manifold (F, solid arrows) and at two positions from the A-state to the lower CT manifold (γ, dashed arrows).

To clarify the the positions in R for pump excitation and probe window, the real potential surfaces adapted from the gasphase and including the matrix induced redshift are depicted in Fig. 5.6. It shows a realistic scenario for single photon pump and two photon probe transitions for 590 nm pulses. The covalent states X, A and A' and the repulsive state C are included as gasphase potentials. For the B-state a Morse potential with the parameters of Ch. 4 was created, which holds

for energies below 18000 cm^{-1} (dash dotted line). The pump arrow with its length corresponding to 590 nm shows the transition from X→B. The centre frequency of the wave packet is shown as solid horizontal line. Out of the CT manifolds two possible states are depicted with their red-shifted gasphase potentials for the f-state and the E state in Fig. 2.1. However, those states have gerade parity and would not be reached in a two photonic transition from the ungerade states A and B. This requires a u↔u transition, but no matching CT states are documented for the free bromine. In analogy to iodine, states were found in Ref. [43] and this assumption is used in Fig. 5.6 as well, leading to the states F (instead of f) and γ (instead of E). The B-state can be probed with two photons to the higher lying F-state as indicated by the two solid arrows on top of each other. However, they do not reach the F potential surface and a difference of around 400 cm^{-1} remains. Thus, the centre frequency of the wave packet might not be efficiently probed and this agrees with a prolongation of the oscillatory period as observed for the B wave packet dynamics at 590 nm. From this potential scheme it is also obvious, why no emission at 300 nm is detected with an excitation wavelength of 490 nm in Fig. 4.13.

For probing the A-state two energetic probe windows are possible under the assumptions being made, as indicated by the dotted double arrows. The first one '1' catches the A wave packet early on its way out. Later on, after the first matrix collision and the following dissipation it is the only remaining probe window deep in the A potential. The second window '2' is situated on the outer wing of the A potential and is only active around the first collision with the matrix. A wave packet born on the B-state can change to the repulsive potential[3] C and reach the A-state, where it is probed as an A wave packet, as well. The latter will be necessary for the control experiments of Ch. 6.

Knowing the position of the probe window on the B potential is required to simulate the B wave packet dynamics, treated next. By comparing the experimental pump - probe spectrum in Fig. 5.1d with the gasphase simulation, details concerning the observed dispersion, vibrational energy relaxation and the vibrational roundtrip time will be discussed.

5.2.1 Simulation of wave packet dynamics on the B-state of free Br_2

The code for gasphase simulation of wave packet dynamics, provided by D. Tannor [26, 236] was extended with a laser field and adapted to the bromine molecule in Ref. [43] where the programme is also described in detail. This code was now further improved to deal with a phase controlled pulse train as pump sequence as will be seen in the discussion of chapter 6. Furthermore, the B-state - potential with Morse parameters obtained for the matrix in Sec. 4.2 was implemented which is valid below 18000 cm^{-1}. This simulation does not include electronic states other than the X and B nor strong matrix effects at high energies like cage effect, phonons created in the matrix or couplings of electronic states and thus no dephasing nor energy relaxation. It is a very useful tool to separate the pure B-state dynamics from the one of a chromophore in the matrix. The simulations were, $e.g.$, used to separate wave packet dispersion due to the anharmonic potential from the matrix induced decoherence [2]. The pump step is realistically included based on time dependent first order perturbation theory. The unperturbed wave function Ψ_0 of the ground state is projected onto the B-state and is propagated there as a B vibrational wave packet $\Psi_B(R,t)$. For calculation speed reasons, the simulation is based on the split operator technique which switches between the R space and the momentum domain (k space) via a fast Fourier transformation. The potential operator only depends on R and is applied in R-space. The kinetic energy part contains the momentum operator and is conveniently applied in k-space. The probing step is included by sampling the B population at different time delays Δt in a window corresponding to the probe window of the pulse which was defined in Sec. 3.3.3. It is possible to include the experimental

[3] C is again the depute for several repulsive states crossing the B potential, as discussed in Sec. 4.2.

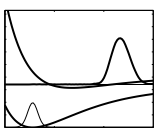

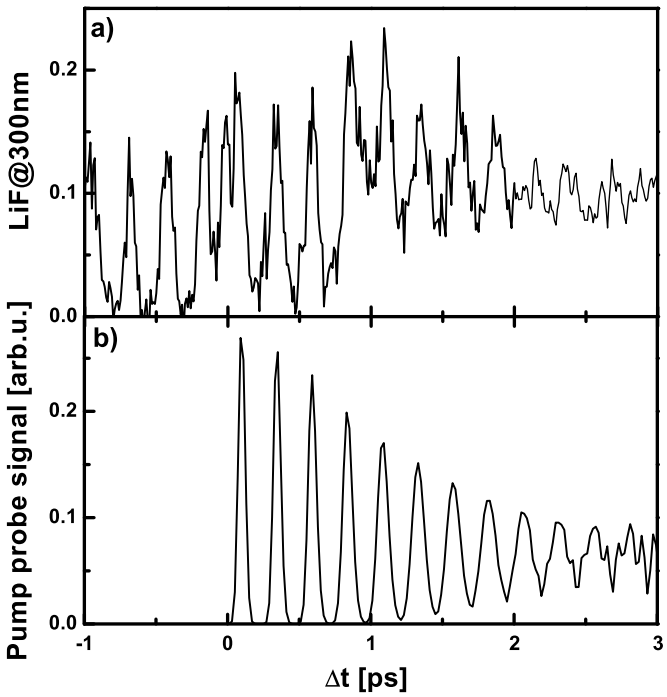

Figure 5.7: Simulation of B wave packet dynamics at 590 nm. Experimental parameters: $\lambda_{probe} = 590\,\text{nm}$, $\Delta\lambda_{pump} = 35\,\text{nm}$, simulation parameters: matrix Morse potential with probe window position = 0.322 nm and a width of the probe window of 0.08 Å which is in accord with $\Delta\lambda_{pump} = 15\,\text{nm}$.

parameters by using the potential differences in Fig. 5.6.

Such a simulation for wave packet dynamics with $\lambda_{pump} = 590\,\text{nm}$ of an unchirped pulse can be seen in Fig. 5.7b for the B wave packet, detected at a fluorescence wavelength of 300 nm in comparison with the experimental trace in plot a). It shows a very good agreement until the A-state starts to show up in the experimental spectrum, mainly as a background at 1 ps. The simulation starts at $t = 0$ and shows the pure B-state dynamics with a roundtrip time of 250 fs. One sees a decaying spectrum due to dispersion and shortly before 3 ps the clear wave packet structure is lost since at this position the 1/3 fractional revival occurs (see Sec. 1.2). However, to obtain such an agreement between simulation and experiment, not all experimental parameters can be adopted as they stand. A simulation with the real experimental width of the pump pulse corresponding to a FWHM of 35 nm leads to a dramatic dispersion of the wave packet. The experimental trace however, is nearly free of dispersion effects. Therefore, the pump pulse width was narrowed to 15 nm in simulation which corresponds to a reduction from seven contributing vibrational levels in the FWHM of the pulse to three.

What are the reasons for a narrowing of the effective experimental wave packet? In the real potential, affected by the matrix, a wave packet undergoes two radiationless transitions introduced in Sec. 2.2: Predissociation and vibrational energy relaxation. Both of them do not act uniformly on all energetic parts of the wave packet. The predissociation probability is higher for lower energies, closer to the crossing. Thus preferentially the low energetic components of the wave packet are removed to other electronic states. Vibrational energy relaxation on the other hand is more effective high up in the potential due to the stronger matrix interaction, thus high energy components of the wave packet are lowered. However, 590 nm is located deep in the bound part of the B potential, and energy relaxation contributes only weakly, as can be seen from the nearly constant average value of the experimental spectrum in Fig. 5.7a. Dominantly, the effective spectral narrowing of the wave packet on the B potential is caused by predissociation. This results in an asymmetric shrinking of the wave packet, since low energy parts are stronger affected than high energy parts which leads to an upward shift in the centre of gravity. The higher up a wave packet oscillates in

the anharmonic B potential, the longer is the vibrational roundtrip time and this coincides with the different trend in oscillation periods calculated from excitation spectra (240 fs) and observed in time resolved simulation (250 fs) and experiment (260 fs).

This trend is furthermore supported in experiment with the potential scheme in Fig. 5.6. Energetic distances indicate, that the higher lying CT state is not reached with the centre energy of the laser pulses. Thus, only the upper part of the wave packet is transferred to the CT state and can be observed at 300 nm.

The same wave packet excitation in Fig. 5.7b and its propagation can be seen in the thumb cinema in the right corner of odd pages. The real time scale in fs can be calculated with $(p+1)/2*5$, where p is the page number.

5.2.2 Open questions

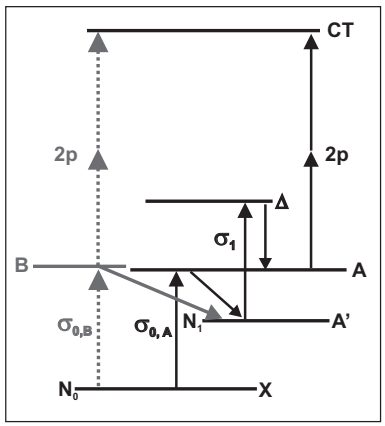

Figure 5.8: Scheme for 3 and 4 photonic excitation from ground state X to CT states with different paths for B and A-state. For details see text.

In some points deviations between my work and earlier results by M. Gühr in Refs. [43, 237] remain. These open questions concerning power dependence of the transient signal and the polarisation dependent suppression of A-state dynamics shall be discussed now. In Fig. 5.5 a four photonic absorption was suggested, which is distributed on the pump and the probe step. However, in Ref. [43] a three photonic scheme with linear pump and two photonic probe step was determined. Since experimental conditions concerning temperature and transparency of the crystal were different in these two investigations, the assumption of a hidden steady state population will be discussed. For the pump - probe experiments of this work with $\lambda_{pump} = \lambda_{probe} = 590\,\text{nm}$, a flow cycle cryostat with a sample temperature of 9 K was utilised[4]. The sample was always milky, independently on annealing procedures. On the other hand, in Ref. [237] a closed cycle cryostat operating at 18 K was employed, which provides clear samples. These differences in temperature and scattering behaviour of the sample might lead to a steady state population in the lowest lying covalent state A'. It has the longest lifetime of 40 ms [107] due to a violation of spin and angular momentum selection rules, as was discussed in Sec. 2.1.4. Lifetime will be shortened at higher temperatures, as is also indicated in line broadening of A' transitions with higher temperature. Furthermore, an increase in lifetime for un-annealed samples was mentioned in Ref. [238]. A comparison with our laser repetition rate of 1 kHz ($i.e.$, subsequent pulses have a delay of 1 ms) shows that a population reservoir in the A' state might build up.

In the case of such a reservoir in A' the pump step would no longer start from the ground state X only, but also from A', as illustrated in Fig. 5.8.

The contributing electronic states are shown as lines, starting from the ground state X which has the population N_0. The sketch shows possible pump - probe scenarios for three and four

[4]The temperature of crystal growth was in all experiments constantly at 19.5 K.

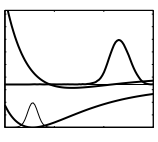

photonic excitation from X to the CT states. On the left hand side the standard scheme for B-state excitation and probing is depicted with dashed arrows. Population from X is pumped with the cross section $\sigma_{0,B}$ to the B-state and from there pumped in a two photonic step to the CT states. For the A-state population the scheme includes two possibilities, painted as solid lines. The first one is in analogy to the B-state a direct excitation to A, with the probability of $\sigma_{0,A}$, and from there with two photons to CT, overall requiring three photons. The second path involves four photons, namely to B or A-state with the first photon. From there population relaxes to the long living A'-state, building up the population N_1. With the next laser pulse population from A' is transfered, tentatively via a repulsive state called Δ with cross section σ_1, quickly back to the A-state and it can propagate there. A possible candidate might be the repulsive state $^3\Delta_u$ of Tab. 4.4 [39, 40] matching in energy difference and also in spin configuration. A pathway from Δ to A is probable, since their potentials merge together at large R due to identical energetic levels. Due to spin - orbit coupling the B-state dissociation limit of the gasphase is located higher and the only population transfer from Δ to B would be the third crossing identified in Sec. 4.2. However, for the lower lying C-state such a population transfer was never observed.

To clarify the probability of this indirect feeding of the A-state, a coarse estimation on the amount of steady state population accumulated in A' is done: The population N_1 which builds up on A' follows the relation

$$N_0\, k_{up} \;=\; N_1\, k_{down} \tag{5.1}$$

where k_{up} is the rate of population excited from X→A and B and k_{down} the rate for population leaving the A'-state to the ground state. Population N_0 can be estimated from the density of particles, which is on the order of 10^{22}/cm^3 for the matrix, reduced by the a concentration of Br_2/Ar of 1:500. At experimental temperatures of <18 K nearly all molecules are situated in $v' = 0$ of the ground state, thus N_0 is roughly 10^{19}/cm^3. The rate k_{down} can be calculated from the lifetime of 40 ms, to be 25s^{-1}. The rate k_{up} follows

$$k_{up} \;=\; \Phi\, \sigma_0, \tag{5.2}$$

with σ_0 being the overall absorption cross section and Φ the photon flux per time and area. At an energy of 0.1μJ at 590 nm ($\widehat{=}$ 5·10^{14}Hz) the number of photons per pulse is 3·10^{11}. With an estimated focus diameter of 50μm and at a repetition rate of 1 kHz, Φ = 7.5·10^{17}/[cm^2 s].

The cross sections σ_0 can be determined from the Br_2 gas phase absorption spectrum in Ref. [51]. There, the molar absorption coefficient ϵ was given as $\epsilon = 5l/[mol\ cm]$ for 590 nm and it can be converted into σ, following Ref. [239]:

$$3.8 \cdot 10^{-21}\ \epsilon \mathrel{\widehat{=}} \sigma_0 \;=\; 1.9 \cdot 10^{-20}\, cm^2. \tag{5.3}$$

The decomposition of the Br_2/Ar excitation spectrum in Sec. 4.2 predicts a ratio of 100:1 for $\sigma_{0,A} : \sigma_{0,B}$.

With that, the ratio of k_{up}/k_{down} is 4·10^{-4}. About 0.04% of the excited population remains in the A'-state.

Now it depends on the strength of the cross section σ_1, how efficiently population can be transferred from A' back into the higher lying covalent state A. Assuming $\sigma_1 \gg \sigma_{0,B}$, this will cause a two photon absorption leading to a four photonic dependence, like it was observed in Fig. 5.5. This scenario will lead to higher contributions of the A-state in the pump - probe signal due to this indirect populating via the A'-state and a repulsive state. The B-state does not benefit from a steady A'-state population, since no population transfer from the lower repulsive states to B was observed. Thus, the A-state will dominate in the time resolved spectra. With this possible pathways in mind, one expects a single photon pump and two photon probe step in the case of shorter A' lifetime at

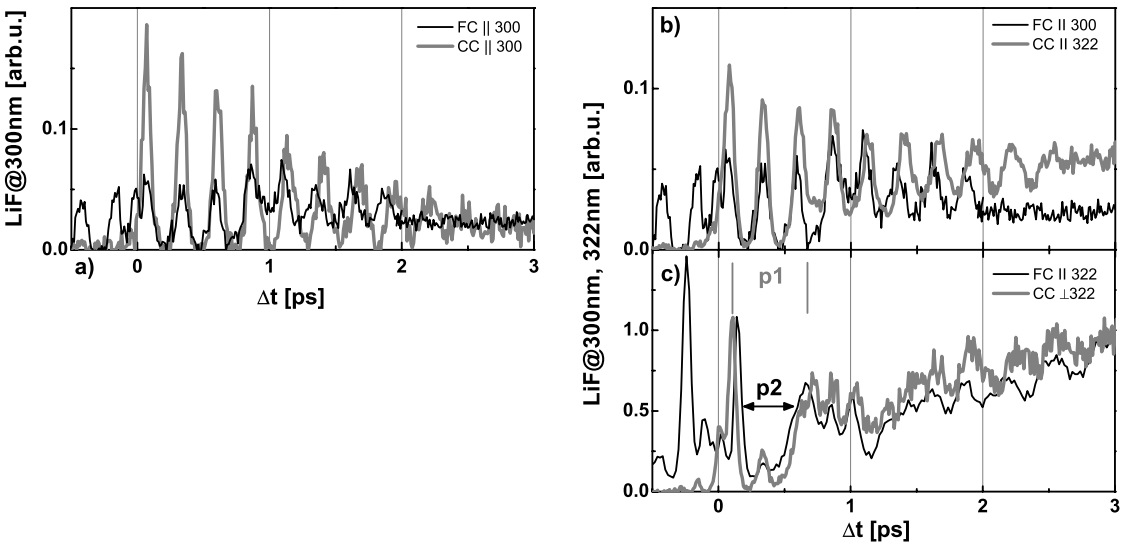

Figure 5.9: Comparison of $\lambda_{pump} = \lambda_{probe} = 590$ nm spectra at different temperatures and cryostats. Black spectra were obtained with a sample cooled with the flow cycle (FC) cryostat at 9 K . The 18 K spectra from Ref. [237] taken with the closed cycle (CC) cryostat are shown as thick grey lines. a) Both spectra in parallel configuration and at $\lambda_{fluor} = 300$ nm. b) Both spectra in parallel configuration, but the CC spectrum was obtained at 322 nm and the FC spectrum at 300 nm. c) For both spectra $\lambda_{fluor} = 322$ nm was recorded, the FC spectrum with parallel, the CC spectrum in perpendicular relative polarisation. For the CC spacing between 1st and 2nd A peak is labeled with "p1". The width of the valley between $\Delta t = 0$ and 1 ps is slightly shorter and indicated by "p2".

higher temperatures. If the A' lifetime is prolonged, both – pump and probe – will be involve two photons. For a fixed lifetime of the A'-state, the only open parameter is Φ and a weaker focussing will then enhance the ratio of B/A contribution.

Such a building up of a steady state population of the A'-state was described in a comparable system, ClF/Ar in Ref. [38].

A population reservoir in A' will populate the A-state and will thus counteract to the photoselection introduced in Sec. 2.1.4. The A-state can no longer be efficiently suppressed. This behaviour is confirmed in a comparison of the results in Figs. 5.3 and 5.1 for pump and probe wavelength being 590 nm with the results of [237], shown in Fig. 5.9.

In plot a) both spectra with a relative polarisation being parallel and a fluorescence wavelength of 300 nm are compared. From $t = 0$ they show mainly the same spectrum with B wave packet dynamics, however, in case of the newer spectrum (black line), the A-state contribution leads to an increasing background at 1 ps, which is missing in the elder spectrum (thick grey line). For the new spectra also a modulated signal at negative times is observed. Here, the pump and the probe pulse exchange their roles. Since it was not observed in the elder spectra, it might be an indication for different focussing conditions of the beams on the sample. The increasing A background is also found in b) for the elder spectrum in comparing the 322 nm fluorescence with the newer one, recorded at 300 nm. Thus, due to the weaker A-state suppression, now A population can also reach the higher lying CT manifold, which was not possible earlier. That the A-state has gained strength with respect to the B-state becomes clear in plot c), where the newer parallel configuration at 322 nm is compared with the elder perpendicular one, which was attributed to an enhancement of the A-state due to the difference in $\Delta\Omega$ discussed in Sec. 2.1.4. Both spectra are very similar and show the admixture of B and A-state features with dominant A character. They differ in the

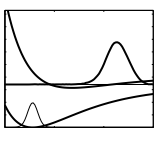

length of the valley attributed to A dynamics, marked with "p1" for the new and "p2" for the old spectrum. "p1" is slightly shorter and this might be an indication, for a probing of the first peak from a repulsive surface and not from the A potential as in the case of "p2". It is refrained from further interpretation, since studies with variable colours of pump and probe beam would be necessary to sample the wave packet at different points.

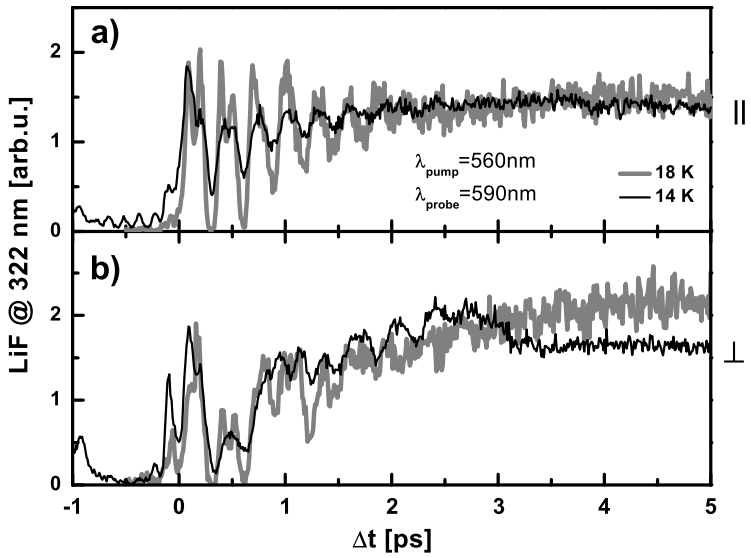

Figure 5.10: Comparison of 560 nm spectra at different temperatures in parallel a) and perpendicular configuration b) at $\lambda_{fluor} = 322\,\text{nm}$. Both spectra were taken with the closed cycle cryostat, the black one at 14 K and the thick grey one at 18 K. The 18 K spectra are from [237].

The scheme of a prolonged A' lifetime in case of the newer spectra presented in this work follows a four photonic absorption distributed equally on the pump and probe steps. It is supported by a comparison of the pump - probe spectra obtained at $\lambda_{pump} = 560\,\text{nm}$ in Figs. 5.1a and 5.3a with Ref. [237] in Fig. 5.10. All spectra were obtained with the closed cycle cryostat, but at different temperatures. For the new spectra (black line) the sample temperature was 14 K, for the elder spectra (thick grey line) it was 18 K. The modulation contrast was reduced in the newer ones, but the main features are the same: In the parallel setup in a) the B dynamics dominates, whereas in the perpendicular one in b) the A signature is clearly present, thus the expectations following the scheme of Sec. 2.1.4 are fulfilled.

However, one has to keep in mind, that the FC factors for B and A absorption approximate at this higher excitation energy.

Another option to describe a polarisation dependent interchange in A-state suppression assumes an one photonic pump step, but a three photonic probe step. With 150 nm (with respect to the ground state) already excimer bound states of a Br_2-Ar complex can be reached. Those molecules are arranged in a triangle with the Ar atom on top and Br_2 being the base, thus the main axis is oriented perpendicularly to the molecular axis. Then the probe step would no longer act parallel as proposed in Sec. 2.1.4, but perpendicular and the rules for photoselection are interchanged. In any case, the observed fluorescence originates from the CT manifolds in Fig. 5.6. But the question remains, whether they are populated directly or indirectly from higher lying states.

Chapter 6

Control: Interference with phase controlled pulse sequences

In the last two chapters the system Br_2/Ar was analysed in the frequency and time domain. The so obtained spectroscopic information is used now to control the molecular dynamics and the effect of the cage influence on the dynamics using a progression of coherently controlled ultrashort laser pulses. Two aims will be achieved: First, the matrix induced predissociation is controlled and second, the B wave packet dynamics which is covered by the A-state is prepared out, due to constructive wave packet interference.

This chapter will be separated into two parts, the tutorial solution as sketched in Fig. 6.1a with phase controlled pulses from a Michelson interferometer. The advanced solution using a pulse shaper to create phase stable pulse sequences, combined with an additional probe pulse to achieve time resolved results is sketched in Fig. 6.1b.

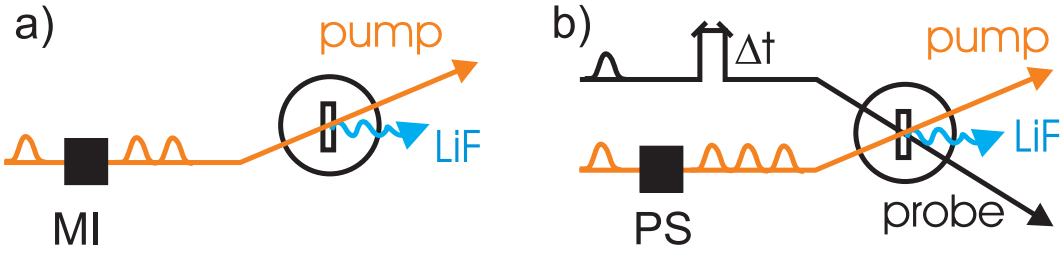

Figure 6.1: a) As a tutorial solution phase controlled double pulses from an Michelson interferometer (MI) were used and their LiF from covalent states was observed. b) In the more advanced solution pulse trains created by a pulse shaper (PS) acted for pumping and another fs pulse provided the time resolved probe step.

6.1 Tutorial solution: Michelson interferometer

The Michelson setup described in Sec. 3.4.1 allows for a phase stable preparation of phase locked pulse pairs, being a helpful tool for determining electronic decoherence times but also for controlling the composition of wave packets regarding ZPL or PSB contributions. The interference of wave packets was introduced in Sec. 3.4.3 and is observed in the following experiments. Interference patterns introduced by two laser pulses with a stable and tunable relative phase have the advantage of being easily manageable and are a good introduction to the task of control experiments.

6.1.1 Double pulse experiment

Figure 6.2 shows a measured interferogram for Br_2 in Ar obtained by recording the intensity of the B→X fluorescence out of $v' = 0$, *vs.* the time difference $\Delta\tau$ of the two pulses. For each $\Delta\tau$ the relative phase Φ between the electric fields of the two pulses was varied between 0 and 2π in

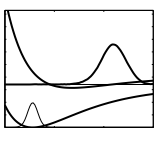

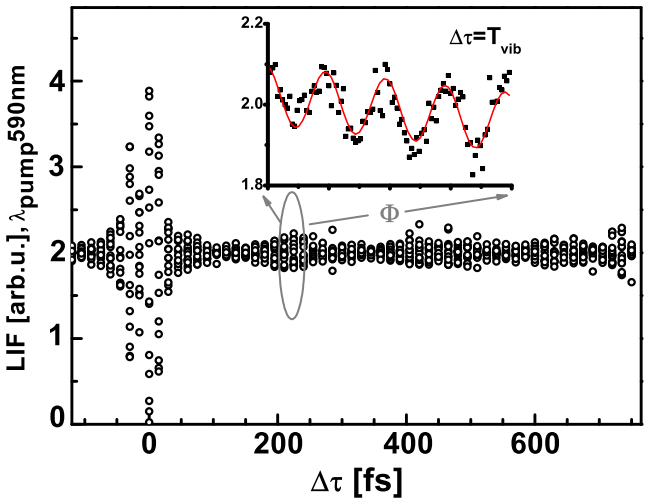

Figure 6.2: PLPP experiment with normalized B→X fluorescence signal *vs.* time delay between the two Michelson pulses at 590 nm (open circles). Constructive and destructive interferences of the excited wave packets lead to maxima and minima of the signal. The inset shows a phase variation for 16 different phases Φ for a time delay fixed at one roundtrip of 240 fs.

16 steps. The intensity for each step is given as the open circles in Fig. 6.2. The pump pulse was centered around 590 nm and covered several vibrational levels around $v' = 9$ of the Br_2 B-state. The first recurrence at $\Delta\tau = 240$ fs represents one vibrational roundtrip time in this energetic range as was discussed in Sec. 5.2 and in Refs. [21,22]. It is marked with the grey ellipse. To investigate the phase dependence of molecular absorption in more detail, $\Delta\tau$ was fixed and the relative phase Φ was varied in small steps covering 8π. The inset in Fig. 6.2 displays the obtained modulation (squares) together with a sine fit (solid line). Each data point is extracted from emission spectra like in Fig. 4.2 by integrating the peak intensity averaged over three B-state emission lines around 860 nm.

This experiment was repeated for several fixed $\Delta\tau$ and a selection is shown in (Fig. 6.3). Experimental values are normalised such, that the incoherent average value is set to two. Plots a-d) originate from 590 nm, e-g) from 570 nm excitation wavelength. The pulse length was 30 fs in both cases. The sinusoidal modulation is maximal for $\Delta\tau = T_{vib}$ in Fig. 6.3a, where the two wave packets meet at the inner turning point and can interfere optimally on the molecule, either constructively (maximum) or destructively (minimum). A significant modulation contrast up to the sixth roundtrip time $\Delta\tau = 6\,T_{vib}$ was observed, however, with decreasing amplitude. For longer time delays the modulation lies within the noise level. Figure 6.3 shows that this modulation, in a) for $\Delta\tau = T_{vib}$ and c) with $\Delta\tau = 5\,T_{vib}$, is really caused by interference, since no modulation is observed in plot b) for $\Delta\tau = 1.5\,T_{vib}$. In this situation, the two wave packets are localised at the inner and outer turning points, respectively, which inhibits interference in the FC region. Irregularities in the modulation period of measured data (squares) are visible by comparison with sine fits (solid lines) and are caused by nonlinearities of the piezo drive, which controls the relative phase Φ. In d) emission from A' is recorded. Indeed, $\Delta\tau = T_{vib}$, but this matches to the B-state vibrational progression. Thus, no interference effects for the A' are observed.
Another experiment that covered the spectral region around 570 nm higher up in the potential around $v' = 13$ is shown in Fig. 6.3 e-g. Here, the FC factors (Fig. 4.20) are larger by a factor of 10. The modulation contrast for $\Delta\tau = T_{vib}$ in e) is comparable to the excitation with 590 nm in a). Plot f) shows clearly the second recurrence of the wave packet. For $\Delta\tau = 5\,T_{vib}$ in g) no interference could be observed anymore. The earlier loss of observed interferences at 570 nm in comparison to the $\lambda_{pump} = 590$ nm case represents the reduction of spectral contrast for ZPL and PSB in the

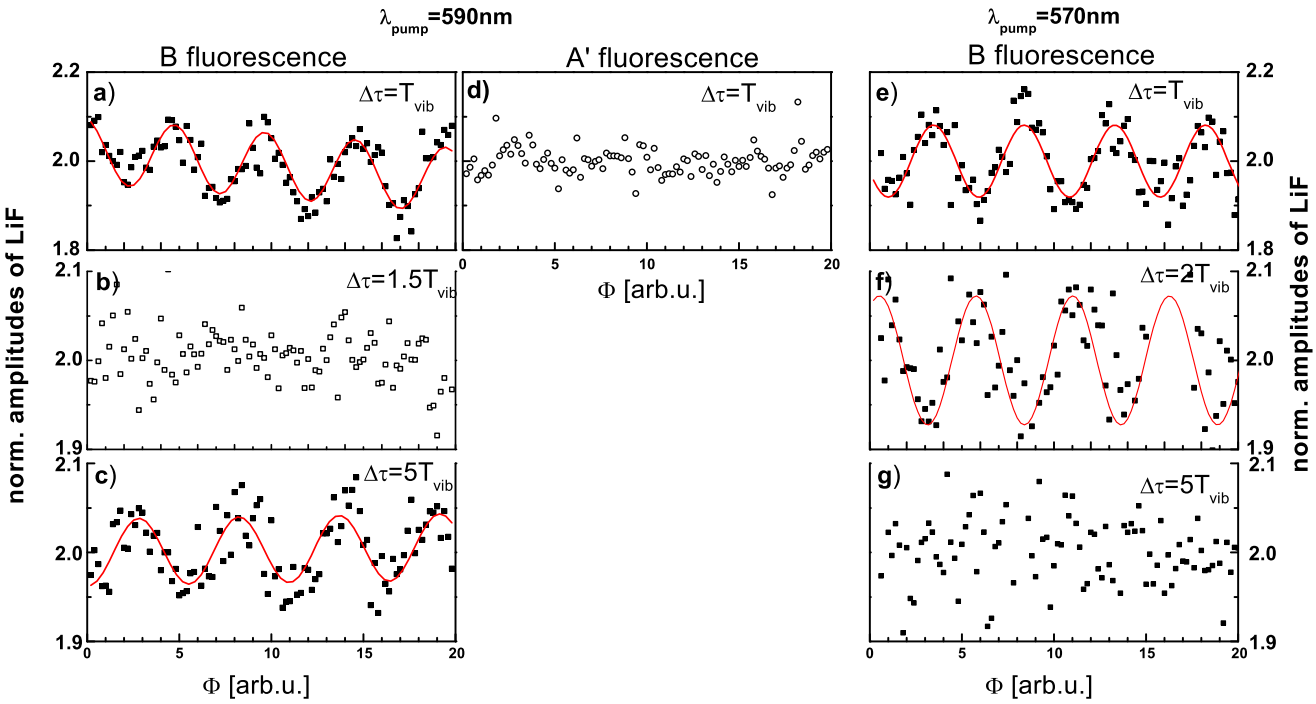

Figure 6.3: B (left column) and A'-state (middle column) fluorescence intensity traces of Br_2/Ar with fixed time delay $\Delta\tau$ versus phase Φ. In a) $\Delta\tau = T_{vib}$, in b) $\Delta\tau = 1.5\,T_{vib}$ and the signal scatters statistically. c) $\Delta\tau = 5\,T_{vib}$. d) Again $\Delta\tau = T_{vib}$ but now A'-state fluorescence is recorded. Right column: Interferences for $\lambda_{pump} = 570$ nm for $\Delta\tau = T_{vib}$ in e), $\Delta\tau = 2\,T_{vib}$ in f) and $\Delta\tau = 5\,T_{vib}$ in g).

excitation spectrum in Fig. 4.5 compared to the overwhelming background. Therefore, this region around 570 nm is not favourable for coherent control and further experiments are performed with pulses centred around 590 nm.

As the slit distance in a double slit experiment defines the fringe spacing in the far field, the time delay $\Delta\tau$ of the two pulses determines the period of spectral features. Furthermore, their relative phase Φ defines the position relative to the pulse envelope. Fig. 6.4 shows the formation of spectral fringes in the interference pattern for $\Delta\tau$ = 1, 2 and 3 roundtrip times at 590 nm excitation. Those corresponding to maximal LiF signal are plotted as a solid line, those to minimal signal as dashed line) observed. For comparison the B-state excitation spectrum is included at the bottom and one immediately sees that the maximal pattern is not centred to the ZPL, as would be expected for a free molecule. For Br_2/Ar it is not possible to position a fringe minimum on a ZPL without exciting a PSB and vice versa. Therefore, the fringe patterns of minimal and maximal LiF signal are positioned in between ZPL and PSB, since the signal height is determined by the overlap of spectral interferogram and excitation spectrum.

The correlation of fringe patterns having their spectral maximum at the ZPL and the corresponding LiF $vs.$ Φ spectrum is depicted in Fig. 6.5. Plot a) contains the interference patterns with maxima at the ZPL for $\Delta\tau$ = 1, 2 and 3 T_{vib}. In panel b) the phase dependent spectra for the same $\Delta\tau$ are displayed. That value of Φ which was obtained with the interference pattern of plot a) is marked with a cross.

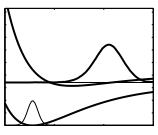

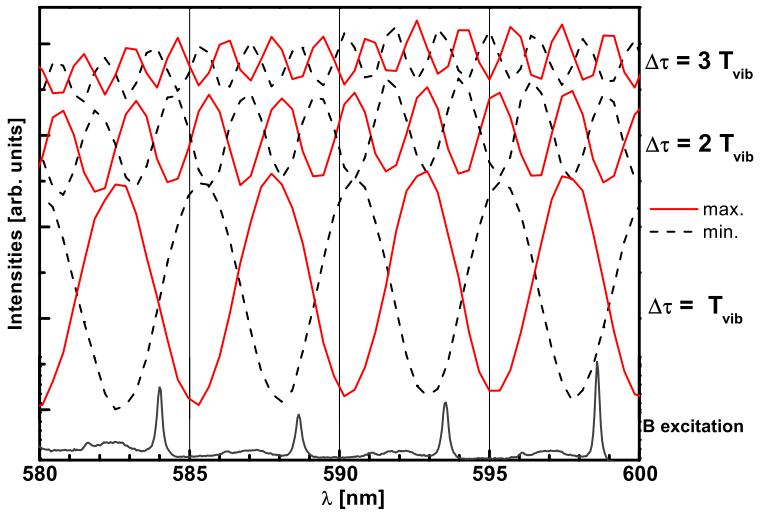

Figure 6.4: Fringe pattern giving maximal molecular absorption (solid line) and minimal absorption (dashed line) for two interfering pulses centered at 590 nm with a time separation of T_{vib}, $2T_{vib}$ and $3T_{vib}$. For comparison the B excitation spectrum is shown as a solid grey line at the bottom. Fringes are plotted with an offset for a better separation.

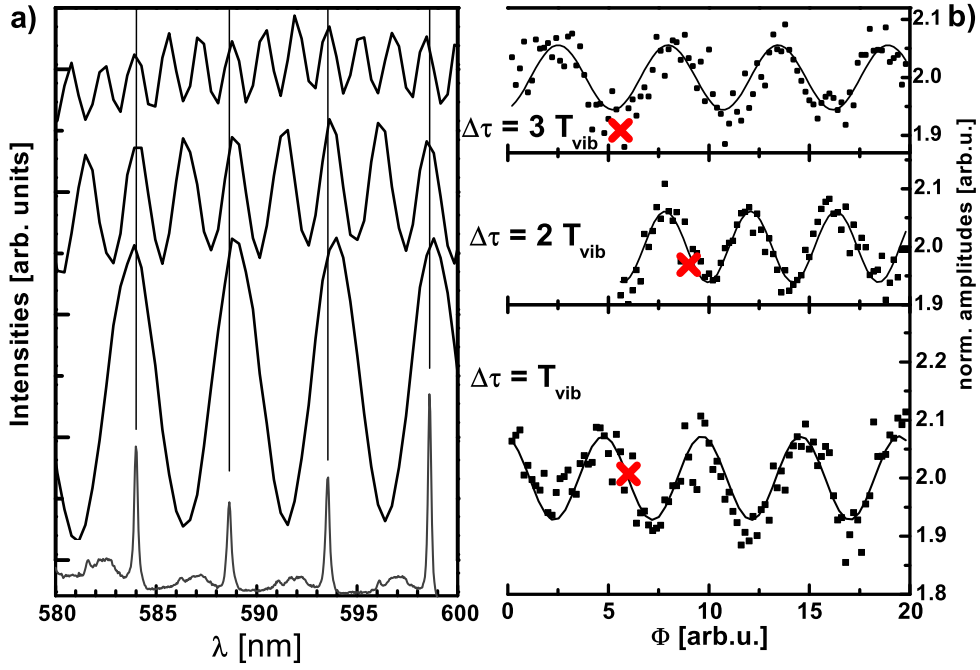

Figure 6.5: a) Sinusoidal spectral fringes obtained by two pulses of the different time delays $\Delta\tau = T_{vib}$, $2T_{vib}$ and $3T_{vib}$ (from bottom to top) with phases fitting to ZPL as can be seen in comparison with the B-state excitation spectrum plotted at the bottom. b) Corresponding LiF (squares) for these fixed time delays $vs.$ phase Φ and sine fits (solid lines). Phase positions of interference patterns of a) are marked with a cross.

6.1.2 Electronic coherence in the PLPP spectra

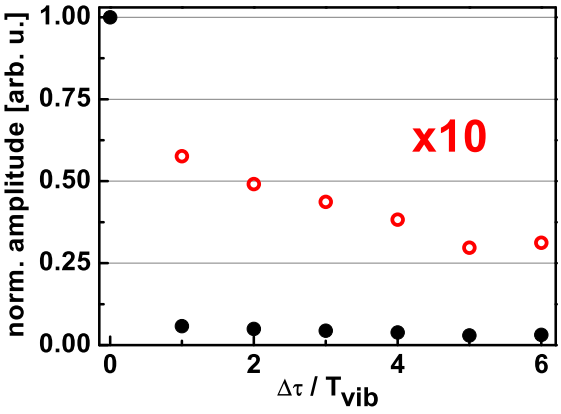

Figure 6.6: Modulation contrasts (Eq. 3.23) of phase dependent signals (*e.g.*, Fig. 6.3) taken at different time delays $n\,T_{vib}$. The amplitude is normalized to the one at $\Delta\tau = 0$ (solid circles) and by a factor of ten magnified (open circles).

Before starting with control experiments which require a coherent superposition of a sequence of pulses lasting for more than one ps, it is desirable to validate that electronic coherence for the investigated electronic transition prevails on such a long timescale. The line width of the ZPL in Fig. 4.7 predicts a lifetime of at least 1 ps at 590 nm. The Michelson test experiments confirm this information.

In these experiments the time delay between the two pulses $\Delta\tau$ was fixed and their relative phase Φ was tuned. When the second pulse interacts with the system, the interference is either constructive ($\Phi = 0$) or destructive ($\Phi = \pi$), related to the ZPL. Thus, the PLPP experiments reflect the absorption step.

The modulation contrast of the B-state fluorescence as in Fig. 6.3a-c is collected in Fig. 6.6 for seven different time delays $\Delta\tau$. The large drop from $\Delta\tau = 0$ to $\Delta\tau = T_{vib}$ is caused by the following fact: In the case of $\Delta\tau = 0$ an observed optical interference of light with a contrast of 0.9 represents the Michelson interferometer quality. This contrast is strongly reduced in the molecule (from $\Delta\tau = T_{vib}$ on and higher) for several reasons. Incoming light is not exclusively absorbed by the B-state, but also by A. The parts absorbed by the A state continuum do not contribute to the interference contrast. Furthermore, population that leaves the B-state via predissociation to a repulsive state or undergoes energy relaxation, does not return to the inner turning point to interfere with the second wave packet.

Strong features of population transfer from the B-state to the lower lying A'-state due to predissociation via repulsive states are observed in the nanosecond excitation spectra shown in Ch. 4. The B-state vibrational progression is detected on the continuum of the A' fluorescence. Since this B-state fraction on the A' excitation spectrum which was interpreted as the complete absorption spectrum of Br_2/Ar in Sec. 4.2 is in the range of 1-2% and the noise level in absorption is much higher, a PLPP dependence is not observed in the detection region of A'-state's fluorescence as shown in Fig. 6.3d.

The PLPP experiment strongly depends on the electronic coherence between the two electronic states since interference can only be observed if coherence is maintained. From vibrational wave packet revivals and focussing experiments in Refs. [2, 21] the vibrational coherence time of Br_2 in solid Ar was determined to be 3 ps. The faster decaying modulation contrast in the PLPP spectrum of the B-state in Fig. 6.6 indicates, therefore, a loss of electronic coherence in the range of $6\,T_{vib}$, corresponding to 1.5 ps for Br_2 in an Ar solid. Indeed, we observe two decays, a very fast one from the first to the second roundtrip time. And a slower one, which persists over 1.5 ps. This is in accord with the linewidth of the ZPL, since this linewidth corresponds to the fastest decay process

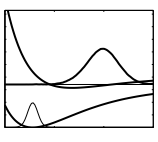

(1 ps at 590 nm), which is usually the electronic coherence. However, the line can additionally be broadened due to inhomogeneous broadening or due to predissociation effects (see Sec. 4.1.2).
For Cl_2/Ar the electronic coherence was observed for more than 660 fs, while the vibrational coherence lasts for more than 3 ps [17].
Finally, the appearance of electronic coherence in the pulse train control experiments will be discussed in Sec. 6.3.4.

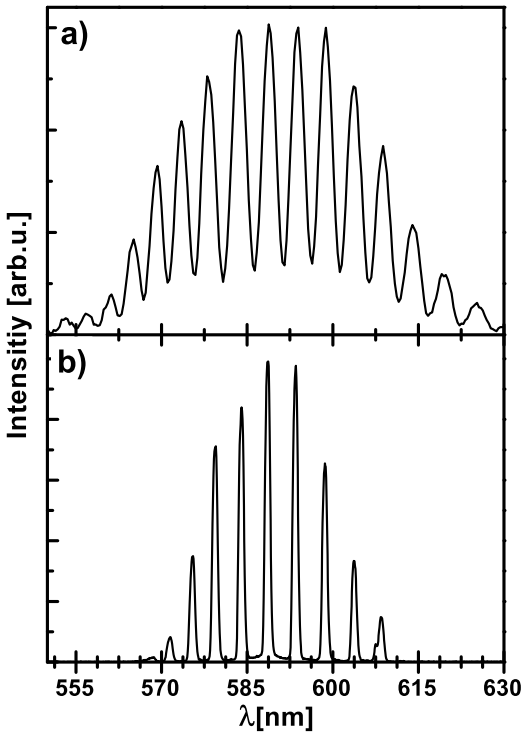

Figure 6.7: Comparison of interferometrically created spectral fringes using a Michelson interferometer a) and a pulse shaper b) with a pulse train of 7 pulses.

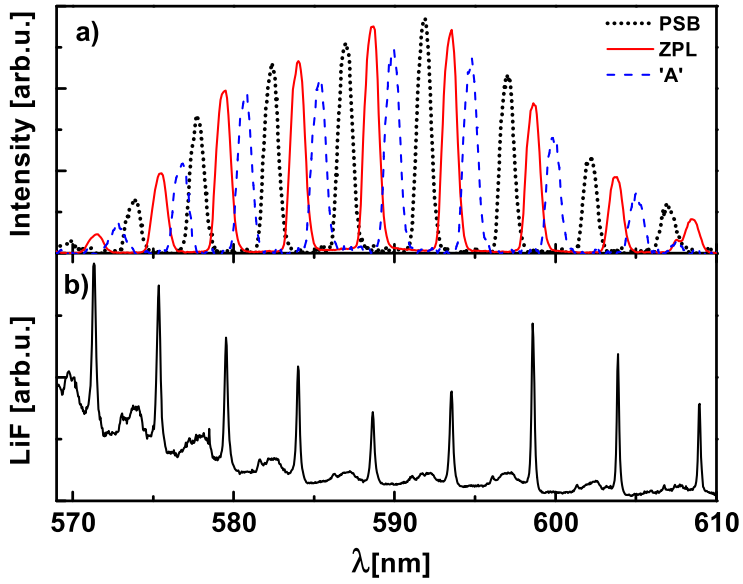

Figure 6.8: a) Three different spectral positions for shaper interferometry patterns created with a pulse train of 7 pulses. Names are given in comparison with the B excitation spectrum in b). Maxima fitting to ZPL are shown as a solid line and to PSB as a dotted one. In between is an unmodulated 'gap' containing no coherent B contributions, therefore this part is labelled "A" (dashed line).

6.2 Advanced solution : Pulse shaper

Challenges and advantages of a computer controlled spatial light modulator were already mentioned in the experimental chapter in Sec. 3.4.2, now the corresponding experiments with phase controlled pulse sequences are presented. Spectral fringe patterns will sharpen with increasing number of interfering pulses, as was shown in the simulation in Fig. 3.15. Figure 6.7 compares the measured pattern generated in a Michelson interferometer in panel a) with fringes obtained by a sequence of seven ultrashort pulses out of a pulse former in plot b). These sharp fringe patterns will be called frequency combs in the following[1].

The FWHM duration of the pulse train was 1.2 ps and its X-FROG trace is shown in Fig. 3.12. One advantage of the pulse shaper is that the phase stability of the sub-pulses does not depend on demanding stability in different optical paths as in a classical interferometer setup. Therefore, a much deeper modulation contrast in a pulse averaged spectrum can be generated. However, one has to keep in mind, that the two spectra in Fig. 6.7 are detected with two different spectrometer devices having different resolutions. As mentioned in Sec. 3.4.1 the contrast of the Michelson interferometer is 0.9 with Eq. 3.23, whereas the one in Fig. 6.7a is apparently reduced to 0.66 by the spectrometer. For the pulse shaper in panel b) the contrast can be determined to 0.99.
The spacing of a) was generated by adjusting $\Delta\tau$ in the Michelson arms and the absolute position of fringes was aligned by varying Φ. For the pulse shaper sequence in b) the phase in the Fourier plane in Fig. 3.10 was not directly manipulated. To obtain the maxima in the frequency comb by amplitude shaping, three pixel were set to full transmittance and the others in between were blocked, completely. In the experiments of this work, three shifted frequency combs were used, as shown in Fig. 6.8. The first one will be called 'ZPL' and is plotted as a solid line in a) with its maxima fitting to the B-state ZPL. The second one 'PSB' (dotted line) matches to the maximum of the broad PSB. A third position shown as a dash-dotted line is labelled with "A" and is situated in between ZPL and PSB where, as discussed for the dye laser experiments, the continuous A-state of bromine is excited. On the bottom of this figure, the B excitation spectrum is plotted for comparison. The following emission spectra are normalised to the area of these fringe patterns. Since they obey different positions relative to the pulse envelope, their relative intensity is different. Due to a linear absorption in the excitation step, a simple normalisation to one of the spectra is sufficient.

6.2.1 Pulse train excitation

First, experiments with such a sharp spectral pattern like shown in Fig. 6.8 were performed, detecting the LiF of covalent states B, A and A' with a cooled CCD camera, like in the dye laser experiments of Ch. 4. But this time, the excitation light source was a coherent sequence of ultrashort NOPA pulses. They interfere on the molecular potential as was discussed schematically in Sec. 3.4.4 and this interference requires electronic coherence. Only a coherent superposition of the wave packets guarantees the development of spectrally sharp features.
Furthermore, a temperature study was done using this setup.

Emission spectra of covalent states

Figure 6.9 contains the emission spectra of the covalent states B and A' in the same spectral region as in Ch. 4. A 1200 l/mm grating was introduced in the monochromator and therefore the spectral range per image is reduced. The graph is organised in two columns containing the two areas of fluorescence wavelength and in three rows for ZPL, PSB and "A" excitation from top to bottom.

[1] The term frequency comb is commonly used for a sequence of peaks being much sharper in frequency and closer together in time than in my experiments, like in an octave spanning oscillator [240].

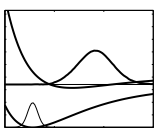

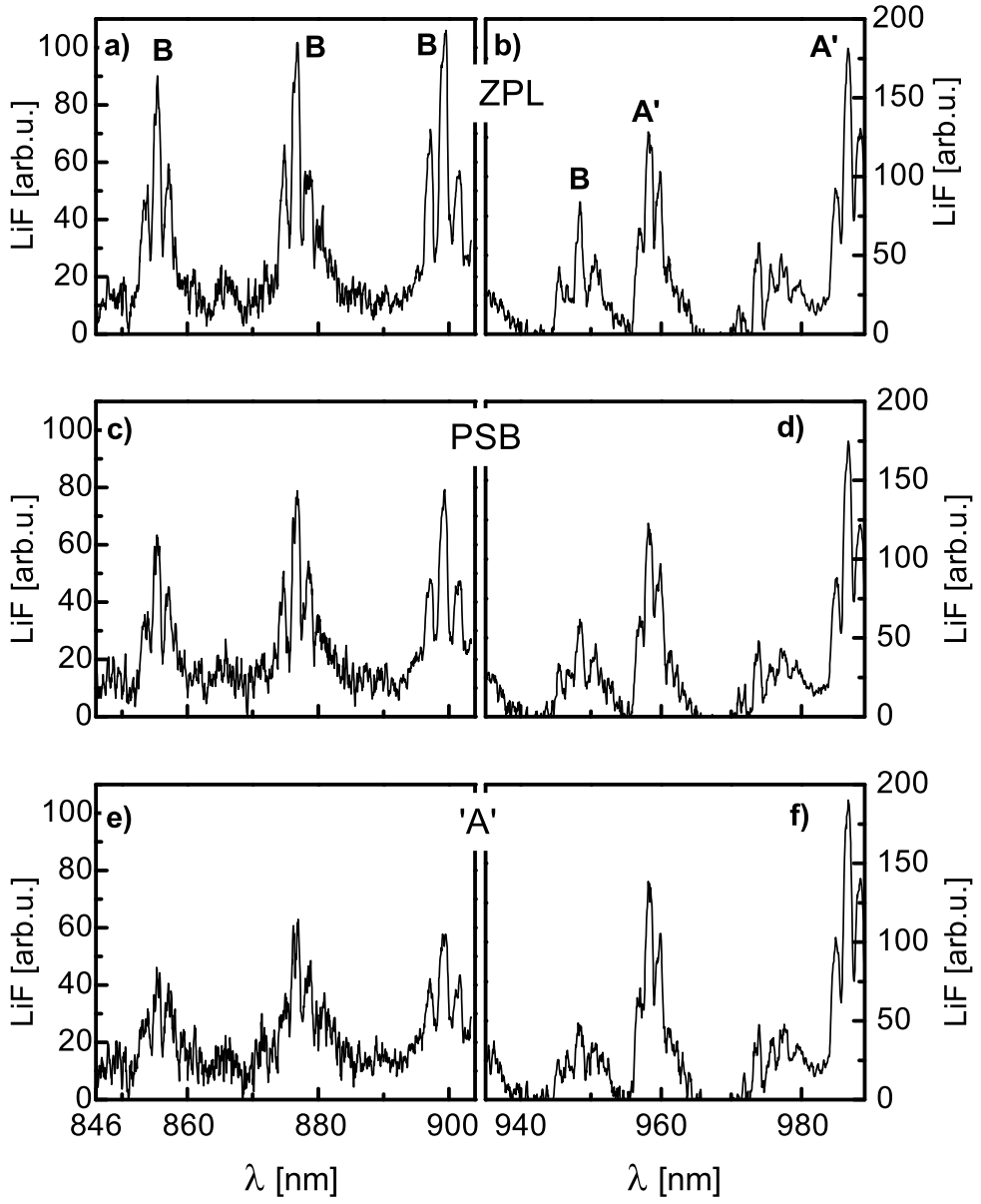

Figure 6.9: Emission spectra of covalent states B and A' with pulse train excitation for the 79/81 isotopomer, following the names in Fig. 6.8 ZPL (a,b), PSB (c,d) and "A" (e,f) for two different wavelength ranges with different scales on the fluorescence axis. Spectral signatures of B and A'-state are labeled, a detailed assignment is given in Fig. 4.2.

With the letters B and A' the main isotopomers 79/81 of these transitions are indicated. A complete spectroscopical assignment is given in Fig. 4.2.

Figs. 6.9a and b) show clearly pronounced parts of B-state emission in the case of ZPL excitation. Those features are strongly affected and reduced by a factor of around 1.5 for PSB excitation in c) and d). If the spectral comb is positioned at "A" in e) and f) the B signature is even weaker and lines are broadened. Emission from the A'-state in b), d) and f) is not affected by the change in excitation, since these peaks have constant heights.

This result was expected, since the chosen spectral fringe pattern match the B-state vibrational progression but excite A and A'-state in the region of continous absorption.

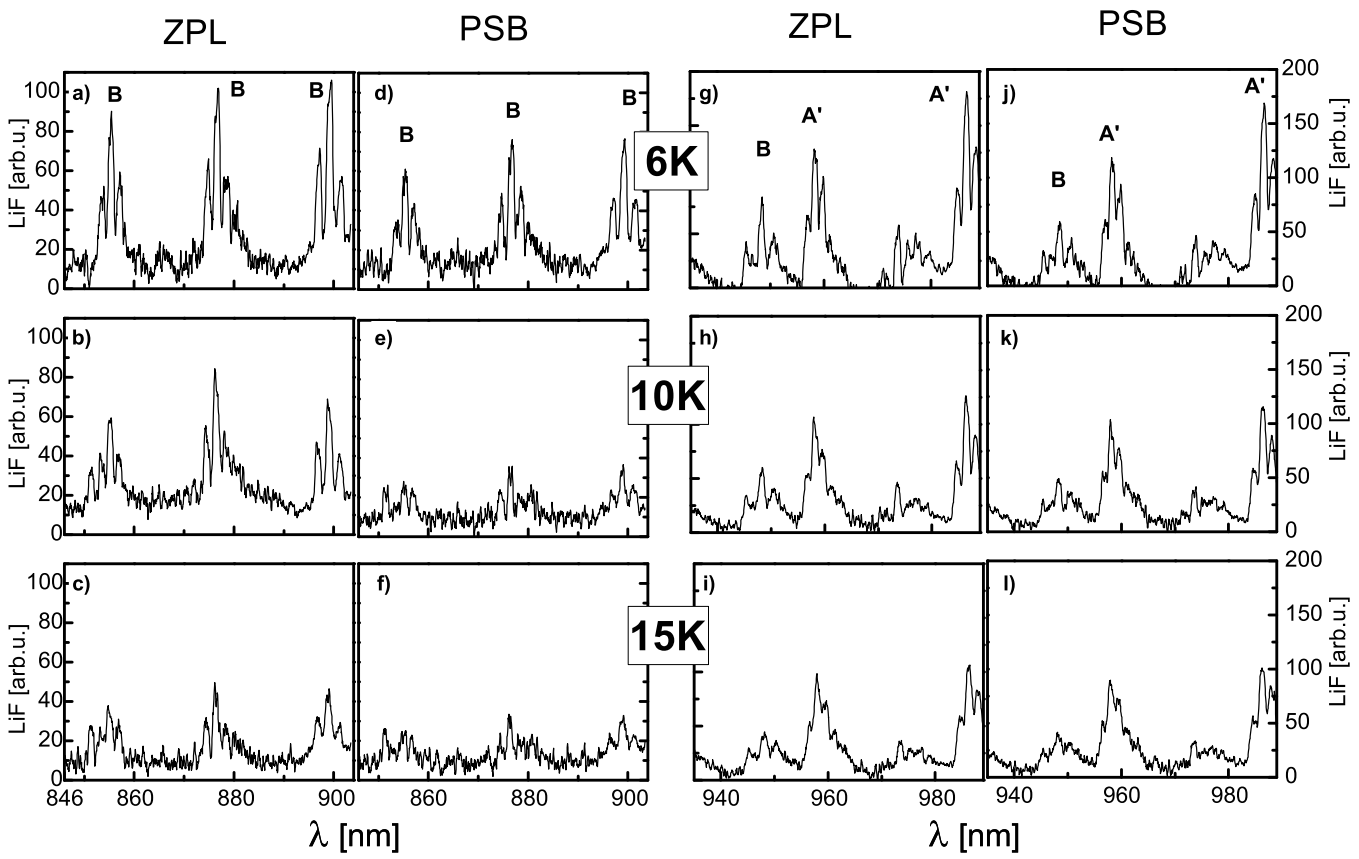

Figure 6.10: Temperature dependence of covalent emission spectra for excitation of ZPL (first and third column) and PSB (second and fourth column) in two different fluorescence wavelength regions. Starting from 6 K in the first row the temperature was increased to 10 K in the second and 15 K in the last line. B and A' emission are labeled.

Temperature dependence

A broadening and shift of ZPL due to higher temperatures was discussed in the context of excitation spectra in Sec. 4.1.3. Now the temperature dependence in emission spectra obtained with pulse trains, like in Fig. 6.8 which selectively excite ZPL and PSB, is investigated in Fig. 6.10. Excitation with a comb matching ZPL is shown in plots a-c and g-i. These spectra with PSB excitation are displayed in d-e and j-l. The temperature was varied from 6 K in the first row to 10 K in the second and 15 K in the third row. All sharp structures of B and A'-state are strongly affected by a change in temperature. In addition, for B-state emission with PSB excitation a stronger extinction of peaks is observed with higher temperatures (Fig. 6.10f). The peak heights of A'-state emission is reduced by a factor of two for a temperature increase from 6 K (plots g and j) to 15K in i) and l). It is not affected by the excitation with different frequency combs.

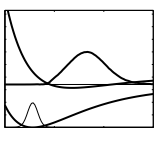

6.2.2 Double pump - probe experiment – time resolved

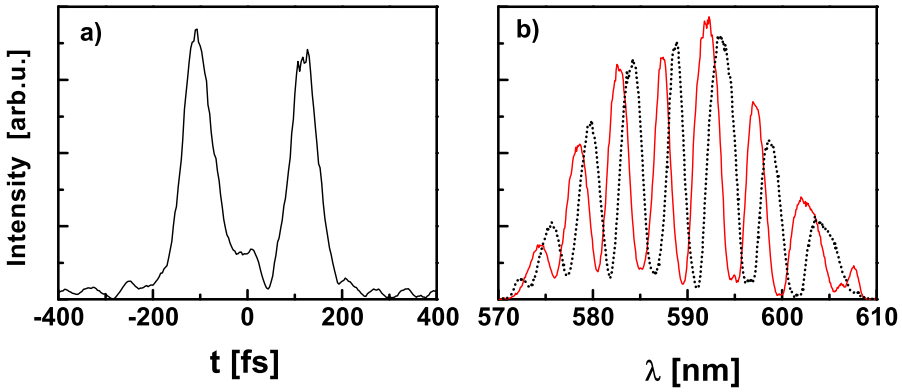

Figure 6.11: a) Cross correlation of double pulse as projection of an X-FROG spectrum to the time axis. b) Corresponding spectral fringes for ZPL (solid) and PSB (dotted line) excitation.

As a first step in time resolved control studies the two phase locked pulses of the Michelson experiment in Sec. 6.1 were combined with a delayed probe pulse. In the experiments with the real Michelson interferometer, fluorescence of the covalent states A' and B was detected. The population initially excited around B ($v' = 9$) relaxes down to $v' = 0$ and from there LiF is recorded. Thus, wave packet dynamics can be deduced, however only in the absorption step due to wave packet interferences at the recurrences which last for multiples of the roundtrip time.

To investigate this wave packet interferometry in a time resolved way and in the upper part of the potential, the double pump experiment was extended by a fs probe pulse. In the following, one NOPA source was split up and used as pump pulse(s) and as probe pulse. The pump pulse pair of two 45 fs pulses with a fixed time delay $\Delta\tau = T_{vib} \approx 240$ fs was created by a combination of amplitude and phase shaping using the spatial light modulator as described in Sec. 3.4.2. Figure 6.11a shows the time representation of the two pulses as projection of an X-FROG trace. In panel b) the spectral representation of the double pulse is plotted for two relative phases. The spectral fringe pattern matching to ZPL has a solid line and the one for PSB is depicted as a dashed line. The shift of the frequency comb cannot be deduced from the intensity $vs.$ time plot of a). This information is kept only with the phases in time domain and can be retrieved from the FROG trace.

Basically, the same parameters like in the pump - probe investigations of Ch. 5 were varied. Fluorescence at 300 nm and 322 nm was recorded and the relative polarisation between all pump pulses and the probe pulse was set to be parallel ($\parallel$) or perpendicular ($\perp$). All spectra were normalised to correct for a signal fading during the experiments which last over more than 20 h. To obtain a consistent series of data it is necessary to utilize data measured at the same day. The results presented in this work were reproduced several times, however, for a better comparability, only one set of spectra is discussed. In general, the signal intensity at $\lambda_{fluor} = 322$ nm was stronger by a factor of 10, compared to $\lambda_{fluor} = 300$ nm. To allow a comparison, as, $e.g.$, between the excitation of ZPL and PSB in the parallel case at the same fluorescence wavelength, the normalisation to unity was done with reference to a strong characteristic peak in the ZPL spectrum and the PSB spectrum was scaled by *the same value*.

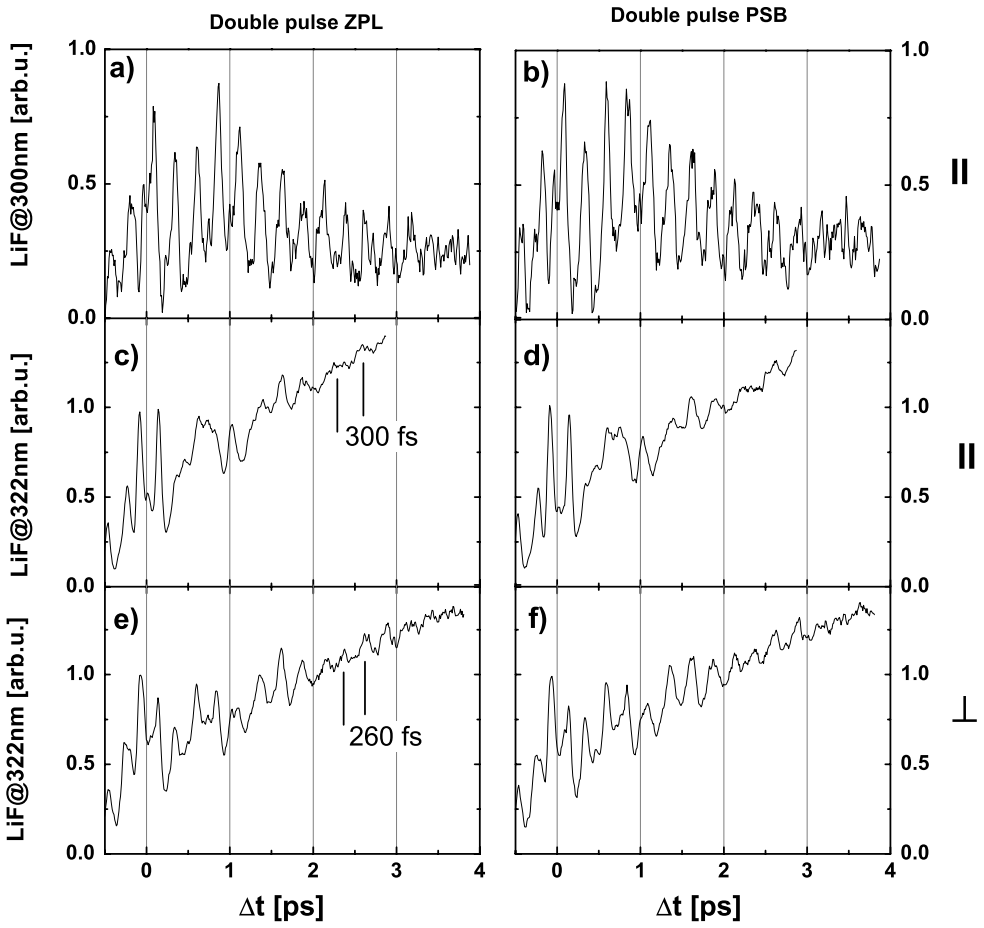

Figure 6.12: Double pump – probe experiment with relative phases between the two pulses being set to optimally excite ZPL (left column) or PSB (right column). Panels a) and b) show fluorescence detected at 300 nm with parallel relative polarisation between pump pulses and probe pulse. Plots c)-f) contain fluorescence from the lower lying CT state recorded at 322 nm, with parallel (c,d) and perpendicular (e,f) relative polarisation.

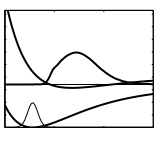

Pump - pump - probe results are shown in Fig. 6.12 which is arranged such, that ZPL excitation is found in the left column and PSB excitation in the right one. In plot a) the excitation with pump pulses adjusted to the ZPL is plotted (Fig. 6.11b, solid line), with pump and probe beams being polarised parallel to each other and recorded at $\lambda_{fluor} = 300\,\text{nm}$. Figure 6.12b includes the excitation comb matching to the PSB and it looks very similar to the spectrum in a).
A characteristic B vibrational period[2] of 260 fs period is present for more than 3 ps. In c) and d) the relative polarisation was parallel as well, but the emission was observed from 322 nm and this leads to very different spectra compared to the fluorescence at 300 nm. Both spectra were normalised to the first strong peak in c) at around 100 fs. The two spectra resemble each other and it is difficult to see clear vibrational signatures of a distinct state. At longer times a period of 300 fs occurs, which can be attributed to the A-state. The first two strong peaks around $\Delta t = 0$ represent the direct response on the double pulse and this will be discussed soon in Fig. 6.13. In the last row in Fig. 6.12 the relative polarisation was tuned to perpendicular and the spectral characteristics changes again. From the very beginning the B-state period of 260 fs is visible, being present for nearly 4 ps. However, it is situated on a strongly modulated background. All spectra, detected with a resolution of 10 fs are averaged over three adjacent data points.

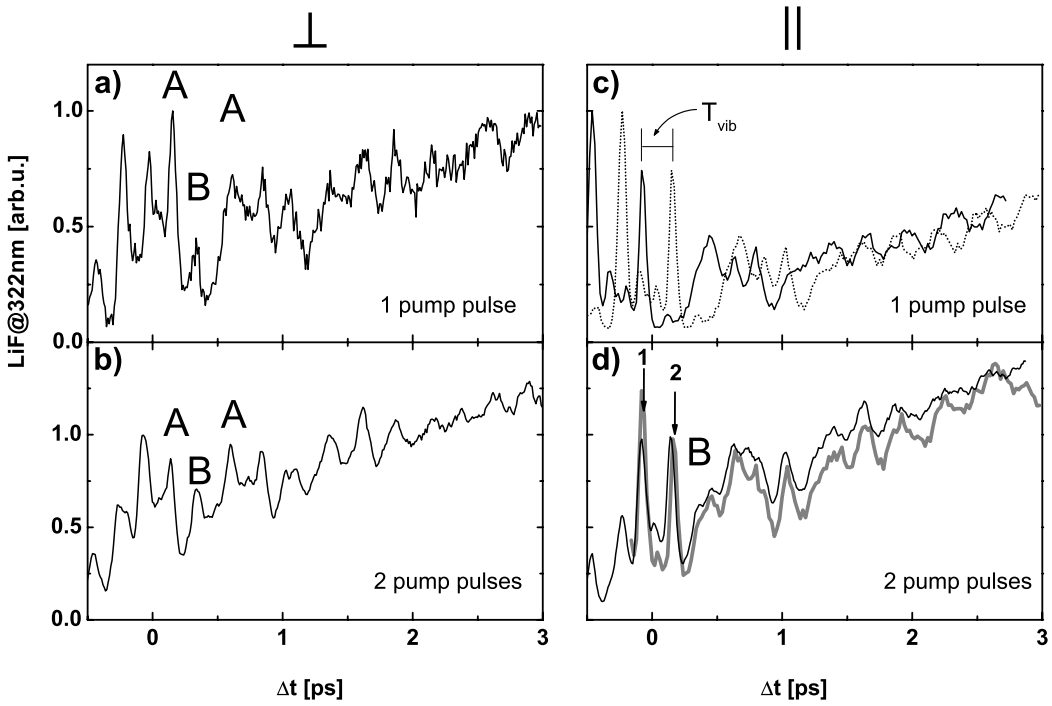

Figure 6.13: Comparison of single pump and double pump - probe spectra at $\lambda_{probe} = 322\,\text{nm}$ with perpendicular (left column) and parallel (right column) relative polarisation. a) Single pump excitation and b) double pump excitation, $\perp$. c) Two identical pump - probe spectra ($\|$), which are time shifted by 240 fs. d) Reconstruction of double pump - probe spectrum as thick grey line and original spectrum with double pulse excitation (thin black line). Details are explained in text.

[2]To give a coarse summary on the main features of different wave packet dynamics at $\lambda_{pump} = 590\,\text{nm}$: The B-state is characterised by a constant period of 260 fs. The A-state, excited above the gasphase dissociation limit shows a strong peak at $\Delta t = 100\,\text{fs}$, followed by a deep valley lasting for around 600 fs. Subsequently a 300 fs period occurs. All time resolved spectra discussed here show a superposition of A and B dynamics with weak A contributions at $\lambda_{fluor} = 300\,\text{nm}$ and weak B signature at $\lambda_{fluor} = 322\,\text{nm}$. Details are discussed in Sec. 5.2.

How does the superposition of two wave packets with a delay corresponding to one roundtrip time modify the transient signal, compared to the single pump - probe experiment? Figure 6.13 shows the two different relative polarisations and the ZPL spectra at $\lambda_{fluor} = 322\,\text{nm}$. Panel a) repeats the perpendicular single pump spectrum from Fig. 5.3c) and three characteristic peaks are assigned to A and B-state dynamics. This is compared with the double pulse spectrum from Fig. 6.12f in Fig. 6.13b. By applying two pulses matching to the B-state vibrational progression one expects an enhancement of B contributions and this is clearly visible: Comparing the heights of the B peak with the first A peak in a) leads to a ratio of 1:3. In panel b) this ratio has equalised to 1:1.5, thus B population growths in higher powers than linear. A - contributions, however, increase not more than linear.

Another distinctive feature is the signal difference at negative time delays. In a single pump - probe experiment the first laser pulse is called pump, the second one probe. However, for two identical pulses their roles are interchanged at negative times and this is nearly fulfilled in a). The spectrum is not perfectly symmetric around $\Delta t = 0$, but dominant peaks occur on both sides. Splitting up the pump pulse into a sequence of pulses violates the identity of pump and probe, since the energy of one pulse is now spread over two or more pulses. From the intensity dependence analysis of Sec. 5.1.2 we know, that the probe step requires at least two photons. Reducing the energy of the sub-pulses of the pulse sequence causes a smaller probability of the probe transition. Thus the signal at negative times in Fig. 6.13b is weaker than at positive times.

The double pulse spectrum taken at parallel relative polarisation in Fig. 6.12c shows a more complex time devolution due to dominant A-state dynamics. For a deeper understanding of its single contributions it was "recreated" from the single pump - probe spectrum in Fig. 5.1c. This spectrum is depicted twice in Fig. 6.13c as solid and dotted lines with a time shift of $\Delta t = T_{vib}$. The original double pump probe spectrum is included in d) as thin black line, together with the sum of the two spectra of c) as thick grey line. Two arrows mark the first response of the pump pulses 1 and 2. All main features of the real double pulse spectrum at positive time delays are reproduced by the constructed spectrum and this clarifies, that an enhancement of B contributions due to constructive interference (marked with B) is hardly visible for the parallel setup, since its appearance is small.

In general, the excitation with only two coherently controlled pulses fitting to ZPL of PSB at an excitation wavelength of around 590 nm is not sufficient to cause strong differences in the pump - probe spectra in the case of Br_2/Ar. It is necessary to superimpose a larger number of pulses to observe a remarkable effect, as will be done in the next section.

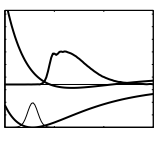

6.2.3 Pulse train pump - probe experiment

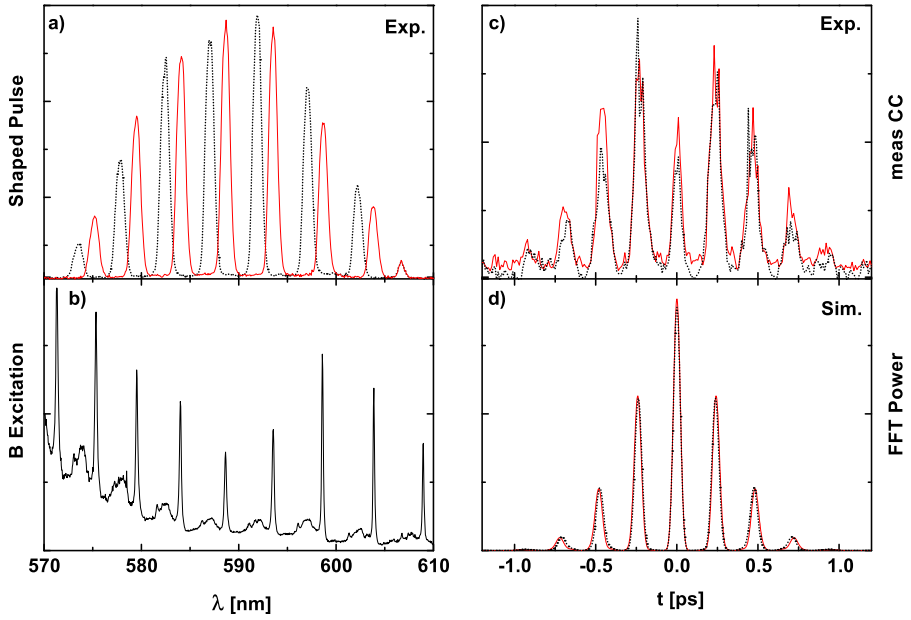

Figure 6.14: a) Spectral representation of the pulse train, matching the ZPL (solid line) or PSB (dotted line). b) B-state excitation spectrum. c) Time representation with measured and d) simulated cross correlation of the pulse train for ZPL (solid line) and PSB (dotted line).

The pump pulse pair was extended to a pulse train as depicted in Fig. 6.14. Panel a) contains the spectral combs of these pulse sequences for ZPL (solid line) and PSB (dotted) excitation, related to the B-state excitation spectrum in plot b). In the right column the intensity $vs.$ time representation of this pulse train is given. Graph c) shows a measured cross - correlation as projection on the time axis of an X-FROG trace with a FWHM of 1.2 ps. This is compared in d) with a power spectrum of the Fourier transformation of the interference pattern of b). In the simulated time course as well as in the experimental one, no significant difference between ZPL and PSB excitation is observable, as expected. The relative phase in the time domain is reflected in a spectral shift of the frequency combs in a). It is invisible in the intensity $vs.$ time plot of c) and d). The reconstruction of those phases will be an important part of the discussion in Sec. 6.3.1.

The measured pulse train in the time domain is repeated in Fig. 6.15a and its centre is chosen at $\Delta t = 0$. However, this value is only a point of reference, since several sub-pulses already excited the molecule at this time. First, the transient signal with excitation matching to the ZPL was recorded in b) at $\lambda_{fluor} = 300\,\text{nm}$ and with parallel relative polarisation. The spectrum contains nearly pure B-state wave packet dynamics of 260 fs which is again visible up to 4 ps. In comparison to the single pump - probe experiment in Fig. 5.1c or the double pulse excitation in Fig. 6.12e, the oscillations at longer times are much more pronounced in Fig. 6.15. The pulse train in a) starts around -1 ps and at this time no LiF from the CT states is observed. As long as the sequence persists, the amplitudes of the B peaks increase continuously up to +1 ps. With every pulse wave packets are created which interfere constructively and the signal growth appears stronger than linear.

The trend of a non - symmetric behaviour between pump and probe pulses, discussed in Fig. 6.13, proceeds. At negative time delays, when the strong "probe" pulse precedes parts of the pulse train an interchange of pump and probe roles takes place. However, a weak pump pulse

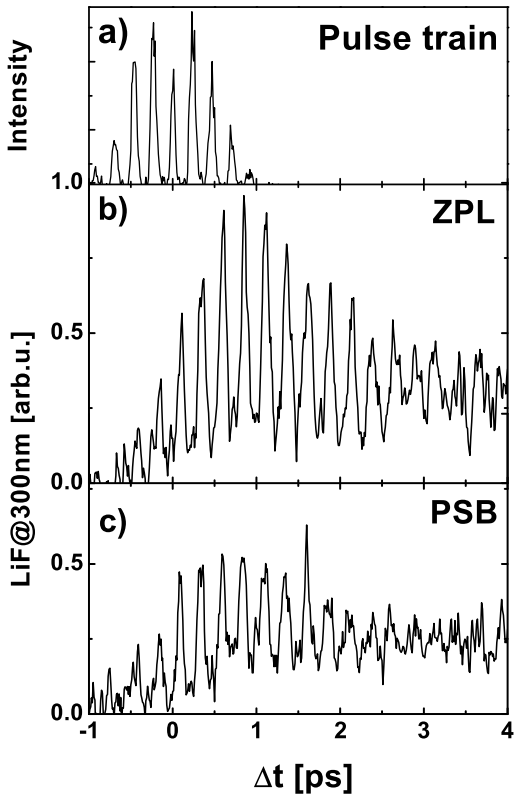

Figure 6.15: Pulse train (a) experiments at $\lambda_{fluor} = 300\,\text{nm}$ with ZPL (b) and PSB excitation (c) for parallel relative polarisation between pump pulse train and probe pulse. For details, see text.

of the sequence is not able to perform a multi photonic probe step anymore. In the PSB case in Fig. 6.15b the B period is again very clearly observable. The absolute height of the B peaks is reduced by a factor of two. Since the intensities of ZPL and PSB spectra in a) and b) are directly comparable, both spectra were normalised to the highest ZPL peak.

Figure 6.16 shows results for the lower fluorescence band at 322 nm. An oscillation with 250 fs, changing to 260 fs at longer Δt, is observed in parallel configuration with ZPL excitation (plot a). As a first attempt, this can be interpreted as B wave packet dynamics. It is situated on a strongly increasing background which can be understood as the incoherent superposition of A contributions, excited with each of the sub-pulses of the pump sequence having a time delay of 250 fs.

This merging of A features was already observed in the double pulse experiments in Fig. 6.12. A resolvable wave packet propagation continues up to 3 ps for ZPL excitation in a) and for 2 ps in the PSB case of b) which is both times longer than the FWHM of the pulse train, given in Fig. 6.14c. For ZPL excitation in a) a signal of 1.60 was reached after 3 ps by the increasing background. In the case of PSB in plot b) it has increased to 1.85.

In this experiment also the third spectral position of the frequency comb, labelled "A" was applied and the pump - probe spectrum is shown in Fig. 6.16e. Here, neither ZPL nor PSB are contained and wave packet dynamics could be observed only during the presence of the pulse train. In the right column the relative polarisation was changed to perpendicular. Plots d)-f) show essentially the same behaviour as in the parallel case, however with a much stronger B wave packet modulation contrast. The overall background is smaller and reaches nearly the same value for all three kinds of excitation. Only the excitation with the pulse train matching the continuous A contributions in f) leads to a weak signal to noise ratio. All spectra were normalised to the ZPL peak at 500 fs, parallel spectra (a-c) and perpendicular ones (d-f) treated separately.

The detailed analysis on the observed oscillation periods is given now. A closer inspection

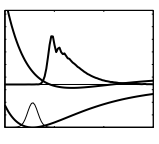

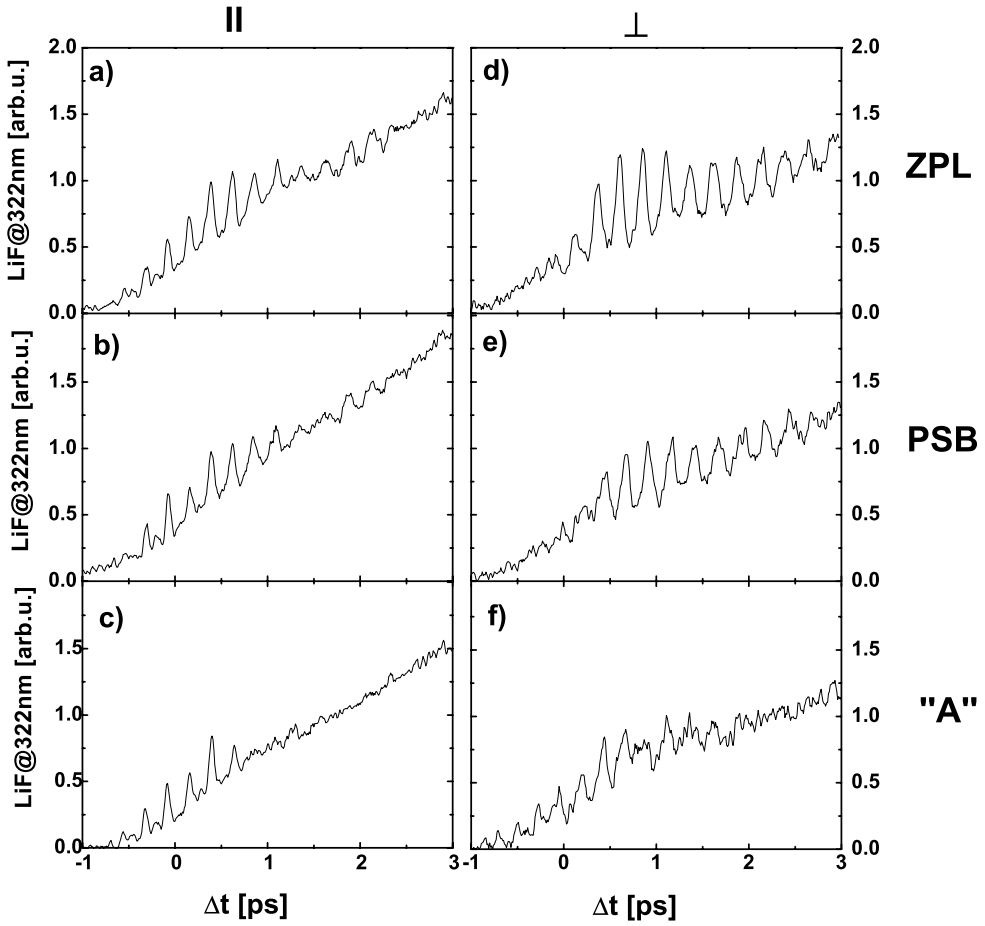

Figure 6.16: Pulse train excitation with $\lambda_{fluor} = 322\,\text{nm}$ for three different spectral positions: ZPL (first row), PSB (second row) and "A" (third row), with parallel polarisation in the left column and perpendicular polarisation in the right one. Parallel and perpendicular spectra were normalised separately to the 500 fs peak with ZPL excitation. Details are given in the text.

of the pulse train excitation spectra in Figs. 6.15 and 6.16 uncovers a relative displacement in the periods for the 300 nm and the 322 nm spectrum. This is shown in Fig. 6.17 for the three excitation combs ZPL in a), PSB in b) and "A" in c) with parallel relative polarisation between the pump pulse train and the probe pulse. The fluorescence signal at 300 nm is shown as a dotted line. From the single pump - probe experiments we know, that the 300 nm fluorescence delivers exclusively B-state wave packet dynamics. The spectra for ZPL and PSB excitation are nearly identically and their maxima from 1 ps on are marked with the dashed vertical lines. The 322 nm spectra, plotted as solid lines also coincide in their periods from 1 ps on, as can be seen in comparison with the solid vertical lines. For "A" excitation in c) the oscillations die out when the pulse train has ended (the centre pulse of the pump sequence is located at 150 fs), but for ZPL in a) and PSB in b) a regular dynamics is observed for more than 2 ps. Comparing this period for longer times with the one of the dotted line with B dynamics, shows a nice agreement. During the presence of the pulse train, however, the solid and dotted spectra clearly deviate. The period below 700 fs in case of

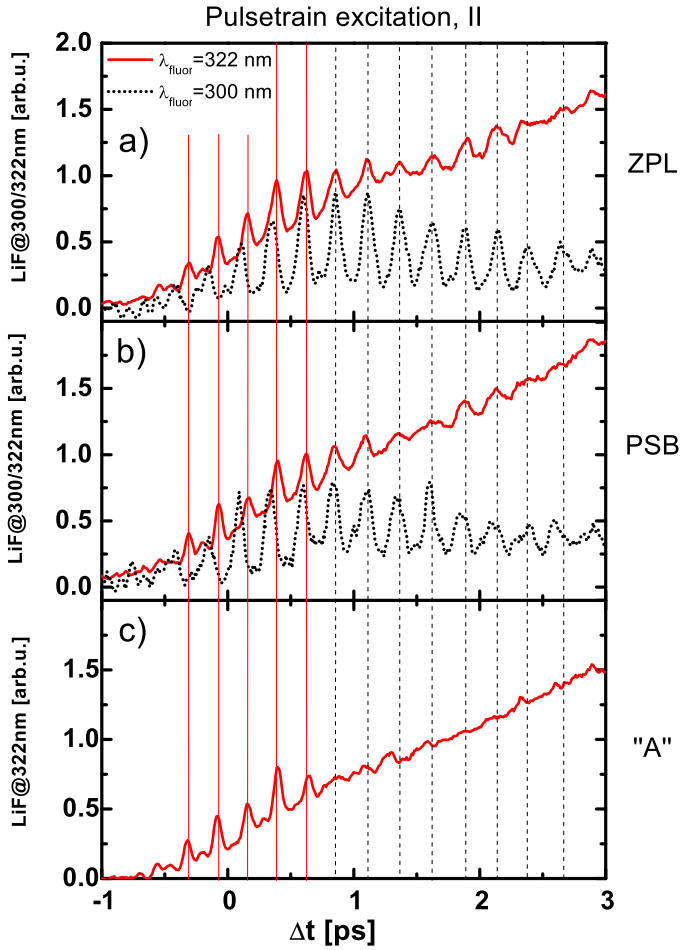

Figure 6.17: Comparison of pulse train spectra in parallel configuration. a) With ZPL excitation, b) with PSB excitation and c) with the pulse train centred at position "A". Fluorescence at 300 nm is shown as a dotted line, the one from 322 nm as solid line. Solid vertical lines < 700 fs are positioned on the maxima of 322 nm spectrum, dashed vertical lines match to the maxima of 300 nm spectrum at later times.

$\lambda_{fluor} = 322\,\text{nm}$ is attributed to the direct response to the incoming light pulses from A-state, or maybe also from repulsive states, as was discussed in Sec. 5.2. The B-state, which is preferentially excited with the ZPL (and also PSB) pulse trains, first has to develop due to the constructive interference of the subpulses. The more pulses contribute, the closer the period in the 322 nm case and the one at 300 nm merge together, until they run in an indistinguishable way from 700 fs on.

Observing the fluorescence at 322 nm yields stronger B contributions in the case of perpendicular relative polarisation than for the parallel setup. Figure 6.18 indicates a different trend for $\lambda_{fluor} = 300\,\text{nm}$. In a) the frequency comb matches to ZPL and in b) to PSB. The signal to noise ratio is weaker than in the parallel case in Fig. 6.15. However, the traces are similar. A stronger modulation is visible in the background in Fig. 6.18 and the B period vanishes earlier than in parallel configuration, namely around 2.5 ps. Currently, we can only ascertain the difference, that emission from the higher CT manifold contains stronger B contributions for parallel relative po-

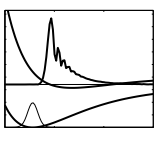

larisation, while in the lower CT manifold B is enhanced relative to A in the perpendicular setup. Clarifying the differences in polarisation dependence is part of the remaining open questions.

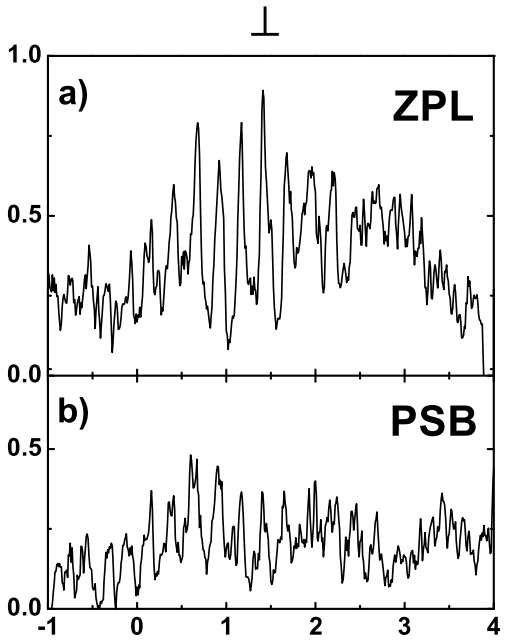

Figure 6.18: Pulse train experiments at $\lambda_{fluor} = 300\,\text{nm}$ with ZPL excitation in a) and PSB excitation b). The relative polarisation between pump pulse train and probe pulse was perpendicular.

The behaviour on a longer timescale up to 8 ps of pump (train) - probe spectra is plotted in Fig. 6.19. In a) and b) single pump - probe spectra are included for comparison. Their signals at short times were already discussed in chapter 5. Both spectra are normalised to the first strong peak around 100 fs. In case of the pump - probe spectrum in a), the A-state dynamics, visible at short times, vanishes around 4 ps. At longer times a 500 fs period appears which persists up to 8 ps. Such a long lasting modulation of the pump - probe signal had been observed earlier [96] and was assigned to the zone boundary phonons excited in the Ar matrix. The single pump - probe spectrum with perpendicular relative polarisation in b) is very noisy, and therefore the weakly modulated 500 fs period at long times is not observed. This background reaches a maximum at 5 ps.

The other spectra show a maximum between 4.2 and 4.8 ps. The climax is reached, however with different slopes and different heights for ZPL comb excitation in c) and d) and PSB comb in e) and f). In this set of data the maximum of the PSB spectra was used for normalisation and the ZPL spectra are related to it. Comparing the parallel cases, the signal increases rapidly for the excitation of PSB in e) until the maximum of 1 is reached at 4.2 ps. Afterwards, the signal decreases with the a slightly weaker slope. The ZPL spectrum in c) climbs up slower and the maximum is already achieved at a height of 0.85 but 600 fs later than in the PSB case. The adjacent signal decay is again slower than the increase was and also slower than for PSB excitation in e). For the perpendicular investigation in d) and f) no difference in maximum height and slope could be observed, comparing the absolute values. Related to the modulated structure at short times, the PSB background would be higher than the ZPL one.

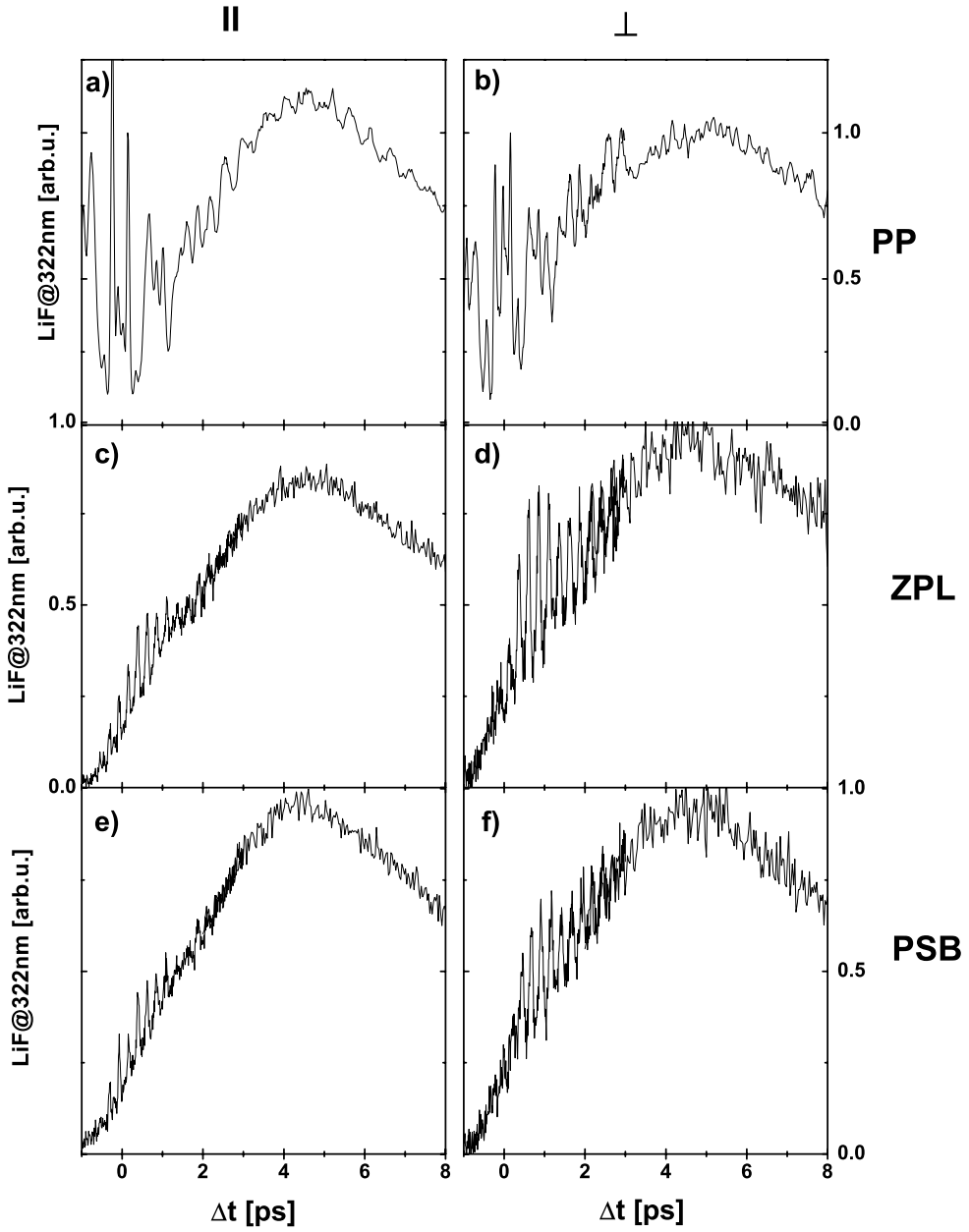

Figure 6.19: Long time study up to 8 ps with coarse resolution for $\lambda_{fluor} = 322\,\text{nm}$ and $\lambda_{pump} = \lambda_{probe} = 590\,\text{nm}$. Again, the left column includes parallel data and the right column the perpendicular one. Plots a) and b) show single pump - probe spectra of Ch. 5 obtained at 9 K. Pulse train excitations for ZPL maxima are given in plots c) and d) and for PSB in plots e) and f) and the temperature was 6 K.

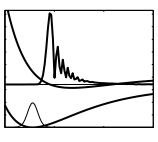

6.3 Discussion of control experiments

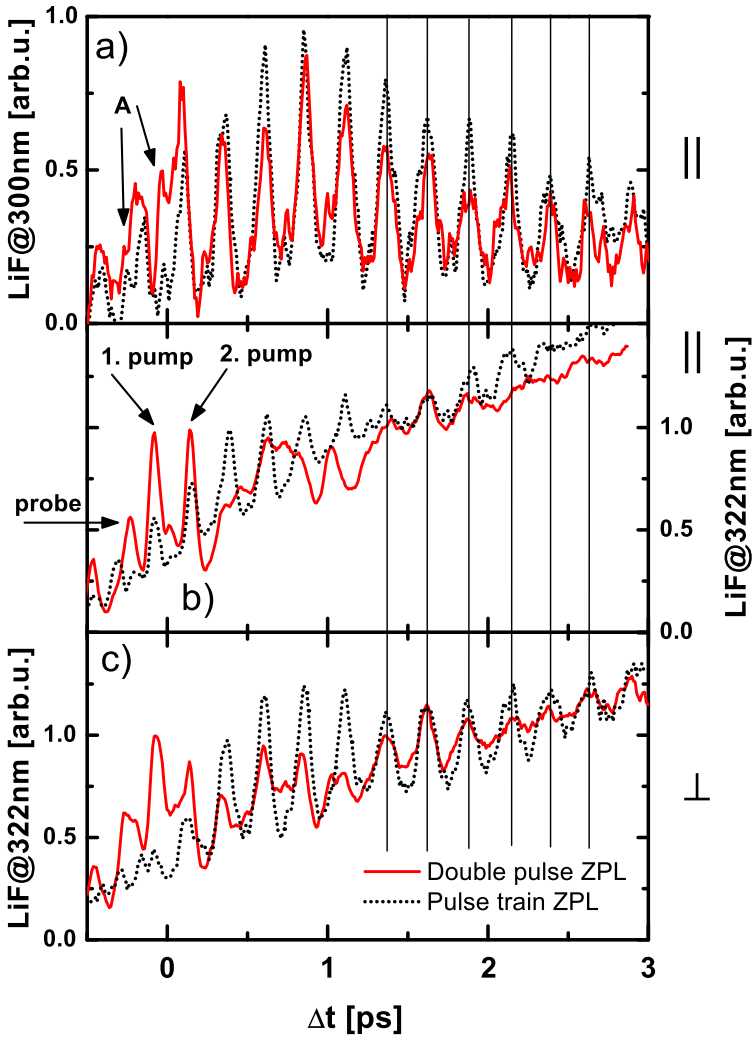

Figure 6.20: Comparison of double pulse (solid line) and pulse train excitation (dotted line), both matching to ZPL excitation in parallel configuration. A detailed description is given in the text.

The time resolved double pulse experiment of Sec. 6.2.2 plays a mediator role in between the single pump - probe experiment of Ch. 5 and the pulse train excitation of Sec. 6.2.3. With a single pump pulse it was not possible to clearly observe B vibrational wave packet dynamics at $\lambda_{fluor} = 322\,\text{nm}$. With perpendicular relative polarisation the B signature was always better visible than for the parallel setup. For the excitation with a ZPL pulse train, wave packets are created, which are predominantly composed of B-state vibrational components and thus the B period is clearly observed. Underlying A-state dynamics adds up to an unmodulated background. Figure 6.20 now includes a comparison of double pump excitation (solid line) and the pulse train (dotted line) with both spectral combs matching the ZPL. It reveals the development of B dynamics with increasing number of interfering pulses. In a) both spectra show the same B-state periodicity of 260 fs for parallel relative polarisation with $\lambda_{fluor} = 300\,\text{nm}$. For double pulse excitation the background contains a stronger A dynamics and the pulse to pulse signal increase is weaker than in the pulse train case, since only two pulses interfere. The peak shortly before 1 ps in the solid line is artificially enhanced due to the increasing background. At -270 and -30 fs two arrows indicate

the direct response to the double pulse and are labeled with "A".

In the case of 322 nm fluorescence in b) mainly A dynamics is observed. The first passage of the A-state probe window of the 1. and 2. pulse is marked with the two arrows. A third pulse at -230 fs is tagged as "probe"; it is caused by an interchange of pump pulse and probe pulse, discussed with Fig. 6.13. The signal is weaker, since the halved pump pulse now holds the probe role. The peaks 1 and 2 of the double pulse spectrum are the only ones, matching to the pulse train spectrum. The double pulse spectrum mostly consists of the superposition of two time shifted pump - probe spectra, as was depicted in Fig. 6.13, while the pulse train excitation shows pronounced B dynamics, coinciding with the one in a) which is indicated by the vertical lines. In the case of perpendicular relative polarisation in c), even two pump pulses already enhance the B-state relative to the A dynamics. For perpendicular polarisations the A-state is suppressed and therefore, the B-state can be prepared out more effectively.

6.3.1 Phase reconstruction

Reconstruction of relative phases between two pulses

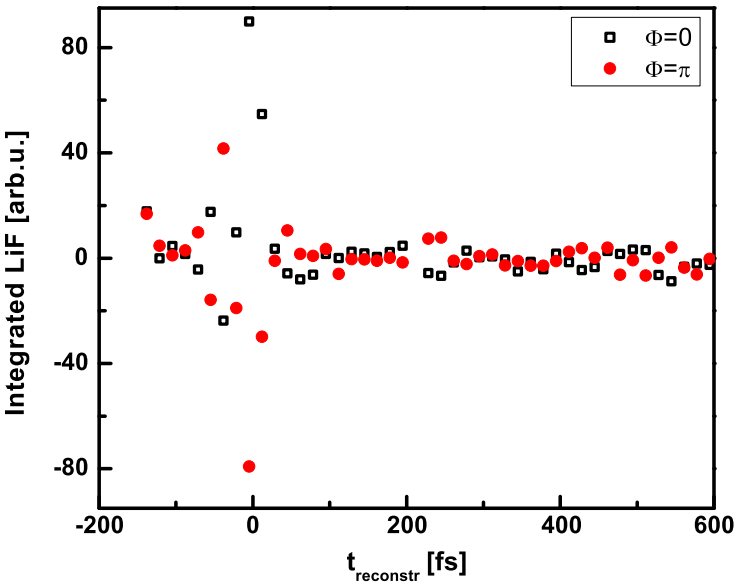

Figure 6.21: Phase reconstruction from measured PLPP fluorescence spectra and interferometric spectral fringes.

An understanding of coherent control experiments using a sequence of two or more pulses depends on the knowledge about the relative phases between two neighbouring pulses.

For the Michelson experiments of Sec. 6.1 the phases can be deduced from the recorded spectral fringes. Their reconstruction and also simulations enlightening the role of ZPL and PSB contributions are discussed now. Concerning the pulse train experiments of Sec. 6.2 the phases are reconstructed mainly using Fourier transformations.

Even if the phases are not locked during the Scherer - type experiment, it is possible to deduce the relative phases Φ between the two pulses, afterwards. For every combination of phase and time delay $\Delta\tau$ the experimental spectral fringes are recorded. We know, that the piezo drive changes the relative phases between the two pulses continuously. The only unknown parameter is the starting point of the sinusoidal phase cycle, since each variation of $\Delta\tau$ with the step motor causes a shaking of the optical table. A reference point for the fringe patterns is the maximum of the spectral envelope, which is called the locking frequency. Now, all other phases could be sorted in connection to this reference point. Then, in case of the $\lambda = 590\,\mathrm{nm}$ experiment the measured spectrum in Fig. 6.2 transforms to that in Fig. 6.21. The two phases delivering maximal ($\Phi = 0$

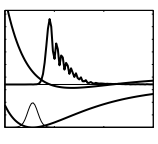

as open squares) and minimal ($\Phi = \pi$ as circles) LiF signal, related to $\Delta\tau = 0$, are given as an example. Beyond 600 fs the measured spectral fringes show a weak contrast due to the limited resolution of the spectrometer and the phase sort algorithm is no longer reliably. Surprisingly, the two phase traces cross several times, $e.g.$, twice at the first recurrence. In the experimental introduction in Fig. 3.13 a clear accordance of upper and lower LiF envelope to $\Phi = 0$ and $\Phi = \pi$ was mentioned. This holds for the excitation of a free molecule with unchirped laser pulses. For more complex systems, like a chromophore embedded in a matrix, always a mixing of ZPL and PSB excitations occurs. A minimum at the ZPL leads to maximal excitation of PSB and vice versa. Therefore fringe positions "in between" can deliver maximal and minimal fluorescence signal and upper and lower traces might cross several times. This is also evident in the fringe patterns in Fig. 6.4.

Simulation of double pulse experiments

The Scherer - type experiment in Fig. 6.2 can be simulated by a multiplication of the spectral fringes ($e.g.$, in Fig. 6.4) with the bromine excitation spectrum (4.5), for each time delay $\Delta\tau$ and each relative phase Φ. A subsequent summation over all wavelengths gives one data point in the simulation for the specific time and phase in Fig. 6.22

$$I_{sim}\left(\Delta\tau, \Phi\right) = \sum_{\lambda} Spectral\ fringes\left(\Delta\tau, \Phi\right) \cdot Excitation\ spectrum. \tag{6.1}$$

For the simulation, calculated spectral fringes were used since experimental fringes were not recorded with sufficient resolution. Therefore the obtained modulation contrast of the computed spectra is too optimistic compared to the real interferometric experiment. The calculated spectral fringes in all simulated spectra were obtained by a Fourier transformation of two laser pulses at different time delays Δt, the first pulse with negative chirp $\beta_1' = -0.3$ fs cm, the second one unchirped. Both pulses were centred around 590 nm and had a spectral width of 40 nm. In the simulations, three different excitation spectra were used to clarify the contribution of an incoherent background to the signal. These excitation spectra are shown in the inset plots Fig. 6.22b, e) and h). In panel a) the simulated PLPP signal for 32 relative phases between 0 and 2π related to the ZPL at 589 nm was obtained by multiplying the fringes with the excitation spectrum shown in b) which is a low energy cut-out of the B-state excitation spectrum in Fig. 4.5, where the background of PSB has not yet developed. The pronounced vibrational recurrences occur in delays of $T_{vib} = 240$ fs. In c) the traces of two distinct phases are shown enlarged in signal, namely $\Phi = 0$ which delivers a maximal signal at $\Delta\tau = 0$ (thick line) and $\Phi = -\pi$ for a minimal signal (thin line). The two spectra reflect the envelope of the spectrum shown in a). Before the first recurrence at $\Delta\tau = 240$ fs more complex structures occur, which are attributed to the chirp of the first laser pulse as was discussed in Ref. [18]. These simulation of a) is artificial in that way, that the used excitation spectrum of b) is far away from the real B excitation spectrum, where an increasing background dominates at higher energies. The real spectrum was used in the second row and is shown in e). The calculated LiF signal in d) has a reduced contrast compared to a) and the modulation drop-down from $\Delta\tau = 0$ to $\Delta\tau = 240$ fs is stronger by a factor of about two. The reason for that is the unmodulated excitation background which does not depend on the applied phase. The Fourier transformation of a spectral continuum leads to a peak at $t = 0$ which is observed here. In the spectrum with identified phases in Fig. 6.22f the distribution has become more complicated, compared to c). Maximum and minimum at $\Delta\tau = 0$ are plotted with thick and thin solid line for the relative phases $\Phi = 0$ and $\Phi = \pi$. For the first recurrence the assignment between envelope and phase is possible, but for later times the two curves cross each other several times. Intuitively, the simulation with the whole B-state excitation spectrum in Fig. 6.22b would be the right choice to reproduce the experimental situation.

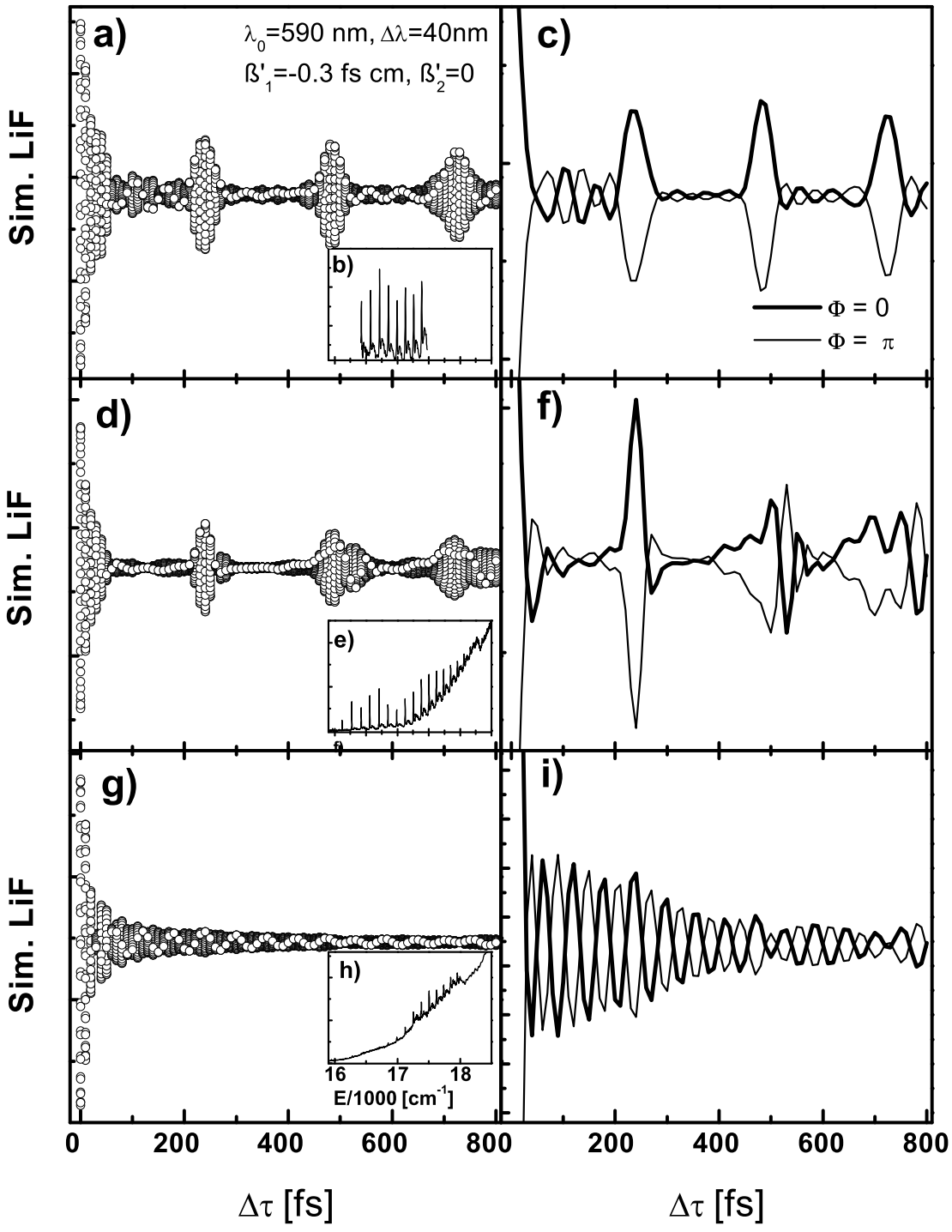

Figure 6.22: Simulation of Scherer - type experiment by multiplication of simulated spectral fringes and Br_2/Ar excitation spectra. The simulation applying the cut-out of the B excitation spectrum of b) is shown in a) for 32 different phases (open circles) covering 2π. In c) an enlargement for two special phases, $\Phi = 0$ giving maximal (thick line) and $\Phi = \pi$ minimal (thin line) signal at $\Delta\tau = 0$. Analogously, the second row contains the simulation for the full B excitation spectrum, plotted in e). In the last row the A' excitation spectrum of h) was used.

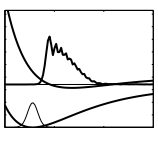

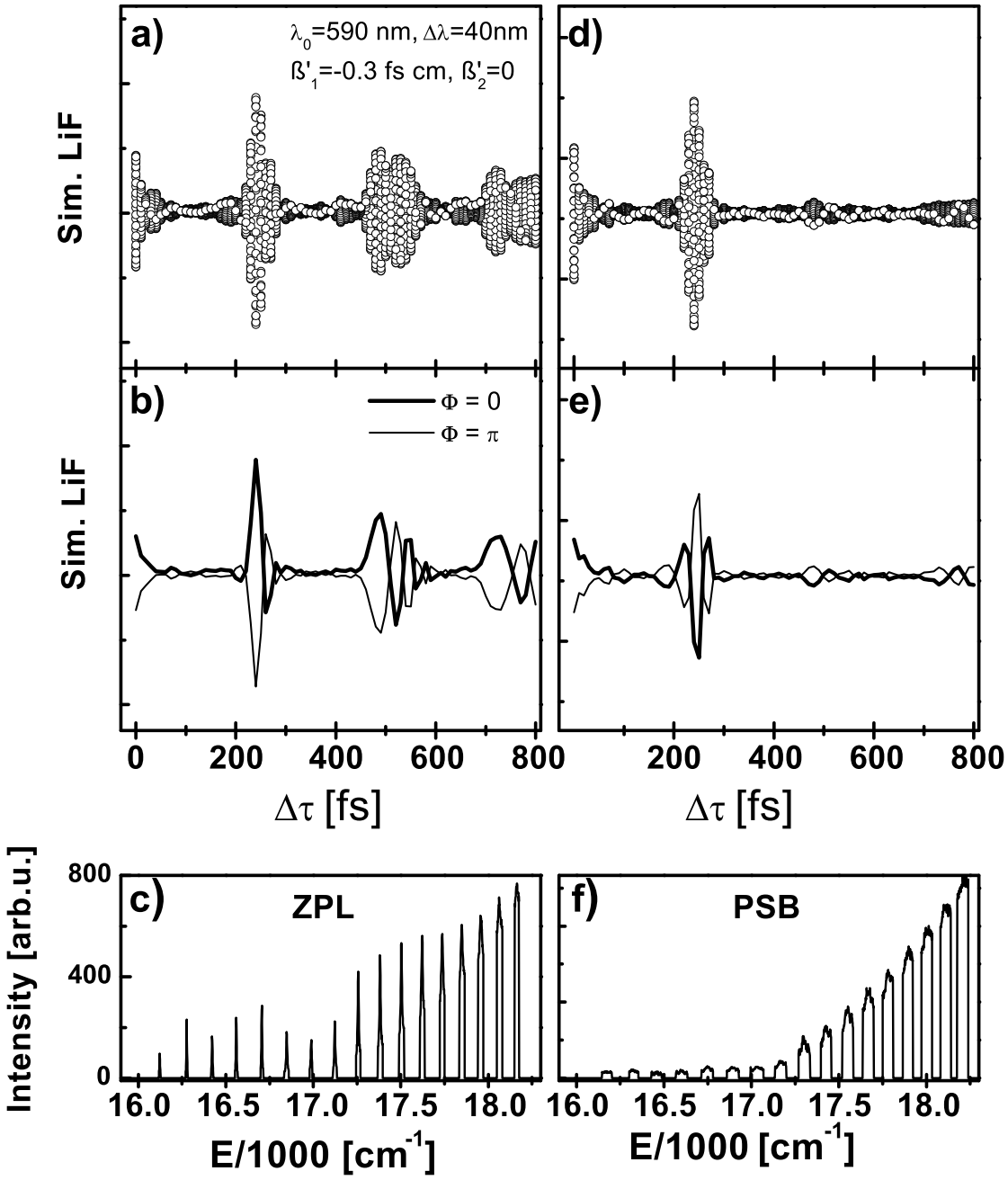

Figure 6.23: Simulation of Scherer - type experiment separated for ZPL and PSB contributions. Left column: An artificial excitation spectrum containing only ZPL (c) was used for the simulation and the results for 32 phases covering 2π are shown in a), those for two distinct phases $\Phi = 0$ (thick line) and $\Phi = \pi$ are plotted in b). In the right column the cut excitation spectrum in f) contains only PSB and their contributions to the spectrum are shown in d) and e).

Nevertheless, from the investigations of Ch. 4 it is known, that the absorption of the complete bromine molecule behaves more like the A' excitation spectrum in Fig. 4.9 and this was used in the simulations in Fig. 6.22g. Then, however, no vibrational recurrences at all are observed and also the representation of i) does only show a harmonic modulation.

Compared with this simulation, taking the full excitation spectrum of A' into account, the experimental results in Fig. 6.2 are surprisingly good. The reason for the better experimental contrast lies in the selective signal detection with the CCD array. Only B-state emission is taken into account since the emission from other covalent states is found at different wavelengths. The simulation in Fig. 6.22g illustrates, how complex a control of the system Br_2/Ar gets. A very small amount of light is absorbed by the B-state in this energetic region and has to assert itself against the dominant incoherent background. The background due to A-state absorption is non - controllable, because a wave packet which is born at the inner limb of the A potential highly above the gasphase dissociation limit does never come back to the FC region to interfere with a second wave packet.

To discriminate which contributions of the simulated spectrum in Fig. 6.22d originate from ZPL and which from PSB absorption, another calculation was done in Fig. 6.23. The first column contains the simulation based on an artificial B excitation spectrum which consists only of ZPL components as shown in panel c). This leads to a simulated signal which has its maximum at $\Delta\tau = T_{vib}$ in a) and not at $\Delta\tau = 0$, like before. Indeed, the modulation contrast is maximal for $\Delta\tau = 0$ for excitation with unchirped pulses. However, the correction of molecular anharmonicity due to the applied chirp difference $\Delta\beta'$ leads to the best overlap of spectral fringes with ZPL structures at 240 fs. The traces of $\Phi = 0$ (thick line) and $\Phi = \pi$ (thin line) are shown in b) and at larger time delays they are interchanged several times leading to broad heaps at the second and third recurrence. This might be of numerical reasons in the calculation, due to chirp parameters, which do not perfectly compensate for the molecular anharmonicity and lead to deviations over nearly 20 vibrational levels. In the simulation in Fig. 6.22a the excitation spectrum was reduced to only 8 vibrational levels and here all recurrences are of equal heights.

A separate excitation of PSB contributions in Fig. 6.23f results in the simulation of d) and e). It consists mainly of a pronounced contribution at $\Delta\tau = T_{vib}$. Later recurrence times in e) are hardly visible and nearly no phase dependence is observed. This plot also explains why the peak heights in Fig. 6.22b for first, second and third recurrence are nearly constant. The PSB adds in a counteracting way to the ZPL excitation and the maximum value for $\Phi = 0$ in Fig. 6.23b is reduced by the minimum for the same relative phase in e).

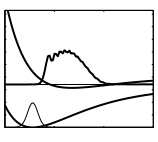

Reconstruction of relative phase between pulse train sub-pulses

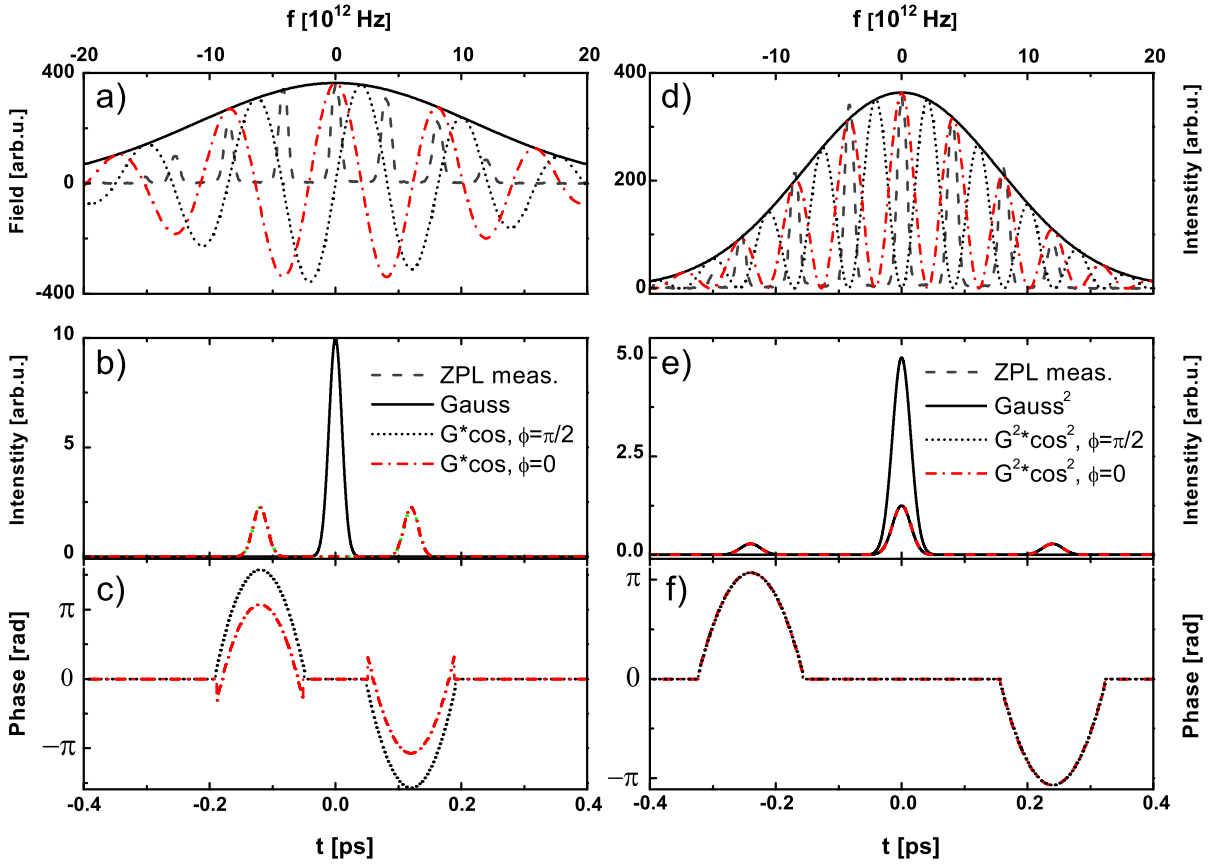

Figure 6.24: Phase reconstruction from the Fourier transformation of simulated frequency resolved spectra using the electric field (left column) or the intensity (right column). a) and d) Spectra in frequency domain (measured ZPL spectrum for comparison, dashed), Gaussian envelope (solid line), cosine spectra with Gaussian envelope for $\Phi = \pi/2$ (dotted line) and $\Phi = 0$ (dash dotted line) b) and e) switching to time domain by Fourier transformation (Power spectrum), c) and f) reconstructed, unwrapped phases, for details see text.

To retrieve the phases of the pulse sequences used in the control experiments of Sec. 6.2 in a first attempt a commercial FROG software [162] was tested. The software did not provide an SHG-X-FROG retrieval algorithm which considers, apart from the FROG trace, additionally a measured frequency resolved spectrum. Therefore, unique retrievals were not possible[3].
Another option to gain information on the phases in the time domain (also called temporal phase in the following) is the Fourier transformation of measured spectral fringes. One has to take some limitations into account, since the measured spectrum contains only the intensity and no explicit phase information. But for the approach of this work it delivered satisfying results, since in case of the pulse train, the spectral phase was not directly manipulated. The interest lies on the phase in time domain which is modified by amplitude shaping of the frequencies. This can be considered as the opposite technique to the Michelson experiments of Sec. 6.1. Indeed, with the Michelson interferometer, the temporal phases were manipulated with a piezo controller, until the observed spectral interferogram matched the desired fringe pattern.

[3]The X-FROG trace in Fig.3.12 has lost the information about sharp spectral features, since the ultrashort gate pulse was broad in frequency.

For the shaped pulse sequence, the systematics were turned around and the spectral shape in the Fourier plane of the SLM was manipulated by blocking distinct pixels. And this automatically adapts the phase in time domain. Therefore, it was possible -in this special situation- to reconstruct the temporal phase by means of the measured fringe pattern, as will be described now.

To test the algorithm and exclude any experimental distortions of the spectrum, first a sine – like interference pattern was created as an anharmonic cosine function with Gaussian envelope. The spectrum was centered around zero, since a shift in time domain causes a linear phase in the spectral domain, which should be excluded. Figure 6.24 compares intensity to electric field Fourier transformations. To rebuild the spectral pattern, a cosine function with changing periodicity, to include the anharmonicity, was multiplied with the Gaussian envelope. Panel a) shows such a modulated Gaussian pulse with relative phase $\Phi = 0$ as a dash-dotted and for $\Phi = \pi/2$ as a dotted line. These phase values can be identified at $f = 0$. The Gaussian envelope is included as a solid line. For comparison the measured spectral fringes exciting the ZPL are shown as dashed grey line. In b) the Fourier power spectrum of simulated spectra in a) is shown. The Gaussian envelope leads to the strong peak at $t = 0$ only, and both cosine show up at the two weaker peaks separated by 250 fs. They are identical for $\Phi = 0$ and $\Phi = \pi/2$, since the absolute square loses the phase information. But since the result of the Fourier transform is a complex number z, its phase Φ can be reconstructed by

$$\Phi = arctan\left\{Im(z)/Re(z)\right\}. \tag{6.2}$$

The result always lies within the interval $[-\pi/2; \pi/2]$, thus an unwrapping of the phase was carried out, following the continuous phase slopes, subsequently. Phase results are shown in Fig. 6.24c which agree with the original phases. The extrema for the dash-dotted line with $\Phi = 0$ are reconstructed to $\pm\pi$, which can be translated to zero. For $\Phi = \pi/2$ (dotted line) the extrema are found at $\pm$ 3/2π. Apart from the maximum position, which is detected with precision, also the curvature of the phases at each peak can be analysed to determine the quadratic phase and thereby the linear chirp parameter γ and β which were introduced in Sec. 3.3.2[4]. With Eq. 3.2, γ can be determined from the quadratic fit of the phases in Fig. 6.24c to $\gamma = 1.86\ 10^{-3}\text{fs}^{-2}$. This leads with Eq. 3.5 to $\beta(\nu) = 1650\ fs^2$ or $\beta'(\nu) = 0.05$ fs cm for the second pulse. For comparison with the experiment, it has to be doubled to 0.10 fs cm, since in this simulation one pulse has a positive, the other one a negative chirp, while in the experiment, one pulse was unchirped and the other had the stronger negative chirp. This result comes by a factor of 3 to the value determined for the Michelson interferometer of 0.29 fs cm.

This calculation shows, that the method to determine the temporal phase via a Fourier transform of a frequency resolved spectrum works sufficiently for the extreme values. It is also possible to obtain a trend for the curvature with the switching of the sign at the symmetry centre of the pulse train[5]. Also the order of magnitude of the chirp is reproduced. A more detailed analysis however, cannot be expected.

The right column in Fig. 6.24 is structured in a similar manner, but now the Gaussian envelope and the cosine function are squared. A comparison of the phases at $f = 0$ reveals now a difference of π. The squaring leads to a narrowing of η, the FWHM in spectral domain, and an elongation of τ, the FWHM in time domain. The frequency spectrum of d) has no longer any negative components and this causes three peaks for each of the modulated squared Gaussians in the Fourier transform

[4]For a harmonic cosine modulation the phase of each pulse would be zero.

[5]From the Michelson experiments of Sec. 6.1 and from wave packet calculations (Sec. 6.3.3) it is known, that the first pulse of a sequence has the most negative chirp and the last one the most positive chirp value. In the phase reconstruction calculations, the absolute timing as a result of Fourier transforming a spectrum, depends on the internal sign convention of the calculation software. For the programmed Matlab – code the resulting time sorting was found to be unique, however with opposite sign. Therefore, the time axis in Figs. 6.24 and 6.25 was multiplied with (-1).

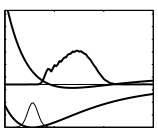

of e) (dash-dotted line for $\Phi = 0$ and dotted line for $\Phi = \pi$). However, the distance between those pulses is again 250 fs.

The phase reconstruction of panel f) delivers curves which are identical by π, which was the input information. The curvature of the parabola and thereby γ is reduced by a factor of two compared to c). This leads to a β larger by a factor of two, since in the quadratic case a larger τ and a larger $1/\eta$ amplify the resulting value.

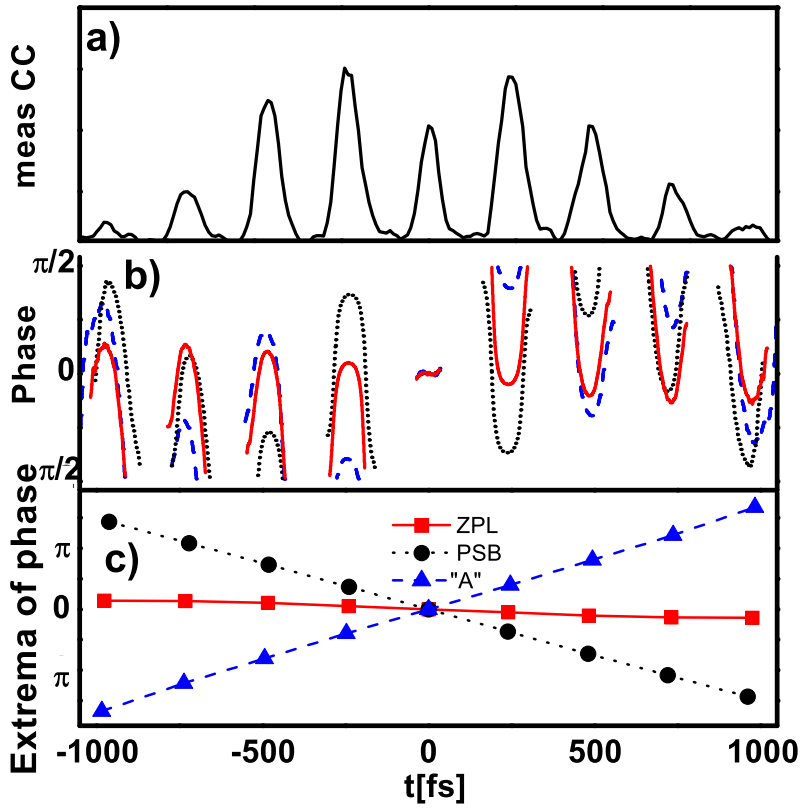

Figure 6.25: Reconstruction of phases from Fourier transformation of measured frequency resolved spectra. a) experimental cross correlation of the pulse train. b) Plot of the relevant phase information (at times where a signal is present) with π uncertainty. The phases show a quadratic dependence, corresponding to a linear chirp with changing sign around time zero. c) Values of extrema from a), unwrapped by following the trend.

With the experience in Fig. 6.24, the method for phase reconstruction from measured intensity spectra was applied to real measured frequency comb spectra in Fig. 6.25. The measured cross correlation in time domain of the pulse train is depicted in a), which contains no phase information. Phases are reconstructed in b) from the three spectral positions of the frequency comb, ZPL (solid line), PSB (dashed line) and "A" (dotted line). The centre peak had a nearly constant phase 0 in all three cases. The early peaks (at negative times) have a quadratic phase with negative curvature which corresponds to a negative linear chirp. For peaks at positive times the sign is switched to positive and this coincides with the expectations for a pulse train, where subsequent pulses should compensate for the molecular anharmonicity. Extreme values of the unwrapped phases are given in c). All extrema follow a linear trend and cross at zero. For ZPL (squares) a horizontal line is observed, as expected, since it is the centre of reference. By changing the relative phase between subsequent pulses the spectral comb can be shifted relative to the envelope and this was done for the PSB spectra (circles) and for the "A" excitation (triangles). In both cases the extrema lie on a straight line covering 3π. They are tilted with opposite sign, since the comb was shifted from ZPL position to higher energies for PSB excitation and to lower energies for the position "A". Thus, this method of phase reconstruction fully reproduces the expectation from the phase shift picture of spectral combs.

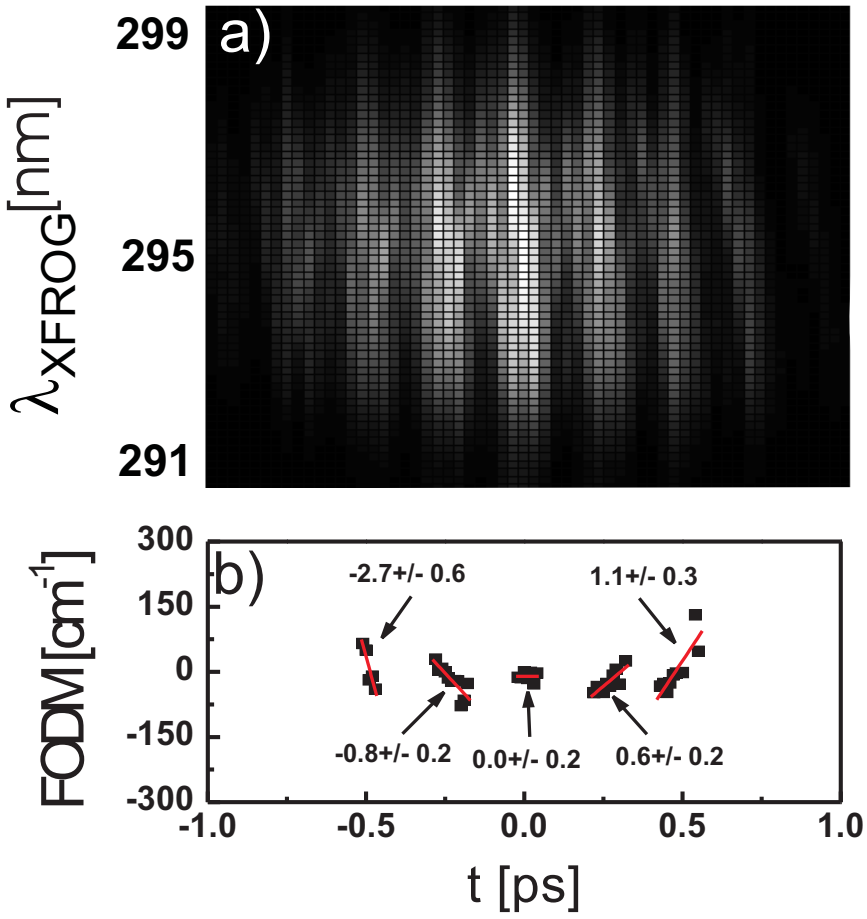

Figure 6.26: a) X-FROG trace for ZPL pulse train. b) FODM (squares) for FROG trace of a) with linear fits. The slopes with errors are given for the five strongest pulses and marked with the arrows. Strongly scattering data because of missing signal in between pulses were removed.

The time resolved pulse characterisation with the X-FROG trace for the ZPL pulse train in Fig. 6.26 confirms the results obtained by Fourier transformation. In a) the original FROG trace with SHG - wavelength $vs.$ time is plotted. Any spectral structure is smeared out due to the spectrally broad gate pulse, as was described in Sec. 3.3.2. Since the chirp of each pulse is very small, it is not directly evident. Therefore in b) the first order delay marginal (FODM), which was introduced with Eq.3.15 is plotted. A cut-out of the whole FODM trace is presented, since it can only deliver reliable data at those times, where enough signal intensity is present. The five centre peaks were fitted linearly and corroborate the trend analysed in Fig. 6.25a. The centre peak is created without any chirp, earlier pulses at negative times have a negative linear chirp and later pulses a positive one. Boundary pulses have the largest chirp difference and this is reasonable, since they have the largest time difference and the wave packet created by the first pulse has propagated for a long time until it is superimposed with the wave packet created by the last pulse. During this long travel the first wave packet has experienced the molecular dispersion and this has to be included in the last wave packet, too.

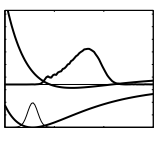

6.3.2 Predissociation

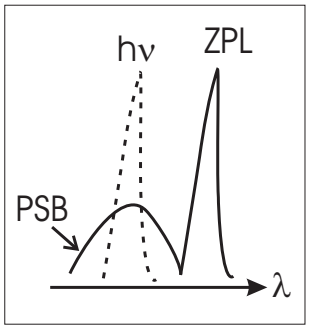

Figure 6.27: Spectral excitation of PSB and ZPL (solid line). One peak of the narrow frequency comb (dashed line, labeled hν) covers nearly half the width of a PSB and selects parts of it. The ZPL is narrow itself and completely covered.

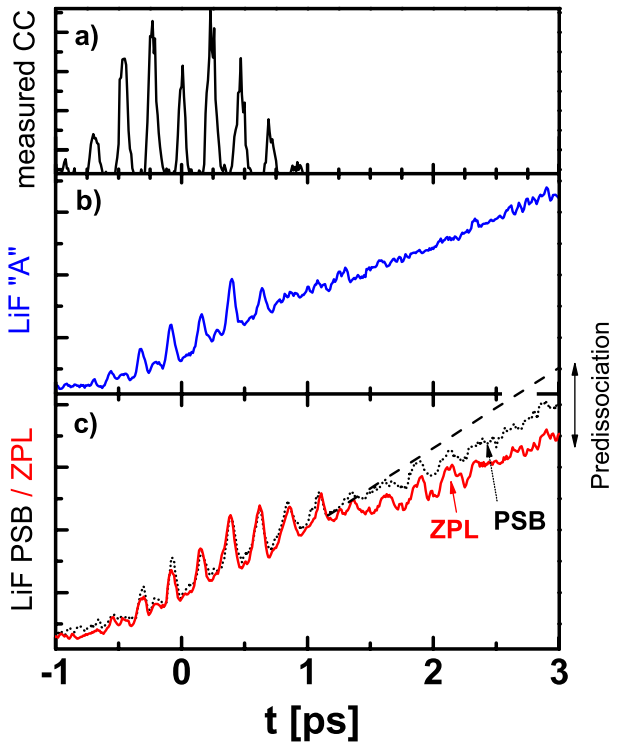

Figure 6.28: Pulse train (a) experiments for three spectral positions "A" (plot b), ZPL and PSB (solid and dotted line in c).

Strong indications for predissociation were observed in the frequency resolved analysis of Ch. 4. Three energetic positions were determined, where population from the B-state is transfered via repulsive states to the lower lying covalent states. The comparison with gasphase values like FC factors or vibrational spacings in Fig. 4.7 showed, that the coupling of repulsive states with the B-state is matrix induced. Predissociation is controlled by the pulse sequence experiments presented in this chapter. Since the position of the spectral fringes is adjustable via Φ, the ratio of ZPL and PSB contributions of the B vibrational wave packets can be manipulated.

Three spectral positions for the frequency comb corresponding to the excitation pulse train are chosen as introduced in Fig. 6.8. ZPL, creating compositions of wave packets predominantly exciting the B vibrational levels. PSB enhances the excitation of phonons in the matrix and the third position "A" is the neutral test, since it excites the A-state, which has a continuous spectrum in this energy region. Predissociation effects will be discussed by means of the experiments with parallel relative polarisation between all laser pulses in Figs. 6.15a, b and 6.16a-c. Fluorescence at 300 nm in Fig. 6.15 delivers a spectrum consisting essentially of B-state dynamics with the clear 260 fs period. It is possible to compare the relative heights for ZPL in a) and PSB in b) excitation and in the case of PSB the signal reaches half the height of a). This is caused by a difference in excitation for those two cases, which is illustrated in Fig. 6.27. The PSB (solid line) is wide in energy and a spectrally narrow peak of the excitation frequency comb (dashed line) covers approximately half of it. But when the comb is shifted to excite the narrow ZPL they completely

overlap and the excitation is more effective by about a factor of two, leading to a higher signal of B fluorescence. This is a coarse approximation, since the process of spectral sharpening is enhanced with every additional pulse and depends on the number of coherently interfering pulses. It will be discussed in more detail with Fig. 6.31 and Tab 6.1.

The time resolved spectra to search for predissociation effects are those obtained at 322 nm in Fig. 6.16a-c. The potential scheme with pump and probe windows is shown in Fig. 5.6. A vibrational wave packet of the B-state can be probed there, according to the solid probe arrows. However, it can also leave the B-state via repulsive states and show up in the A-state. This probe step is indicated with dashed arrows. This scheme includes one of the repulsive states, the C-state. All identified crossing states are collected in Fig. 4.17 and the one closest to the excitation with 590 nm is the $a(1g)$ state, which crosses the B-state 400 cm^{-1} above the C-state.
Figure 6.28a contains the cross - correlation trace of the experimental pulse sequence, which is indistinguishable for the three spectral positions ZPL, PSB and "A" in this intensity representation, as was discussed in Sec. 6.2.3. In Fig. 6.28b the fluorescence excited with the test position "A" is recorded and only the prompt response from the A-state to the excitation with the pulse train can be observed. At times longer than 1 ps no wave packet dynamics is visible and the background continuously increases. Every 250 fs the A-state is excited by another pulse, but this period does not match to the A signature observed in the pump - probe spectra in Fig. 5.1c. Therefore, those A wave packets which are already present cannot interfere in a constructive way with the freshly created ones and they add up incoherently to the smeared out background leading to the A - reference spectrum in Fig. 6.28b.
For ZPL (solid line) and PSB (dotted line) in plot c) the dynamics is completely different. When the pulse train has ended at 1 ps the B period of 260 fs occurs on the background. From both states B and A population is transfered in the probe step to CT states and both contribute to the 322 nm emission. Both signals, with ZPL and PSB excitation start with the same signature of the pulse train at short times, but when the light is off, the background in the PSB spectrum increases more strongly until it is higher by 15% at 3 ps. This increase is attributed to enforced predissociation, following the scheme of Sec. 5.2. B population which has left the B-state via a repulsive state reaches the A-state.
Once in the A potential, the former B wave packet follows the A dynamics and collides with the cage. There, it looses energy and slides down the A potential, recombines and oscillates with a 300 fs period. However, this can no longer be resolved, since with every B roundtrip roughly 10% of the population leave the potential and arrive on A, as was discussed in Sec. 4.2. All those wave packets merge to a continuum which cannot be separated from the A continuum.
Another indication for this process is the longterm study in Fig. 6.19c and e). The maximum at 4.5 ps in the case of PSB excitation in e) is reached with a steeper slope than for ZPL excitation. This is interpreted, that with the excitation of phonons, the coupling between B-state and repulsive states is stronger and predissociation is more efficient. Therefore, in a distinct time interval more B population leaves the B-state and the B reservoir is emptied more quickly. Consequently, the maximum should also decay more rapidly and this can be seen in Fig. 6.19e, compared to the ZPL excitation of c).
The fact, that at the spectral position "A" no B dynamics is observed is the proof, that ZPL and PSB excitation lead to real interference effects and will be discussed in Sec. 6.3.3. Collating these predissociation effects with the information obtained from the 300 nm spectra discussed before, the increase can be multiplied by a factor of two, since PSB excitation is weaker in general. This is indicated by the dashed tilted line above the PSB spectrum in Fig. 6.28c and the two-sided arrow on the right hand side shows the amount of B population which has reached the A-state due to the controlled matrix induced predissociation. The control aspect here, is the enhancement of predis-

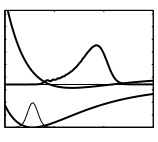

sociation by excitation of PSB wave packets with respect to ZPL wave packets. It is in good accord with the matrix induced nature of predissociation due to the excitation of phonons, predicted by theory [39].

The spectra obtained with perpendicular relative polarisation ($e.g.$, Fig. 6.19d, f) contain more B-state than in the parallel case and here the predissociation effect can be directly seen in the strength of the B modulation at times where the pulse sequence is present. For ZPL excitation in d) the B modulation is strongly pronounced and for PSB stimulation in f) it is weaker. The background at longer times reaches nearly the same value for both types of excitation. Nevertheless, also in the perpendicular case, the 300 nm spectra differ by a factor of two in Fig. 6.15c and d), thus the predissociation is again enhanced in the case of stronger coupling of B-state and repulsive states for PSB excitation.

Concerning the predissociation rates, from the frequency resolved investigations in Sec. 4.2 a value of 5% per roundtrip for the first crossing and 10% per roundtrip for the second crossing (the more relevant one for the control experiments) was determined. However, we expect this rate to be time dependent. Low energy parts of the wave packet have a higher predissociation probability since they are more close to the crossing. Thus their reservoir is emptied faster than that of high energy components. One indication for this mechanism is the prolongation of the pump - probe oscillation period discussed in Sec. 5.2.1.

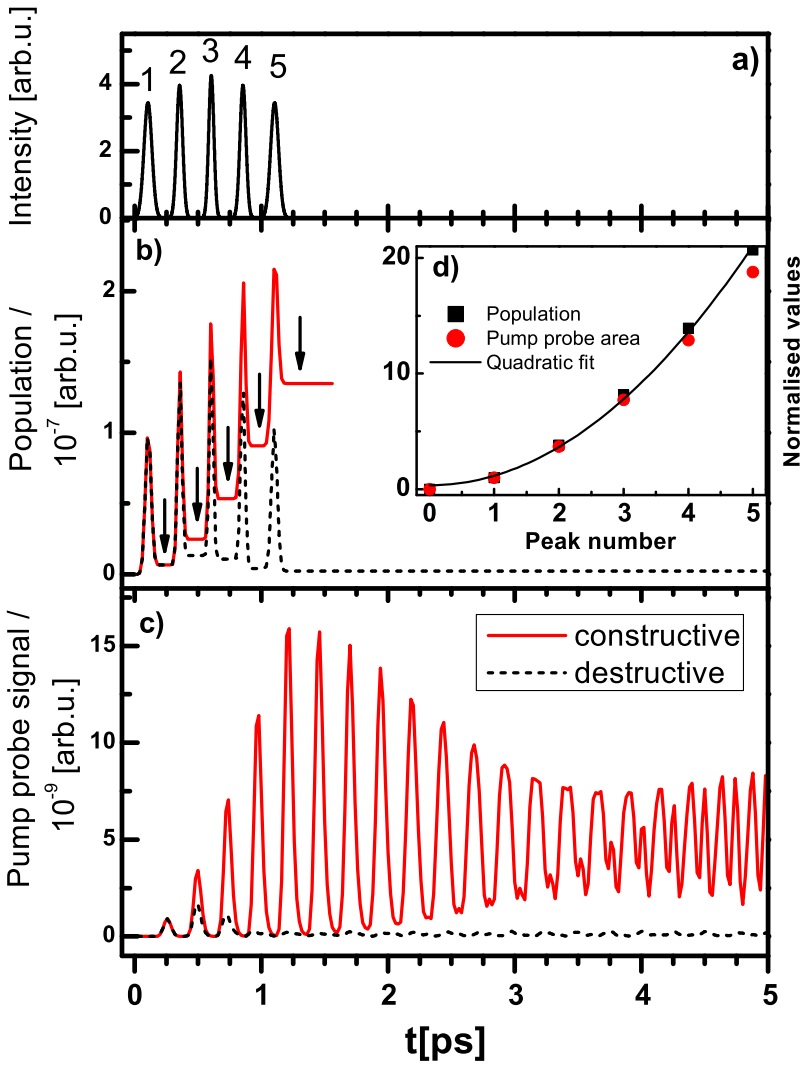

Figure 6.29: Simulation of pulse train probe spectra. a) Absolute square of the pulse train. b) Excited B-state population for constructive interference (solid line) and destructive interference (dashed line). c) Pump sequence - probe signal for constructive (solid) and destructive (dashed) interferences. d) Remaining population after each pulse (squares) with quadratic fit (solid line) and area under each pump - probe peak (circles).

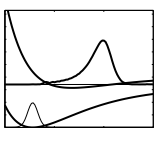

6.3.3 Wave packet interferometry

Simulation of pulse train pump - probe spectra

To support a deeper understanding of the wave packet interferometry, the simulation which was introduced in Sec. 5.2.1 was extended to deal with five laser pulses with a variable time delay Δt, chirp β' and relative phase Φ. Based on the parameters known for the Michelson experiment in Sec. 6.1.1 and the trend of chirp differences determined in Fig. 6.25 and 6.26, the following pulse sequence was used: $\Delta t = 250\,\text{fs}$ for all pulses, the chirp was varied from pulse to pulse starting with the negative chirp $\beta'_1 = -0.58\,\text{fs cm}$ for the first pulse, $\beta'_2 = -0.29\,\text{fs cm}$, $\beta'_3 = 0\,\text{fs cm}$, $\beta'_4 = +0.29\,\text{fs cm}$ and the last pulse with $\beta'_5 = +0.58\,\text{fs cm}$. In the case of constructive interference the phase of all pulses was zero, related to the locking frequency which was set to the ZPL maximum at 589 nm.
Destructive interference requires a phase shift of $2\pi/n$ between two neighbouring pulses, with n being the number of pulses which should interfere destructively. Interference effects were simulated for five pulses of equal intensity in Fig. 6.29. Panel a) includes the intensity of the simulated pulse train. A lengthening due to the strongest chirps at the border pulses is clearly visible. The populations on the B potential for constructive (solid line) and destructive interferences (dotted line) are depicted in b). The peaks show the maximal population obtained at the centre of each laser pulse, which is reduced to a constant level indicated by the vertical arrows when the second half of each pulse is interacting. This dumping of population to the ground state has its origin in the non-resonant electronic excitation, as was described in Sec. 1.1.1. When the first pulse is terminated, roughly 1% of the maximum population remains. Interference effects occur for all following pulses, until a contrast of 100:1 appears for constructive to destructive interference, at the termination of the pulse sequence. Thus, in the case of destructive interference the amount of population which is interfered away from the excited state, goes back to the ground state. This can be seen in analogy to the Michelson interferometer: For destructive interference light is leaving the interferometer through the entrance and goes back to the light source.

The pump - sequence - probe signals for the two extreme cases (solid: constructive, dotted: destructive interference) are shown in c) using the same parameters for pump and probe energies and width as discussed for Fig. 5.7. In fact, the area of each peak in the constructive signal in Fig. 6.29c evolves quadratically with the number of interfering pulses. This is plotted as circles in the inset d). The stable population values at the end of each pulse in the constructive case of b) are plotted as squares in d). Such a quadratic dependence is expected, and shall be derived in analogy to interferences of light pulses. It has to be pointed out, that in the experiments discussed here, no direct interference of laser pulses is observed since they are well separated in time. Each pulse generates a wave packet and these evolved wave packets interfere on the potential surface, following the same scheme.

With the standard equation for two interfering light pulses E_1 and E_2 with relative phase Φ, the intensity I is [30]

$$I \propto E_1^2 + E_2^2 + 2E_1E_2cos(\Phi). \tag{6.3}$$

A phase $\Phi = 0$ leads to the largest intensity for constructive interference and $\Phi = \pi$ gives destructive interference. The increase from peak to peak in the case of constructive interference is:

$$\begin{aligned}
I_1 &\propto E^2 \\
I_2 &\propto (E_1 + E_2)^2 \overset{constr.}{=} E_1^2 + E_2^2 + 2E_1E_2 \overset{E_i=E}{=} 4E^2 \\
I_3 &\propto (E_1 + E_2 + E_3)^2 \overset{constr.}{=} (E_1 + E_2)^2 + 2(E_1 + E_2)E_3 + E_3^3 = \\
&\qquad E_1^2 + E_2^2 + E_3^2 + 2(E_1E_2 + E_1E_3 + E_2E_3) \overset{E_i=E}{=} 9E^2
\end{aligned}$$

or in a general way:

$$I_n \propto n^2 E^2 \tag{6.4}$$

for constructive interference of n pulses with equal intensity. Here, I_i is the intensity for i pulses interfering and E_i the electric field of the ith pulse. The proportionality of electric field and intensity stands also for wave packets and populations. Such a quadratic behaviour for constructive interference was simulated for 5 laser pulses having the right chirp. They create wave packets which interfere on the B potential and the results for simulated population increase can be seen in Fig. 6.29d. A general theoretical investigation on how population depends on a pulse train was carried out, $e.g.$, in Ref. [9] and confirms these simulated results. A remark comparing the simulation for constructive interference with the one for a single pulse experiment in Fig. 5.7b: The modulation contrast in Fig. 6.29c is visible up to 4 ps before dispersion leads to the development of the 1/3 revival, which is delayed by 1 ps compared to the single pump pulse experiment. This is caused by the excitation of a pulse train with subsequent chirped pulses which compensate the dispersion effects for roughly 1 ps.

It is interesting to compare *coherent* and *incoherent* contributions of the population, depending on the number of wave packets. In this comparison the term coherent describes the amount of population which is sensitive on the relative phase. Incoherent parts ($i.e.$, the field squares) do not depend on the phase. For the example of three interfering wave packets this leads with Eq. 6.4 to an incoherent amount of population of

$$E_1^2 + E_2^2 + E_3^2, \tag{6.5}$$

and the coherent counter part is

$$2(E_1E_2 + E_1E_3 + E_2E_3). \tag{6.6}$$

The ratio of the incoherent components ($i.e.$, non - controllable) to the overall population is then

$$\frac{incoherent}{incoherent + coherent} = \frac{1}{n}, \tag{6.7}$$

with n being the number of wave packets. The more pulses used, the higher is the amount of population which allows for a coherent control.

In Fig. 6.30 the obtained simulated pump - probe spectra for a sequence of five pulses are compared with the experimental ones in Fig. 6.15. Figure 6.30a shows the cross - correlation trace of the experimental pulse sequence, consisting of seven relevant pulses. In b) the LiF spectrum recorded at 300 nm for ZPL excitation is shown. It consists of two components. Those fragments, which show the nearly prompt response on the pulse train probed on the A-state are marked with the thick grey line and the connection is indicated by the horizontal dashed lines. These parts have a time delay of 250 fs, which was the period of the pulse train in a). They keep a constant height as long as the pulse sequence acts and vanish when the light has terminated.
As a thin black line in b) the B-state wave packet dynamics is shown. It is transposed to the prompt response and the signal increases with every additional pulse until it reaches a maximum around 1 ps. This signal trace of the B-state is modelled in c) with a very nice agreement, using the wave packet simulation with the parameters for constructive interference discussed in Fig. 6.29. An exact quadratic increase cannot be expected, since the experimental pulses were not of precise equal height. The A response is not visible, since the A-state is not included in the simulation. In d) the relative phase between the pulses was changed to achieve destructive interference and when the pulse train has terminated, the pump - probe signal is nearly completely eliminated, since plots

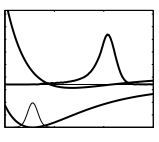

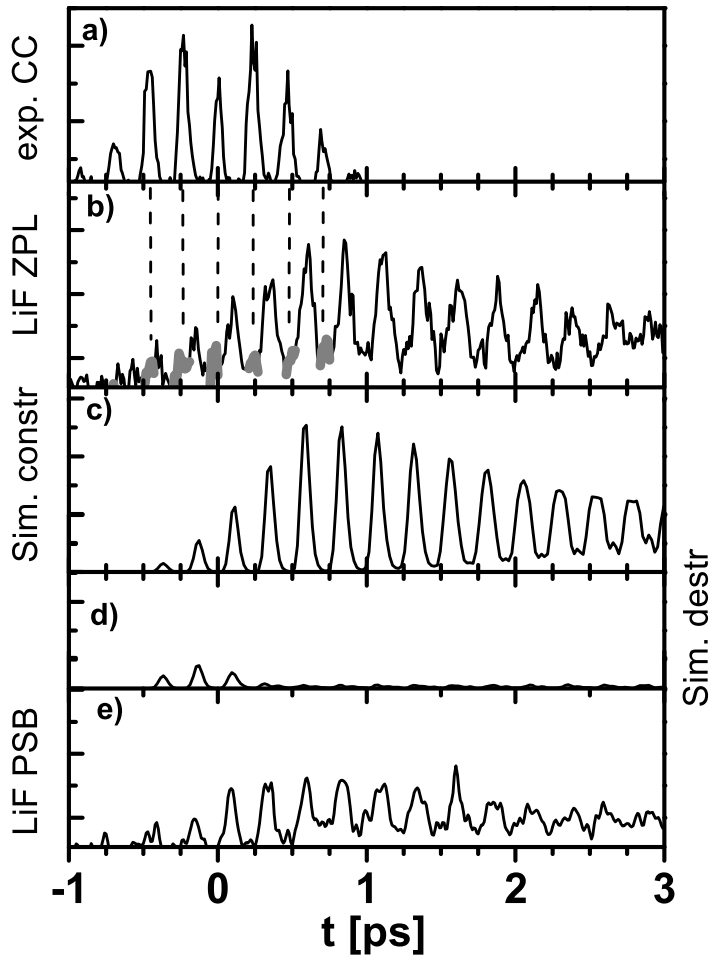

Figure 6.30: a) Experimental pulse sequence. b) Measured LiF detected at 300 nm for pulse train excitation matching to ZPL. Corresponding simulated pump - probe spectrum for constructive interference in c) and for destructive interference in d) on the same scale. e) Measured LiF signal for PSB excitation on the same scale as b).

c) and d) are printed with the same scale. In e) the experimental phase was changed to excite the PSB and the scale is the same as in b). Compared to d) this trace looks different. In the experiment (e), ZPL of the B-state are excited with this pulse train and destructive interference is obtained. However, simultaneously, constructive interference on the PSB takes place. And since the spacings of ZPL and PSB in the excitation spectrum in Fig. 4.5 are very similar, this also excites the B-state. The overall signal intensity in Fig. 6.30e is reduced by a factor of two and this was illustrated in Fig. 6.27. Since the spectrally narrow frequency comb (dashed line) covers the broad PSB (solid line) only partially, in this kind of excitation light reduced by roughly a factor of two is absorbed. Therefore, also the corresponding LiF signal is weaker by a factor of two.

As a first attempt for extracting information on the experimental signal increase from pulse to pulse the area below each peak in the 300 nm pump sequence probe spectra in Fig. 6.15a and b) was determined. Those values are shown in Fig. 6.31, for the ZPL enhanced spectrum as squares in a) and for the PSB spectrum as circles in b). Both plots show as crosses the accumulated intensity of the pulse train in Fig. 6.28a. Accumulating the intensity means, the first data point has the value of the intensity of the first laser pulse, the second data point is the sum of intensities for

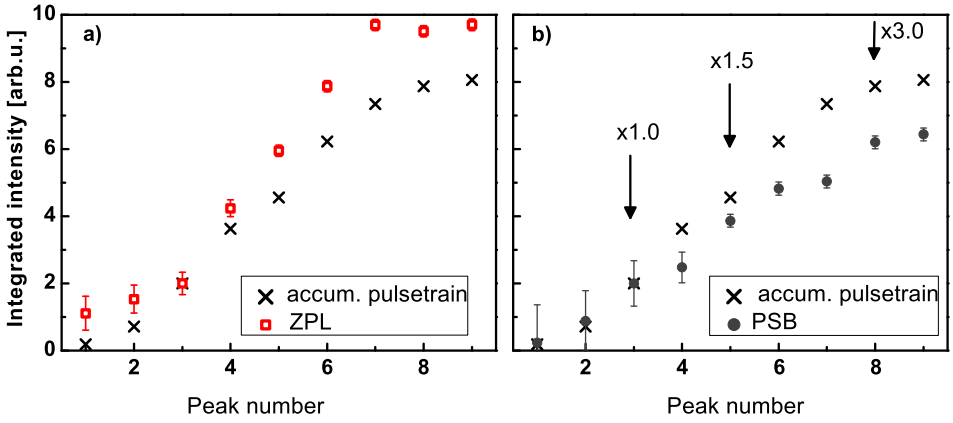

Figure 6.31: Pulse train intensity accumulated for each peak (crosses) together with the area below pulse train - probe spectra for ZPL excitation in a) (squares) and PSB excitation in b) (circles) at $\lambda_{fluor} = 300\,\text{nm}$. A detailed explanation is given in the text.

first and second pulse and so on. This is a representation of the light which was brought into the sample without taking any interference effects into account. In Fig. 6.31a, ZPL area values are scaled to the third data point of the accumulated pulse train values, since this is the first one of the experimental peaks having reasonable strength. Later measured peaks in the pump - probe spectrum exceed the simple accumulated intensity, which is an indication for constructive interference. For the comparison of peak areas of the pulse train with PSB excitation the increase seems to be smaller than linear. This is however an artefact which was mentioned earlier and is caused in the spectral narrowing due to the interference of several pulses which was discussed in Fig. 3.15. The more pulses interfere, the sharper the spectral structures become and some exemple numbers are given in Tab 6.1.
This does not affect the ZPL excitation, since the line is spectrally sharp. For the first three interfering pulses the width of the PSB is also not affected. Since the relative height of ZPL/PSB is 6/1 and the relative width equals 1/6 both, ZPL and PSB are excited with the same strength. However, for the broad PSB with each additional pulse, spectral width is clipped. This means for the PSB spectrum that values at later times have to be scaled with a correction factor which is indicated by the vertical arrows in Fig. 6.31b. Thus, the correction factor of two, introduced in Fig. 6.27, still holds as an average value. The area values have to be taken with caution, since the height of the background could not be identified exactly. The background in ZPL and PSB excitation was determined in the same way, and therefore those two spectra are comparable to each other.

Figure 6.32 shows the comparison of pulse train experiment and simulation for coherent excitation of ZPL with a pump sequence probe trace and this is in very convenient agreement. The measured cross - correlation of the pulse train is plotted in a). In b) the experimental curve in Fig. 6.15a (thin black line) and the simulation for five constructively interfering laser pulses are given, using the parameters in Fig. 6.30c. Peaks in the pump - probe spectrum occur with a time shift, since wave packets are prepared at the inner potential branch and the probe position is at the outer one, as indicated by the tilted dashed lines. Both spectra are normalized to the fifth peak. A small offset was added to the simulated trace, to account for the experimental background. Then, both spectra show a very nice agreement at those peaks with representable intensity, following the increase for constructive interference. For the simulation this increase was shown to be quadratic in Fig. 6.30d.

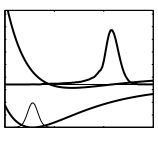

Table 6.1: The first and second row show the measured line width and relative peak heights for ZPL and PSB and values around 590 nm. Interferences of several pulses lead to spectral narrowing, depending on the number of pulses, shown in the other rows. These simulated pulses are normalised to unity.

	FWHM [10^{12}Hz]	rel. height
ZPL	0.2	6
PSB	1.2	1
1 pulse	21.5	1
2 pulse	2.2	1
3 pulse	1.2	1
4 pulse	0.8	1
5 pulse	0.4	1

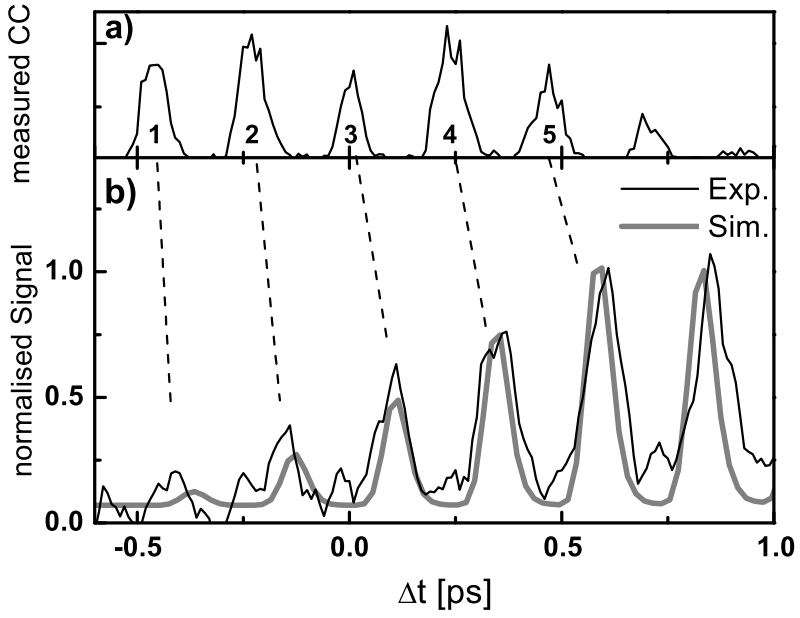

Figure 6.32: a) Experimental pulse sequence. b) Measured LiF detected at 300 nm for pulse train excitation matching to ZPL (thin black line) together with the simulation for 5 constructively interfering laser pulses with different chirps (thick grey line), normalised to the 5th peak.

6.3.4 Electronic coherence

Figure 6.6 gave first indications that the electronic coherence time for the halogen bromine, embedded in the Ar matrix surrounding, extends 1.5 ps. These results were confirmed by the observed wave packet interferences by excitation with a phase controlled pulse train. The time resolved spectra for the superposition of two and more than five laser pulses differ significantly. Indeed, the more pulses interfere, the more clearly the B-state is prepared out while the A-state is suppressed. Furthermore, a comparison of experimental signal increase from pulse to pulse with a simulation of interference effects on the free molecule showed a good agreement over several pulses in Fig. 6.32. Both spectra are normalised to the 5th peak. The simulated signal increases quadratically and this trend is very well reproduced in the experiment. Small deviations can be attributed to different relative intensities of the pulses in experiment and simulation.

At later times, decoherence effects will come into play. Incoherent parts add up linearly and will contribute an incoherent background. This might be the background observed in the experimental trace at 300 nm fluorescence wavelength.

The molecular response on complex pulse trains is very complex, itself. Many processes occur simultaneously and leave their footprint on the transient spectra. Around 1.5 ps electronic decoherence might limit the interference of wave packets. However, also predissociation plays a crucial role, as was discussed in Sec. 5.2.1. At this time the predissociation probability of 10% per roundtrip has removed almost 50% of the B-state population excited with the first pulse of the sequence. In any case, with a pulse train of seven pulses exceeding a total length of 2 ps, the control experiments operate at the limit. Sequences containing more sub-pulses would not enhance the control effects, if the first and the last pulse are no longer superimposed coherently. Thus, only the overall signal intensity would be reduced.

For the sharp ZPL, electronic coherence is preserved during the pulse train excitation, since constructive interference is observed. The question on electronic coherence times of the broad PSB is difficult to answer, concerning this peak – to – peak increase in Fig. 6.30e. Here, it is more convenient, to argue inversely with the extinction of wave packets caused by destructive interference. This is carried out by comparing the excitation of ZPL and PSB in Fig. 6.28c with the spectral comb adjusted in between at the position called "A" in b). Both, ZPL and PSB in c) give rise to B wave packet dynamics exceeding the duration of the pulse train. Also the first pulse of the "A" sequence excites B dynamics since it covers a broad spectral range, including ZPL and PSB. But once the pulse train is terminated, only an unmodulated background remains. Thus, ZPL and PSB contributions have to interfere destructively to extinguish B wave packet dynamics.

Destructive interference however, relies on electronic coherence, as the constructive one does and this is the proof, that the superposition of ZPL and PSB wave packets, created by the pulse train is - to a large extent - coherent.

The results concerning the coherence in the narrow ZPL coincide with the observed linewidth in Fig. 4.7. However, for the broad PSB, the determination of comparable long coherence times of at least 1 ps is very surprising. We deal with a diatomic molecule, however, it is surrounded by 18 Ar atoms already in the first shell. Hence, the whole contributing system is large. To estimate the distance, phonons can propagate in an Ar matrix within 1 ps, the longitudinal zone center phonons with a group velocity v_g of 1.64 nm/ps are considered. With the Ar lattice constant of 0.53 nm, this phonon propagates over three shells within one ps [241]. For such a large unit of atoms fast dephasing is expected in general.

The observed coherence indicates, that the broad sideband displays the superposition of several narrow coherent bands, and thus, is coherent itself. This idea is supported by an experimental feature observed in the PSB spectrum in Fig. 4.8: The sharp peak at 70 cm^{-1}, which is evident in all resolved PSB.
From theory [39, 99, 242] distinct phonon modes and their displacement vectors in the cage are known. However, it is very difficult to predict the coherence of certain modes in the entire system.

To observe the cancellation of PSB and ZPL due to destructive interference, it is required to perform the control experiments deep in the B potential with linear phonon contributions. Excitation higher up in the potential leads to the excitation of multi phonon bands. Indeed, they are spread over many vibrational levels, thus even if they remain coherent, they cannot be addressed selectively. However, coherence might be evident there, due to new effects.

In fact, analysing the long lasting coherence in the PSB is a very challenging task and the answer is left to further experiments and theoretical investigations.

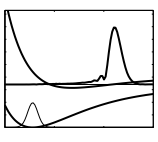

Summary

In the framework of this thesis a tracking of coherent structures in an incoherent background due to the specific excitation of sharp zero phonon lines (ZPL) with phase controlled pulse sequences is achieved. The pulses are chosen in delay and chirp to match the B-state vibrational roundtrip time of Br_2/Ar. Thus, they correct for molecular anharmonicity. With every constructively interfering pulse, the coherently excited B-state population is enhanced compared to the matrix bound incoherent A-state population. While the B wave packets build up, no A contributions return to the Franck - Condon region due to vibrational energy relaxation. The A contributions only add to an unmodulated incoherent background.

To execute the control scenario a precise knowledge on spectroscopic signatures is required. Due to weak transitions probabilities of the bound part of the B potential and a dominant A absorption at low energies, no vibrational progression is observed in absorption spectra. However, the B-state vibrational progression was determined in extensive high resolution emission excitation spectra covering the excitation wavelength of 630 – 540 nm. By observing selected emission wavelengths, the B-state excitation spectrum could be separated from the one of the lowest covalent state A'. The latter serves as a population sink - also for relaxed A-state population - and thus represents the ratios of B and A-state absorption.

The two dimensional B-state emission / excitation spectrum shows the isotopic splittings and allows to clarify spectroscopic constants of the B-state. In the B-state excitation spectrum sharp ZPL and broad phonon sidebands (PSB) are well resolved from $v' = 2$ up to $v' = 19$. The matrix influence increases with higher v', resulting in line broadening of the ZPL and increasing PSB contributions. The background was assigned to originate exclusively from higher order PSB. The increase in ZPL intensities with higher v' due to rising Franck - Condon factors is distorted for the matrix isolated molecule. Matrix induced predissociation, originating from an enhanced coupling to repulsive states, depopulates the B-state. Furthermore, this coupling leads to line broadening and spectral shifts around the crossings. Two positions between $v' = 4 - 5$ and $v' = 7 - 9$ were identified, where repulsive states cross the B-state potential. Predissociation probabilities of 5% and 10% per roundtrip, respectively, were determined. Thus Br_2/Ar is an ideal system to control the strength of predissociation, these probabilies are strong enough to be observed and weak enough to allow several vibrational roundtrips. Since the ZPL broaden with temperature and the addressing of sharp spectral structures is essential for coherent control, the experiments were carried out at 6 K.

A single ultrashort pulse is always broad in frequency. To obtain sharp spectral structures in the molecule, a sequence of several pulses is required, where the individual phases can be addressed. These structures can develop due to interferences of subsequently created vibrational wave packets. This however, requires the coherent superposition of several wave packets. Vibrational coherence is known to extend for 3 ps in Br_2/Ar. In tutorial experiments with double pulses of a Michelson interferometer, the minimal electronic coherence time is determined to 1.5 ps. This allows for the coherent absorption of 4-6 pulses separated by the vibrational roundtrip time.

These pulse sequences are generated by directly writing the desired spectroscopic signature to

a pulse shaper, which is positioned in the Fourier plane where the separate frequencies of the pulse can be manipulated individually. The programmed vibrational progression generates inevitably a pulse train with the required phase and timing properties. The thereby obtained frequency combs can be shifted to positions matching to ZPL or PSB. A third control position excites only unmodulated energies of the B-state and is used as a reference for A-state contributions.

For several reasons the energetic region around 590 nm was most interesting to start with: The PSB and ZPL cover nearly the same area in the excitation spectrum according to the Huang - Rhys coupling constant S, which represents the electron - phonon coupling strength and was determined to S = 1. Furthermore, the second curve crossing of repulsive states with the B-state was found in this energy region, opening interesting channels for predissociation.

Unfortunately, the ratio of coherently controllable B-state to the incoherently summed up A-state was determined to 1:100 in the frequency resolved experiments of this energy region. This represents a challenge for the control experiments of this work.

The coherent control succeeded with pulse trains aligned to the ZPL. The first pulse is absorbed likewise by ZPL and PSB of the B-state and also by the A-state. But with the following pulses the B-state is enhanced more and more due to constructive interference, whereas the A-state dynamics is suppressed. All created population in the A-state is added in an incoherent way and thus merges to an unmodulated background. On top of it, a clearly pronounced B dynamics grows, which persists for several ps. A second fluorescence band allows the wave packet dynamics to be detected exclusively from the B-state.

Also the excitation of PSB with the pulse train supported the development of the B progression, however weaker by a factor of two. The possibility to coherently address the PSB was demonstrated, and a surprisingly long lasting coherence extending for 1 ps was shown. Thus, the broad PSB can be attributed to a superposition of coherent narrow bands. This coherence was proved via the destructive interference and elimination of PSB contributions which were originally excited as well, with the first pulse of the pulse sequence. With higher v' the background develops to multi phonon order sidebands, which is reflected in the quadratic increase to $S = 4$ at $v' = 19$ due to an increase in vibrational coupling of molecule and matrix. Still, the PSB contributions in the background can be coherent. However, the appearance of destructive interference will be hindered due to the wide spread overlapping of higher order sidebands.

The efficiency of predissociation depends on the coupling strength of the B-state with repulsive states. This coupling again depends on the strength of the coupling between chromophore and matrix. Exciting preferentially ZPL reduces this matrix effect, shifting the frequency comb to PSB and thereby exciting matrix phonons enhances the coupling. This aim of controlling the predissociation probability was achieved at the second crossing, by probing the A-state. When changing the excitation frequency comb from ZPL to PSB a signal increase in A due to predissociated B population was observed, which could be doubled in the first 3 ps.

All time resolved experiments were carried out in a polarisation sensitive way, by varying the relative polarisation between pump and probe pulses from parallel to perpendicular. This allows to enhance or suppress the B-state with respect to the A-state, depending on the fluorescence wavelength.

In this work, efficient tools for coherent control of weak coherences buried a dissipative background were demonstrated, exemplarily.

In future experiments, a variation of the probe wavelength will allow to sample the created interfering wave packets above and below crossings with repulsive states and thus follow the population flow to other electronic states. The experiments presented here are energetically located close to the bottom of the B potential to maximise the ratio of sharp ZPL and broad PSB in this

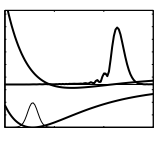

basic study. The PSB turned out to be surprisingly coherent, thus it will be interesting, how the control experiments with sharp spectral features evolve with shorter pump wavelengths and whether coherence persists. From the theoretical side two modes were presented which are mainly responsible for predissociation due to distortions in the cage symmetry. Addressing these modes in future experiments can enhance the observed change in predissociation rates, further.

The obtained results can be applied to other chromophore - bath combinations, as well. A dissipative background is present in many systems. Transferring the chromophore, $e.g.$, into a softer environment like a hydrogen matrix will be interesting, since the surrounding matrix atoms are much more flexible than in the stiff Ar cage and thus the coupling can be manipulated efficiently.

Bibliography

[1] S. Meyer and V. Engel. Vibrational revivals and the control of photochemical reactions. *J. Phys. Chem. A*, 101:7749–7753, 1997.

[2] M. Gühr, H. Ibrahim, and N. Schwentner. Controlling vibrational wave packet revivals in condensed phase: Dispersion and coherence for Br_2:Ar. *Phys. Chem. Chem. Phys.*, 6:5353–5361, 2004.

[3] M. Karavitis, T. Kumada, I. U. Goldschleger, and V. A. Apkarian. Vibrational dissipation and dephasing of $I_2(v$=19) in solid Kr. *Phys. Chem. Chem. Phys.*, 7:791–796, 2005.

[4] H. Katsuki, H. Chiba, B. Girard, C. Meier, and K. Ohmori. Visualizing picometric quantum ripples of ultrafast wave-packet interference. *Science*, 311:1589, 2006.

[5] A. H. Zewail. *Femtochemistry, Ultrafast Dynamics of the Chemical Bond Vol. I + II*. World Scientific, Singapore, 1994.

[6] M. Bargheer, N. Zhavoronkov, Y. Gritsai, J. C. Woo, D. S. Kim, M. Woerner, and T. Elsaesser. Coherent atomic motions in a nanostructure studied by femtosecond x-ray diffraction. *Science*, 306:1771–1773, 2004.

[7] A. M. Weiner, D. E. Leaird, G. P. Wiederrecht, and K. A. Nelson. Femtosecond pulse sequences used for optical manipulation of molecular motion. *Science*, 247:1317, 1990.

[8] M. Wollenhaupt, V. Engel, and T. Baumert. Femtosecond laser photoelectron spectroscopy on atoms and small molecules: Prototype studies in quantum control. *Annual Review of Physical Chemistry*, 56:25–56, 2005.

[9] S. Gräfe, C. Meier, and V. Engel. Instantaneous dynamics and quantum control fields: Principle and numerical applications. *J. Chem. Phys.*, 122:184103, 2005.

[10] J. Hauer, T. Buckup, and M. Motzkusa. Enhancement of molecular modes by electronically resonant multipulse excitation: Further progress towards mode selective chemistry. *J. Chem. Phys.*, 125:061101, 2006.

[11] M. Wollenhaupt, A. Assion, and T. Baumert. *Handbook of Lasers and Optics, F. Träger, Ed., Chapter 12: Femtosecond Laser Pulses: Linear Properties, Manipulation, Generation and Measurement*. Springer Science and Business Media, New York, 2007.

[12] H. Katsuki, K. Hosaka, H. Chiba, and K. Ohmori. Read and write amplitude and phase information by using high-precision molecular wave-packet interferometry. *Phys. Rev. A.*, 76:013403, 2007.

[13] J. A. Cina. Wave packet interferometry and molecular state reconstruction: Spectroscopic adventures on the left-hand side of the Schrödinger equation. *Annu. Rev.Phys.Chem.*

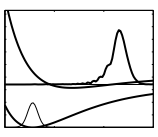

[14] H. Kawashima, M. M. Wefers, and K. Nelson. Femtosecond pulse shaping, multiple-pulse spectroscopy, and optical control. *Annu. Rev. Phys. Chem.*, 46:627–56, 1995.

[15] G. Katz, M. A. Ratner, and R. Kosloff. Decoherence control by tracking a hamiltonian reference molecule. *Phys. Rev. Lett.*, 98:203006, 2007.

[16] J. Degert, C. Meier, B. Chatel, and B. Girard. Coherent control of matter-wave interference in molecular predissociation. *Phys. Rev. A*, 67:041402, 2003.

[17] M. Fushitani, M. Bargheer, M. Gühr, and N. Schwentner. Pump-probe spectroscopy with phase-locked pulses in the condensed phase: decoherence and control of vibrational wavepackets. *Phys. Chem. Chem. Phys.*, 7:3143–3149, 2005.

[18] M. Fushitani, M. Bargheer, M. Gühr, H. Ibrahim, and N. Schwentner. Control of chromophore to bath coupling by interferometry: Cl_2 vibrational wave packets in solid Ar. *J.Phys.B: At. Mol. Opt. Phys.*, 41:074013, 2008.

[19] S. M. Weber, F. Sauer, M. Plewicki, A. Merli, L. Wöste, and A. Lindinger. Multi-objective optimization on alkali dimers. *J. Mod. Opt.*

[20] P. Nuernberger, G. Vogt, T. Brixner, and G. Gerber. Femtosecond quantum control of molecular dynamics in the condensed phase. *Phys. Chem. Chem. Phys*, 9:2470–2497, 2007.

[21] M. Bargheer, A. Borowski, A. Cohen, M. Fushitani, R.B. Gerber, M. Gühr, P. Hamm, H. Ibrahim, T. Kiljunen, M.V. Korolkov, O. Kühn, J. Manz, B. Schmidt, M. Schröder, and N. Schwentner. *Analysis and Control of Ultrafast Photoinduced Reactions, Coherence and control of molecular dynamics in rare gas matrices, Chapter 4*, volume 87, Springer Series in Chemical Physics, O. Kühn, L. Wöste (eds.). Springer, Heidelberg, 2007.

[22] H. Ibrahim, M. Gühr, and N. Schwentner. Valence transitions of Br_2 in Ar matrices: Interaction with the lattice and predissociation. *J. Chem. Phys.*, 128:064504, 2008.

[23] E. J. Heller. The semiclassical way to molecular spectroscopy. *Acc. Chem. Res.*, 14:368, 1981.

[24] E. J. Heller and S. Tomsovic. Postmodern quantum mechanics. *Physics Today*, 46:38, 1993.

[25] C. L. Cohen-Tannoudji, B. Diu, and F. Laloë. *Quantenmechanik*, volume I. Walter de Gruyter, Berlin, 1999.

[26] D. J. Tannor. *Introduction to Quantum Mechanics, A Time-Dependent Perspective*. University Science Books, Sausalito, 2007.

[27] H. Haken and H.C. Wolf. *Molekülphysik und Quantenchemie*. Springer, Berlin.

[28] S. Ruhman, A. Joly, and K. Nelson. Coherent molecular vibrational motion observed in the time domain trough impulsive stimulated raman scattering. *IEEE J. Quant. Electron.*, 24:460–468, 1988.

[29] Ed. H. Paul. *Lexikon der Optik I,II*. Spektrum Akademischer Verlag, Heidelberg, 2003.

[30] Ed. H. Niedrig. *Bergmann Schaefer Lehrbuch der Experimentalphysik Band 3*. Walter de Gruyter, Berlin, 1993.

[31] M. Karavitis, D. Segale, Z. Bihary, M. Pettersson, and V. A. Apkarian. Time-resolved CARS measurements of the vibrational decoherence of I_2 isolated in an Ar matrix. *Low Temp. Phys.*, 29:814–821, 2003.

[32] M. Karavitis and V. A. Apkarian. Vibrational coherence of I_2 in solid Kr. *J. Chem. Phys.*, 120:292–299, 2004.

[33] Z. Bihary, M. Karavitis, and V. A. Apkarian. Onset of decoherence: Six-wave mixing measurements of vibrational decoherence on the excited state of I_2 in solid argon. *J. Chem. Phys.*, 120:8144–8156, 2004.

[34] M. Gühr, M. Bargheer, M. Fushitani, T. Kiljunen, and N. Schwentner. Ultrafast dynamics of halogens in rare gas solids. *Phys. Chem. Chem. Phys.*, 9:779–801, 2007.

[35] W. H. Zurek. Decoherence and the transition from quantum to classical - revisted. *Los Alamos Science*, 27, 2002.

[36] C. Meier and J. A. Beswick. Femtosecond pump-probe spectroscopy of I_2 in a dense rare gas environment: A mixed quantum/classical study of vibrational decoherence. *J. Chem. Phys.*, 121:4550–4558, 2004.

[37] A. Cohen and R. B. Gerber. Photodissociation of F_2 in solid Ar: Electronic state distribution in cage-exit. *Chem. Phys.*

[38] M. Bargheer, A. Cohen, R. B. Gerber, M. Gühr, M. V. Korolkov, J. Manz, M. Y. Niv, M. Schröder, and N. Schwentner. Dynamics of electronic states and spin-flip for photodissociation of dihalogens in matrices: Experiment and semiclassical surface-hopping and quantum model simulations for F_2 and ClF in solid Ar. *J. Phys. Chem. A*, 111:9573–9585, 2007.

[39] A. Borowski and O. Kühn. Towards a quantum mechanical description of the photochemistry of dihalogens in rare gas matrices. *J. of Photochemistry and Photobiology A*, 190:169–176, 2007.

[40] A. Borowski and O. Kühn. Tailoring model hamiltonians for dihalogen - rare gas matrix problems. *Theor. Chem. Acc.*, 117:521–533, 2007.

[41] M. V. Korolkov and J. Manz. Design of uv laser pulses for the preparation of matrix isolated homonuclear diatomic molecules in selective vibrational superposition states. *J. Chem. Phys.*, 126:174306, 2007.

[42] G. Herzberg. *Molecular Spectra and Molecular Structure I. Spectra of Diatomic Molecules*. Van Nostrand Reinhold Company Inc., New York, 1950.

[43] M. Gühr. *Coherent Dynamics of Small Molecules in Rare Gas Crystals*. Cuvillier Verlag, Göttingen, 2005.

[44] T. Young. The Bakerian Lecture. Experiments and Calculations relative to physical optics. *Phil. Trans.*, 94:1–16, 1803.

[45] M. W. Noel and C. R. Stroud. Young's double-slit interferometry within an atom. *Phys. Rev. Lett.*, 75:1252–1255, 1995.

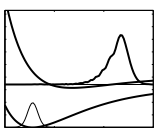

[46] L'Air liquide. *Gas encyclopedia*. Elsevier/North Holland Inc., New York, 1976.

[47] Deutsche Gesetzliche Unfallversicherung. www.dguv.de/bgia/stoffdatenbank.

[48] Merck AG. Sicherheitsdatenblatt Br_2. *www.chemdat.de*.

[49] M. Mandich, P. Beeken, and G. Flynn. Emission spectra and relaxation dynamics of excited $^{79}Br_2$ in Ar and Kr matrices. *J. Chem. Phys.*, 77:702–713, 1982.

[50] W. G. Brown. Vibrational quantum analysis of the visible absorption bands of bromine. *Physical Review*, 38:1179, 1931.

[51] A. A. Passchier, J. D. Christian, and N. W. Gregory. The ultraviolet-visible absorption spectrum of bromine between room temperature and 440°C. *J. Phys. Chem.*, 71:937–942, 1967.

[52] J. Tellinghuisen. Transition strength and potential curves for the valence transitions in Br_2 from reanalysis of the ultraviolet-visible absorption at low resolution. *J. Chem. Phys.*, 115:10417, 2001.

[53] J. Tellinghuisen. Erratum: "Transition strength and potential curves for the valence transitions in Br_2 from reanalysis of the ultraviolet-visible absorption at low resolution". *J. Chem. Phys.*, 118:1573, 2003.

[54] G. Capelle, K. Sakurai, and H. P. Broida. Lifetime and self-quenching cross sections of vibrational levels in the B state of bromine excited by a tunable dye laser. *J. Chem. Phys.*, 54:1728–1730, 1971.

[55] J. A. Coxon. $B^3\Pi 0_u^+ - X^1\Sigma_g^+$ system of ^{79}Br^{79}Br. *J. Mol. Spectr.*, 37:39, 1971.

[56] R. F. Barrow, T. C. Clark, J. A. Coxon, and K. K. Yee. The $B^3\Pi 0_u^+ - X^1\Sigma_g^+$ system of Br_2: Rotational analysis, Franck-Condon factors, and long range potential in the $B^3\Pi 0_u^+$ state. *J. Mol. Spectrosc.*, 51:428–449, 1974.

[57] J. A. Coxon. The Extreme Red Absorption Spectrum of Br_2, $A^3\Pi(1_u) \leftarrow X^1\Sigma_u^+$. *J. Mol. Spectrosc.*, 41:548–565, 1972.

[58] J.A. Coxon. *Low-lying Electronic States of Diatomic Halogen Molecules*. The Chemical Society, Eds. R. F. Barrow, D. A. Long and D. J. Millen, 1973.

[59] J. A. Coxon. Franck-condon factors and r-centroids for halogen molecules - II. the $B^3\Pi(0_u^+)$–$X^1\Sigma_g^+$ system of $^{79}Br^{81}Br$. *J. Quant. Spectrosc. Radiat. Transfer., Pergamon Press*, 12:639–650, 1972.

[60] M. Gühr and N. Schwentner. Effective chromophore potential, dissipative trajectories and vibrational energy relaxation: Br_2 in Ar matrix. *J. Chem. Phys.*, 123:244506, 2005.

[61] A. Sur and J. Tellinghuisen. The D'→A' Transition in Br_2. *J. Mol. Spectrosc.*, 88:323–346, 1981.

[62] E. Hwang, P. J. Dagdigan, and J. Tellinghuisen. Spectroscopy of metastable species in a free-jet expansion: The $\beta \leftarrow A$ transition in Br_2. *J. Mol. Spectrosc.*, 181:297–306, 1997.

[63] P. Berwanger, K. S. Viswanathan, and J. Tellinghuisen. The E→B transition (3000–3140 Å) in Br_2. *J. Mol. Spectrosc.*, 91:275–285, 1982.

[64] S. Yabushita. unpublished ab-initio potentials for Br_2.

[65] Y. Asano and S. Yabushita. Theoretical study of nonadiabatic transitions in the photodissociation of Cl_2 and Br_2. *Chem. Phys. Lett.*, 372:348–354, 2003.

[66] A. C. Albrecht. Polarization and assignments of transitions: The method of photoselection. *J. Mol. Spectrosc.*, 6:84–108, 1961.

[67] J. Michl and E. Thulstrup. *Spectroscopy with polarized light*. VCH Publishers, New York, 1986.

[68] M. L. Klein and J. A. Venables. *Rare Gas Solids Vol. I + II*. Academic Press, London, 1976.

[69] V. A. Apkarian and N. Schwentner. Moleular photodynamics in rare gas solids. *Chem. Rev.*, 99:1481–1514, 1999.

[70] L. Khriachtchev, M. Pettersson, N. Runeberg, J. Lundell, and M. Räsänen. A stable argon compound. *Nature*, 406:874–876, 2000.

[71] R. B. Gerber. Formation of novel rare-gas molecules in low-temperature matrices. *Ann. Rev. Phys. Chem.*, 55:55–78, 2004.

[72] B. S. Ault, W. F. Howard, and L. Andrews. Laser-induced fluorescence and raman spectra of chlorine and bromine molecules isolated in inert matrices. *J. Mol. Spectrosc.*, 55:217–228, 1975.

[73] M. Bargheer, M. Gühr, and N. Schwentner. Depolarization as a probe for ultrafast reorientation of diatomics in condensed phase: ClF vs I_2 in rare gas solids. *J. Chem. Phys.*, 117:5–8, 2002.

[74] T. Kiljunen, M. Bargheer, M. Gühr, N. Schwentner, and B. Schmidt. Photodynamics and ground state librational states of ClF molecule in solid Ar. Comparison of experiment and theory. *Phys. Chem. Chem. Phys.*, 6:2932–2939, 2004.

[75] T. Kiljunen, M. Bargheer, M. Gühr, and N. Schwentner. A potential energy surface and a trajectory study of photodynamics and strong field alignment of ClF molecule in rare gas (Ar,Kr) solids. *Phys. Chem. Chem. Phys.*, 6:2185–2197, 2004.

[76] T. Kiljunen, B. Schmidt, and N. Schwentner. Intense-field alignment of molecules confined in octahedral fields. *Phys. Rev. Lett.*, 94:123003, 2005.

[77] T. Kiljunen, B. Schmidt, and N. Schwentner. Aligning and orienting molecules trapped in octahedral crystal fields. *Phys. Rev. A*, 72:053415, 2005.

[78] T. Kiljunen, B. Schmidt, and N. Schwentner. Time-dependent alignment of molecules trapped in octahedral crystal fields. *J. Chem. Phys.*, 124:164502, 2006.

[79] E. Riedel. *Anorganische Chemie*. Walter de Gruyter, Berlin, 1994.

[80] J. Franck and E. Rabinowitch. Some remarks about free radicals and the photochemistry of solutions. *Trans. Faraday Soc.*, 30:120–131, 1934.

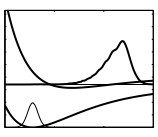

[81] M. Karavitis, R. Zadoyan, and V. A. Apkarian. Time resolved coherent anti-Stokes Raman scattering of I_2 isolated in matrix argon: Vibrational dynamics on the ground electronic state. *J. Chem. Phys.*, 114:4131–4140, 2001.

[82] M. Bargheer, P. Dietrich, K. Donovang, and N. Schwentner. Extraction of potentials and dynamics from condensed phase pump-probe spectra: Application to I_2 in Kr matrices. *J. Chem. Phys.*, 111:8556–8564, 1999.

[83] M. Bargheer, M. Gühr, P. Dietrich, and N. Schwentner. Femtosecond spectroscopy of fragment-cage dynamics: I_2 in Kr. *Phys. Chem. Chem. Phys.*, 4:78–81, 2002.

[84] M. Gühr, M. Bargheer, P. Dietrich, and N. Schwentner. Predissociation and vibrational relaxation in the B state of I_2 in a Kr matrix. *J. Phys. Chem. A*, 106:12002–12011, 2002.

[85] R. Alimi, R. B. Gerber, J. G. McCaffrey, H. Kunz, and N. Schwentner. Delayed and direct cage exit in photodissociation of cl2 in solid ar. *Phys. Rev. Lett.*, 69:856–859, 1992.

[86] A. I. Krylov and R. B. Gerber. Photodissociation dynamics of HCl in solid Ar: Cage exit, nonadiabatic transitions, and recombination. *J. Chem. Phys.*, 106:6574–6587, 1997.

[87] M. Y. Niv, A. I. Krylov, and R. B. Gerber. Photodissociation, electronic relaxation and recombination of HCl in Ar-n(HCl) clusters - Non-adiabatic molecular dynamics simulations. *Farad. Diss.*, 108:243–254, 1997.

[88] M. Y. Niv, M. Bargheer, and R. B. Gerber. Photodissociation and recombination of F_2 molecule in Ar-54 cluster: Nonadiabatic molecular dynamics simulations. *J. Chem. Phys.*, 113:6660–6672, 2000.

[89] M. Bargheer, R. B. Gerber, M. V. Korolkov, O. Kühn, J. Manz, M. Schröder, and N. Schwentner. Subpicosecond spin-flip induced by the photodissociation dynamics of ClF in an Ar matrix. *Phys. Chem. Chem. Phys.*, 4:5554–5562, 2002.

[90] R. B. Gerber, M. V. Korolkov, J. Manz, M. Y. Niv, and B. Schmidt. A reflection principle for the control of molecular photodissociation in solids: Model simulation for f2 in ar. *Chem. Phys. Lett.*, 327:76–84, 2000.

[91] G. Chaban, R. B. Gerber, M. V. Korolkov, J. Manz, M. Y. Niv, and B. Schmidt. Photodissociation dynamics of molecular fluorine in an argon matrix induced by ultrashort laser pulses. *J. Phys. Chem. A*, 105:2770–2782, 2001.

[92] M. V. Korolkov and J. Manz. Initial processes of laser induced diatomic molecular photodissociation in matrices: Quantum simulations for F_2 in ar in reduced dimensionality. *Z. Phys. Chem.*, 217:115–131, 2003.

[93] V. S. Batista and D. F. Coker. Nonadiabatic molecular dynamics simulation of photodissociation and geminate recombination of I_2 in liquid xenon. *J. Chem. Phys.*, 105:4033–4054, 1996.

[94] V. S. Batista and D. F. Coker. Nonadiabatic molecular dynamics simulation of ultrafast pump-probe experiments on I_2 in solid rare gases. *J. Chem. Phys.*, 106:6923–6941, 1997.

[95] M. Gühr, M. Bargheer, and N. Schwentner. Generation of coherent zone boundary phonons by impulsive excitation of molecules. *Phys. Rev. Lett.*, 91:085504, 2003.

[96] M. Gühr and N. Schwentner. Coherent phonon dynamics: Br_2 in solid Ar. *Phys. Chem. Chem. Phys.*, 6:760–767, 2005.

[97] V. E. Bondybey, S. S. Bearder, and C. Fletcher. Br_2 $B^3\Pi(0_u^+)$ excitation spectra and radiative lifetimes in rare gas solids. *J. Chem. Phys.*, 64:5243–5246, 1976.

[98] V. E. Bondybey and C. Fletcher. Photophysics of low-lying electronic states of Cl_2 in rare-gas solids. *J. Chem. Phys.*, 64:3615–3620, 1976.

[99] M. Ovchinnikov and V. A. Apkarian. Mixed-order semiclassical dynamics in coherent state representation: The connection between phonon sidebands and guest-host dynamics. *J. Chem. Phys.*, 108:2277–2284, 1998.

[100] R. H. Silesbee and D. B. Fitchen. Optical analogs of the Mössbauer effect in solids. *Rev. Mod. Phys.*, 36:432–436, 1964.

[101] D. B. Fitchen. *Physics of Color Centers, Ed. w. B. Fowler, Ch. 5: Zero Phonon Transitions*. Academic Press, New York, 1968.

[102] R. Englman, editor. *Non-Radiative Decay of Ions and Molecules in Solids*. North Holland, Amsterdam, 1979.

[103] N. Schwentner. Dynamics of localized excitations from energy and time resolved spectroscopy. *Applied Optics*, 19:4104, 1980.

[104] N. Schwentner, E.-E. Koch, and J. Jortner. *Electronic Excitations in Condensed Rare Gases*. Springer Verlag, Berlin, Heidelberg, 1985.

[105] K. Huang and A. Rhys. Theory of light absorption and non-radiative transitions in F-centres. *Proc. Roy. Soc. London A*, 204:406–423, 1950.

[106] C. J. Delbecq and P. Pringsheim. Absorption bands and lines in irradiated LiF. *J. Chem. Phys.*, 21:794, 1953.

[107] J. Langen, K.-P. Lodemann, and U. Schurath. Effect of guest-host interaction on spectra and relaxation dynamics of matrix isolated Br_2 $B^3\Pi_{0_u^+}$, $A^3\Pi_{1_u}$, and $A'^3\Pi_{2_u}$. *Chem. Phys.*, 112:393–408, 1987.

[108] L. Andrews. Optical spectra of the dibromide and diiodide ions in the matrix-isolated $M^+Br_2^-$ and $M^+I_2^-$. *J. Am. Chem. Soc.*, 98:2152–2156, 1976.

[109] R. Schinke. *Photodissociation Dynamics*. Cambridge University Press, Cambridge / England, 1993.

[110] J. M. Friedman, V. E. Bondybey, and D. L. Rousseau. Br_2 in an Ar matrix: an example of complete damping of the resonance Raman scattering amplitude in the discrete resonance limit. *Chem. Phys. Lett.*, 70:499–503, 1980.

[111] P. Beeken, M. Mandich, and G. Flynn. Photochemical dynamics of $^{79}Br_2$ in Xe matrices. *J. Chem. Phys.*, 76:5995–6001, 1982.

[112] J.-P. Nicolai, L. J. Van De Burgt, and M. C. Heaven. The A' $^3\Pi(2_u)$-$X^1\Sigma_g^+$ emission spectrum of Br_2 in argon matrix. *Chem. Phys. Lett.*, 115:496–500, 1985.

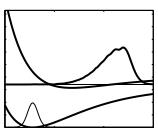

[113] J.-P. Nicolai and M. C. Heaven. Photoselection study of the Br_2 $A \rightarrow X$ emission system in an argon matrix. *J. Chem. Phys.*, 83:6538–6539, 1985.

[114] L. Onsager. Electric moments of molecules in liquids. *J. Am. Chem. Soc.*, 58:1486–1493, 1936.

[115] L. D. Landau and E. M. Lifschitz. *Lehrbuch der theoretischen Physik*, volume III: Quantenmechanik. Akademie-Verlag, Berlin, 1979.

[116] C. Zener. Non-adiabatic crossing of energy levels. *Proc. R. Soc.*, 137:696–702, 1932.

[117] C. Zhu and H. Nakamura. Theroy of nonadiabatic transition for general two-state curve crossing problems. I. nonadiabatic tunneling case. *J. Chem. Phys*, 101, 1994.

[118] C. Zhu and H. Nakamura. Theroy of nonadiabatic transition for general two-state curve crossing problems. II. landau-zener case. *J. Chem. Phys*, 102, 1995.

[119] H. Lefebvre-Brion and R. W. Field. *Perturbations in the Spectra of Diatomic Molecules*. Academic Press, London, 1986.

[120] M. S. Child. Analytical interpretation of predissociation rates: the $B^3\Pi_{0u^+}$ state of Br_2. *J. Phys. B*, 13:2557–2563, 1980.

[121] K. B. McAfee, R. M. Lum, and R. S. Hozack. Excited state bromine atom and molecule reactions. *J. Chem. Phys.*, 64:5073–5076, 1976.

[122] K. B. McAfee and R. S. Hozack. Lifetimes and energy transfer near the dissociation limit in bromine. *J. Chem. Phys.*, 64:2491–2495, 1976.

[123] R. S. Hozack, A. P. Kennedy, and K. B. McAfee. Krypton ion laser-excited fluorescence in bromine. *J. Mol. Spectr.*, 80:239–243, 1980.

[124] M. A. A. Clyne and Michael C. Heaven. Theoretical treatment of the spontaneous predissociation of Br_2, $B^3\Pi(0_u^+)$. *J. Chem. Phys.*, 76:5341–5349, 1982.

[125] Q. Liu, C. Wan, and A. H. Zewail. Solvation ultrafast dynamics of reactions. 13. Theoretical and experimental studies of wave packet reaction coherence and its density dependence. *J. Phys. Chem.*, 100:18666–18682, 1996.

[126] R. Zadoyan, M. Sterling, and V. A. Apkarian. Dynamical spectroscopy of many body interactions, coherent vibrations and predissociation of I_2(B) in solid Kr. *J. Chem. Soc., Faraday. Trans.*, 92:1821–1829, 1996.

[127] R. Zadoyan, M. Sterling, M. Ovchinnikov, and V. A. Apkarian. Predissociation dynamics of I_2 in liquid CCl_4 observed through femtosecond pump-probe measurements: Electronic caging through solvent symmetry. *J. Chem. Phys.*, 107:8446–8460, 1997.

[128] N. F. Scherer, L. D. Ziegler, and G. R. Fleming. Heterodyne-detected time-domain measurement of I_2 predissociation and vibrational dynamics in solution. *J. Chem. Phys.*, 96:5544–5547, 1992.

[129] O. Roncero, N. Halberstadt, and J. A. Beswick. A wave-packet study of Ar...I_2(B) $\rightarrow$ Ar+I+I electronic predissociation. *Chem. Phys. Lett.*, 226:82–87, 1994.

[130] O. Roncero, N. Halberstadt, and J. A. Beswick. A three-dimensional wave packet study of ar ... i-2(b)->ar+i+i electronic predissociation. *J. Chem. Phys.*, 104:7554 – 7560, 1996.

[131] N. Yu, C. J. Margulis, and D. F. Coker. Influence of solvation environment on excited state avoided crossings and photodissociation dynamics. *J. Phys. Chem. B*, 105:6728–6737, 2001.

[132] N. Yu and D. F. Coker. Ion pair state emission from I_2 in rare gas matrices: effects of solvent induced symmetry breaking. *Mol. Phys.*, 102:1031–1044, 2004.

[133] M. Bargheer, M. Gühr, and N. Schwentner. Collisions transfer coherence. *Israel J. Chem.*, 44:9–17, 2004.

[134] V. A. Ermoshin, A. K. Kazansky, and V. Engel. Quantum-classical molecular dynamis simulation of femtosecond spectroscopy on I_2 in inert gases: Mechanisms for the decay of pump-probe signals. *J. Chem. Phys.*, 111:7807–7817, 1999.

[135] V.A. Ermoshin, V. Engel, and C. Meier. Collision-induced bound state motion in I_2. A classical molecular dynamics study. *J. Chem. Phys.*, 113:6585–6591, 2000.

[136] V. A. Ermoshin, V. Engel, and C. Meier. Oscillatory pump-probe signals from deloclized wave packets. *J. Chem. Phys.*, 113:5770–5775, 2000.

[137] V. A. Ermoshin, V. Engel, and A. K. Kazanky. Phase and energy relaxation of vibrational motion and its manifestation in femtosecond pump-probe experiments on I_2 in rare gas enironment. *J. Phys. Chem. A*, 105:7501–7507, 2001.

[138] A. K. Kazansky, V. A. Ermoshin, and V. Engel. Phase-energy approach to collision-induced vibrational relaxation. *J.Chem. Phys.*, 113:8865–8868, 2000.

[139] H. Dubost. *Inert Gases, Chapter 4: Spectroscopy of Vibrational and Rotational Levels of Diatomic Molecules in Rare-Gas Crystals*. Springer, Ed. M. L. Klein, Berlin, 1984.

[140] R. Englman. *Non-Radiative Decay of Ions and Molecules in Solids*. North-Holland Publishing Company, Amsterdam, 1979.

[141] D. Segale, M. Karavitis, E. Fredj, and V. A. Apkarian. Quantum coherent dissipation: A glimpse of the "cat". *J. Chem. Phys.*, 122:111104, 2005.

[142] J. M. Riga and C. C. Martens. Simulation of environmental effects on coherent quantum dynamics in many body systems. *J. Chem. Phys.*, 120:6863, 2004.

[143] M. Comstock, V. V. Lozovoy, and M. Dantus. Rotational wavepcket revivals for phase modulation of ultrafast pulses. *Chem. Phys. Lett.*, 372:739–744, 2003.

[144] EG&G camera manual.

[145] T. C. Gunaratne, X. Zhu, V. V. Lozovoy, and M. Dantus. Symmetry of nonlinear optical response to time inversion of shaped femtosecond pulses as a clock of ultrafast dynamics. *Chem. Phys.*, 338:259–267, 2007.

[146] J.-C. Diels and W. Rudolph. *Ultrashort Laser Pulse Phenomena*. Academic Press, San Diego, California, 1996.

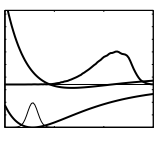

[147] C. Rullière. *Femtosecond Laser Pulses*. Springer Verlag, Berlin, Heidelberg, 1998.

[148] Robert W. Boyd. *Nonlinear Optics*. Academic Press, London, 2003.

[149] Peter Dietrich. Refractn, 1999.

[150] R.L. Fork, O. E. Martinez, and J. P. Gordon. Negative dispersion using pairs of prisms. *Opt. Lett.*, 9:150–152, 1984.

[151] E.B. Treacy. Optical pulse compression with diffraction gratings. *IEEE J. Quantum Eletron.*, QE-5:454–460, 1969.

[152] T. Wilhelm, J. Piel, and E. Riedle. Sub-20-fs pulses tunable across the visible from a blue-pumped single-pass noncollinear parameteric converter. *Opt. Lett.*, 22:1494–1496, 1997.

[153] S. Lochbrunner, J. Piel, S. Schenkl, S. Spörlein, W. Zinth, E. Riedle, and M. Beuttner. Generation of 10 to 50 fs pulses tunable through all the visible and the NIR. *Appl. Phys. B*, 71:457, 2000.

[154] A. Shirakawa and T. Kobayashi. Noncollinearly phase-matched femtosecond optical parameteric amplification with a 2000 cm^{-1} bandwidth. *Appl. Phys. Lett.*, 72:147–149, 1998.

[155] G. Cerullo and S. De Silvestri. Ultrafast optical parametric amplifiers. *Rev. Sci. Instr.*, 74:1, 2003.

[156] S. Linden, H. Giessen, and J. Kuhl. XFROG – a new method for amplitude and phase characterization of weak ultrashort pulses. *Phys. stat. sol. (b)*, 206:119, 1998.

[157] T. M. Shuman, M. E. Anderson, J. Bromage, L. Waxer C. Iaconis, and I. A. Walmsley. Real-time spider: ultrashort pulse characterization at 20 hz. *Opt. Exp.*, 5:134, 1999.

[158] M. M. Wefers and K. A. Nelson. Analysis of programmable ultrashort waveform generation using liquid-crystal spatial light modulators. *J. Opt. Soc. Am. B*, 12:1343, 1995.

[159] R. Trebino, K. W. DeLong, D. N. Fittinghoff, J. N. Sweetser, M. A. Krumbügel, B. A. Richman, and D.J. Kane. Measuring ultrashort laser pulses in the time-frequency domain using frequency-resolved optical gating. *Rev. Sci. Instrum.*, 68:3277–3295, 1997.

[160] J. E. Nicholson, J. Jasapara, W. Rudolph, F.G. Omenetto, and A. J. Taylor. Full-field characterization of femtosecond pulses by spectrum and cross-correlation measurements. *Optics letters*, 24:1774, 1999.

[161] K.W. DeLong, D.N. Fittinghoff, R. Trebino, B.K. Kohler, and K. Wilson. Phase retrieval in frequency-resolved optical gating based on the method of generalized projections. *Opt. Lett.*, 19:2152–2154, 1994.

[162] Software frog 3.2.2. *Femtosoft Technologies*.

[163] M. Dantus, M. J. Rosker, and A. H. Zewail. Real-time femtosecond probing of "transition states" in chemical reactions. *J. Chem. Phys.*, 87:2395–2397, 1987.

[164] R. Zadoyan, P. Ashjian, C. C. Martens, and V. A. Apkarian. Femtosecond dynamics of coherent photodissociation-recombination of I_2 isolated in matrix Ar. *Chem. Phys. Lett.*, 218:504–514, 1994.

[165] N. F. Scherer, R. J. Carlson, A. Matro, M. Du, A. J. Ruggiero, V. Romero-Rochin, J. A. Cina, and G. R. Fleming. Fluorescence-detected wave packet interferometry: Time resolved molecular spectroscopy with sequences of femtosecond phase locked pulses. *J. Chem. Phys.*, 95:1487–1511, 1991.

[166] N. F. Scherer, A. Matro, L. D. Ziegler, M. Du, R. J. Carlson, J. A. Cina, and G. R. Fleming. Fluorescence-detected wave packet interferometry. II. Role of rotations and determination of the susceptibility. *J. Chem. Phys.*, 96:4180–4194, 1992.

[167] M. Born and E. Wolf. *Principles of Optics*. Pergamon Press, London, 1959.

[168] A. M. Weiner. Femtosecond pulse shaping using spatial light modulators. *Rev. Sci. Instr.*, 71:1929, 2000.

[169] J. P. Heritage, A. M. Weiner, and R. N. Thurston. Picosecond pulse shaping by spectral phase and amplitude manipulation. *Opt. Expr.*, 10:609, 1985.

[170] Y. Ding, R. M. Brubaker, D. D. Nolte, M. R. Melloch, and A. M. Weiner. Femtosecond pulse shaping by dynamic holograms in photorefractive multiple quantum wells. *Opt. Lett.*, 22:718, 1996.

[171] D. Kaplan and P. Tournois. *Ultrafast Optics IV, Acousto-optic spectral filtering of femtosecond laser pulses*. Springer, Ed. F. Krausz, 2004.

[172] M. A. Dugan, J. X. Tull, and W. S. Warren. *J. Opt. Soc. Am. B*, 14:2348, 1997.

[173] M.R. Fetterman, D. Goswami, D. Keusters, W. Yang, J.-K. Rhee, and W.S. Warren. Ultrafast pulse shaping: amplification and characterization. *Opt. Exp.*, 3:366, 1998.

[174] A. Weiner, J.P. Heritage, and E. M. Kirschner. High-resolution femtosecond pulse shaping. *J. Opt. Soc. Am. B*, 5:1563, 1988.

[175] G. Stobrawa, M. Hacker, T. Feurer, D. Zeidler, M. Motzkus, and F. Reichel. A new high-resolution femtosecond pulse shaper. *Appl. Phys. B*, 72:627–630, 2001.

[176] S. Postma, P. van der Walle, H. L. Offerhaus, and N. F. van Hulst. Compact high-resolution spectral phase shaper. *Rev. Sci. Instr.*, 76:123105, 2005.

[177] S. M. Weber, A. Lindinger, M. Plewicki, C. Lupulescu, F. Vetter, and L.Wöste. Temporal and spectral optimization course analysis of coherent control experiments. *Chem. Phys.*, 306.

[178] A. Lindinger, S. M. Weber, C. Lupulescu, F. Vetter, M. Plewicki, A. Merli, L. Wöste, A. F. Bartelt, and H. Rabitz. Revealing spectral field features and mechanistic insights by control pulse cleaning. *Phys. Rev. A*, 71.

[179] T. Brixner, G. Krampert, and R. Selle T. Pfeifer, M. Wollenhaupt G. Gerber, O. Graefe, C. Horn, D. Liese, and T. Baumert. Quantum control by ultrafast polarization shaping. *Phys. Rev. Lett.*, 92:20, 2004.

[180] M. Plewicki, F. Weise, S. M. Weber, and A. Lindinger. Phase, amplitude, and polarization shaping with a pulse shaper in a mach-zehnder interferometer. *Appl. Opt*, 45.

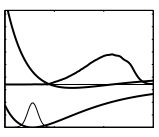

[181] M. Plewicki, S. M. Weber, F. Weise, and A. Lindinger. Independent control over the amplitude, phase, and polarization of femtosecond pulses. *Appl. Phys. B*, 86.

[182] O. E.. Martínez. 3000 times grating compressor with positive group velocity dispersion: Application to fiber compensation in 1.3-1.6 μm region. *IEEE J. Quantum Electronics*, 23:59, 1987.

[183] O. E.. Martínez. Design of high-power ultrashort pulse amplifiers by expansion and recompression. *IEEE J. Quantum Electronics*, 23:1385, 1987.

[184] A. Bartelt. *Steuerung der Wellenpaketdynamik in kleinen Alkaliclustern mit optimierten Femtosekundenpulsen*. Thesis, FU Berlin, 2002.

[185] Spatial light modulator system. *User's manual*. Cambridge Research & Instrumentation, Inc., 2003.

[186] J. C. Vaughan, T. Feurer, K. W. Stone, and K. A. Nelson. Analysis of replica pulses in femtosecond pulse shaping with pixelated devices. *Optics Express*, 14:1314, 2006.

[187] T. Baumert, T. Brixner, V. Seyfried, M. Strehle, and G. Gerber. Femtosecond pulse shaping by an evolutionary algorithm with feedback. *Appl. Phys. B*, 65:779, 1997.

[188] F. Weise, S. M. Weber, M. Plewicki, and A. Lindinger. Application of phase, amplitude, and polarization shaped pulses for optimal control on molecules. *Chem. Phys.*, 332:313–317, 2007.

[189] B. Schmidt, M. Hacker, G. Stobrawa, and T. Feurer. LAB2-a virtual femtosecond laser lab, http://www.lab2.de, 2002.

[190] N. F. Scherer, A. J. Ruggiero, M. Du, and G. R. Fleming. Time resolved dynamics of isolated molecular systems studied with phase-locked femtosecond pulse pairs. *J. Chem. Phys.*, 93:856–857, 1990.

[191] J. F. Christian, B. Broers, J. H. Hoogenraad, W. J. van der Zande, and L. D. Noordam. Rubidium electronic wavepackets probed by a phase-sensitive pump-probe technique. *Optics Communications*, 103:79–84, 1993.

[192] R. R. Jones, D. W. Schumacher, T. F. Gallagher, and P. H. Bucksbaum. Bound-state interferometry using incoherent light. *J. Phys. B: At. Mol. Opt. Phys.*, 28:L405–L411, 1995.

[193] M. A. Bouchene, C. Nicole, and B. Girard. Wavepacket interferometry with chirped pulses. *J. Phys. B: At. Mol. Opt. Phys.*, 32:5167–5177, 1999.

[194] Y. Liau, A. N. Unterreiner, Q. Chang, and N. F. Scherer. Ultrafast dephasing of single nanoparticles studied by two-pulse second-order interferometry. *J. Phys. Chem. B*, 105:2135 – 2142, 2001.

[195] M. Wollenhaupt, A. Assion, D. Liese, Ch. Sarpe-Tudoran, T. Baumert, S. Zamith, M. A. Bouchene, B. Girard, A. Flettner, U. Weichmann, and G. Gerber. Interferences of ultrashort free electron wave packets. *Phys. Rev. Lett.*, 89:173001, 2002.

[196] S.Sato, Y. Nishimura, Y. Sakata, and I. Yamazaki. Coherent control of oscillatory excitation transfer in dithia-1,5[3,3]anthracenophane by a phase-locked femtosecond pulse pair. *J. Phys. Chem. A*, 107:10019 – 10025, 2003.

[197] C. Petersen, E. Péronne, J. Thogersen, H. Stapelfeldt, and M. Machholm. Control and imaging of interfering wave packets in dissociating i_2 molecules. *Phys. Rev. A*, 70:033404, 2004.

[198] P. C. M. Planken, I. Brener, M. C. Nuss, M. S. C. Luo, and S. L. Chuang. Coherent control of terahertz charge oscillations in a coupled quantum well using phase-locked optical pulses. *Phys. Rev. B*, 48:4903–4906, 1993.

[199] Q. Hong, J. Durrant, G. Hastings, G. Porter, and D. R. Klug. Sub-picosecond oscillatory phenomena in silica glasses. *Chem. Phys. Lett.*, 202:183–185, 1993.

[200] A. P. Heberle, J. J. Baumberg, and K. Köhler. Ultrafast coherent control and destruction of excitons in quantum wells. *Phys. Rev. Lett.*, 75:2598–2601, 1995.

[201] H. Petek, A. P. Heberle, W. Nessler, H. Nagano, S. Kubota, S. Matsunami, N. Moriya, and S. Ogawa. Optical phase control of coherent electron dynamics in metals. *Phys. Rev. Lett.*, 79:4649–4652, 1997.

[202] M. Woerner and J. Shah. Resonant secondary emission from two-dimensional excitons: Femtosecond time evolution of the coherence properties. *Phys. Rev. Lett.*, 81:4208–4211, 1998.

[203] N. H. Bonadeo, J. Erland, D. Gammon, D. Park, D. S. Katzer, and D. G. Steel. Coherent optical control of the quantum state of a single quantum dot. *Science*, 282:1473–1476, 1998.

[204] P. I. Tamborenea and H. Metiu. Intersubband wave packet interferometry with semiconductor nanostructures. *Phys. Lett. A*, 240:265–270, 1998.

[205] Y. Mitsumori, M. Mizuno, S. Tanji, T. Kuroda, and F. Minami. Coherent transients involving 2p excitons in znse. *J. Luminescence*, 76.

[206] C. Leichtle, W. P. Schleich, I. Sh. Averbukh, and M. Shapiro. Wave packet interferometry without phase-locking. *J. Chem. Phys.*, 108:6057–6067, 1998.

[207] V. Szöcs and H. F. Kauffmann. Fluorescence interference noise in a two-site system: Excitation transfer dynamics from intensity fluctuations. *J. Chem. Phys.*, 109:7431–7442, 1998.

[208] A. Tortschanoff, K. Brunner, Ch. Warmuth, and H. F. Kauffmann. Interference of optical coherent transients in pentacene/p-terphenyl: Femtosecond beats probed by correlated fluorescence fluctuations. *J. Phys. Chem. A*, 103:2907 – 2911, 1999.

[209] A. Tortschanoff, K. Brunner, Ch. Warmuth, and H. F. Kauffmann. Coherence from fluorescence correlations: Oscillatory femtosecond fluorescence in pentacene/p-terphenyl. *J. Chem. Phys.*, 110:4493–4504, 1999.

[210] J. Bok, A. Tortschanoff, F. Šanda, V. Čáek, and H. F. Kauffmann. The convolution problem in coin spectroscopy. *Chem. Phys.*, 244:89–100, 1999.

[211] T. Yoda, T. Fuji, T. Hattori, and H. Nakatsuka. Observation of the waveform of accumulated photon echoes in a dye-doped polymer film by use of an interferometer. *J. Opt. Soc. Am. B*, 16:1768–1772, 1999.

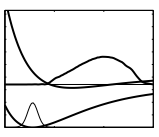

[212] Ch. Warmuth, A. Tortschanoff, F. Milota, M. Shapiro, Y. Prior, I. Sh. Averbukh, W. Schleich, W. Jakubetz, and H. F. Kauffmann. Studying vibrational wavepacket dynamics by measuring fluorescence interference fluctuations. *J. Chem. Phys.*, 112:5060–5069, 2000.

[213] Y. Mitsumori, T. Kuroda, and F. Minami. Manipulation of 2p excitonic wave function in znse. *J. Luminescence*, 87-89:914–916, 2000.

[214] H. Petek, H. Nagano, M. J. Weida, and S. Ogawa. Surface femtochemistry: Frustrated desorption of alkali atoms from noble metals. *J. Phys. Chem. B*, 105:6767 – 6779, 2001.

[215] Q. Luo, D. C. Dai, G. Q. Wang, V. Ninulescu, X. Y. Yu, L. Luo, J. Y. Zhou, and Y. J. Yan. Theory and experiment of coherent wave packet dynamics in rare earth solids: Absorption spectrum vs femtosecond fringe-resolved interferogram. *J. Chem. Phys.*, 114:1870–1875, 2001.

[216] Ch. Warmuth, A. Tortschanoff, F. Milota, M. Leibscher, M. Shapiro, Y. Prior, I. Sh. Averbukh, W. Schleich, W. Jakubetz, and H. F. Kauffmann. Molecular quantum dynamics in a thermal system: Fractional wave packet revivals probed by random-phase fluorescence interferometry. *J. Chem. Phys.*, 114:9901–9910, 2001.

[217] J. Sperling, F. Milota, A. Tortschanoff, Ch. Warmuth, B. Mollay, H. Bässler, and H. F. Kauffmann. Femtosecond excitation tuning and site energy memory of population transfer in poly(p-phenylenevinylene): Gated luminescence experiments and simulation. *J. Chem. Phys.*, 117:10877, 2002.

[218] F. Milota, J. Sperling, A. Tortschanoff, V. Szöcs, L. Kuna, and H. F. Kauffmann. Probing phase relaxation by measuring fluorescence interference: polarization beating and electronÐphonon coupling in conjugated polymers. *J. Luminescence*, 108:205–209, 2004.

[219] F. Milota, A. Tortschanoff, J. Sperling, L. Kuna, V. Szöcs, and H.F. Kauffmann. Femtosecond coherence in poly(p-phenylene- vinylene) Ð polarization beatings and phase-relaxation probed by wavepacket fluorescence interferometry. *Appl. Phys. A*, 78:497–503, 2004.

[220] Y. Cao, L. Zhang, Z. Sun Y. Yang, and Z. Wang. Molecular rovibrational dynamics investigated by two-photon wavepacket interferometry with phase-locked pulse pairs. *Chem. Phys. Lett.*, 442:53–57, 2007.

[221] K. Ohmori, Y. Sato, E. E. Nikitin, and S.A. Rice. High-precision molecular wave-packet interferometry with HgAr dimers. *Phys. Rev. Lett.*, 91:243003, 2003.

[222] O. Kinrot, I. Sh. Averbukh, and Y. Prior. Measuring coherence while observing noise. *Phys. Rev. Lett.*, 75:3822–3825, 1995.

[223] P. Brumer and M. Shapiro. Control of unimolecular reactions using coherent light. *Chem. Phys. Lett.*, 126:541–546, 1986.

[224] C. Chen, Y. Yin, and D.S. Elliott. Interference between optical transitions. *Phys. Rev. Lett.*, 64:507, 1990.

[225] D. J. Tannor, R. Kosloff, and S. A. Rice. Coherent pulse sequence induced control selectivity of reactions: Exact quantum mechanical calculations. *J. Chem. Phys.*, 85:5805, 1986.

[226] T. Baumert, M. Grosser, R. Thalweiser, and G. Gerber. Femtosecond time-resolved molecular multiphoton ionization: The na_2 system. *Phys. Rev. Lett.*, 67:3753, 1991.

[227] S. Shi, A. Woody, and H. Rabitz. Optimal control of selective vibrational excitation in harmonic linear chain molecules. *J. Chem. Phys.*, 88:6870, 1988.

[228] C. J. Bardeen, V. V. Yakovlev, K. R. Wilson, S. D. Carpenter, P. M. Weber, and W. S. Warren. Feedback quantum control of molecular electronic population transfer. *Chem. Phys. Lett.*, 280:151, 1997.

[229] V. D. Kleiman, S. M. Arrivo, E. J. Heilweil, and J. S. Melinger. Controlling condensed phase vibrational excitation with tailored infrared pulses. *Chem. Phys*, 223:207, 1998.

[230] Y. Fujii, N. A. Lurie, R. Pynn, and G. Shirane. Inelastic neutron scattering from solid ^{36}Ar. *Phys. Rev. B*, 10:3647–3659, 1974.

[231] K. K. Rebane. *Impurity Spectra of Solids*. Plenum Press, New York, 1970.

[232] D. Hsu and J. L. Skinner. Nonperturbative theory of temperature-dependent optical dephasing in crystals. II. pseudolocal phonons. *J. Chem. Phys.*, 83:2097–2106, 1985.

[233] D. Kuszner and N. Schwentner. Vibrational relaxation in the lowest electronically excited state of N_2 in solid Kr and Xe. *J. Chem. Phys*, 98:6965, 1993.

[234] M. Bargheer, J. Pietzner, P. Dietrich, and N. Schwentner. Ultrafast laser control of iononic-bond formation: ClF in Ar solids. *J. Chem. Phys.*, 115:9827–9833, 2001.

[235] M. Bargheer. *Ultrafast Photodynamics in Condensed Phase: ClF, Cl_2 and I_2 in Solid Rare Gases*. Shaker Verlag, Aachen, 2002.

[236] D. Tannor. Homepage http://www.weizmann.ac.il/chemphys/tannor/home.html.

[237] M. Gühr. unpublished results.

[238] J. Langen. *Laserinduzierte Fluoreszent matrixisolierter Halogene und ihrer Edelgas Excimere*. Dissertation, Bonn, 1985.

[239] H. Okabe. *Photochemistry of small molecules*. John Wiley & Sons, New York, 1978.

[240] Th. Udem, R. Holzwarth, and T. W. Hänsch. Optical frequency metrology. *Nature*, 416:233–237, 2002.

[241] A. Borrmann and C. C. Martens. Nanoscale shock wave generation by photodissociation of impurities in solids: A molecular dynamics study. *J. Chem. Phys.*, 102:1905–1916, 1995.

[242] R. Zadoyan, J. Almy, and V. A. Apkarian. Lattice dynamics from the 'eyes' of the chromophore, real-time studies of I_2 isolated in rare gas matrices. *Faraday Discuss.*, 108:255–269, 1997.

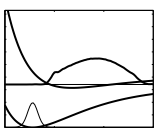

Appendix A

Example of chirped pulses, chirp parameters γ and β

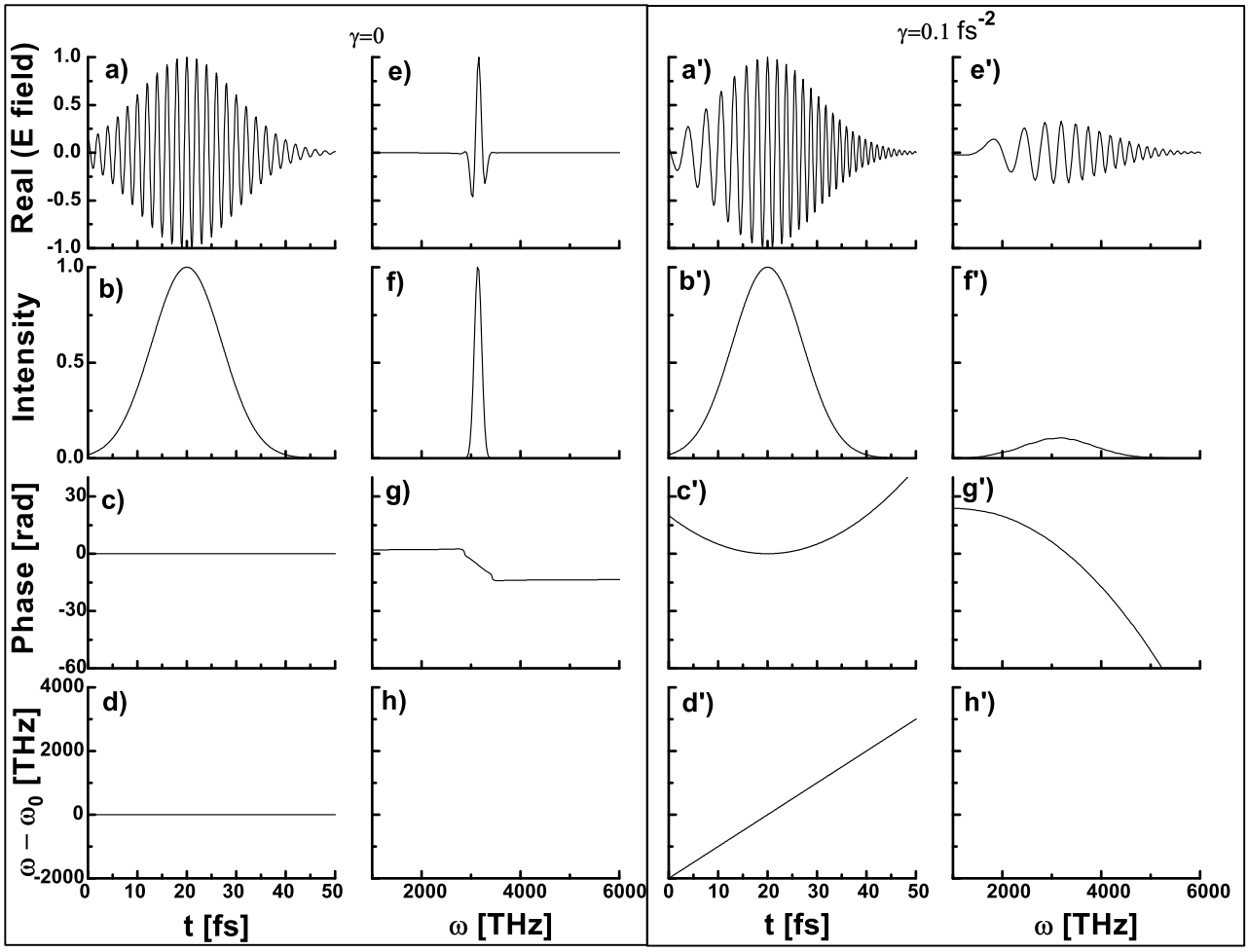

Figure 7.1: Chirp effect when applying a positive chirp in the time domain to a Gaussian pulse. First and second column represent the time domain, second and fourth column the frequency domain. Herewith the left box includes the unchirped pulse and the right box a chirp of $\gamma = 0.1\,\mathrm{fs}^{-2}$. First row contains the real part of the electric field and the power spectrum is given in the second row. Phases are shown in the third row and for the time domain also their derivative, showing the frequency distribution around the centre frequency ω_0.

Figures 7.1 and 7.2 give an overview on the different chirp parameters γ and β which were introduced in Sec. 3.3.2 and their consequence on electric field and intensity distribution, respectively. Initial situation is an unchirped Gaussian pulse ($\gamma = 0, \omega_0 = 2\pi 5 \cdot 10^{14}\,\mathrm{Hz}$, corresponding to 600 nm) in time domain with a duration of $\tau = 10\,\mathrm{fs}$ (Fig. 7.1a, real part of the electric field), corresponding to a FWHM length of 17 fs in intensity (Fig. 7.1b). Phase $vs.$ time is shown in Fig. 7.1c

with a linear behaviour, since the pulse is centred at 20 fs, and further the frequency distribution around centre frequency ω_0 in Fig. 7.1d. The second column displays the Fourier transform of the complex field, again with real part of the electric field (Fig. 7.1e, which is mathematically correct, but physically hardly to interpret), its power spectrum in Fig. 7.1f and the phase in Fig. 7.1g. For having no physical interpretation, Fig. 7.1h is left empty. Analogously, the next two columns give the situation for applying a positive chirp of $\gamma = 0.1\,\mathrm{fs}^{-2}$. The time envelope in Figs. 7.1a' and b') is unchanged but now the quadratic phase results in a linear frequency variation with time (c' and d'). Especially Figs. 7.1a' and d') illustrate that in the case of positive chirp lower frequencies occur at earlier times and higher frequencies at later times. Fourier transforming this reveals the generation of new frequencies, since the spectrum in Fig. 7.1f' is broadened by a factor of ten; its maximum was normalized to the one of the unchirped pulse of Fig. 7.1f.

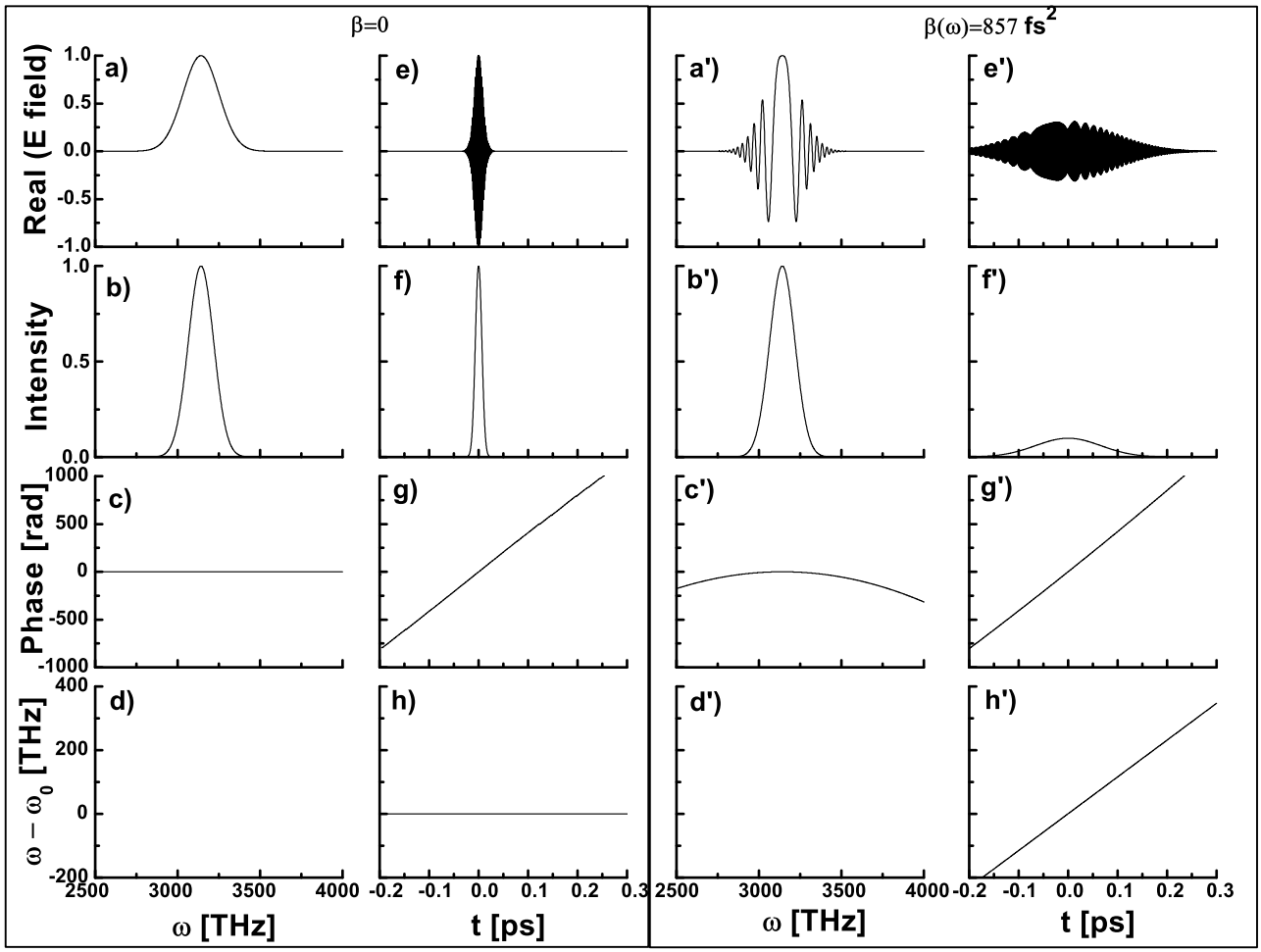

Figure 7.2: This figure is the counterpart to Fig. 7.1, here the corresponding positive chirp of $\beta = 857 fs^2$ is utilized in the spectral domain resulting in a time broadening, whereas the spectral width is unchanged. For a further explanation see text.

The relation of Eq. 3.5 was used in Fig. 7.2 to determine the corresponding parameters in frequency domain, where η was determined to be $108.5 \cdot 10^{14}$Hz leading to $\beta = 857\mathrm{fs}^2$ for the right box. Here the initial definition of $\epsilon(\omega)$ was Fourier transformed into time domain, the structure was kept as in Fig. 7.1, only with switched columns and one can see the contrary behaviour, whether the chirp is applied in time or in frequency domain. The latter leads to a broadening by a factor of ten of the time duration ($\Delta\tau$ in Fig. 7.2 f and f'), whereas the spectral width is not affected ($\Delta\eta$

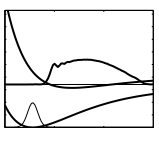

in Fig. 7.2 b and b'). Without a chirp (left box) the time dependent phase is zero (Fig. 7.2 c) and the phase over frequency shows a linear dependence, since the pulse was centred around ω_0. In the case of positive chirp in the right box, the quadratic phase in time (Fig. 7.2 g) causes a quadratic phase of opposite curvature in frequency. However, the superimposed linear phase is so strong, that it cannot be observed in Fig. 7.2 g'. Nevertheless, its derivative in Fig. 7.2 h' clearly gives the linear dependence of frequency $\omega(t)$, which had the constant value ω_0 for $\beta = 0$ (Fig. 7.2 h).

Concerning the chirp units, for the example value of $\beta(\omega) = 857\,\mathrm{fs}^2$ used above, the experimental chirp unit leads with Eqs. 3.12 and 3.13 to $\beta(\nu) = 33833\,\mathrm{fs}^2$ or $\beta'(\nu) = 1.01\,\mathrm{fs\ cm}$.

The Wigner representation is an approach to observe the effects in spectral and time domain simultaneously, as is shown in Sec. 3.3.2 and helps to transfer the results of Fourier transformation to the real experimental situation. For example one has to keep in mind, that an extension of the spectral width η can only occur in nonlinear optical processes.

Publications

Articles and book chapters:

- H. Ibrahim, M. Héjjas, and N. Schwentner, "Tracking intra-molecular and matrix coherences by ultrashort pulse trains", *Phys. Rev. Lett.*, 2008, submitted
- H. Ibrahim, M. Gühr, and N. Schwentner, "Valence transitions of Br_2 in Ar matrices: Interaction with the lattice and predissociation", *J. Chem. Phys.*, 128:064504, 2008
- M. Fushitani, M. Bargheer, M. Gühr, H. Ibrahim and N. Schwentner, "Control of chromophore to bath coupling by interferometry: Cl_2 vibrational wave packets in solid Ar", *J.Phys.B: At. Mol. Opt. Phys.*, 41:074013, 2008
- M. Bargheer, A. Borowski, A. Cohen, M. Fushitani, R.B. Gerber, M. Gühr, P. Hamm, H. Ibrahim, T. Kiljunen, M.V. Korolkov, O. Kühn, J. Manz, B. Schmidt, M. Schröder and N. Schwentner, "Analysis and Control of Ultrafast Photoinduced Reactions, Coherence and control of molecular dynamics in rare gas matrices", Springer Series in Chemical Physics 87, Chapter 4, O. Kühn, L. Wöste (eds.), Heidelberg, 2007
- M. Eichelbaum, B. E. Schmidt, H. Ibrahim and K. Rademann, "Three-photon-induced luminescence of gold nanoparticles embedded in and located on the surface of glassy nanolayers", *Nanotechnology*, 18:1-8(355702), 2007
- M. Gühr, H. Ibrahim and N. Schwentner, ”Controlling vibrational wave packets revivals in condensed phase: Dispersion and coherence for Br_2 in solid Ar”, *Phys. Chem. Chem. Phys.*,6:5353-5361, 2004

Conference contributions:

Talks:

- 6th International Conference on Cryo Crystals, Charkov/Ukraine, 2006
- DPG Frühjahrstagungen 2006, 2007 und 2008

Poster presentations:

- 5th International Conference on Low Temperature Chemistry, Berlin, 2004
- Gordon Research Conference on Quantum Control of Light and Matter, New Port/USA, 2007

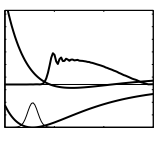

Mein Lebenslauf wird aus datenschutzrechtlichen Gründen nicht veröffentlicht

Danksagung

Mein grösster Dank gilt Herrn Prof. Schwentner für das Schaffen einer herzlichen Arbeitsatmosphäre und seine herausragende Betreuung, die das gedankliche Fortbewegen in Potentialtälern ebenso mit einschloss, wie das reale Gleiten auf schneebedeckten Bergen. Die Superposition mit intensiven Diskussionen hat diese Arbeit konstruktiv interferieren lassen.
Meinen Einstieg in die Wellepaketdynamik und die Experimente am Brom hat Dr. Markus Gühr durch viele anschauliche Erklärungen sehr erleichtert. So durfte ich z.B. lernen, wie Matrix - Phononen durch ABBA angeregt werden. Ihm verdanke ich sehr wertvolle Hinweise für die Korrektur meiner Arbeit und ultraschnelle Reaktionen.
Moniká Héjjas hat mich bei den Pulse - Shaper Experimenten tatkräftig unterstützt und viele kritische Fragen gestellt. Vielen Dank dafür und viel Erfolg bei den weiteren Meßnächten.
Bei Dr. Mizuho Fushitani möchte ich mich für die sehr gute Zusammenarbeit bei den Interferometer - Experimenten bedanken, sowie für den Einblick in eine andere Kultur. Das gilt ebenso für den redseligen Finnen Dr. Toni Kiljunen.
Vielen Dank an die Vertreter der theoretischen Chemie: Prof. Manz, Prof. Kühn, Dr. Korolkov und ganz besonders Alexander Borowski, für das erfolgreiche Streben nach einer gemeinsamen Sprache für Theorie und Experiment. Prof. Yabushita hat freundlicherweise die Ab - initio Potentiale von Br_2 zur Verfügung gestellt.
Die jetzigen und ehemaligen Mitglieder der Arbeitsgruppe, Nina und Leo Owschimikow, Lisa Krocker, Falk Königsmann, Jochen Maurer, Philipp Giese, Ingeborg Twesten und Dr. Manfred Soltwisch tragen und trugen zu einer sehr angenehmen Arbeitsatmosphäre bei, die den Aufenthalt in der Uni mit viel Spaß versieht - solange es nicht ums Essen geht. Vielen Dank auch an Prof. David Anderson für die sprachlichen Korrekturen dieser Arbeit.
Dank auch an Roswitha Brunn für die Beratung in der Handhabung des Broms und den intensiv färbenden Pülverchen, sowie an die Männer, in deren Adern flüssiges Helium fließt.
Von der ZEDV wurde ich in Rat und Tat im Umgang mit Urzeit – Rechnern, virtuellen Festplatten und ZIP - Laufwerken unterstützt, welche mich bewahrten, 500 MB Daten per Disketten zu sichern. Danke dafür und auch an Dr. Stefan Weber, für den Strickkurs mit LabVIEW - Fäden.
Dank auch an die DFG mit dem SFB 450, für die finanzielle Unterstützung, sowie ihren Vertretern auf Erden, Frau Apelt und Herrn Abt.
Bei meinen Eltern bedanke ich mich für alles was sie mir mitgegeben haben. Und bei Bruno für die Koexistenz von Himmelsspinnen und Lasern. Viel Glück für den Endspurt.